Interactions Within and Between Cytoskeletal Filaments

Dissertation

for the award of the degree
“Doctor rerum naturalium” (Dr. rer. nat.)
of the Georg-August-Universität Göttingen

within the doctoral program
Physics
of the Georg-August University School of Science (GAUSS)

submitted by
Charlotta Marian Lorenz
from Oldenburg

Göttingen, 2021

Thesis Committee

Prof. Dr. Sarah Köster
Institute for X-Ray Physics
University of Göttingen

Prof. Dr. Stefan Klumpp
Institute for the Dynamics of Complex Systems
University of Göttingen

Prof. Dr. Sebastian Kruss
Department of Physical Chemistry II
University of Bochum

Members of the Examination Board

Reviewer: Prof. Dr. Sarah Köster
Institute for X-Ray Physics
University of Göttingen

2nd Reviewer: Prof. Dr. Stefan Klumpp
Institute for the Dynamics of Complex Systems
University of Göttingen

Further Members of the Examination Board

Prof. Dr. Sebastian Kruss
Department of Physical Chemistry II
University of Bochum

Prof. Dr. Timo Betz
Third Institute of Physics
University of Göttingen

Dr. Sarah Adio
Institute of Microbiology and Genetics
University of Göttingen

Prof. Dr. Annette Zippelius
Institute for Theoretical Physics
University of Göttingen

Date of oral examination: 06.10.2021

“Nothing in life is to be feared, it is only to be understood. Now is the time to understand more, so that we may fear less.”

– Marie Skłodowska Curie.

Contents

1 Introduction 1

2 State of the Art 5
2.1 Intermediate Filaments 5
2.1.1 Assembly and Structure of Intermediate Filaments 5
2.1.2 Different Types of Intermediate Filaments 7
2.2 Experiments on Intermediate Filaments Under Load 8
2.2.1 Bundles Under Load 8
2.2.2 Individual Filaments Under Load 9
2.2.3 Individual Filaments Under Repeated Load 10
2.3 Models and Simulations of Intermediate Filaments Under Load 12
2.3.1 Molecular Dynamics Simulations 12
2.3.2 Two- and Three-State Models 12
2.3.3 Monte-Carlo Simulations 13
2.4 Microtubules 16
2.4.1 Structure and Assembly of Microtubules 16
2.4.2 Dynamic Instability of Microtubules 18
2.4.3 Binding Energy of Tubulin Dimers Within the Microtubule 18
2.5 Models and Simulations of Dynamic Microtubules 20
2.6 Reconstituted Cytoskeletal Networks 21
2.6.1 Reconstituted Cytoskeletal Networks of Intermediate Filaments 22
2.6.2 Reconstituted Composite Cytoskeletal Networks 22
2.7 Scope of this thesis 24

3 Theoretical Background 27
3.1 Optical Tweezers 27
3.1.1 Physics of Optical Tweezers 28
3.1.2 Calibration of Optical Tweezers 30
3.2 Bonds Under Tension 32
3.2.1 Bell-Evans Kinetics and Energy Landscapes of Single Bonds 32
3.2.2 Parallel Bonds 34

4 Materials and Methods 37
4.1 Protein Purification 37
4.1.1 Intermediate Filament Proteins 37
4.1.2 Tubulin 38
4.2 Protein Labeling 38
4.2.1 Intermediate Filament Proteins 38
4.2.2 Tubulin 39

4.3 Filament Assembly . . . 39
  4.3.1 Keratin Intermediate Filaments . . . 39
  4.3.2 Vimentin Intermediate Filaments . . . 39
  4.3.3 Stabilized Microtubules . . . 39
  4.3.4 Determination of Vimentin Filament Length Distributions . . . 40
4.4 Optical Tweezers Measurements . . . 41
  4.4.1 Stretching of Single Intermediate Filaments . . . 41
  4.4.2 Analysis of the Force-Strain Curve of Single Intermediate Filaments . 41
  4.4.3 Measurements of Interactions Between Single Filaments . . . 45
  4.4.4 Analysis of the Interactions Between Single Filaments . . . 46
4.5 Atomic Force Microscopy . . . 50
  4.5.1 Sample Preparation and Measurement . . . 50
  4.5.2 Analysis of Filament Height . . . 50
4.6 Total Internal Reflection Microscopy . . . 51
  4.6.1 Measurements of Dynamic Microtubules . . . 51
  4.6.2 Analysis of Microtubule Dynamics . . . 51

5 Models and Simulations 53
5.1 Monte-Carlo Simulations of Intermediate Filaments under Load . . . 53
  5.1.1 Uncoupled Subunits Within the Intermediate Filament . . . 54
  5.1.2 Coupled Subunits Within the Intermediate Filament . . . 55
  5.1.3 Subunits Coupled by Springs Within the Intermediate Filament . . . 58
5.2 Interactions Between Filaments . . . 60
  5.2.1 Estimate of the Bundling Probability of Microtubules and Vimentin Intermediate Filaments . . . 60
  5.2.2 Model . . . 61
  5.2.3 Numerical Solution . . . 63
  5.2.4 Simulation . . . 63
5.3 Dynamic Microtubules Interacting With Intermediate Filaments . . . 64
  5.3.1 Dynamic Microtubules Without Additional Interactions . . . 64
  5.3.2 Dynamic Microtubules Interacting with Intermediate Filaments . . . 66
  5.3.3 Estimate of the Binding Energy of Tubulin Dimers Within the Microtubule Lattice . . . 68

6 Interactions and Mechanics Within Single Intermediate Filaments Under Load 69
6.1 Lateral Subunit Coupling Determines Intermediate Filament Mechanics . . . 69
  6.1.1 Abstract . . . 70
  6.1.2 Introduction . . . 70
  6.1.3 Materials and Methods . . . 71
  6.1.4 Results . . . 72
  6.1.5 Discussion and Summary . . . 76
  6.1.6 Supplementary Material . . . 77
6.2 Mechanics of Single, Chemically Stabilized Keratin Intermediate Filaments . 79
6.3 Tuning Intermediate Filament Mechanics by Variation of pH and Ion Charge 80

6.4 Softening of Vimentin Intermediate Filaments due to Post-translational Modifications . . . 84

7 Effects of Interactions Within Intermediate Filaments on Filament Mechanics During Repeated Load 89

7.1 Introduction . . . 89
7.2 Materials and Methods . . . 91
7.3 Results and Discussion . . . 92
7.4 Discussion and Summary . . . 96
7.5 Supplementary Information . . . 97

8 Direct Interactions Between Cytoskeletal Filaments 99

8.1 Vimentin Intermediate Filaments Stabilize Dynamic Microtubules by Direct Interactions . . . 99
  8.1.1 Abstract . . . 100
  8.1.2 Introduction . . . 100
  8.1.3 Results . . . 101
  8.1.4 Discussion . . . 111
  8.1.5 Supplementary Figures . . . 113
8.2 Multiscale Mechanics and Temporal Evolution of Vimentin Intermediate Filament Networks . . . 115

9 Discussion, Outlook and Conclusion 119

9.1 Discussion and Outlook . . . 119
9.2 Conclusion . . . 125

References 127

Acknowledgements 147

List of Abbreviations . . . 149
List of Variables . . . 150
Curriculum Vitae . . . 161

Appendix 162

List of Publications . . . 162

Chapter 1

Introduction

The human body consists of more than 15 trillion cells which can be classified into more than 200 different cell types [1, 2]. Each cell type has a very specific function to ensure the well-being of the entire organism [3]. These functions strongly rely on the "skeleton of the cell", the cytoskeleton. The cytoskeleton consists of several different biopolymers, passive crosslinkers and active motor proteins which interact with each other. Actin filaments, microtubules and intermediate filaments (IFs) are three cytoskeletal biopolymer families, shown in fluorescence images in Fig. 1.1. Each of these biopolymers is responsible for certain cellular tasks: Amongst other functions, actin filaments regulate cell motility, form the contractile ring during cell division, contract the cell together with myosin motor proteins and maintain the cell shape [3]. Together with other proteins, microtubules pull the chromosomes apart during cell division and operate as a "railway system" for nutrient transport inside the cell [3]. Microtubules are also highly dynamic filaments which, for example, allows them to efficiently couple to chromosomes during cell division [3–5]. IFs act as "shock absorbers" in cells, they ensure mechanical stability of the cell and they connect and stabilize cell-cell junctions in desmosomes [3, 6–9].

In contrast to actin and tubulin, IF proteins are expressed in a cell-type specific manner [10–12]. For example, smooth muscle cells primarily express desmin, fibroblasts primarily express

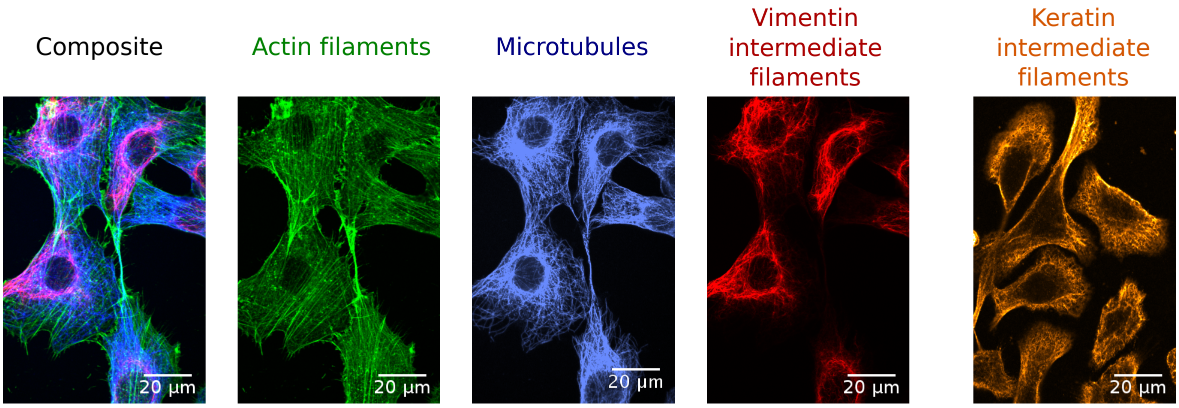
Composite
Actin filaments
Microtubules
Vimentin intermediate filaments
Keratin intermediate filaments
20 µm
20 µm
20 µm
20 µm
20 µm

Figure 1.1: Confocal fluorescence images of National-Institutes-of-Health-3T3 fibroblasts and their cytoskeletal filaments (composite on the left): Actin filaments (green), microtubules (blue) and vimentin IFs (red). All keratins stained in a keratinocyte (orange). Imaged by Dr. U. Rölleke (University of Göttingen).

vimentin, and epithelial cells and keratinocytes mainly express keratins [3], see Fig. 1.1 for stained vimentin and keratin IFs in fibroblasts and keratinocytes, respectively. The cell-type specific expression makes IFs ideal candidates to fine-tune the mechanical properties of cells [12]. Important cellular processes associated with a change in cell mechanics involve a change in IF type expression, which happens, for example, during the epithelial-to-mesenchymal-transition (EMT). EMT occurs during embryogenesis [13], wound healing [14] and cancer metastasis [15]. During EMT, the IF protein keratin is downregulated and the IF protein vimentin is upregulated [16, 17]. Since EMT happens during cancer metastasis, vimentin expression increases and high vimentin expression levels serve as a tumor marker [18–20]. Mesenchymal and metastizing cells are more motile and might be exposed to larger stresses and strains than endothelial or stationary tumor cells. However, it is unclear whether the expression of different IF proteins is the only cause of different mechanical behaviors.

In cells, cytoskeletal filaments form networks as shown in Fig. 1.1. The interactions between these networks are crucial for homeostasis [21]: For example, the interactions between actin filaments and vimentin IFs are required for successful mitosis [22, 23], actin filament-microtubule crosstalk supports the cell shape and cell polarity during migration [24, 25] and vimentin IFs and microtubules form closely associated bundles in migrating epithelial cells [26]. The vimentin network collapses to the perinuclear region when microtubules are depolymerized [27], and vimentin IFs stabilize microtubules against lateral fluctuations [28].

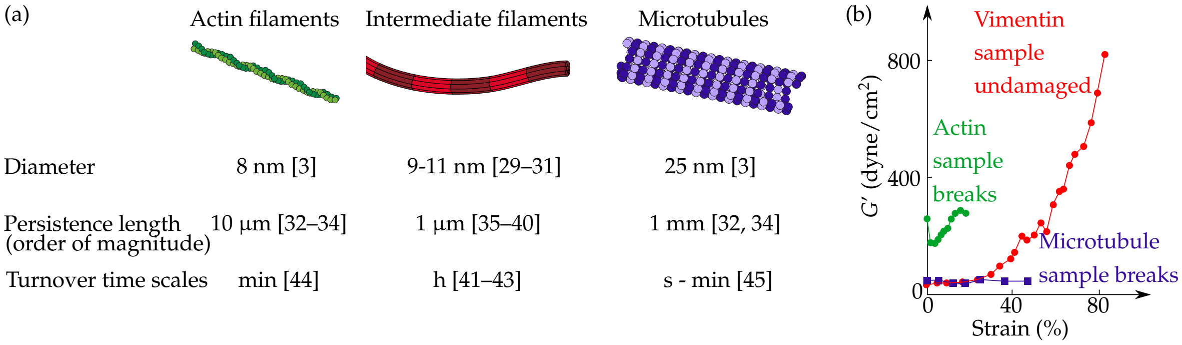

(a)	Actin filaments	Intermediate filaments	Microtubules
Diameter	8 nm [3]	9-11 nm [29–31]	25 nm [3]
Persistence length (order of magnitude)	10 μm [32–34]	1 μm [35–40]	1 mm [32, 34]
Turnover time scales	min [44]	h [41–43]	s - min [45]

Figure 1.2: Overview of cytoskeletal filaments, (a) their physical properties and (b) their network properties under strain (Used with permission of Rockefeller University Press, from Ref. [46]; permission conveyed through Copyright Clearance Center, Inc).

On top of physiological relevance, composite systems of different cytoskeletal filaments are highly interesting from a physics point of view: The three different cytoskeletal filaments mentioned above have different physical properties, such as different diameters (8–25 nm), highly different persistence lengths (1 μm–1 mm) and different turnover time scales (1 s–1 day) as summarized in Fig. 1.2a. Networks consisting of these three different cytoskeletal filaments have very different extensibility and stretchability, with the most stable and extensible one being the IF network, as shown in Fig. 1.2b. In a composite system, interactions between cytoskeletal filaments can lead to a different physical behavior than the mere average behavior of both, i.e. these systems can exhibit new physical properties. To better understand these systems, it is vital to disentangle the properties of single components from the new properties emerging from the interaction between these components. Next to the expression of different IF proteins, the three named cytoskeletal filaments with their highly different properties and their interactions equip the cell with a mechanical "toolbox" to adapt and control cellular mechanics [21]. To understand the specific mechanics of each "tool" better, in vitro studies offer a precise control over the studied protein and its environment.

In this thesis, we quantify and characterize the interactions within and between cytoskeletal filaments by focusing on two different in vitro systems: (i) On the molecular scale, the mechanical behavior of stretched keratin and vimentin IFs is studied and compared and (ii), on the filament scale, the interactions between microtubules and vimentin IFs are examined. Both studies are conducted with optical tweezers which allow for a quantitative control of forces, extension and buffer condition in combination with microfluidics. In case of single filaments, we present how interactions within these filaments determine their stiffness and extensibility. In case of the two-filament system, the influence of interactions between microtubules and vimentin IFs on dynamic microtubules are investigated. With theoretical modeling and simulations, we link the mechanical properties of different IFs to their molecular architecture and interactions within the filament. With the modeling approach we show how direct interactions between microtubules and vimentin IFs affect microtubule dynamics. Furthermore, modeling these interactions between filaments allows us to draw conclusions about the interactions within dynamic microtubules. The combination of experiments and modeling enables us to distinguish between single component and emerging properties. In both studied systems, interactions within and between filaments result in a different behavior than expected from the mere sum of the single parts of each system. Thus, on top of the differences between the filaments summarized in Fig. 1.2, the results in this thesis show that tuning interactions within and between the filaments might be another vital tool for cells to adapt their mechanics.

In Chapter 2, we review the current literature and theoretical models on the cytoskeletal filaments discussed above with a focus on IFs and microtubules. In the case of IFs, the molecular architecture and physical properties of keratin and vimentin IFs are directly compared. In its first half, Chapter 3 offers a brief description of the physical principles of optical tweezers. Models of single and parallel bonds, which are needed to describe the interactions within and between filaments, are summarized in the second half of Chapter 3. The details of protein preparation, the usage of optical tweezers and the microscopy techniques employed in this work are explained in Chapter 4. The detailed simulations and models of interactions within and between filaments can be found in Chapter 5.

Chapter 6 presents the implications of different lateral interactions strength within keratin and vimentin IFs. The different mechanical behaviors might be a possibility for cells to tune their mechanical properties via a change in IF protein expression as it happens during EMT. A theoretical model explains how different lateral interactions within the filaments coin filament mechanics. Other options for cells to tune filament mechanics on different spatial and temporal scales are changes in local buffer concentrations and pH (see Section 6.3) and post-translational modifications (see Section 6.4). We study the effect of these changes on the interactions within filaments and their impact on mechanics.

In Chapter 7, the mechanical behavior of repeatedly loaded keratin and vimentin IFs including their softening, elongation and dissipated energy is compared. Keratin and vimentin IFs behave highly differently under repeated loading which we explain again with modeling of their molecular architecture.

The effects of interactions between cytoskeletal filaments on filament dynamics and mechanics are studied in Chapter 8. We find that a single interaction between a microtubule and a vimentin IF strongly affects the behavior of the entire microtubule (Section 8.1). With optical tweezers, we measure the direct interactions between a single microtubule and a single vimentin IF. By taking measurements in different buffer conditions, we can differentiate between electrostatic and hydrophobic contributions. Theoretical modeling allows for the decoupling of the properties of the filaments themselves from effects resulting from their interactions. Thus, modeling shows how the direct interactions result in changes of dynamic microtubules, i.e. the composite system has different properties than the sum of the single systems. These interactions between different cytoskeletal filaments might be another way for cells to fine-tune microtubule dynamics. Direct interactions might also be a tool for cells to adjust filament network mechanics as we show in Section 8.2 for the interactions between two single vimentin IFs and vimentin networks.

In Chapter 9, we discuss and summarize the common principles of mechanics and the interactions within and between cytoskeletal filaments. We observe that interactions play an important role in regulating filament dynamics and mechanics. Reasonable speculations about the biological functions of the studied interactions are made and ideas for further experiments are suggested.

CHAPTER 2

State of the Art

Figure 2.7 is part of the book chapter "Mechanics of single vimentin intermediate filaments under load" by Anna V. Schepers*, Julia Kraxner*, Charlotta Lorenz* and Sarah Köster. The book chapter will be published in the second edition of "Optical Tweezers – Methods and Protocols" by Arne Gennerich (editor) (2021, Copyright ©2021, Springer Science Business Media New York) [47]. The original figure is published in Ref. [7].
* Equal Contribution.

2.1 Intermediate Filaments

IFs, actin filaments and microtubules are part of the cytoskeleton. In contrast to tubulin and actin, IF proteins are expressed in a cell-type specific manner [10–12]. A cell can express different types of IF proteins at the same time and the level of expression can change. For example, during EMT, vimentin expression is upregulated and keratin expression is downregulated [12, 18–20]. In total, more than 70 different human IF proteins exist [48, 49] and even more can be found in other species [50]. Based on their amino acid sequences, IF proteins are categorized into different sequence homology classes (SHCs), of which the five largest ones are summarized in Table 2.1 [48, 49]. A keratin of the SHC I has to associate with a keratin of the SHC II to form a filament [3, 51, 52], while proteins of the SHC III-V do not pair. Keratins are further classified as soft keratins with a relatively low concentration of cysteines in the protein or as hard keratins with a relatively high concentration of cysteines in the protein [53]. α keratins mainly contain α helices and β keratins mainly contain β sheets [53]. Epithelial cells typically express soft α keratins, while more motile cells such as mesenchymal or muscle cells express vimentin or desmin (SHC III) [3], respectively. Neurofilament proteins (SHC IV) are the IF proteins expressed in neurons [3]. Lamins (SHC V) protect the nucleus from large deformations by forming a network which is attached to the inner membrane of the nucleus [3].

2.1.1 Assembly and Structure of Intermediate Filaments

Although there are many different IF proteins with different primary structures, they share the same monomeric, secondary structure as shown with the schematic in Fig. 2.1. An unstructured head and tail domain flank the central rod, which consists of three α-helical

Sequence homology class	IF proteins	Typical cell type / occurrence
I	Acidic keratins (e. g. keratin 18)	Epithelial cells
II	Basic keratins (e. g. keratin 8)	Epithelial cells
III	Vimentin, desmin, glial fibrillary acidic protein, peripherin, syncoilin	Mesenchymal cells, muscle cells, cells of the central nervous system, neurons
IV	Neurofilament proteins, α-internexin, nestin, synemins	Neurons
V	Lamins	Associated with the inner membrane of the nucleus

Table 2.1: Overview of the five largest SHCs of IF proteins [48, 49].

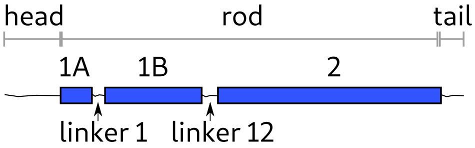

Figure 2.1: Schematic of an IF monomer consisting of an unstructured head and tail and a rod, which includes three α-helical sections (1A, 1B, 2) and linkers (linker 1, linker 2) which connect the α-helical sections [31].

domains (1A, 1B, 2) and two unstructured linkers (linker 1, linker 12), which connect the α-helices [31].

In contrast to microtubules and actin filaments, IFs assemble in a very hierarchical manner as shown in Fig. 2.2 [31, 41]. Two monomers laterally associate in a parallel way to form a dimer [10, 52]. In the case of keratins, a monomer from SHC I and II associate to a dimer, e.g. a monomer of keratin 8 and keratin 18 [38]. There are keratin pairs such as keratin 8/18, but the matching is not unique, e.g. keratin 8 and keratin 19 form filaments as well [51, 52].

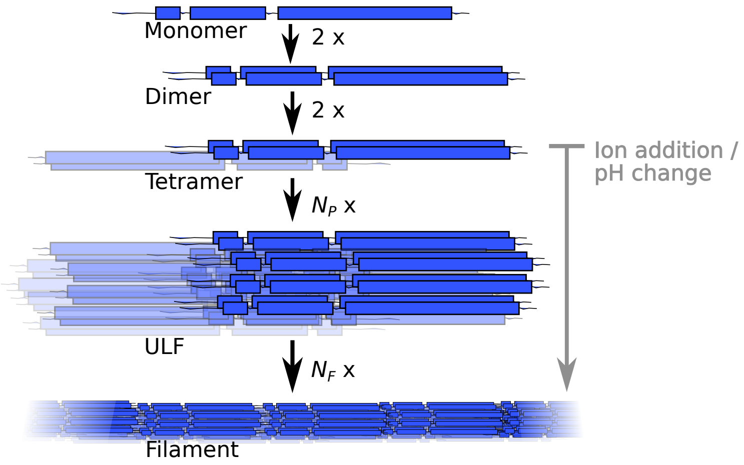

Figure 2.2: Schematic of IF assembly: IF monomers associate laterally to form a parallel dimer. Dimers associate in an antiparallel manner to form a tetramer. Upon change in pH or addition of salt, N_P tetramers associate laterally to a ULF. ULFs associate longitudinally to form a filament. N_F is the number of ULFs in a filament [31, 41].

Two dimers associate laterally, in an antiparallel way to form a tetramer [31]. To initiate further assembly from tetramers to filaments, either the pH or the ionic strength of the buffer is changed [10, 54–59]. N_P tetramers associate again laterally to form unit-length filaments (ULFs). The precise number of tetramers in a ULF depends on the IF protein, e.g. in case of vimentin $N_P = 8$ and in case of keratin 8/18 $N_P = 4$ [10, 31]. ULFs associate longitudinally to form a filament [41].

2.1.2 Different Types of Intermediate Filaments

Although IFs share the same secondary structure and highly similar assembly pathways, their amino acid sequences vary. Thus, IF dimer structure, electrostatics, hydrophobicity, assembly speeds and final filament properties such as the persistence length, diameter and number of tetramers per ULF may vary. For a direct comparison, I here focus on vimentin and keratin 8/18 IFs here since they belong to different SHCs, they are frequent in the human body, K8/18 is the first IF protein expressed during mammalian embryogenesis [13] and they are important during EMT [16, 17]. An overview of the comparison is shown in Table 2.2. In the following, I refer to keratin 8/18 as keratin.

Vimentin monomers are at least 1.7 times more negatively charged and around 1.9 times less hydrophobic than keratin monomers. Thus, keratin monomers electrostatically repel

Property	**Keratin 8/18**	**Vimentin**
monomer charge	Keratin 8: 6 e, keratin 18: 11 e [49]	19 e [49]
Average monomer hydrophobicity (higher value: more hydrophobic)	Keratin 8: -59, Keratin 18: -54 [49, 60]	-107 [49, 60]
Dimer type	Heterodimer (keratin 8 and keratin 18 monomer) [3]	Homodimer (two vimentin monomers) [3]
Average number of parallel tetramers per ULF	4 [38]	8 [31]
Compaction step	Does not compact [38]	Compacts [10, 61]
Average filament diameter	9-11 nm [29, 30]	11 nm [31]
Persistence length and method to determine it	0.65 μm (rheology) [40], 0.3-0.48 μm (electron microscopy) [38]	0.4 μm (rheology) [36], 0.5 μm (bulk rheology) [37], 1.0 μm (AFM, electron microscopy) [35], 2.0-2.1 μm (fluorescence microscopy) [39] 3.3 μm (stretching with optical tweezers) [6]

Table 2.2: Comparison of keratin 8/18 and vimentin IF protein, assembly or filament properties.

each other less than vimentin monomers, and hydrophobic forces cause a higher attraction between the keratin monomers in comparison to vimentin monomers. Keratin IFs assemble around 100 times faster than vimentin IFs [62]. Keratin dimers consist of two different monomers, keratin 8 and keratin 18, while vimentin dimers are homo-dimers made of the same vimentin monomers. 4 parallel tetramers form a ULF in case of keratin and 8 parallel tetramers in the case of vimentin. The diameter of vimentin IFs decreases during assembly from above 16 nm to around 11 nm, a step, which is called compaction [10]. It is assumed, that a closer arrangement between coil 1A and the beginning of coil 2 of different dimers causes the compaction [61]. This closer arrangement is possible due to very specific charge patterns of the amino acids at the end of linker 1, at the beginning of coil 1B and in linker 12 [61]. Thus, although vimentin has twice as many monomers per cross-section as keratin, the filaments have a similar diameter of about 9-11 nm [29–31]. Keratin IFs are more flexible and their persistence length is approximately half the persistence length of vimentin IFs [35–40].

2.2 Experiments on Intermediate Filaments Under Load

In general, important techniques to study the structural changes of IFs during stretching are wide-angle X-ray scattering, atomic-force microscopy (AFM), optical tweezers [6, 7, 63] and nonlinear Raman and infrared spectroscopy [64, 65].

2.2.1 Bundles Under Load

In the 1920s, macroscopic samples such as hair or wool consisting of hard α keratin fibers were studied to understand the mechanical properties of IFs since techniques to investigate microscopic samples or even single IFs had not been developed yet. For example, crossbred wool fibers were repeatedly stretched by S. A. Shorter with and without breaks after extension and relaxation of the fiber [66]. He observed an elastic behavior of the fibers, but also a hysteresis upon relaxation. The fibers got softer after previous stretching and did not return to their original length unless they were left to recover for several days. A few years later, J. Speakman observed very similar effects [67]. Additionally, he loaded the fibers at different rates and faster loaded fibers exhibited a higher apparent stiffness. Explanations for the observed effects relied on ideas about the structural changes inside the fibers, but they were not experimentally proven.

In the 1930s, W. Astbury discovered differences in the small-angle X-ray photographs of unstretched and stretched hair, which he called α and β keratin, respectively [68–71]. He concluded that the polypeptide chains inside the hairs unfolded and could form parallel sheets. 20 years later, L. Pauling and R. Corey identified the structural changes in the hair as an unfolding of the α helices and a formation of β sheets [72]. W. Astbury's observation and naming of α and β keratin resulted in the modern nomenclature of α helices and β sheets. In 1960, E. G. Bendit observed the unfolding of α helices and the formation of β sheets already at 5% extension. The unfolding of α helices was proportional to the fiber extension [73].

Next to wool fibers and hair keratin, hagfish slime threads shed light on soft-keratin-like IF mechanics under load [74, 75]. Keratins inside hagflish slime threads exhibit an α-helix-to-β-sheet transition. Irreversibility of the deformation and subfilament sliding were observed as well. In 2014, N. Pinto et al. studied stretched threads made of reconstituted vimentin IFs with wide-angle X-ray scattering and observed an α-helix-to-β-sheet transition [76].

2.2.2 Individual Filaments Under Load

To understand the mechanics of these IF bundles or even IF networks better, single IFs were studied as described in the following. L. Kreplak et al. stretched single murine desmin IFs, human keratin K5/14 IFs and neurofilaments from rat brain with AFM while the IFs were adhering to a surface as sketched in Fig. 2.3 [77, 78]. The IFs exhibited an enormous elongation potential up to 3.6-fold their unstretched length at forces up to 3.5 nN before they broke. Typical AFM images of keratin 5/14 filament are shown in Fig. 2.4 (a) before and (b,c) after stretching. The elongation was explained with the α-helix-to-β-sheet transition, but dimer sliding was discussed as a possibility for large elongation and for a reduction in IF diameter as well [12, 35, 64]. However, IFs were adsorbed to a substrate in all these studies which influences their mechanical properties [35].

C. Guzmán et al. pushed with an AFM tip on single vimentin IFs dangling above a pore of a porous membrane [79]. A typical filament and hole profile is shown in Fig. 2.5. The authors concluded that axial sliding of structures inside the filament was likely. K. T. Sapra et al. indented lamin IFs embedded in a lamin IF network and attached to nuclear pore complexes with AFM [80]. They concluded that the lamin network properties determine the single filament response as well.

Studies with optical tweezers allowed for studies on IFs, which were not adsorbed to a surface, but free in solution [6, 7, 63, 81, 82]. Simultaneously, the filament was observed with fluorescence microscopy so that it was easier to ensure that the filament was not a bundle and that it did not slip off the loading probe. In combination with a microfluidic channel, the buffer conditions can be changed easily.

The stretching of single vimentin IFs with optical tweezers showed that the stress-strain curves of vimentin IFs exhibited a very characteristic shape with three different regimes as

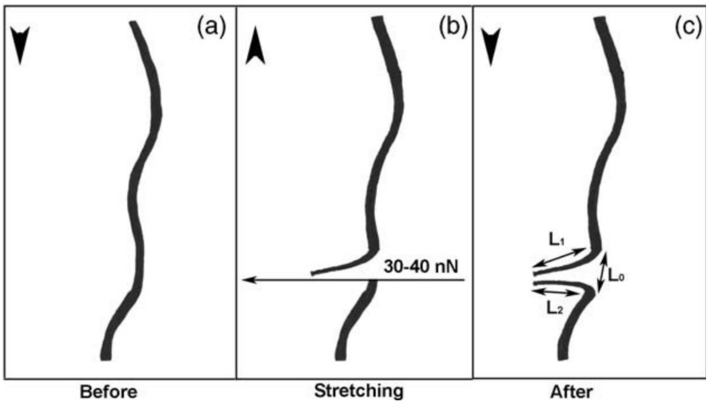

Figure 2.3: Sketch of an AFM stretching experiment. The arrowhead in the top left corner indicates the scanning direction of the AFM. (a) The filament was adsorbed by the surface and imaged with AFM. (b) During one scanned line, the force applied by the tip was increased to 30-40 nN and the filament was stretched (black arrow). (c) The filament was imaged after the stretching experiment and the total amount of stretching was approximated by $(L_1 + L_2)/L_0$. Fig. from Ref. [77] (2021, Copyright ©2021, with permission from Elsevier).

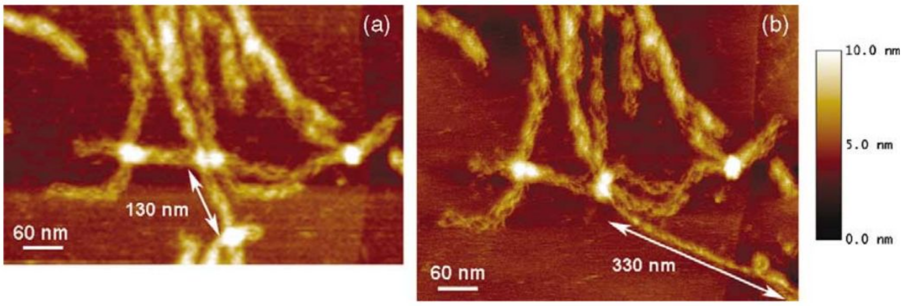

Figure 2.4: AFM images of human keratin 5/14 IFs adsorbed to a highly oriented pyrolitic graphite (a) before and (b) after stretching. A piece of the filament was stretched from 130 to 330 nm, i.e. 2.5-fold. Subfilamentous structures were visible and the diameter of the filament after stretching appeared to be reduced. Fig. from Ref. [77] (2021, Copyright ©2021, with permission from Elsevier).

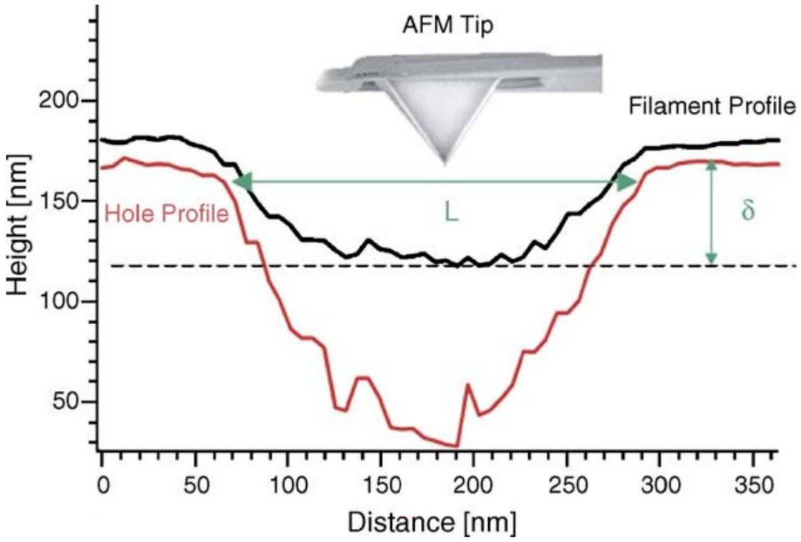

Figure 2.5: Typical profile of a vimentin IF spanned over a hole. The filament was stretched by pushing with an AFM tip. Fig. from Ref. [79] (2021, Copyright ©2021, with permission from Elsevier).

shown in Fig. 2.6 [6]. The elastic stretching of the α helices causes the first, linear regime (see 1 in Fig. 2.6). At a certain force, the α helices start to unfold, which results in a plateau-like behavior of the force-strain curve, the second regime. After α-helical unfolding, the remaining filament is again elastically stretched resulting in a third regime (see Fig. 2.6). With increasing loading rate, the plateau starts at higher forces and the maximum strain to which the filament can be stretched decreased [6]. The experimental force-strain curves agree very well with a mechanical model consisting of a two-state equivalent freely-jointed chain model and an elastic spring, which is described in detail in Section 2.3.2 [6].

2.2.3 Individual Filaments Under Repeated Load

Repeated loading of IFs sheds light on possible plastic deformations of the IFs. Thus, it is vital to consider the behavior of single IFs under repeated load. Block, Witt et al. [7] observed a strong hysteresis and tensile memory of repeatedly stretched vimentin IFs as shown in Fig. 2.7: The forces during relaxation of a stretching cycle are lower than the loading trace

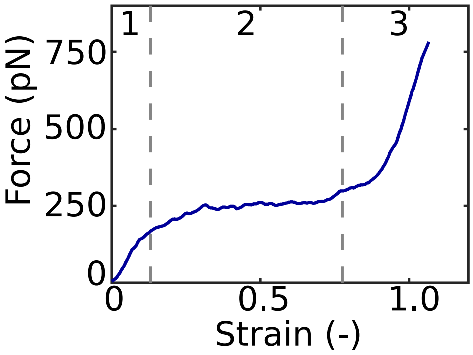

Figure 2.6: Force-strain curve of a vimentin IF stretched with 0.5 µm/s. In the first regime (1), the α helices in the filament are elastically stretched and open in the second regime (2). The cooperative, stepwise opening causes a plateau-like behavior of the force-strain curve. After unfolding, the filament is elastically stretched again (3). Data recorded by J. Forsting.

and the loading forces decrease with each repetition. About 70%-80% of the input stretching energy are dissipated. Monte-Carlo simulations showed that the unfolding of α helices and the structure of IFs (see Section 2.1.1) result in hysteresis, a high dissipated energy and a softening after repeated stretching as further explained in Section 2.3.3.

The observed softening of the IFs raised the question of whether vimentin IFs were able to fully recover after waiting times. Therefore, J. Forsting, J. Kraxner, H. Witt et al. stretched single vimentin IFs and allowed for a waiting time up to 60 min at a strain close to 0 after a first stretching cycle [63]. After the waiting time, the IFs did not recover so that the second cycle did not resemble the first cycle. However, a third cycle resembled the second one at waiting times of only five minutes. The authors concluded that the α helices unfold under extension, but do not refold upon relaxation. Instead, the α helices unfold into a third state, likely a random coil, which is repeatedly stretched. This third state can form a β sheet and can be trapped in this configuration. This three-state model consisting of the α helix, likely a random coil and β sheet is described in detail in Section 2.3.2.

Yet, it remains unknown how other single IFs such as keratin IFs react to different loading rates, buffer conditions and to repeated loading and whether they can act as cellular "shock absorbers" as well by dissipating a high amount of input energy.

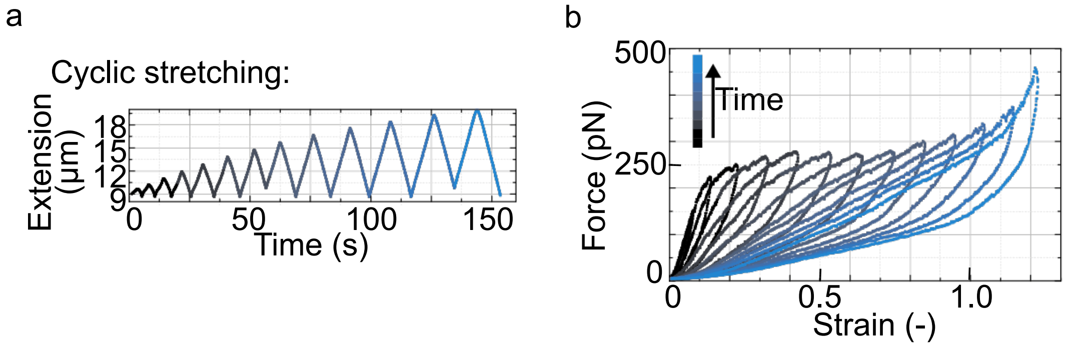

Figure 2.7: Vimentin IFs soften when loaded repeatedly. (a) Extension-time protocol for cyclic stretching. (b) Force-strain data of a cyclically stretched vimentin IF according to the protocol shown in (a) [7, 47].

2.3 Models and Simulations of Intermediate Filaments Under Load

There are three main different strategies to model and simulate the force-strain behavior of IFs under load: (i) Molecular dynamics simulations yield the changes in secondary structure on an amino acid scale, (ii) two- and three-state models describe the overall behavior of α helices under load and (iii) Monte-Carlo simulations based on the two-state model result in a qualitative explanation of repetitively stretched IFs.

2.3.1 Molecular Dynamics Simulations

To resolve the unfolding of vimentin dimers and tetramers under load on the scale of single amino acids, molecular dynamics simulations are necessary [83, 84]. Notably, the force-strain curves of single dimers and tetramers resemble the force-strain curves of entire filaments and they exhibit the same three regimes explained in Section 2.2 shown in Fig. 2.8a. The advantage of molecular dynamics simulations is that the unfolding of α helices to β sheets or to an unfolded state can be observed on the scale of single amino acids as shown in Fig. 2.8b. However, it is not possible to study an entire IF with molecular dynamics simulations since these simulations would require excessive computational power. Thus, more coarse-grained models are necessary to capture the mechanics of an entire IF.

2.3.2 Two- and Three-State Models

To describe the force-strain curve of an entire IF as shown in Fig. 2.9a, Block et al. [6] considered a two-state model. Each α helix in a vimentin IF ULF is modeled as an elastic spring which is connected to an equivalent freely jointed chain (eFJC) as sketched in Fig. 2.9b. The eFJC can open from an α-helical state into a longer, unfolded state under force. These models of α helices are connected in series to model an entire filament.

The number N_F of α helices per vimentin IF is calculated from its initial length L and the lengths of the three different α helices $i = 1, 2, 3$ in a monomer and their linkers. The

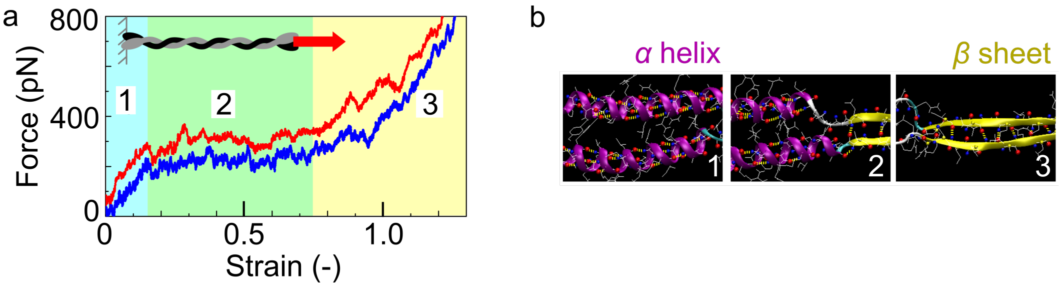

Figure 2.8: Molecular dynamics simulations of the stretching of a vimentin dimer. (a) Molecular dynamics simulations result in three regimes of the force-strain curve of vimentin dimers at different loading rates (red: 0.1 Å/ps, blue: 0.01 Å/ps): 1. Elastic, 2. plateau and 3. strain stiffening. From Ref. [83]. (b) Molecular dynamics simulations show the transition of α helices to β sheets in the three regimes marked in (a): In regime 1, α helices (magenta) are elastically stretched (left panel). In regime 2, α helices open and start forming β sheets (yellow; center panel). β sheets continue to form in regime 3 (right panel). From Ref. [83]. Entire figure is adapted by permission from Springer Nature: Springer Nature, *Mechanics of single vimentin intermediate filaments under load* by Anna V. Schepers, Julia Kraxner, Charlotta Lorenz and Sarah Köster, © Springer Science+Business Media New York 2021.

independent opening of the α helices under force is described by Bell-Evans kinetics. Thus, the sum of all ith α helices in the filament at force F at time t is described by:

$$\frac{\mathrm{d}N_{u,i}}{\mathrm{d}t} = (N_F - N_{u,i})k_{0,i} \exp\left(\frac{Fx_{\alpha,i}}{k_B T}\right) , \tag{2.1}$$

where $k_{0,i}$ is the force-independent opening rate, $k_B T$ is the thermal energy and $x_{\alpha,i}$ the potential width of the α-helical state as sketched in Fig. 2.9b.

The force a filament experiences at a constant loading rate v for a filament contour length L_C and a Kuhn length L_K, results from the eFJC model:

$$F(t) = k_{\mathrm{eff}} \left(vt - L_C(F,t) \left(1 - \frac{F_K}{F} \right) \right) , \tag{2.2}$$

where k_{eff} is a spring constant which takes the filament contribution as well as the stiffness of the experimental setup into account, and $F_K = k_B T / L_K$ is the force scale resulting from the Kuhn length. The transition rates to the unfolded state are numerically calculated from Eq. 2.1 and are used for the analytic calculation of the force from Eq. 2.2. The experimental data are fitted with this model resulting in the average parameters $x_{\alpha,1} = (0.09 \pm 0.04)$ nm, $x_{\alpha,2} = (0.12 \pm 0.04)$ nm, $x_{\alpha,3} = (0.18 \pm 0.06)$ nm and $k_{\mathrm{eff}} = (0.22 \pm 0.06)$ pN/nm.

The two-state model is well suited to quantitatively describe the force-strain curves of vimentin IFs, however, it does not capture the filament recovery behavior upon relaxation of the force.

To understand the behavior of repeatedly stretched vimentin IFs with waiting times in between cycles, the two-state model is supplemented by a third state, likely a random coil, to a three-state model [63]: A filament is stretched, relaxed, kept at about 5 pN for a certain time and then stretched again. In case of vimentin IFs, the shape of the first cycle is not restored after reasonable waiting times, however, the shape of the second cycle is the same as the third cycle. Forsting, Kraxner, Witt et al. [63] conclude that α helices unfold during the first stretching cycle while in the subsequent cycles, the unfolded state is repeatedly stretched, but without another conformational change. At high strains, a β sheet can form and the corresponding amino acids are "locked" in this state [63]. A representation of the energy landscape of these transitions is shown in Fig. 2.9c.

The three-state model describes the behavior of stretched and unfolded α helices and random coils, but it cannot reproduce the tensile memory shown in Fig. 2.10a-c.

2.3.3 Monte-Carlo Simulations

Block, Witt et al. [7] designed a Monte-Carlo simulation to describe the hysteresis and tensile memory of vimentin IFs after cyclic loading. In this simulation, each monomer is represented by an elastic spring with a dimensionless spring constant κ_α connected in series to an element which can open under force to a unfolded state u which has an additional dimensionless length of ΔL. The monomers are connected in parallel and in series in a way that they resemble the structure of a vimentin IF as sketched in Fig. 2.10d: $N_P = 32$ monomers are connected in parallel to represent a ULF with 32 parallel monomers in vitro [31]. Springs with a dimensionless stiffness κ_L represent the linkers between the ULFs. The total number

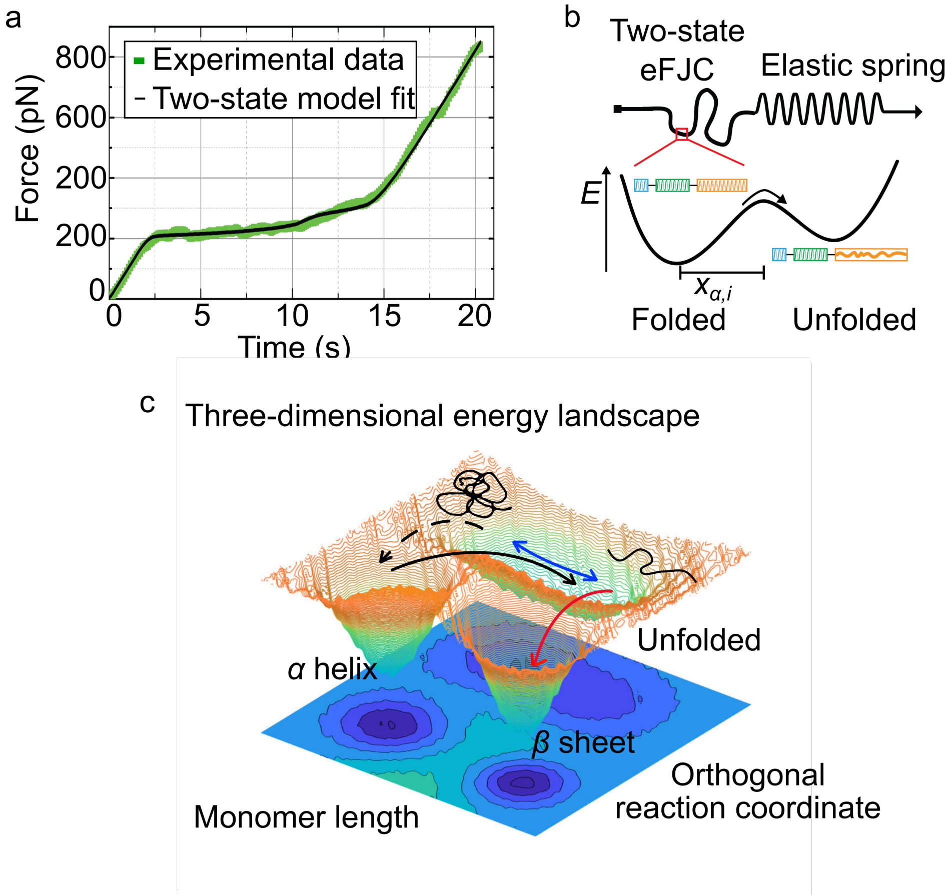

Figure 2.9: A two-state model quantitatively describes the force-strain and force-time behavior of single vimentin IFs under load. To describe the behavior of vimentin IFs under cyclic loading, a three-state model is necessary. (a) Experimental force-time data of a typical vimentin IF (green). The data are well described and fitted with a two-state model (black) sketched in (b). From Ref. [6]. (b) The two-state model consists of an equivalent freely jointed chain (eFJC) with potential width $x_{\alpha,i}$ in series with an elastic spring. From Ref. [6]. (c) Three-dimensional energy landscape representation of our current understanding of α helix unfolding behavior during vimentin IF stretching. Under force, α helices unfold to an unfolded, random coil state (black solid arrow); during force relaxation, the random coil shortens (blue arrow). By repeated stretching and relaxing, the random coil is stretched and relaxed (blue arrow). The extended coil may form into a β sheet (red arrow) which cannot return into a random coil. Adapted with permission from Ref. [63]. Copyright 2019 American Chemical Society. Entire figure is adapted by permission from Springer Nature: Springer Nature, *Mechanics of single vimentin intermediate filaments under load* by Anna V. Schepers, Julia Kraxner, Charlotta Lorenz and Sarah Köster, © Springer Science+Business Media New York 2021.

of connected elements is $N_F = 100$. For simplicity, elements taking into account entropic contributions during filament loading are not included in this model.

To calculate the force-strain behavior of a filament, the spring constant of the filament and the reaction rates of the α-helical elements to the unfolded state have to be calculated. The dimensionless spring constant κ_f of the entire filament is:

$$\kappa_f = \left(\sum_{j=1}^{N_F} \left(\frac{1}{\kappa_L} + \frac{1}{\kappa_\alpha A_j} \right)^{-1} \right)^{-1},$$

where j is the index of the jth ULF and A_j the number of closed α helices in the jth ULF. If all monomers in a ULF are in the unfolded state, the ULF elongates by a dimensionless length, ΔL. The sum of all ΔL of all elongated ULFs results in the total additional extension of the filament λ_{tot}. Thus, the total, dimensionless force ϕ acting on a filament is:

$$\phi = \kappa_f (x - \lambda_{\text{tot}}),$$

where x is the end-to-end distance of the filament. The filament is stretched and relaxed with a constant velocity v, so that $x = vt$ during stretching and $x = x_m - v(t - t_m)$ for a relaxation

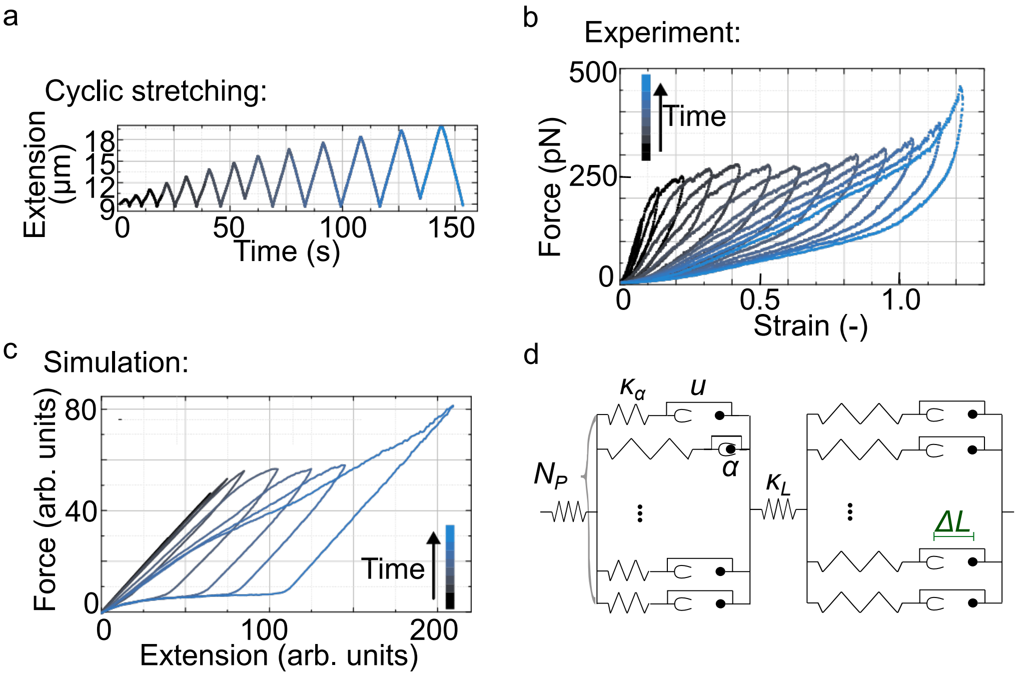

Figure 2.10: During cyclic stretching, the extension may be increased or kept constant for each cycle. (a) Extension-time protocol for cyclic stretching. (b) Force-strain data of cyclically stretched vimentin IFs according to the protocol shown in (a). (c) A Monte-Carlo simulation of a cyclically stretched vimentin IF qualitatively resembles the experimental data shown in (b). (a,b,c) Adapted from Ref. [7]. Reprinted with permission from AAAS. (d) For the Monte-Carlo simulation, springs and elements, which can open under load (i.e. transition from an α helix to an unfolded state u), are arranged like the monomers in a vimentin IF: $N_M = 32$ monomers are arranged in parallel (missing monomers indicated by the three dots) to a ULF and ULFs are placed in series. In case all monomers of one ULF are in the unfolded state, the ULFs elongates by ΔL (green). Here, only two ULFs are shown for clarity. Entire figure adapted by permission from Springer Nature: Springer Nature, *Mechanics of single vimentin intermediate filaments under load* by Anna V. Schepers, Julia Kraxner, Charlotta Lorenz and Sarah Köster, © Springer Science+Business Media New York 2021.

starting at t_m at a filament length x_m.

If there is at least one monomer of the jth ULF in the α-helical state, the force acting on the monomers in the α-helical state is shared so that the force acting on each α helix is ϕ/A_j. The reaction rate $r_{A_j}^{\alpha\to u}$ from the α-helical state to the unfolded state of a single monomer in the jth ULF is:

$$r_{A_j}^{\alpha\to u} = A_j r_0^{\alpha\to u} \exp\left(\frac{\phi}{A_j}\right),$$

with the zero-force reaction rate $r_0^{\alpha\to u}$.

Unfolded monomers in ULFs, which contain at least one monomer in the α-helical state, can refold to a state with the same length of the α-helical state with an equilibrium reaction rate $\gamma = r_0^{u\to\alpha}/r_0^{\alpha\to u}$ since the force mainly acts on the intact α helices. $r_0^{u\to\alpha}$ is the zero-force reaction rate of a monomer from the unfolded state to a state with the same length of the α-helical state. If all monomers are in the unfolded state, the force is equally distributed, so that each monomer experiences the force ϕ/N_P. Thus, the refolding rate $r_{A_j}^{u\to\alpha}$ of unfolded elements to a state as long as the α-helical state is:

$$r_{A_j}^{u\to\alpha} = \begin{cases} B_j\gamma & \text{for } A_j > 0 \\ N_P\gamma \exp\left(\frac{-\phi}{N_P}\right) & \text{for } A_j = 0, \end{cases}$$

where $B_j = N_P - A_j$ is the number of elements in the unfolded state in the jth ULF. The free energy difference between the α-helical state and the unfolded state determines γ by $\Delta G/(k_B T) = \ln\gamma$.

To obtain the force-extension behavior shown in Fig. 2.10c, the model is Monte-Carlo simulated with the Gillespie algorithm. At the beginning of the first stretching cycle, all monomers are in the α-helical state. To simulate the elongation during the next stretching cycle, the monomer states resulting from the loading and relaxation of the the previous are set as the initial states.

2.4 Microtubules

Next to IFs and actin filaments, microtubules are essential cytoskeletal filaments since they secure nutrient transport, the formation of the mitotic spindle and cellular structure [3].

2.4.1 Structure and Assembly of Microtubules

Microtubules are hollow cylinders with an outer diameter of about 25 nm [3] and an inner diameter of about 13 nm [85] as indicated in blue and white measurement marks in Fig. 2.11a. In contrast to IFs, microtubules do not follow a highly hierarchical assembly, but tubulin dimers polymerize and depolymerize at the ends (see Fig. 2.11a) [3]. Tubulin dimers consist of an α- and a β-tubulin monomer, which share about 40% identical residues [3]. After purification and in physiological conditions, tubulin is only found in the form of dimers [3].

Microtubules typically nucleate from centrosomes in vivo or from stabilized seeds in vitro at 37°C in buffer conditions described in Section 4.3.3 and 4.6 [3]. The assembling tubulin dimers form a hollow cylinder with usually 13 parallel tubulin strands, the protofilaments, as sketched in Fig. 2.11a [3]. Between the first and thirteenth protofilament, most microtubules exhibit an offset of 1.5 dimers, called the seam. Compared to IFs, microtubules are polar and have a faster and a slower assembly end, the plus and the minus end, respectively. The association and disassociation rates of single tubulin dimers depend on the microtubule end, on the nucleotide which is incorporated in the dimer and on the free tubulin concentration M_f in the surrounding solution [86]. A tubulin dimer can only polymerize when it is bound to a guanosine triphosphate (GTP) molecule. Once the GTP dimer is incorporated into the microtubule lattice, the GTP hydrolyzes to guanosine diphosphate (GDP) with a specific rate. Thus, GTP dimers are mainly located at the tip of a microtubule. This part of the microtubule is often referred to as the GTP tip or cap. GDP dimers are less stable in the microtubule lattice configuration than GTP dimers. Thus, GDP dimers dissociate with a higher rate than GTP dimers so that microtubules rapidly shrink if the GTP cap is lost.

The effective growth rate r_t at the end of the microtubule is described by Eq. 2.3 with the dimer association rate r_g and the constant dimer dissociation rate r_{dt}. For GTP dimers, typical values are $r_g = (8.9 \pm 0.3)\ (\mu\mathrm{M\,s})^{-1}$ and $r_{dt} = (44 \pm 14)\ \mathrm{s}^{-1}$ at the plus end and $r_g = (4.3 \pm 0.3)\ (\mu\mathrm{M\,s})^{-1}$ and $r_{dt} = (23 \pm 9)\ \mathrm{s}^{-1}$ at the minus end [86]. During rapid disassembly, GPD dimers disassociate with rates of around $(733 \pm 23)\ \mathrm{s}^{-1}$ at the plus end and with around $(915 \pm 72)\ \mathrm{s}^{-1}$ at the minus end [86]. At a higher free tubulin concentration, microtubules grow faster. Microtubules only grow if the free tubulin concentration is above a critical concentration because otherwise dimers dissociate faster than new dimers can bind. The equilibrium association and dissociation rate of dimers determine the critical concentration M_C, as described by Eq. 2.4.

$$r_t = r_g M_f - r_{\mathrm{dt}}\,, \tag{2.3}$$

$$M_C = r_{\mathrm{dt}}/r_g\,. \tag{2.4}$$

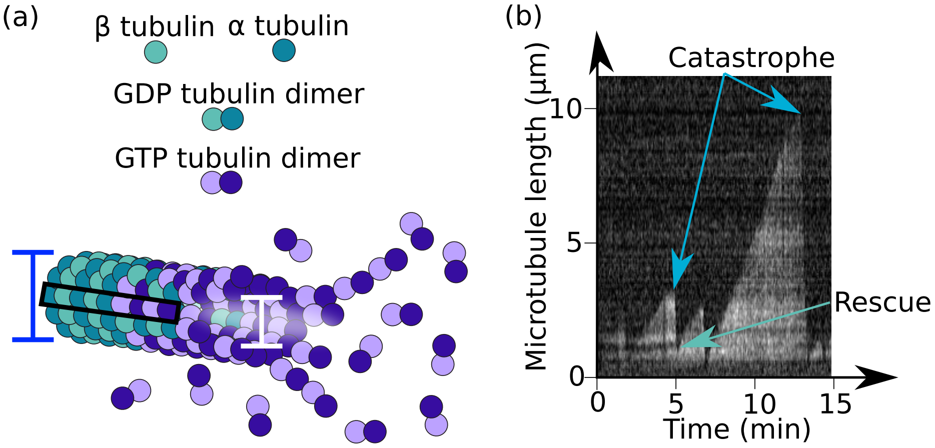

Figure 2.11: (a) Schematic of microtubule structure and assembly. GTP tubulin dimers polymerize into a microtubule, a hollow cylinder with an outer diameter of about 25 nm (blue measurement mark) [3] and an inner diameter of about 13 nm (white measurement mark) [85]. A typical in vitro microtubule has 13 parallel tubulin strands, the protofilaments (black box) [3]. GTP dimers hydrolyze to GDP dimers after incorporation into the microtubule lattice. (b) Typical kymograph of a labeled, dynamic microtubule imaged with TIRFM. The microtubule starts rapid depolymerization several times (two catastrophes are highlighted with light blue arrows) and switches back to polymerization during rapid disassembly once (one rescue; light green arrow).

The critical concentration is around 5 µM at typical buffer conditions [86]. Thus, when labeled microtubules are observed with fluorescence microscopy, it is essential to only illuminate the surface of the sample because otherwise the background signal is too high to differentiate between microtubules and free tubulin. Total internal reflection fluorescence microscopy (TIRFM) is ideal to image microtubules since it penetrates only 100-200 nm into the sample [87, 88], so that microtubules at the surface can be imaged. To analyze microtubule dynamics, these data are plotted as a kymograph. A typical kymograph of a dynamic, labeled microtubule recorded with TIRFM is shown in Fig. 2.11b.

2.4.2 Dynamic Instability of Microtubules

The switching between polymerization and rapid shrinking of microtubules is called dynamic instability [3]. This behavior is unique to microtubules. When a microtubule grows and the turnover of GTP to GDP overtakes the polymerization of GTP at the microtubule tip, the microtubule rapidly depolymerizes. Additionally, missing lateral contacts of newly polymerized protofilaments can cause the start of a rapid depolymerization [89, 90]. The switching from polymerization to rapid shrinking is called catastrophe as shown in Fig. 2.11b (light blue arrow). The switching back to polymerization while the microtubule rapidly depolymerizes is called rescue (see light green arrow in Fig. 2.11b). GTP islands in the microtubule lattice, other irregularities in the lattice or polymerizing GTP dimers can cause rescue [91].

The growth rate, depolymerization rate, catastrophe frequency and rescue frequency are typical parameters to describe the dynamic instability of microtubules. These parameters are sensitive to changes in the free tubulin concentration, the ion concentration and pH of the surrounding solution [45, 91–93]. For example, the catastrophe frequency decreases and the rescue rate increases for a higher free tubulin concentration. Furthermore, instead of GTP, microtubules can be grown with a guanosine-5′-[(α,β)-methyleno]triphosphate (GMPCPP), a slowly hydrolyzing analog of GTP, which suppresses depolymerization [94]. Taxol is another chemical that stabilizes normally assembled microtubules from their inner shaft so that the microtubules cannot depolymerize [95].

Dynamic instability of microtubules is still not completely understood in every detail. There are different theoretical approaches to understand the underlying physics of microtubule dynamics which are explained in Section 2.5.

2.4.3 Binding Energy of Tubulin Dimers Within the Microtubule

An important parameter to understand the physics of dynamic instability is the binding energy of tubulin dimers to neighboring dimers. This binding energy has to be different between GTP and GDP dimers to cause rapid disassembly of a microtubule. However, it is experimentally challenging to pull a single dimer out of a dynamic microtubule lattice. Yet, the binding energy can be experimentally measured without pulling a dimer out of its lattice. Also, molecular dynamics simulations of an entire microtubule are computationally too extensive, but other computational approaches allow for an estimation of the tubulin binding energy, as an overview in Table 2.3 shows. V. Van Buren et al. are often referred to for

Method	**GTP dimer binding energy ($k_B T$)**		**GDP dimer binding energy ($k_B T$)**	
	long.	lat.	long.	lat.
Monte-Carlo simulations compared to experimental data [96]	6.8 to 9.4	3.2 to 5.7	6.8 to 9.4	0.7 to 3.6
Coarse-grained molecular dynamics simulations [97]	15.5	9.1	-	-
Electron tomography of microtubules and modeling [98]	16.6	5.3	16.6	4.3
Imaging of individual dimers with interferometric scattering microscopy [101]	12±0.2	3.6±0.4	-	-
Pulling out taxol-stabilized dimers from the microtubule lattice with an AFM tip [100]	-	-	10	3.9
Estimate from molecular dynamics simulations [99]	31.8±1.9	4.9	25.2±2.0	4.2

Table 2.3: Overview of longitudinal (long.) and lateral (lat.) tubulin binding energies.

tubulin binding energies since they were among the first ones to estimate the binding energy by comparing Monte-Carlo simulations to experimental data [96]. Coarse-grained molecular dynamics simulations of tubulin dimer-dimer interactions resulted in values for binding energies [97]. These simulations took the bending of protofilaments into account and were later complemented with electron tomography images of microtubules [98]. From molecular dynamics simulations of the interactions between single dimers, Hemmat et al. estimated the binding energy of single tubulin dimers [99]. They increased the scale to more coarse-grained simulations which referred to the binding energies from molecular dynamics simulations as input parameters. C. Ganser et al. indented a taxol-stabilized microtubule with an AFM tip and pulled out single or several dimers [100]. K. J. Mickolajczyk et al. observed single tubulin dimers binding and unbinding to a microtubule by interferometric scattering microscopy. From the observed kinetics, they deduced the binding energies.

Taking into account all these studies, the lateral binding energy varies between 1 and 10 $k_B T$ and is smaller than the longitudinal binding energy for all dimers. Thus, the dimers are more stabilized by neighboring dimers within the same protofilament than by neighboring dimers in neighboring protofilaments. GDP dimers are less strongly bound in the lattice which is important for the rapid depolymerization. The longitudinal binding energies vary between 7 and 33 $k_B T$ for GTP dimers and between 7 and 28 $k_B T$ for GDP dimers. Most of these approaches to calculate the binding energies rely on computational modeling. Additionally, further experimental approaches are highly needed to measure the tubulin binding energies.

2.5 Models and Simulations of Dynamic Microtubules

There are three main approaches how to model dynamic microtubules: Analytic approaches, Monte-Carlo simulations and molecular dynamics simulations. Analytic approaches describe the dynamics of microtubules with comparably low computational effort. However, Monte-Carlo and molecular dynamics simulations result in a more precise picture of the dynamics on the scale of single tubulin dimers. As we are interested in the interaction of single vimentin IFs with tubulin dimers, I will focus on previous studies involving either Monte-Carlo simulations or molecular dynamics simulations.

One of the first and most important Monte-Carlo simulations of a dynamic microtubule was developed by Odde et al. in 2002 [96]. In brief, they develop a stochastic model which reproduces the experimentally observed microtubule dynamics: A microtubule is described as a matrix with an entry for each dimer. The lattice of the microtubule is described with 13 protofilaments and a helical pitch of 1.5 tubulin dimers per turn as sketched in Fig. 2.12. The first and 13th protofilament are adjacent protofilaments. Four different reaction rates described the microtubule dynamics: (i) a constant polymerization rate r_g, (ii) a neighbor-dependent depolymerization rate of GTP dimers r_{dt}, (iii) a neighbor-dependent depolymerization rate of GDP dimers r_{dd} and (iv) a constant hydrolysis rate r_{hy}. The polymerization rate (i) is set to a constant value resulting in the same growth rates observed in experiments. The depolymerization rates (ii) and (iii) depend on the number and position of neighboring dimers. A lateral association of a dimer to a GTP dimer or GDP dimer increases the total binding energy by $|\Delta G_{\mathrm{latt}}|$ or $|\Delta G_{\mathrm{latd}}|$, respectively. The longitudinal association energy of a dimer to a dimer in the same protofilament increases the binding energy by $|\Delta G_{\mathrm{long}}|$. Thus, from a given r_g, the depolymerization rate is calculated:

$$r_d = r_g \exp\left(\frac{\Delta G}{k_B T}\right) ,$$

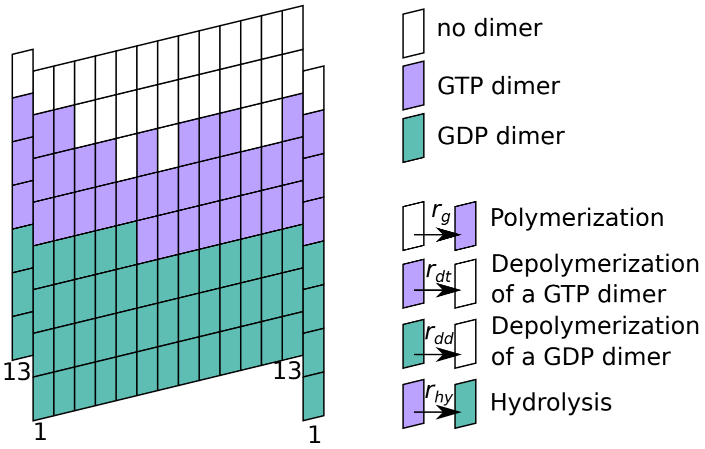

Figure 2.12: Sketch of the microtubule lattice model by Odde et al. [96]. A microtubule is modeled as a matrix with 13 columns, which represent the 13 protofilaments in a microtubule. There is a pitch of 1.5 dimers between the first and the thirteenth microtubule. Microtubule dynamics are described by four rates: (i) The polymerization rate r_g of a GTP dimer, (i) the depolymerization rate r_{dt} of a GTP dimer, (iii) the depolymerization rate r_{dd} of a GDP dimer and the hydrolysis rate r_{hy} of a GTP dimer to a GDP dimer.

where ΔG is the sum of all binding energies. To calculate the binding energy of a dimer inside the microtubule lattice, all binding energies of the dimers between the respective dimer and the microtubule tip are summed up. Thus, tubulin dimers in the microtubule lattice far away from the tip have a very low chance of depolymerization since all dimers in the protofilament up to the tip have to depolymerize as well.

A hydrolysis rate of $r_{hy} = 0.95\ \mathrm{s}^{-1}$ reproduces experimentally observed microtubule dynamics [96]. The binding energies resulting in microtubule dynamics similar to experiments are: $\Delta G_{\mathrm{latt}} = -3.2$ to $-5.7\, k_B T$, $\Delta G_{\mathrm{latd}} = -0.7$ to $-3.6\, k_B T$ and $\Delta G_{\mathrm{long}} = -6.8$ to $-9.4\, k_B T$.

The Monte-Carlo simulation by Schaedel et al. modified this model so that dynamics within the microtubule shaft were described as well [102]. To better understand the rescue behavior of dynamic microtubules, Fees et al. [91] created two models, which assume different molecular mechanisms during rescue. They ran Monte-Carlo simulations with a rescue rate known from the experiments to study the resulting microtubule dynamics. Other Monte-Carlo simulations capture different features of microtubule dynamics, however, only molecular dynamics simulations allow for a precise understanding of configurational dimer changes upon hydrolysis and how these changes affect microtubule dynamics.

For example, molecular dynamics simulations showed that GDP dimers increase the longitudinal strain along the microtubule lattice [103]. As a consequence, the microtubules splay apart once the GTP cap vanished. In a multiscale approach, Hemmat and Odde [99] investigate the interaction energies between single tubulin dimers with molecular dynamics simulations. They transfer the results to the scale of an entire microtubule so that a molecular dynamics simulation of all tubulin dimers in the microtubule is not necessary. The microtubule dynamics are determined from Monte-Carlo simulations as described by Ref. [96] with slight modifications [99]. Most recently, Stewman et al. were able to fully explain dynamic instability by conformational changes of tubulin based on molecular dynamics simulations [104]. An overview of tubulin dimer binding energies derived with different approaches is shown in Table 2.3 in Section 2.4.

2.6 Reconstituted Cytoskeletal Networks

In cells, single filaments are incorporated into networks. Thus, it is vital to understand the properties of single filaments as described for IFs and microtubules above, but also the properties of cytoskeletal interactions and networks. It is possible to measure the direct interactions between two single filaments with optical tweezers: N. Laurens, R. P. C. Driessen et al., I. Brouwer, G. Sitters et al. and P. Gutierrez-Escribano, M. D. Newton et al. studied interactions between two DNA molecules [105–107]. Interactions between two single fibrin fibers were observed by N. A. Kurniawan et al. and Vos et al. [108, 109]. Bergman et al. used holographic optical tweezers to build three-dimensional microtubule networks consisting of two or more overlapping microtubules [110]. However, none of these studies include an analysis with interaction force measurements of many filament pairs nor an analysis of these data resulting in binding and unbinding rates and interaction energies of the filaments.

2.6.1 Reconstituted Cytoskeletal Networks of Intermediate Filaments

As mentioned in the introduction, IF networks have astonishing mechanical properties in comparison to actin filament or microtubule networks: IF networks are highly deformable and very extensible without rupturing [36, 46]. A relatively soft behavior and strain stiffening at higher strains is characteristic for IF networks [36, 37, 40, 46, 111–114]. The precise elastic and viscous moduli vary between the studied IF networks, e.g. between vimentin [36, 46, 112–114], desmin [36, 111], keratin [40, 114–116], IF networks and neurofilament networks [37]. The network properties can be tuned by adding ions, hydrophobic agents, crosslinkers, changing the temperature and changing the protein concentration. For example, hydrophobic agents such as Triton-X100 soften keratin IF networks since the hydrophobic agent blocks interactions between hydrophobic amino acids [40, 115]. Divalent ions such as magnesium tune the stiffness of vimentin and keratin networks. For example, vimentin networks in microfluidic droplets form denser networks for magnesium concentrations above 10 mM [117]. In contrast to vimentin networks, keratin networks already stiffen with the addition of 0.25 mM magnesium [116]. The kinetic trapping of keratin networks can be tuned by temperature, protein concentration or ion concentration and was observed by epifluorescence microscopy of labeled keratin IFs [118].

2.6.2 Reconstituted Composite Cytoskeletal Networks

Next to pure IF networks, systems consisting of different cytoskeletal filaments were studied since their interactions are essential for homeostasis as well [21]. Additionally, composite networks are highly interesting from a physics point of view since they can exhibit different mechanical properties than a linear combination of the two separate networks. A major challenge in preparing composite networks is the buffer choice, since proteins can have very different standard buffers and the composite buffer must not significantly disturb the protein assembly or stability. Yet, some suitable buffer conditions especially for filamentous actin (F-actin)-microtubule and F-actin-vimentin systems are known and an overview of all previously published work on composite network studies is shown in Fig. 2.13.

Filamentous Actin-Microtubule Networks

Microrheology of F-actin-microtubule networks showed that these networks behave as a linear composition of separate F-actin and microtubule networks [119]. Yet, when a bead was displaced in an F-actin-microtubule network, stress relaxation of F-actin-microtubule networks nonlinearly depends on the ratio of actin filaments to microtubules due to different levels of filament mobility [120]. Studies on dynamic microtubules revealed that microtubule plus-ends accelerate actin filament assembly via several proteins [121]. Vice versa, actin filaments reduce the catastrophe frequency of dynamic microtubules depending on the actin network structure [122]. However, here, the precise interaction mechanism remains unknown. The structure, stiffness, particle transport properties and bundling of these composite networks can be further tuned by adding crosslinkers [123–127]. Motor proteins can switch to another filament at the intersection of actin filaments and microtubules, and

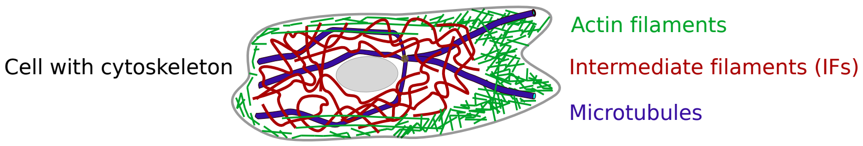

In vitro reconstituted systems

	Actin filaments + microtubules	Actin filaments + IFs	Microtubules + IFs
Pure protein studies, not focused on dynamic filaments	Passive microrheology by Pelletier 2009 [119] Active microrheology by Ricketts 2018 [120]	Bulk rheology with vimentin IFs by Janmey 1998 [129], by Esue 2006 [130], by Jensen, Morris 2014 [131], by Golde 2018 [132] Fluorescence microscopy with keratin IFs by Deek 2018 [134] Fluorescence microscopy with desmin IFs by Miysaka 2019 [133] Bulk rheolog with vimentin and keratin IFs by Elbalasy, Mollenkopf 2021 [135]	Co-sedimentation with neurofilaments by Hisanaga 1990 [138] Bulk rheology with vimentin IFs by Janmey 1998 [129], by Piechocka 2011 [136] Binding of short peptides of vimentin IFs by Bocquet 2009 [137]
Including motor proteins or other crosslinkers	Bulk rheology by Lin 2011 [123] Active microrheology by Ricketts 2019 [125] Fluorescence microscopy by Farhadi 2020 [126] Passive microrheology by Anderson 2021 [127] Dynamic differential microscopy by Lee 2021 [128]		
Dynamic filaments	Fluorescence microscopy by Lopez 2014 [124], by Henty-Ridilla 2016 [121], by Colin, Singaravelu 2018 [122]		

Figure 2.13: Overview of studies on composite cytoskeletal systems.

increase the rigidity and connectivity of the network compared to pure actin networks with motor proteins [128].

Filamentous Actin-Intermediate Filament Networks

Most F-actin-IF studies refer to vimentin IFs. In one of the first in vitro studies of F-actin-vimentin composites, P. Janmey et al. observed a drastic stiffness increase at strains between 0 and 1, which the single-component networks did not exhibit [129]. Thus, apparently, interactions are likely, but their physical origin and strength remains unclear. O. Esue et al. observed that F-actin-vimentin networks were stiffer than F-actin or vimentin networks alone and their interaction was likely mediated by the tail [130]. On the contrary, M. H. Jensen et al. found a concentration dependent softening or stiffening of F-actin-vimentin networks [131]. In contrast to all previous studies, T. Golde et al. did not report any emergent effects from the mixture of actin and vimentin IFs [132]. The interaction between F-actin and desmin or keratin networks were studied in lipid droplets: Desmin and actin filaments were colocalized [133] and actin filaments stabilized keratin IF networks [134]. Interestingly, keratin networks cause strain stiffening in F-actin-keratin networks which is about one order of magnitude stronger than in F-actin-vimentin networks [135].

Intermediate Filament-Microtubule Networks

Studies about vimentin IF and microtubule networks are also not conclusive: P. Janmey et al. did not observe cooperative effects [129], while I.K. Piechocka observed a decreased strain stiffening for a vimentin-microtubule mixture with a vimentin concentration of 1 mg/mL [136]. Concerning the assembly of microtubules, vimentin IFs contain tubulin binding sites and short peptides of these binding sites inhibited microtubule assembly [137]. Similarly, dephosphorylated neurofilaments were observed to bind to microtubules [138].

Especially the interactions between IFs and microtubules remain unclear as also apparent from Fig. 2.13. So far, a direct interaction measurement of two different, single cytoskeletal filaments has not been carried out. Furthermore, mostly stabilized microtubules or stabilized actin filaments were studied so that the influence of interactions on the dynamics of actin filaments or microtubules are barely investigated (see Fig. 2.13). Yet, dynamic filaments are vital for many cellular functions so that an influence on the dynamics by interactions with other cytoskeletal filaments is important to understand.

2.7 Scope of this thesis

In summary, it is known that cytoskeletal filaments with their different mechanical properties and interactions within and between filaments offer a “toolbox” for cells to tune their dynamics and mechanics. Yet, these interactions have not been quantified and it is unclear which physical forces contribute to these interactions. In this thesis, we measure these interactions, identify their physical origin and their influence on filament dynamics and mechanics.

In case of IFs, the mechanical behavior of vimentin IFs is already characterized and they exhibit properties which make them ideal candidates to act as cellular “shock absorbers” and "safety belts". These properties are closely linked to the molecular architecture of the filaments. However, the mechanical behavior of other IF types, for example, of keratins, and the relation of the mechanics to their molecular structure remains unknown. IF monomers have the same secondary structure, thus, differences in the mechanics of IFs might be associated with differences in the interactions between the monomers. I answer the question on how interactions within IFs tune their mechanics in Chapters 6 and 7. We quantify and characterize the interactions within IFs. In case the filament mechanics differ between vimentin and keratin IFs, the expression of different IF proteins might be a way for the cell to tune its mechanical properties on a long time scale. Shorter time scales and a more local adaption of vimentin IF mechanics might be possible via charge changes within or around the filament (Section 6.3 and 6.4).

The next larger scale after single filament mechanics are filament interactions, which are also crucial for cellular mechanics as cytoskeletal filaments form interacting networks in cells. Tuning interactions between cytoskeletal filaments might be another possibility for cells to control their mechanical properties. As described above in detail, cytoskeletal networks have been mainly studied separately and often via rheology. In case of composite systems specifically, a variety of F-actin-microtubule systems with and without crosslinkers and with dynamic or stable filaments were investigated. Yet, as it is also apparent from Fig. 2.13, systems involving IFs were considered far less. Especially, dynamic filaments such as dynamic microtubules in combination with IFs were not studied at all. In chapter 8, I present our results of an IF-microtubule system with the most abundant IF protein in the human body, vimentin. We answer the question how IFs interact with dynamic microtubules by directly measuring and quantifying the interactions between a single microtubule and a single vimentin IF. In previous studies, it also remains unclear, which forces contribute how strongly to interactions between different cytoskeletal filaments. Here, we decouple hydrophobic and electrostatic contributions with our experiments in combination with modeling approaches. With these modeling approaches, we show how vimentin IFs directly influence microtubule dynamics.

As summarized above, a plethora of methods to determine tubulin binding energy exists, but they often involve molecular dynamics simulations or stabilization of microtubules. We suggest a new way of estimating this binding energy without referring to molecular dynamics simulations and without interfering with the mechanical and binding properties of microtubule dimers. This estimate relies on theoretical modeling combining interactions within and between cytoskeletal filaments.

CHAPTER 3

Theoretical Background

Figure 2.8, Figure 2.9, Figure 2.10 and parts of Section 2.3.2 are part of the book chapter "Mechanics of single vimentin intermediate filaments under load" by Anna V. Schepers*, Julia Kraxner*, Charlotta Lorenz* and Sarah Köster. The book chapter will be published in the second edition of "Optical Tweezers – Methods and Protocols" by Arne Gennerich (editor) (2021, Copyright ©2021, Springer Science Business Media New York). The original figures are published in Refs. [7, 63, 83].
* Equal Contribution.

3.1 Optical Tweezers

Optical tweezers trap small objects and measure forces exerted on these trapped objects. The size of trapped objects may range from 0.1 nm to 10 µm in diameter and typical forces measured with optical tweezers are 1-1000 pN [139]. In total, four people were awarded a Nobel Prize for the development or advancement of optical trapping techniques [140]: Steven Chu (Nobel Prize in Physics 1997), Claude Cohen-Tannoudji (Nobel Prize in Physics 1997), William D. Phillips (Nobel Prize in Physics 1997) and Arthur Ashkin (Nobel Prize in Physics 2018).

The effect of radiation pressure on µm-sized particles was discovered in 1970 by Arthur Ashkin [141]: With a single laser beam, he was able to push forward such particles. With two laser beams, he could trap a bead. In 1986, Ashkin et al. worked with a more focused laser beam, so that trapping of a particle with a single laser beam in three dimensions became possible [142]. Since then, the technique was further developed, on the one hand, to cool atoms by trapping [143], and, on the other hand, to study biological samples. In the biological context, optical tweezers allow for the investigation of systems on various orders of magnitude in length scale and force, such as protein folding and motor proteins (pN, nm), force-extension curves of filaments (pN to nN, µm) or microrheology (pN, µm) as sketched in Fig. 3.1 [139, 144].

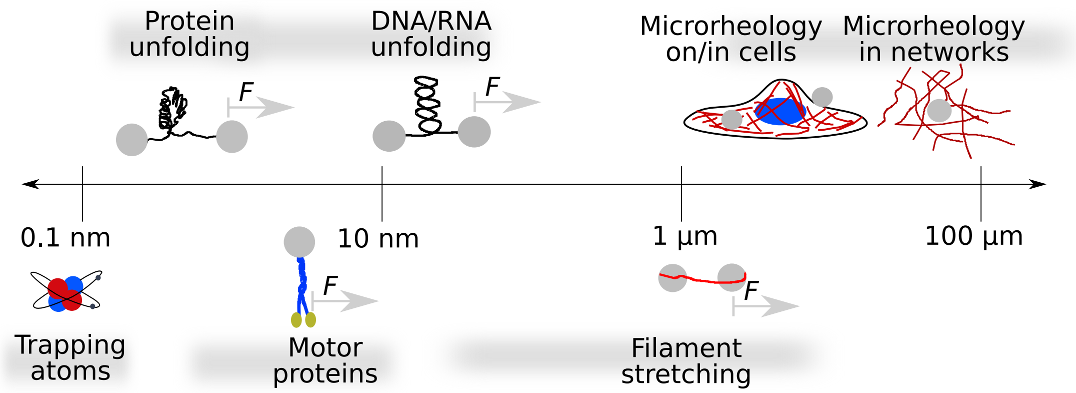

Figure 3.1: Optical tweezers can access properties of samples at very different orders of magnitude in length scale: On the sub-nm to nm scale, atoms are trapped and protein unfolding under force is studied. The stepping of motor proteins on the order of 1 nm to 10 nm is measured with optical tweezers. DNA/RNA and protein filaments are stretched on the order of 10–100 nm and 1 µm–20µm, respectively. Biological cells and properties of networks on the scale of 10-100 µm and beyond can be studied with particles trapped by optical tweezers (microrheology) [139, 144].

3.1.1 Physics of Optical Tweezers

Depending on the size of the trapped object, two different regimes of the trapping force are distinguished [145]: (i) The Mie regime in which the trapped particle is larger than the laser wavelength λ and (ii) the Rayleigh regime in which the trapped particle is smaller than the laser wavelength. In the Mie regime, the refraction of the incoming photons at the surface of the bead and the resulting change in momentum cause a force that acts on the particle. The change in momentum is sketched in Fig. 3.2 for two rays, sketched as ray 1 and ray 2. In Fig. 3.2a, the particle is slightly displaced in the direction of the laser beam. The change in momentum of the photons pushes the particle to its stably trapped position close to the focus of the laser beam. Similarly, the changed momentum pushes the particle back towards the center of the beam if the particle is slightly laterally displaced, as sketched in Fig. 3.2b.

In the Rayleigh regime, the changing photon momentum is not sufficient to explain the particle trapping. The laser wavelength is larger than the particle so that the "ray picture" in Fig. 3.2 cannot be applied. To calculate the force acting on a particle, we assume that the particle diameter is significantly smaller than the wavelength of the laser. This assumption allows for a rather simple calculation of the trapping forces. The Rayleigh approximation assumes that the dielectric, trapped particle consists of dipoles. The dipole interaction with the electric and magnetic field of the laser light results in the Lorentz force acting on the particle. The total force $\vec{F}_{\text{opt}}$ acting on a particle with volume V and with a polarizability α at a vacuum permittivity ϵ_0 with the refractive index of the surrounding medium n_m with an incident electric field $\vec{E}_i$ and a scattered electric field $\vec{E}_s$ is [145]:

$$\vec{F}_{\text{opt}} = \overbrace{\frac{\epsilon_0 n_m^2 \text{Re}(\alpha)}{4} \int_V \nabla |\vec{E}_i|^2 \text{d}V}^{\text{gradient force}} + \overbrace{\frac{\epsilon_0 n_m^2 \text{Re}(\alpha)}{4} \left(\nabla |\vec{E}_i|^2 + \vec{E}_i \vec{E}_s^* + \vec{E}_i^* \vec{E}_s \right) \text{d}V}^{\text{scattering force}},$$

where * represents the complex conjugate of the respective field. A complete derivation can

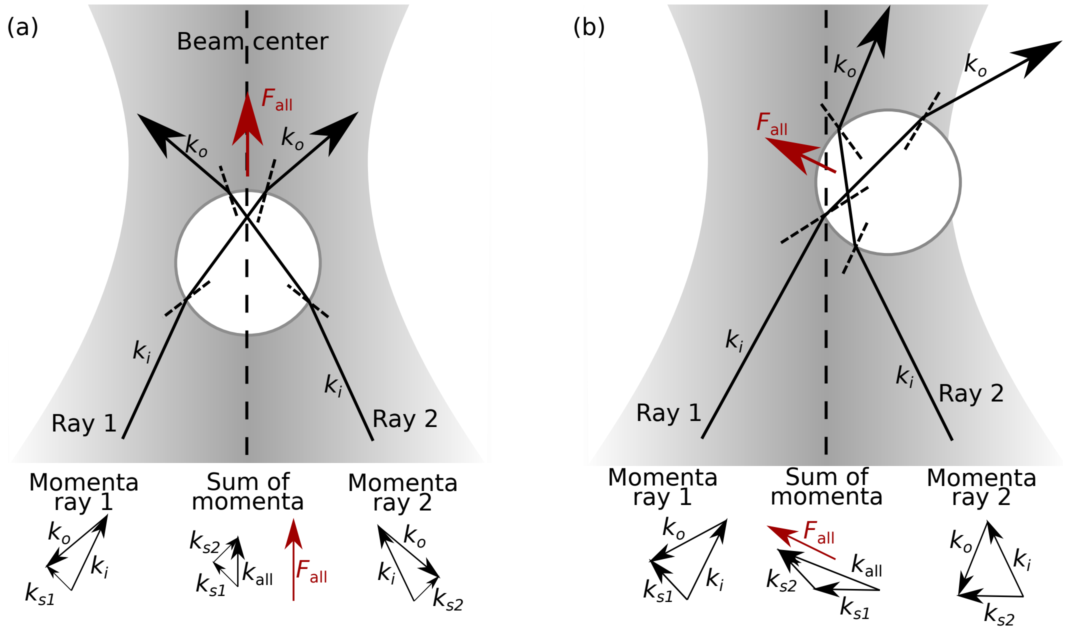
(a)
Beam center
F_{all}
k_o
k_o
k_i
k_i
Ray 1
Ray 2
Momenta ray 1
k_o
k_i
k_{s1}
Sum of momenta
k_{s2}
k_{s1}
k_{all}
F_{all}
Momenta ray 2
k_o
k_i
k_{s2}
(b)
k_o
k_o
F_{all}
k_i
k_i
Ray 1
Ray 2
Momenta ray 1
k_o
k_{s1}
k_i
Sum of momenta
F_{all}
k_{all}
k_{s2}
k_{s1}
Momenta ray 2
k_o
k_i
k_{s2}

Figure 3.2: Sketch of a spherical particle trapped in a laser beam. The light is refracted since the particle has a higher refractive index than the surrounding medium. Two light rays (ray 1, ray 2) are sketched to illustrate the scattering with the simplified picture of light as rays. The light scatters at the transition from the surrounding medium to the particle and when it leaves the particle. Thus, the incoming momentum of the light rays, k_i, changes to the outcoming momentum k_o. The difference in the momenta is $k_{s(1,2)}$. The addition of all changes of the momenta k_{all} results in the direction of the force F_{all} pushing the particle back into the focus. (a) If the particle is displaced parallel to the beam direction, it is pushed back towards the focus. (b) If the particle is displaced from the beam center, it is pushed back [139].

be found in Ref. [139]. Since the intensity of the laser beam does not change over the volume of the small particle, the integral of the gradient force $\vec{F}_{\text{grad}}$ with the laser beam intensity I can be solved [145]:

$$\vec{F}_{\text{grad}} = \frac{n_m \text{Re}(\alpha) V}{2c} \nabla I \, . \tag{3.1}$$

The resulting gradient force along the beam axis is sketched in blue in Fig. 3.3.

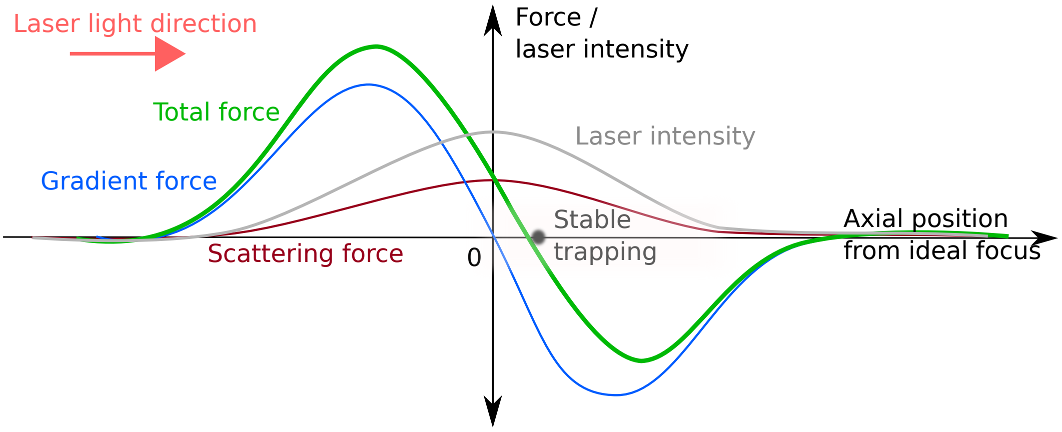

Figure 3.3: Schematic of the gradient and scattering forces (blue and dark red, respectively) acting on an optically trapped particle resulting from a focused laser beam (bright red). The total force (green) acting on the particle vanishes at the stably trapped position (gray dot). The particle is stably trapped slightly behind the focus of the laser beam due to the gradient force [145, 146].

A similar, easy calculation of the scattering force is not possible and an elaborated one can be found in detail in Ref. [147]. The scattering force is sketched in dark red in Fig. 3.3. It is approximately constant for small displacements so that it causes a small position offset which is typically neglected [145]. As sketched in green in Fig. 3.3, gradient and scattering force result in a force-free trapping position (gray dot in Fig. 3.3) behind the ideal focus of the laser.

The gradient force increases linearly for small displacements $\Delta\vec{r}$ of the particle from the stably trapped position, so that the force increase can be described with a optical trap spring constant, κ_i, in the direction $i = x, y, z$. Assuming a Gaussian beam with width $\sigma_x = \sigma_y$ in the transversal direction and σ_z as the characteristic length in the axial direction and an intensity I_0 with the speed of light c, the Taylor approximation of Eq. 3.1 results in [145]:

$$\vec{F}_{\text{grad}} = \vec{F}_{\text{grad}}(\Delta\vec{r} = 0) + \nabla\vec{F}_{\text{grad}}(\Delta\vec{r} = 0)\Delta\vec{r} + O(\Delta\vec{r}^2) \tag{3.2}$$

$$= \frac{n_m \text{Re}(\alpha) V I_0}{c\sqrt{8\pi}} \begin{pmatrix} \sigma_x^{-3} & 0 & 0 \\ 0 & \sigma_y^{-3} & 0 \\ 0 & 0 & \sigma_z^{-3} \end{pmatrix} \Delta\vec{r} \qquad = -\begin{pmatrix} \kappa_x & \kappa_y & \kappa_z \end{pmatrix} \cdot \Delta\vec{r} \tag{3.3}$$

$$= -\vec{\kappa}\Delta\vec{r}\,. \tag{3.4}$$

Thus, the optical trap spring constant resulting from the gradient force is determined by the laser, the experimental setup, the surrounding medium and by the trapped particle itself. Many of these parameters are known, but not to sufficient precision to directly calculate the optical trap spring constant. Additionally, the contribution of the scattering force to the total force acting on the particle increases for particles larger than 500 nm, so that the calculated spring constant in Eq. 3.2–3.4 is not sufficiently accurate.

3.1.2 Calibration of Optical Tweezers

To determine $\vec{\kappa}$ as in Eq. 3.4, there are different calibration methods. The setup we used (C-Trap, Lumicks, The Netherlands) calibrates the force readout of particle and tweezers with back focal plane (BFP) interferometry. Small changes of the particle position strongly amplify the interference signal at the BFP, e.g. a 1% change in scattered incident light causes a change in BFP interference signal of 20% [145]. In our setup, a position sensitive diode detects the BFP signal with a frequency of 78 kHz. A detailed calculation of the expected interference pattern in the BFP can be found in Ref. [145]. A simulated BFP signal is shown in red in Fig. 3.4a (left panel).

Our setup utilizes the Langevin or power-spectrum approach to calculate the spring constant from the BFP detector signal. The Langevin equation describes the motion of a trapped particle with position $\vec{r}$ subject to stochastic forces $\vec{F}_{\text{stoch}}$ caused by diffusion at time t:

$$\gamma_b \frac{\mathrm{d}\vec{r}}{\mathrm{d}t} + \vec{\kappa} \cdot \vec{r} = \vec{F}_{\text{stoch}}\,, \tag{3.5}$$

where $\gamma_b = 6\pi\eta_b r_b$ is the drag coefficient of the spherical particle with a radius r_b in a liquid with viscosity η_b. The particle oscillates in the trap due to stochastic thermal forces. However,

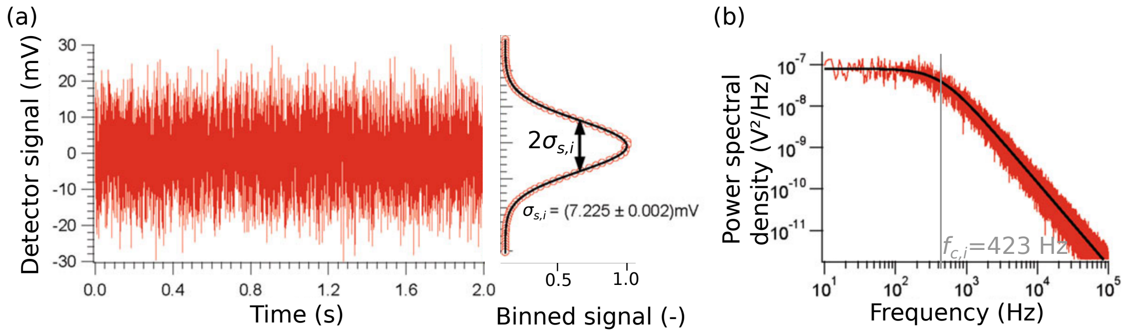

Figure 3.4: (a) The signal (red) on the BFP signal is recorded and binned. A Gaussian distribution is fitted to the signal histogram (black) and the width of the Gaussian distribution is the signal width $\sigma_{s,i}$. (b) The Fourier transform of the BFP signal in (a) results in the power spectral density, which is fitted with a Lorentzian (black). From the fit, the corner frequency $f_{c,i} = \omega_{c,i}/2\pi$ is determined. Adapted by permission from Springer Nature: Springer Nature, *Introduction to Optical Tweezers* by Matthias D. Koch and Joshua W. Shaevitz, © Springer Science+Business Media New York 2017 [145].

since the particle is trapped, the particle cannot freely fluctuate and this damping of the oscillations is visible in the power spectral density (PSD). The PSD represents the distribution of energy on the oscillation frequencies in a certain time interval: The PSD for a trapped particle is constant for small frequencies and decreases with a power law for frequencies higher than the corner frequency $\omega_{c,i} = 2\pi f_{c,i}$ in the direction $i = x, y$, as shown in Fig. 3.4b. The PSD with frequencies ω_i is calculated from the Fourier transform of the Langevin equation in Eq. 3.5 [145]:

$$\mathrm{PSD}(\omega_i) = \frac{2k_B T}{\gamma_b(\omega_i^2 + \omega_{c,i}^2)} .$$

$\omega_{c,i}$ is determined from the fit of this function to the measured PSD. Since γ_b is calculated from known parameters, the trap stiffness is directly calculated [145]:

$$\kappa_i = \omega_{c,i}\gamma_b .$$

$\vec{\kappa}$ relates the particle displacement from the central position in the laser beam to a force acting on the particle. However, the detector measures the BFP signal as a voltage, so that the conversion factor from the detector signal to the particle displacement has to be determined [145]. This conversion factor is called the detector sensitivity.

The detector sensitivity can be determined from the comparison of the detected Gaussian distribution of the particle position with a signal width $\sigma_{s,i}$ to the Gaussian distribution expected from the equipartition theorem with a width $\sigma_{p,i}$ in the direction $i = x, y$. The Gaussian fit to the binned simulated detector signal is plotted in black in Fig. 3.4a. The width of the signal $\sigma_{s,i}$ is determined from this fit. The expected distribution of the particle position results from the equipartition theorem:

$$\sigma_{p,i} = \sqrt{\frac{k_B T}{\kappa_i^2}} . \tag{3.6}$$

Thus, if κ_i is determined as described above, $\sigma_{p,i}$ can be calculated with Eq. 3.6. The detector sensitivity s_d is calculated by $s_{d,i} = \sigma_{s,i}/\sigma_{p,i}$.

If the particle is displaced from its trapped position, the interference pattern detected by the position sensitive diode changes. With this change in interference pattern, the displacement in µm is calculated with the detector sensitivity. The force acting on the particle in pN is then calculated from the displacement with the trap stiffness. Corrections and additional factors in the calculation of the detector sensitivity and the spring constant might be necessary, e.g. to account for the change in refractive indices at the glass-water interface of a sample chamber [148]. We do not carry out a calibration in the z-direction.

3.2 Bonds Under Tension

Bonds involved in biological processes are subject to force in many different situations, e.g. during growth, movements or reproduction. Thus, studying the behavior of bonds under force broadens the understanding of living matter. Molecular dynamics simulations would be necessary to analyze the precise position of all molecules involved in the bond. However, these simulations are computationally too extensive to calculate, for example, an entire IF. Furthermore, the precise role of each involved molecule might not increase the physical understanding of larger bond complexes. Therefore, more coarse-grained models, as described in the following, are helpful to analyze bonds within and between cytoskeletal filaments.

3.2.1 Bell-Evans Kinetics and Energy Landscapes of Single Bonds

In 1889, S. Arrhenius formulated the Arrhenius equation which describes the binding and unbinding processes of many chemical and physical bonds. The Arrhenius equation relates the force-free binding rate $r_{b,0}$ and the force-free unbinding rate $r_{u,0}$ of two components with an activation energy E_{Ab} or E_{Au}, which are required to close or open the bond, respectively, as sketched in Fig. 3.5a [149]:

$$r_{b,0} = r_{b,g} \exp\left(\frac{-E_{Ab}}{k_B T}\right), r_{u,0} = r_{u,g} \exp\left(\frac{-E_{Au}}{k_B T}\right).$$

$r_{u,g}$ and $r_{b,g}$ account for all unknown factors that are not related to the activation energy and the force. For example, the collision direction of two possible binding sites enters into $r_{b,g}$ [150].

In 1978, G. Bell described the force dependence of the bond opening rate involved in cell-to-cell contacts [151]. E. Evans and K. Ritchie extended Bell's theory later [152] so that the general theory became known as Bell-Evans theory or kinetics. The main statement of the theory describes the unbinding rate r_u of bonds as increasing exponentially with the force F which acts on the bond:

$$r_u(F) = r_{u,0} \exp\left(\frac{F x_u}{k_B T}\right), \tag{3.7}$$

where x_u is the distance from the bound state to the transition state of the bond as sketched in Fig. 3.5a, and $k_B T$ the thermal energy. x_u determines how strongly the opening reaction depends on the force: A higher x_u value increases the influence of the force on the unbinding

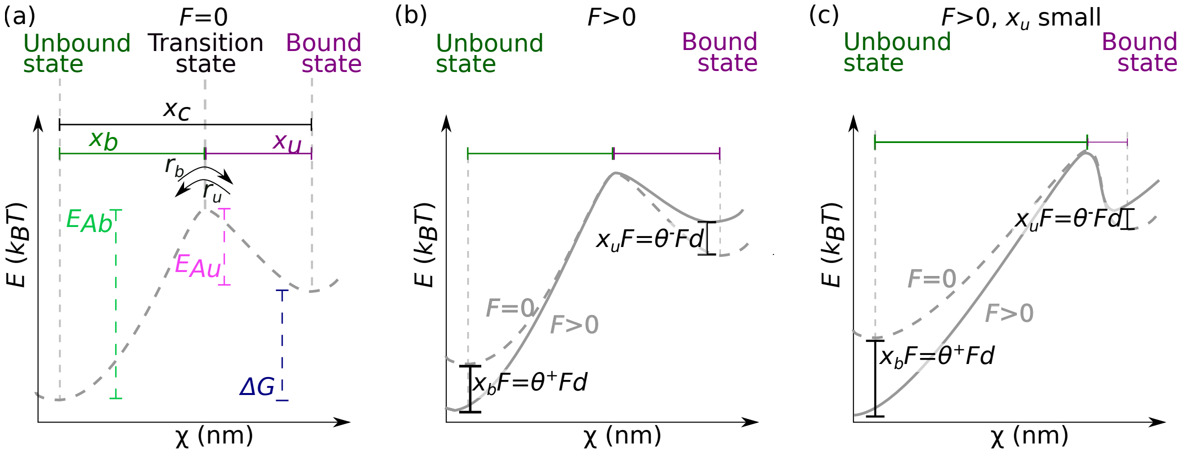

Figure 3.5: Energy landscapes of single bonds describe the energy E at the distance χ between two components which can bind and unbind. The two components can transition from an unbound state to a bound state via a transition state. The distance between the unbound or bound state and the transition state is x_b or x_u, respectively. The two components bind with rate r_b and unbind with rate r_u. To open or close the bond, the activation energies E_{Ab} or E_{Au}, respectively, are necessary. (a) At force $F = 0$, the equilibrium free energy difference between the two states is $\mathit{\Delta} G$. (b) If a force is applied to the bond (continuous line vs. dashed line from (a)), the energy of the unbound state shifts by $x_b F = \theta^+ Fd$ and the energy of the bound state by $x_u F = \theta^- Fd$. (c) If a force is applied to the bond (continuous line) and x_u is smaller than in (b) (dashed line), the energy of the bound state changes less than in (b), while the energy of the unbound state decreases more than in (b) [153].

rate. x_u in Fig. 3.5b is larger than in Fig. 3.5c, $x_u F$ is consequently larger and therefore the energy difference to the transition state is smaller and the bond opens faster at $F > 0$.

In general, a bond is not only characterized by its unbinding rate, but also by the binding rate r_b. The equilibrium constant K_{eq} is the ratio of the unbinding and binding rate [153]:

$$K_{eq}(F=0) = \frac{r_{u,0}}{r_{b,0}} = \exp\left(-\frac{\mathit{\Delta} G}{k_B T}\right) , \tag{3.8}$$

where $\mathit{\Delta} G$ describes the equilibrium energy difference between the bound and unbound state as sketched in Fig. 3.5a. At force $F > 0$, the equilibrium constant changes [153]:

$$K_{eq}(F) = K_{eg}(F=0) \exp\left(\frac{F x_c}{k_B T}\right) , \tag{3.9}$$

where x_c characterizes the influence of the force on the equilibrium. x_c can further be interpreted as a characteristic length scale of the system, e.g. in the case of the motor protein myosin $x_c = 8$ nm [153]. Eq. 3.9 holds true, if the binding rate depends on the force if $x_c > x_u$:

$$\begin{aligned} K_{eq}(F) &= \frac{r_u(F)}{r_b(F)} \\ \Rightarrow r_b(F) &= \frac{r_u(F)}{K_{eq}(F)} = \frac{r_{u,0} \exp\left(\frac{F x_u}{k_B T}\right)}{K_{eg}(F=0) \exp\left(\frac{F x_c}{k_B T}\right)} \\ &= r_{b,0} \exp\left(\frac{F(x_u - x_c)}{k_B T}\right) = r_{b,0} \exp\left(\frac{-F(x_c - x_u)}{k_B T}\right) , \\ r_b(F) &= r_{b,0} \exp\left(\frac{-F x_b}{k_B T}\right) \quad \text{with } x_b = x_c - x_u \, . \end{aligned}$$

To stress the relative changes of the reaction rates due to force on the bound and unbound state, x_b and x_u can be replaced with load-distribution factors, θ^+ and θ^-, where $x_b = \theta^+ x_c$ and $x_u = \theta^- x_c$, so that $\theta^+ + \theta^- = 1$:

$$\begin{aligned} r_b(F) &= r_{b,0} \exp\left(\frac{-\theta^+ F x_c}{k_B T}\right), \\ r_u(F) &= r_{u,0} \exp\left(\frac{\theta^- F x_c}{k_B T}\right). \end{aligned}$$

The changes in the energy landscape due to an applied force and the contributions of the load-distribution factors are shown in Fig. 3.5b,c.

3.2.2 Parallel Bonds

Bell's theory was originally applied to the reaction of several parallel bonds, although it is only a single reaction in the equation describing the unbinding process [151]. However, if the parallel bonds cannot be described as one effective bond as in case of Bell's theory, the force acting on each bond depends on the state of the other bonds, i.e. whether they are open or closed. For example, a closed bond is loaded with a higher force if the other parallel bonds are open. Considering A parallel, closed bonds in a closed state a, which can open into an unfolded state u, the unbinding rate $r_{u,A}$ of all closed bonds with a force-free unbinding rate $r_{u,A,0}$ is [154, 155]:

$$r_{u,A}(F) = A r_{u,A,0} \exp\left(\frac{F x_u}{A k_B T}\right).$$

If the opened bonds do not close again quickly, the whole bond cluster can "zip" open because the force acting on the closed bonds increases with each opened bond [155]. The cluster dynamics depend on the force-independent opening and closing rates of the bonds, the spring constants of the bonds, the number of bonds and the number of bonds connected in series, if applicable.

A typical scenario of such bonds connected in parallel and in series is sketched in Fig. 3.6: N_P parallel bonds with a spring constant κ_p can be elastically stretched and can be opened. These elements are connected to a spring with a spring constant κ_t, which is the force transducer. In case of reversible bonds, i.e. when the bonds can close after opening, the transducer of the system sketched in Fig. 3.6 can be classified as a soft or stiff transducer. If

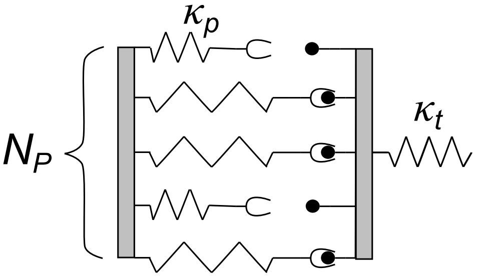

Figure 3.6: Sketch of N_P parallel bonds which can be elastically stretched with spring constant κ_p and can be opened. These elements are connected in series to a spring, the force transducer with a spring constant κ_t [154].

$\kappa_t \lesssim \kappa_p$, the transducer is soft and the force on a bond depends on the number of bonds. In the other limiting case with N_{eq} as the equilibrium number of closed bonds, $\kappa_t \gtrsim N_{eq}\kappa_p$, the force on a bond does almost not depend on the number of bonds [154]. This description and classification is vital for the modeling of biopolymers, such as IFs, under load.

CHAPTER 4

Materials and Methods

Sections 4.2.1, 4.3.1, 4.3.2, 4.4.1, 4.4.2 and 4.5 are either part of the main text or part of the supplementary material of the publication "Lateral Subunit Coupling Determines Intermediate Filament Mechanics" published in *Physical Review Letters* **123** (188102) by Charlotta Lorenz, Johanna Forsting, Anna V. Schepers, Julia Kraxner, Susanne Bauch, Hannes Witt, Stefan Klumpp, and Sarah Köster in 2019 (© 2019 American Physical Society) [156]. Section 6.1 contains the entire main text of this publication.

Sections 4.3.3, 4.4.3, 4.4.4 and 4.6 are either part of the materials and methods or part of the supplementary information of the publication "Vimentin Intermediate Filaments Stabilize Dynamic Microtubules by Direct Interactions" in *Nature Communications* **12** (3799) by Laura Schaedel*, Charlotta Lorenz*, Anna V. Schepers, Stefan Klumpp, and Sarah Köster in 2021 (Creative Commons Attribution 4.0 International License) [157]. Section 8.1 contains the entire main text of this publication.
* Equal Contribution.

IF proteins were purified by Susanne Bauch and Kamila Sabagh. Tubulin was purified and labeled by Jérémie Gaillard or purified together with Susanne Bauch and Kerstin von Roden.

4.1 Protein Purification

4.1.1 Intermediate Filament Proteins

In brief, E. Coli bacteria were incubated with a plasmid, and the bacteria expressed the corresponding protein in inclusion bodies as described in detail in Refs. [7, 158]. The protein was purified from these inclusion bodies by two different ion-exchange chromatography columns. In this way, we purified human wild-type keratin 8 and keratin 18 and variants of the human IF proteins vimentin and keratin 8 containing an additional cysteine. The additional cysteine allows for fluorescently labeling the proteins via malemeide coupling and for attaching the assembled filaments to malemeide coated beads. In case of the vimentin variant, an alanine in the rod at position 328 was expressed instead of a cysteine and the amino acid sequence glycine-glycine-cysteine was additionally expressed at the end of the monomer tail. In case of the keratin 8 variant, a cysteine was added at the end of the tail. We will refer to this variant as cys-keratin 8 to differentiate between the wild-type keratin 8 and the variant.

4.1.2 Tubulin

To purify unlabeled tubulin from fresh bovine brain as described in detail in Ref. [159], we carried out several cycles of microtubule polymerization and depolymerization. We polymerized microtubules at 37°C for 1 h and centrifuged them for 90 min at 160000 × g at 35°C. Microtubules in the pellet were depolymerized for 30 min at 0°C. Again, we polymerized microtubules at 37°C for 1 h and centrifuged for 1 h at 200000 × g at 35°C. The microtubules in the pellet were depolymerized for 30 min at 0°C. Microtubules were polymerized for 1 h at 37°C and layered on prewarmed glycerol cushions. The microtubules were centrifuged through the cushions for 1 h at 200000 × g at 37°C. We resuspended microtubules in cold buffer and another cycle of polymerization and depolymerization was performed. We snap-froze the tubulin in liquid nitrogen and stored it there.

4.2 Protein Labeling

4.2.1 Intermediate Filament Proteins

Fluorescent labeling of cys-keratin 8 or vimentin protein: The cys-keratin 8 or vimentin was labeled with ATTO647N (AttoTech GmbH, Siegen, Germany) via maleimide bonding [160]: 1 mL of cys-keratin 8 or vimentin at 1 mg/mL was dialyzed (Spectra/Por 25 kDa for cys-keratin 8, Spectra/Por 50 kDa for vimentin, Spectrum Laboratories, Piscataway, NJ, USA) into 5 M urea, 50 mM phosphate buffer, pH 7.0 (labeling buffer) overnight. 20 µL of 10 mM ATTO647N, dissolved in DMSO, were added to the dialyzed protein in 5 µL portions with an incubation time of 5 min each. The final mixture was incubated for 2 h. 100 µL of 1 M L-cystein (Carl Roth, Karlsruhe, Germany) were added to bind free dye molecules. After 1 h of incubation, the labeled protein was separated from the free dye by size exclusion chromatography (Bio-Gel P-30, Bio-Rad, München, Germany) with a 27 mL column [160]. The labeled protein was washed through the column by adding labeling buffer. The protein concentration was measured by UV/Vis-spectroscopy (NanoDrop One/OneC, ThermoFisher, Schwerte, Germany). Afterwards, the labeled cys-keratin 8 was dialyzed to 8 M urea, 50 mM TRIS, pH 9.0 (keratin storage buffer) [160]. Vimentin was dialyzed to 8 M urea, 50 mM phosphate buffer, pH 7.5 (vimentin storage buffer). All proteins were stored at -80°C.

Biotin Labeling of Vimentin: Biotin-maleimide (Jena Bioscience GmbH, Jena, Germany) was coupled to vimentin with the same procedure as described for the fluorescent labeling protocol with the exception of the size exclusion chromatography. After 1h incubation with the L-cystein, three PD25 Miditrap columns (GE Healthcare, Freiburg, Germany) were equilibrated with labeling buffer. Biotin-labeled and free biotin were separated by a double elution of the dye and labeled protein mixture over the PD25 Miditrap columns. Labeled protein was dialyzed to 8 M urea, 50 mM phosphate buffer, pH 7.5 and stored at -80°C.

4.2.2 Tubulin

Fluorescent Labeling of Tubulin: After the centrifugation of the microtubules through the glycerol cushion described in Section 4.1.2, we mixed microtubules with ATTO488-esterderivative (AttoTech) or ATTO565-esterderivative (AttoTech) and incubated the mixture at 37° for 10 min. The labeled microtubules were layered on a glycerol cushion and centrifuged through the cushion for 30 min at 250000 × *g* at 37°C. Afterwards, microtubules were treated as unlabeled tubulin after the centrifugation through the glycerol cushion.

Biotin Labeling of Tubulin: After the centrifugation of the microtubules through the glycerol cushion described in Section 4.1.2, we mixed the microtubules with a biotin NSH-ester derivative (NHS-biotin, Thermo Scientific, Waltham, MA, USA) and incubated them at 37°C for 20 min. The labeled microtubules were layered on a glycerol cushion and centrifuged through the cushion for 1 h at 200000 × *g* at 37°. Afterwards, microtubules were treated as unlabeled tubulin after the centrifugation through the glycerol cushion.

4.3 Filament Assembly

4.3.1 Keratin Intermediate Filaments

For preparation of assembly, K18 (50%), K8 (25%), unlabeled Cys-K8 (20%) and labeled Cys-K8 (5%) were dialyzed at a total protein concentration of 0.1 mg/mL in a stepwise manner (8 M, 6 M, 4 M, 2 M, 1 M urea) from keratin storage buffer to 2 mM TRIS, pH 9.0, overnight [58]. Before assembly initiation, the protein solution was centrifuged for 10 min at 12100 × *g* with a Eppendorf MiniSpin centrifuge (Eppendorf AG, Hamburg, Germany) to remove large aggregates. Keratin IFs were assembled by dialyzing the protein mixture at 0.1 mg/mL into the standard keratin assembly buffer, 10 mM TRIS, pH 7.5, (LB) at 36°C overnight [10, 54–58]. About 4% of all monomers had an ATTO647N molecule attached to the C-terminus.

4.3.2 Vimentin Intermediate Filaments

Labeled and unlabeled vimentin were mixed so that in total 4% were fluorescently labeled and in case biotin-labeled filaments were required, a maximum of 20% biotin labeled monomers were included. Vimentin monomers were dialyzed at a concentration of 0.2 mg/ml in a stepwise manner (8 M, 6 M, 4 M, 2 M, 1 M urea) from 8 M urea, 50 mM phosphate buffer (PB), pH 7.5, to 2 mM sodium PB, pH 7.5, and assembled by dialysis at 36°C overnight to vimentin assembly buffer, a physiological, high ionic strength buffer, 100 mM KCl, 2 mM PB, pH 7.5 (HB) [54–56, 59, 161, 162].

4.3.3 Stabilized Microtubules

We prepared stabilized microtubules with biotinylated ends for optical tweezers by first polymerizing the central part of the microtubules through stepwise increase of the tubulin concentration as sketched in Fig. 4.1. Initially, a 3 μM tubulin (5% ATTO-488-labeled) solution in M2B buffer (BRB80 buffer supplemented with 1 mM $MgCl_2$; BRB80: 80 mM PIPES, 1 mM $MgCl_2$, 1 mM EGTA, pH 6.8 with KOH) in the presence of 1 mM GMPCPP

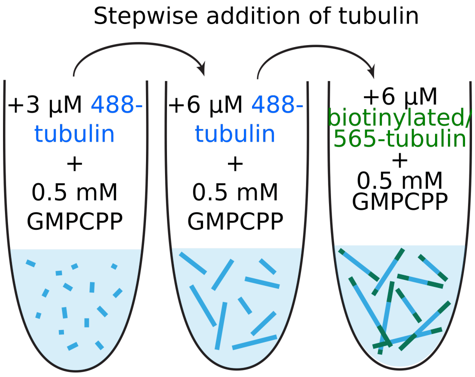

Figure 4.1: Schematic of microtubule preparation. GMPCPP stabilized microtubules were prepared by first growing the central, biotin-free part through stepwise addition of ATTO488 labeled tubulin (blue). Biotinylated ends were added by stepwise addition of ATTO565 labeled and biotinylated tubulin (green).

(Jena Bioscience) was prepared at 37°C to nucleate short microtubule seeds. Next, the concentration was increased to a total of 9 µM tubulin in order to grow long microtubules. To avoid further microtubule nucleation, we added 1 µM tubulin at a time from a 42 µM stock solution (5% ATTO-488-labeled) and waited 15 min between the successive steps. To grow biotinylated ends, we added a mix of 90% biotinylated and 10% ATTO-565-labeled tubulin in steps of 0.5 µM from a 42 µM stock solution up to a total tubulin concentration of 15 µM. We centrifuged polymerized microtubules for 10 min at 13000 $\times$ g to remove any non-polymerized tubulin and short microtubules. We discarded the supernatant and carefully resuspended the pellet in 800 µL M2B-taxol (M2B buffer supplemented with 10 µM taxol (Merck)). By keeping the central part of the microtubules biotin-free, we ensured that any streptavidin molecules detaching from the beads could not affect interaction measurements by cross-linking the filaments.

4.3.4 Determination of Vimentin Filament Length Distributions

To measure the lengths of vimentin IFs (see Supplementary Fig. 8.1), we prepared five 1.5 mL reaction tubes with 15 µL of a mix of 2.3 µM vimentin in combination buffer (see Section 4.4.3) including all additions as used for the TIRF experiments, such as methyl cellulose, GTP, and oxygen scavenger (see the previous section for the exact composition of the buffer). We then incubated the mix at 37°C for 5, 10, 20, 30, or 45 min. The filament assembly was stopped by adding 25 volumes of buffer to the tubes. 5 µL of each diluted mix was then pipetted on a cover glass and a second cover glass was placed on top. Images were taken with an inverted microscope (IX81, Olympus) using the cellSens Dimensions software (version 1.18, Olympus), a 60× oil-immersion PlanApoN objective (Olympus), and an ORCA-Flash 4.0 camera (Hamamatsu Photonics). The filament lengths were determined using the semi-automated JFilament 2D plugin (Lehigh University, Bethlehem, PA, USA, version 1.02) for ImageJ (version 2.0.0-rc-69/1.52p).

4.4 Optical Tweezers Measurements

4.4.1 Stretching of Single Intermediate Filaments

For optical tweezers measurements, the assembled keratin and vimentin IFs were diluted 1:70 and 1:100, respectively, with the corresponding assembly buffer. The optical tweezers setup (C-Trap, LUMICKS, Amsterdam, Netherlands) was equipped with a confocal fluorescence microscope and a microfluidic device as sketched in Fig. 4.2. Polystyrene beads (Kisker Biotech, Steinfurt, Germany) with a diameter of 4.5 µm were maleimide coated [163] to allow for covalent binding to the IFs via cysteines. The beads were diluted with the assembly buffer of the respective studied protein, which was also used as a buffer in the calibration channel. The buffer in channel (4) was either 10 mM TRIS, pH 7.5, or 100 mM KCl, 2 mM phosphate buffer, pH 7.5, and each IF was studied in both buffers.

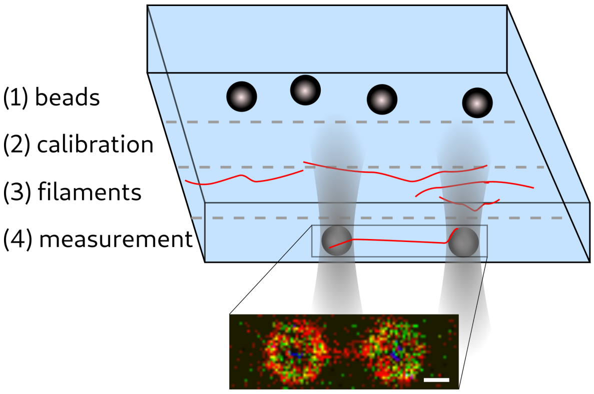

Figure 4.2: Top: Schematic of the microfluidic device used for measurements with the optical tweezers for stretching single filaments. Bottom: Confocal image of a fluorescently labeled keratin IF captured between two 4.42 µm-diameter-beads; scale bar 2 µm.

Before each measurement, two beads were captured with the optical tweezers in channel (1), and the trap stiffness was calibrated via their thermal noise spectrum in channel (2). IFs were attached to the beads in channel (3), and it was ensured by fluorescence microscopy that only one IF was bound to the beads. The traps with the IF were moved to channel (4) and incubated for 30 s, unless the measurement was intended to take place in the assembly buffer of the respective IF protein. One optical trap was moved with speeds between 0.3 µm/s and 2.5 µm/s to stretch the IF in channel (4). The force exerted on the IF by the optical trap as well as the bead positions were recorded.

For repeated loading of IFs as presented in Chapter 7, one of the traps was moved either to the same distance or up to the same force value.

4.4.2 Analysis of the Force-Strain Curve of Single Intermediate Filaments

From the optical tweezers data, the strain $\varepsilon = L/L_0 - 1$ was calculated [7] using the measured IF length L and the IF length L_0 at 5 pN. The averages were calculated by averaging both force and strain data.

Averaging of force-strain curves: Average force-strain curves were calculated by averaging the force and strain data for all curves in three steps as shown for typical single data

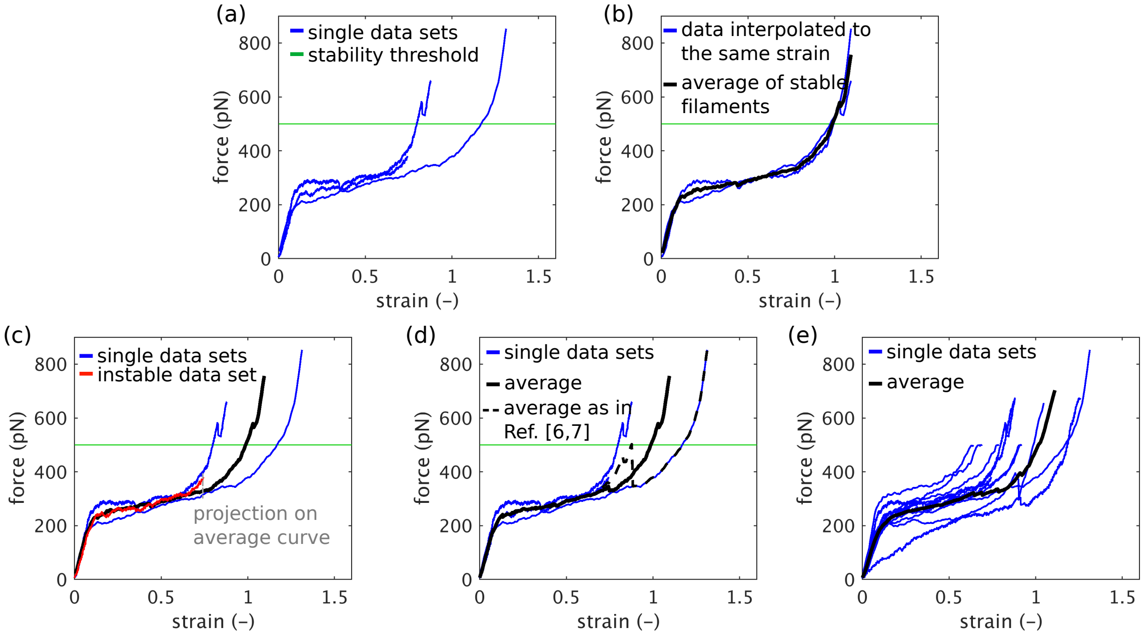

Figure 4.3: (a-d) Force-strain averaging method for three typical force-strain data sets of single vimentin IFs in vimentin assembly buffer. (a) Typical force-strain data sets (blue) and stability threshold force (green). (b) Interpolation of stable force and strain data sets to 200 data points (blue) and average data (black). (c) Projection of the strain data of the instable filament on the average strain data calculated so far. (d) Average of all force data (black, solid line) and average calculated with the method used in Refs. [6, 7] (black, dashed line). (e) All data sets of vimentin force-strain curves measured in vimentin assembly buffer (blue lines) and their average (thick black line). Note the one outlier curve which does not show the typical plateau-like behavior as the other curves.

sets in Fig. 4.3: (1) The force-strain data sets were classified as stable if the measured force exceeded 500 pN. For the curves in Fig. 4.3a, one filament was not stable and two were stable. (2) The force data from the stable filaments were interpolated to the same number of data points (200). The average of the maximum strain values of all stable filaments was calculated and set to the maximum strain for all stable filaments as shown in Fig. 4.3b. The strain data consisted of 200 equally spaced data points from 0 up to the average maximum strain. The force data of all stable filaments were averaged for each strain value to obtain the average force-strain curve of all stable filaments as shown in Fig. 4.3b. (3) All instable filaments were additionally taken into account: The strain value of the average curve of all stable filaments closest to the maximum strain value of the instable filament was determined as shown in Fig. 4.3c. The force data of the instable filament were interpolated to the number of data points which were required to describe the average force data for stable filaments up to the point where the instable filament broke. The force data of the instable filament were averaged with the average force curve for stable filaments for each strain value as in Fig. 4.3d. Since only one filament was instable, but the average force data were calculated from two stable filaments in steps (1) and (2), the data from the instable filament were weighted as one third of the average of the two stable curves. The data from the instable filament were only taken into account up to the strain at which it breaks. 4.3e shows all data sets of vimentin force-strain curves measured in 100 mM KCl, 2 mM phosphate buffer, pH 7.5, (blue lines) and their average (thick black line).

In Refs. [6, 7], the force data were averaged without calculating the average strain data.

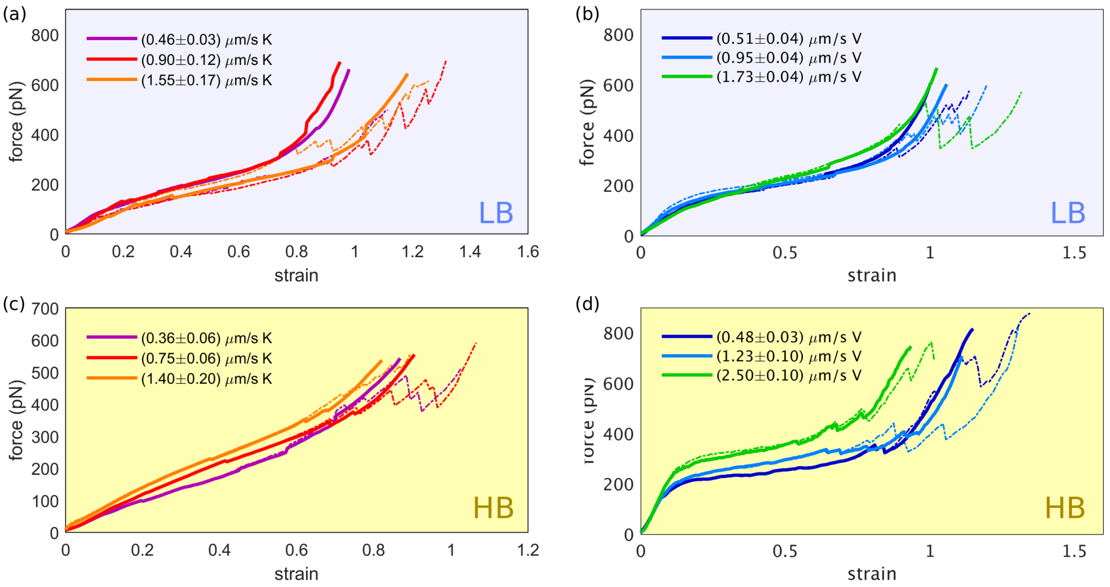

Figure 4.4: Force-strain curves comparing the force averaging method as in Refs. [6, 7] (dashed lines) and the averaging method used here (solid lines) for keratin and vimentin IFs in varying buffer conditions: (a) Keratin (K) IFs in keratin assembly buffer (LB), (b) vimentin IFs (V) in keratin assembly buffer (LB; blue background), (c) keratin IFs in vimentin assembly buffer (HB), (d) vimentin IFs in vimentin assembly buffer (HB; yellow background).

By contrast, the method presented here also takes the average strain into account, avoids kinks for high strain values and does not calculate the average force-strain curve from a few data curves only in the high strain regime. Both methods are compared in Fig. 4.3d and Fig. 4.4.

Slope analysis for intermediate strains: For each data set, a linear regression was fitted to the force data for strains between 30% and 70% of the maximum strain value. All fits are shown in Fig. 4.5.

Input energy calculation: We integrated the force-strain curves within the force range of 0 to 500 pN using the MatLab function `trapz`. The results in units of $k_B T$ are shown in Fig. 4.6.

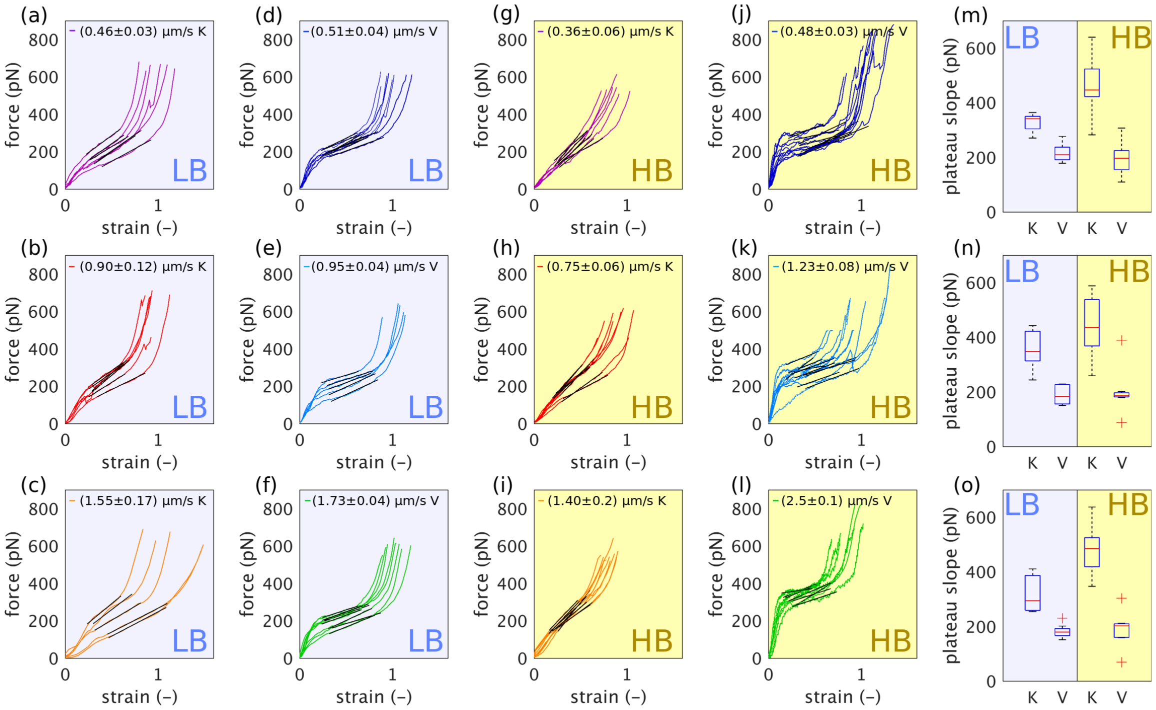

Figure 4.5: Analysis of the slopes of the intermediate regime of the force-strain curves: (a-l) Linear regressions to the force-strain data from 30% to 70% of the maximum strain. (m-o) Boxplots of the resulting slopes. From top row to bottom row: increasing loading rates. When comparing vimentin (V) IFs in keratin assembly buffer (LB) and vimentin assembly buffer (HB) for each loading rates, the slopes did not differ considerably.

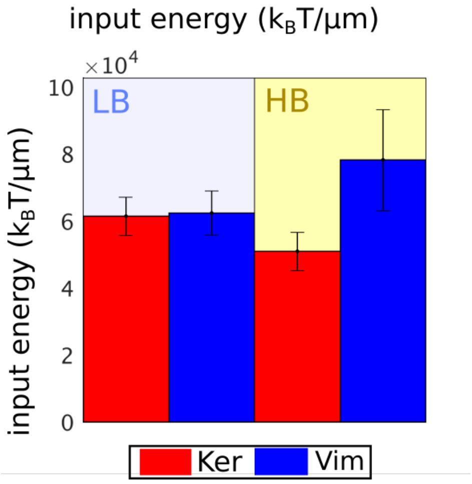

Figure 4.6: Input energy of keratin and vimentin IFs in two buffer conditions (blue background: keratin assembly buffer (LB), yellow background: vimentin assembly buffer (HB)).

4.4.3 Measurements of Interactions Between Single Filaments

For measurements in the microfluidic chip by optical tweezers, we prepared four solutions for the four different microfluidic channels as sketched in Fig. 4.7: (I) We diluted streptavidin-coated beads with an average diameter of 4.5 µm (Kisker Biotech) 1:83 with vimentin assembly buffer. (II) We diluted the vimentin IFs 1:667 with vimentin assembly buffer. (III.) We diluted the resuspended microtubules 1:333 with combination buffer (see IV.). (IV.) We combined suitable buffer conditions for microtubules and for vimentin IFs, respectively, to a combination buffer (CB) containing 1 mM EGTA (Merck), 2 mM magnesium chloride, 25 mM PIPES (Carl Roth), 60 mM potassium chloride (Carl Roth) and 2 mM sodium phosphate (Carl Roth) at pH 7.5. We included an oxygen scavenging system consisting of 1.2 mg/mL glucose (Merck), 0.04 mg/mL glucose oxidase (Merck), 0.008 mg/mL catalase (Merck) and 20 mM DTT (Carl Roth). Additional 0.01 mM taxol (Merck) stabilized the microtubules. For measurements with TX100, we added 0.1 % (w/v) Triton-X 100 (TX100; Carl Roth) and in case of measurements with a total magnesium concentration of 20 mM, we added 18 mM $MgCl_2$. We filtered the solutions through a cellulose acetate membrane filter with a pore size of 0.2 µm (Th. Geyer, Renningen, Germany).

We performed the optical tweezers experiments using a commercial setup (C-Trap, LUMICKS) equipped with quadruple optical tweezers, a microfluidic chip and a confocal microscope. Beads, microtubules, measuring buffer and IFs were flushed into four inlets of the microfluidic chip as sketched in Fig. 4.7. For each measurement, four beads were captured and then calibrated in the buffer channel using the thermal noise spectrum. One bead pair (beads 3 and 4) was moved to the vimentin IF channel and incubated there until a filament bound to the beads (Fig. 4.7II.). Meanwhile, the other bead pair (beads 1 and 2) was kept in the measuring buffer channel, so that no filaments adhered to those beads. To

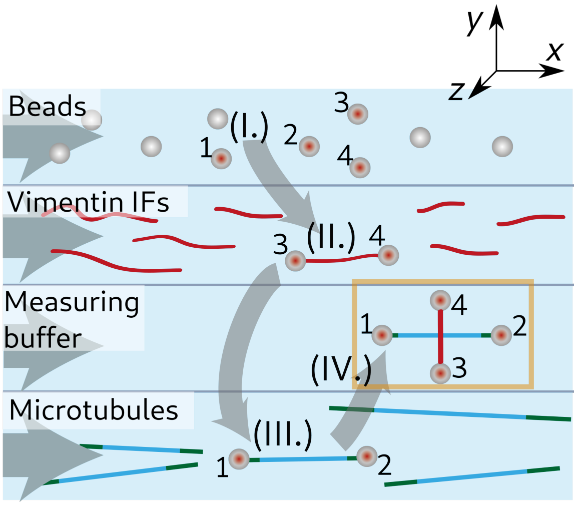

Figure 4.7: Schematic of the setup for the optical tweezers experiments for interaction measurements in microfluidic flow channels. Four streptavidin-coated beads were captured by optical tweezers (I.). We used one bead pair (beads 3 and 4) to attach a vimentin IF (II., red), and the other bead pair (beads 1 and 2) to attach a microtubule (III., green-cyan). We brought the IF and the microtubule into contact in a crossed configuration (IV.). Next, we moved the IF perpendicularly to the microtubule to study the IF-microtubule interactions while we took confocal fluorescence images.

capture a microtubule (Fig. 4.7III.), beads 1 and 2 were moved to the microtubule channel, while bead 3 and 4 stayed in the measuring buffer channel. Once a microtubule was bound to beads 1 and 2 and an IF to beads 3 and 4, the bead pair with the IF was horizontally turned by 90° (Fig. 4.8a) and moved up in z-direction by 4.9 µm. The bead pair holding the IF was moved in the x-y-plane so that the central part of the IF was positioned above the center of the microtubule (Fig. 4.8aIV.). To bring the IF and microtubule into contact, the IF was moved down in z-direction until the microtubule was pushed into focus or slightly out of focus. In a portion of the experiments, we turned the microtubule by 45° and visually controlled the angle by fluorescence microscopy.

The IF was moved perpendicularly to the microtubule in the y-direction in the x-y-plane at 0.55 µm/s, while we measured the forces in the x- and y-direction on bead 1. For a horizontal movement, we moved the IF perpendicularly to the microtubule in the x-direction in the x-y-plane at 0.55 µm/s. Simultaneously, we recorded confocal images to see whether an interaction occurred. In case no interaction occurred after two movements in the x-y-plane, the IF was moved down in z-direction by 0.4 µm and the movement in the x-y-plane was repeated. The experiment ended when the microtubule broke off the bead, or the IF or microtubule broke. In case of the vertical movement in a perpendicular configuration, we measured 57 pairs of microtubules and vimentin IFs in CB, 38 pairs with TX100 and 36 pairs with additional magnesium chloride. In total, we moved the IFs 744 times vertically and perpendicularly to the microtubules in CB, 704 times in CB with TX100 and 542 times in CB with additional magnesium chloride. In the case of the 45°-configuration we studied 49 pairs of microtubules and vimentin IFs and completed 467 movements. In the case of horizontal movement of the IF in perpendicular configuration with respect to the microtubule, we studied 43 filament pairs and completed 504 movements.

4.4.4 Analysis of the Interactions Between Single Filaments

The optical tweezers data were processed with self-written Matlab (MathWorks, Natick, MA, USA) scripts. In case of the vimentin IF movement in the y-direction and a perpendicular orientation to the microtubule, we analyzed the component of the force F_{1y} acting on bead 1 in the y-direction for each filament pair, since the forces in x-direction were balanced by the IF, as sketched in Fig. 4.8b. From the raw force data, we manually selected the force data containing an interaction. Due to interactions of the energy potentials of the different traps, some data sets exhibited a linear offset which we subtracted from the data. From the interaction-free force data, we determined the experimental error by calculating the standard deviation in the force of the first 20 data points. We defined an interaction as soon as the force F_{1y} deviated by more than $5\sigma_F$ from the mean of the first 20 data points, where σ_F is the standard deviation of the force without interactions in each data set. Typically, the force increased until the interaction ended with a fast force decrease as marked by ΔF_{1y}. We did not take breaking forces below 0.5 pN into account because they may be caused by force fluctuations. Since the force detection of trap 1 is the most accurate one in the setup, we analyzed the force on bead 1 only. To determine the total breaking force F_B, we multiplied the force F_{1y} acting on bead 1 in y-direction with a correction factor c_F that is based on the geometry of the experiment. c_F depends on the distance d_{MT} between bead 1 and 2 and the

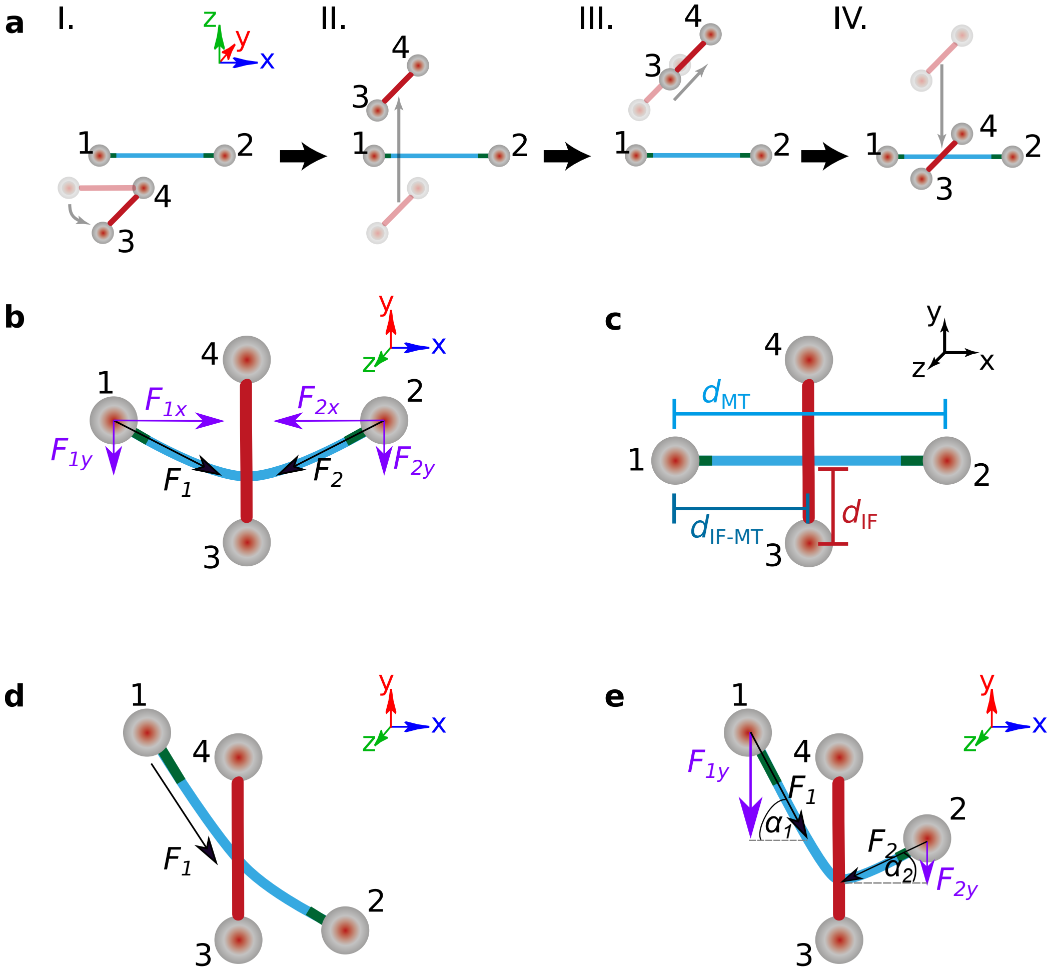

Figure 4.8: Protocol and geometry of the optical tweezers experiments. (a) To measure direct interactions between a single IF (red) and a single microtubule (blue), we turned the vimentin IF in the x-y plane so that it was perpendicularly aligned to the microtubule (MT in x-direction, IF in y-direction) (I). We moved the IF upwards in z-direction (II.) and moved it in the x-y plane so that the center of the IF was positioned above the center of the microtubule (III.). Next (IV.), we moved the IF downwards in z-direction until it was in the same x-y plane as the microtubule; the IF and microtubule were then in contact. (b) Forces acting on the IF and the microtubule. (c) Definition of the length scales required for the analysis of the optical tweezers data. (d) Geometric configuration and analyzed force if the vimentin IF was moved in the y-direction, the microtubule was turned by 45°, and the point of interaction was located higher in y than bead 2. (e) Definition of forces and angles for the same configuration as in d if the point of interaction was located lower in y than bead 2.

distance $d_{\text{IF-MT}}$ from bead 1 to the contact point of the IF and the microtubule as sketched in Fig. 4.8c:

$$c_F = \frac{d_{\text{MT}}}{d_{\text{IF-MT}}} \,. \tag{4.1}$$

For the total force F_C acting on the IF-microtubule bond, we get:

$$F_C = c_F F_{1y} \,.$$

Thus, when an IF-microtubule bond breaks, the total force difference F_B is:

$$F_B = c_F \Delta F_{1y} \,. \tag{4.2}$$

In case of a 45° angle between microtubule and vimentin IF and in case of IF movement in the x-direction the force data were analyzed in the same way as described above with the following differences:

For the case, where the microtubule was turned by 45°, we calculated the geometric factor in two different ways, depending on the geometry at the moment of bond breakage: (i) If the bond breaks at a higher y-position than bead 2 (see Fig. 4.8d), we assume that the total force acting on the IF-microtubule bond is measured by the complete force F_1 acting on bead 1. Thus, $c_F = 1$, and the breaking force is:

$$F_B = \Delta F_1 \,.$$

(ii) If the bond breaks at a lower y-position than bead 2 (see Fig. 4.8e), we calculate the geometric factor differently, since a significant part of the total force also acts on bead 2. We assume that the forces are balanced in x, i.e. $F_{1x} = F_{2x}$ (see Fig. 4.8b). The total force acting in the x-direction on bead i relates to the total force acting on bead i:

$$\begin{aligned} F_{ix} = \cos\alpha_i F_i &\xRightarrow{F_{1x}=F_{2x}} \cos\alpha_1 F_1 = \cos\alpha_2 F_2 \,, \\ &\Rightarrow F_2 = \frac{\cos\alpha_1}{\cos\alpha_2} F_1 \,. \end{aligned} \tag{4.3}$$

Similarly, the total force acting on bead i in the y-direction relates to the total force as:

$$F_{iy} = \sin\alpha_i F_i \Rightarrow F_i = \frac{F_{iy}}{\sin\alpha_i} \,. \tag{4.4}$$

Thus, for the force acting on bead 2 in the y-direction, we get:

$$\begin{aligned} F_{2y} &= \sin\alpha_2 F_2 \\ &\overset{\text{Eq. 4.3}}{=} \sin\alpha_2 \frac{\cos\alpha_1}{\cos\alpha_2} F_1 \\ &\overset{\text{Eq. 4.4}}{=} \sin\alpha_2 \frac{\cos\alpha_1}{\cos\alpha_2} \frac{F_{1y}}{\sin\alpha_1} \\ &= \frac{sin\alpha_2}{\cos\alpha_2} \frac{\cos\alpha_1}{\sin\alpha_1} F_{1y} \\ &= \frac{\tan\alpha_2}{\tan\alpha_1} F_{1y} \,. \end{aligned}$$

Consequently, the correction factor c_F as defined by Eq. 4.2 is:

$$c_F = 1 + \frac{\tan \alpha_2}{\tan \alpha_1} .$$

We analyzed F_{1y} again and the breaking force was calculated with Eq. 4.2.

In case the IF was moved perpendicularly to the microtubule in the x-direction, we analyzed the force F_{1x} acting on bead 1 in the x-direction. We did not need to correct for the geometry of the experiment, thus, $c_F = 1$:

$$F_B = \Delta F_{1x} .$$

To compare the three binding rates of the three different measurement geometries in the optical tweezers experiments, we modeled the binding rates, which depend on the following parameters: The velocity v with which periodic microtubule and vimentin subunits pass each other, the length $l_{u,\mathrm{IF}}$ of the ULFs and the length $l_{u,\mathrm{MT}}$ of a tubulin dimer, the probability of a tubulin dimer and vimentin ULF to bind to each other $p_{\text{IF-MT}}$, and the number of dimers and ULFs in the overlapping area of both filaments $a_{\mathrm{IF}}/l_{u,\mathrm{MT}}$ or $a_{\mathrm{MT}}/l_{u,\mathrm{IF}}$. Thus, the binding rate for a vertical movement of the IF perpendicular to the microtubule is described as the product of an encounter rate and the probability $p_{\text{IF-MT}}$ that a bond is formed. The encounter rate in turn is given by the rate at which potential binding sites pass each other and the number of binding sites in the overlap area, which results in:

$$r_{b,\mathrm{eff},y} = \frac{v}{l_{u,\mathrm{IF}}} \frac{a_{\mathrm{IF}}}{l_{u,\mathrm{MT}}} p_{\text{IF-MT}} . \tag{4.5}$$

Note that here we describe binding between one subunit on each filament (tubulin dimer and vimentin ULF, respectively). If binding involves contacts with several subunits on a filament, potential effective binding sites are bigger, but due to the periodic structure of the filaments there is the same number of binding sites per filament length and thus the same encounter rate. If there is more than one potential binding site within one filament subunit, the encounter rate is increased, and the inferred binding probability is reduced by the same factor, so that their product is the same. In all these cases, our binding parameters can be interpreted as effective parameters for the binding between a microtubule dimer and a vimentin ULF.

When the microtubule is turned by 45°, the binding rate is expected to change by a factor of $\sqrt{2}$ because the overlap area increases by a factor of $1/\cos(45^\circ)$. Thus, the binding rate for the 45°-configuration with a vertical movement of the IF becomes:

$$r_{b,\mathrm{eff},45^\circ} = \frac{v}{l_{u,\mathrm{IF}}} \frac{a_{\mathrm{IF}}}{l_{u,\mathrm{MT}}} p_{\text{IF-MT}} \sqrt{2} . \tag{4.6}$$

In case of the horizontal movement of the IF along the microtubule, the rate of passing subunits changes to $v/l_{u,\mathrm{MT}}$ and the number of encounters of subunits is $a_{\mathrm{MT}}/l_{u,\mathrm{IF}}$:

$$r_{b,\mathrm{eff},x} = \frac{v}{l_{u,\mathrm{MT}}} \frac{a_{\mathrm{MT}}}{l_{u,\mathrm{IF}}} p_{\text{IF-MT}} . \tag{4.7}$$

We calculated the ratios of the binding rates for each pairing of measuring geometries. Comparison with the results from equations 4.5-4.7 shows good agreement:

$$\text{theoretical: } \frac{r_{b,\text{eff},y}}{r_{b,\text{eff},45^\circ}} = \frac{1}{\sqrt{2}} \simeq 0.71, \qquad \text{experimental: } 0.65$$

$$\text{theoretical: } \frac{r_{b,\text{eff},y}}{r_{b,\text{eff},x}} = \frac{a_{\text{IF}}}{a_{\text{MT}}} \simeq 0.44, \qquad \text{experimental: } 0.44,$$

$$\text{theoretical: } \frac{r_{b,\text{eff},45^\circ}}{r_{b,\text{eff},x}} = \frac{\sqrt{2}a_{\text{IF}}}{a_{\text{MT}}} \simeq 0.62, \qquad \text{experimental: } 0.67.$$

Alternatively, we can calculate the probability of a tubulin subunit to bind to a vimentin subunit from the experimental data using Eqs. 4.5-4.7:

$$\begin{aligned}
\text{vertical movement, } 90^\circ &: p_{\text{IF-MT}} \simeq 5.9 \cdot 10^{-4}\,, \\
\text{vertical movement, } 45^\circ &: p_{\text{IF-MT}} \simeq 6.4 \cdot 10^{-4}\,, \\
\text{horizontal movement, } 90^\circ &: p_{\text{IF-MT}} \simeq 6.0 \cdot 10^{-4}\,.
\end{aligned}$$

4.5 Atomic Force Microscopy

4.5.1 Sample Preparation and Measurement

The assembled protein was diluted 1:10 in the case of vimentin and 1:5 in the case of keratin with the corresponding assembly buffer and incubated for 30 s. Glutaraldehyde (2.5% in PBS) was prepared at a final concentration of 0.25% by dilution with the buffer that the protein was studied in, keratin assembly buffer or vimentin assembly buffer. The diluted glutaraldehyde and the diluted protein were mixed 1:1 and incubated for 30 s. The mixture was transferred to a piece of silicon wafer (Crystec, Berlin, Germany), 0.8 cm × 1.2 cm, and incubated for 3 to 5 min. 100 µL of fresh buffer were added three times and removed again to wash non-adhered filaments off the silicon wafer. About 150 µL of buffer were left on the sample during imaging. The smallest tip on the multi-tip cantilever (MLCT, Bruker, Billerica, MA, USA) with a tip radius of about 20 nm was used for imaging in tapping mode.

4.5.2 Analysis of Filament Height

The areas of interest in AFM height images were chosen manually. The selection was thresholded, so that the filament was clearly distinguishable from the background. Since the side length of the AFM images was merely 3–3.5 µm, single filaments did not form loops, so that it was possible to describe the filament contour as a function $y = L(x)$. The x-coordinate was obtained by averaging the positions of pixels which were occupied by the filament at x. The `smoothingspline`-fit function from MatLab was used to smooth the filament contour. The filament height was measured along perpendicular lines to the filament contour.

4.6 Total Internal Reflection Microscopy

4.6.1 Measurements of Dynamic Microtubules

We cleaned cover glasses (26 × 76 mm^2, no. 1, Thermo Scientific) by successive chemical treatments: (i) We incubated the cover glasses for 30 min in acetone and then (ii) for 15 min in ethanol (96% denatured, VWR, Radnor, PA, USA), (iii) rinsed them with ultrapure water, (iv) left them for 2 h in Hellmanex III (2% (v/v) in water (Hellma Analytics, Müllheim, Germany)), and (v) rinsed them with ultrapure water. Subsequently, we dried the cover glasses using nitrogen gas flow and incubated them for three days in a 1 g/L solution of 1:10 silane-PEG-biotin (Creative PEG Works, Chapel Hill, NC, USA) and silane-PEG (30 kDa, Creative PEG Works) in 96% ethanol and 0.02% v/v hydrochloric acid, with gentle agitation at room temperature. We subsequently washed the cover glasses in ethanol and ultrapure water, dried them with nitrogen gas and stored them at 4°C for a maximum of four weeks.

We used an inverted microscope (IX71, Olympus, Hamburg, Germany) in TIRF mode equipped with a 488-nm laser (06-MLD, 240 mW, COBOLT, Solna, Sweden), a 561-nm laser (06-DPL, 100 mW, COBOLT), and an oil immersion TIRF objective (NA =1.45, 150×, Olympus). We observed microtubule dynamics by taking an image every 5 s for 15–45 min using the cellSens Dimensions software (version 1.18, Olympus) and a digital CMOS camera (ORCA-Flash4.0, Hamamatsu Photonics, Hamamatsu, Japan).

For TIRF experiments, we built flow chambers from passivated cover glasses and a double-sided tape (70 µm height, 0000P70PC3003, LiMA, Couzeix, France). We flushed 50 µg/mL neutravidin (A-2666, Invitrogen, Carlsbad, CA, USA) in BRB80 into the chamber and incubated for 30 s. To remove free neutravidin, we washed with BRB80. Afterwards, we flushed microtubule seeds diluted 300 × in BRB80 into the chamber and incubated for 1 min before we removed free-floating seeds by washing with BRB80 supplemented with 1% BSA (bovine serum albumin). Then, a mix containing 0.5 mg/mL or 0.8 mg/mL (corresponding to 2.34 or 3.74 µM) vimentin tetramers (4% ATTO-565-labeled), 20 or 25 µM tubulin dimers (20% ATTO488-labeled), 0.65% BSA, 0.09% methyl cellulose, 2 mM phosphate buffer, 2 mM $MgCl_2$, 25 mM PIPES, 1 mM EGTA, 60 mM KCl, 20 mM DTT, 1.2 mg/mL glucose, 8 µg/mL catalase, and 40 µg/mL glucose oxidase, pH 7.5, was perfused into the chamber. To avoid evaporation and convective flow, we closed the chamber with vacuum grease and placed it on the stage of the TIRF microscope that was kept at 37°C. We used the cellSens Dimensions software (version 1.18, Olympus).

4.6.2 Analysis of Microtubule Dynamics

From the TIRF movies, kymographs were created using the reslice function of ImageJ (ImageJ V, version 2.0.0-rc-69/1.52p). From the kymographs, microtubule growth and depolymerization velocities, catastrophe and rescue frequencies were estimated. We calculated the catastrophe frequency for each experiment as

$$f_{\mathrm{cat,exp}} = \frac{\text{total number of catastrophe events}}{\text{total microtubule growth time}}$$

and the rescue frequency as

$$f_{\text{resc}} = \frac{\text{total number of rescue events}}{\text{total microtubule depolymerization time}} .$$

The total growth time was 800-2000 min per condition, the total depolymerization time 50-70 min per condition. The growth rate plot in the main text of the publication in Fig. 8.1d contains between 106 and 163 measurements per condition.

CHAPTER 5

Models and Simulations

Section 5.1 is part of the supplementary material of the publication "Lateral Subunit Coupling Determines Intermediate Filament Mechanics" in *Physical Review Letters* **123** (188102) by Charlotta Lorenz, Johanna Forsting, Anna V. Schepers, Julia Kraxner, Susanne Bauch, Hannes Witt, Stefan Klumpp, and Sarah Köster in 2019 (© 2019 American Physical Society) [156]. Section 6.1 contains the entire main text of this publication.

Section 5.1.3 is part of the supplementary material of the publication "Post-Translational Modifications Soften Vimentin Intermediate Filaments" in *Nanoscale* **1** by Julia Kraxner, Charlotta Lorenz, Julia Menzel, Iwan Parfentev, Ivan Silbern, Manuela Denz, Henning Urlaub, Blanche Schwappach and Sarah Köster in 2021 (Creative Commons Attribution-NonCommercial 3.0 Unported) [82]. Section 6.4 contains a summary of this publication.

Sections 5.3.1 and 5.2 are part of the supplementary information of the publication "Vimentin Intermediate Filaments Stabilize Dynamic Microtubules by Direct Interactions" in *Nature Communications* **12** (3799) by Laura Schaedel*, Charlotta Lorenz*, Anna V. Schepers, Stefan Klumpp, and Sarah Köster in 2021 (Creative Commons Attribution 4.0 International License) [157]. Section 8.2 contains the entire main text of this publication.

* Equal Contribution.

5.1 Monte-Carlo Simulations of Intermediate Filaments under Load

Single keratin and vimentin IFs under tension were modeled with a mechanical model which was based on Refs. [7, 63, 151, 155]. One unit length filament (ULF) had N_P parallel monomers, which were arranged in parallel and all have the same length before loading. The monomers could be divided into N_C N_M-mers. E.g., a ULF with $N_P = 32$ monomers could be divided into 16 dimers as we assumed in the simulation of vimentin IFs in LB ($N_C = 16$, $N_M = 2$) [77, 164]. In the following, we will assume two different coupling cases: In case 1, the N_M-mers acted as independent units; in case 2, the N_M-mers were coupled to one another. Thus, in case 1, the subunits were allowed to slide past each other, but they were still laterally arranged. This also supports the idea of a protofilament structure of the filament after assembly in which the protofilaments can slide past each other [165–167]. The total number of ULFs connected in series in one filament before loading was N_F.

5.1.1 Uncoupled Subunits Within the Intermediate Filament

When the N_M-mers could elongate independently, the ULF elongated once all monomers in one N_M-mer were in the unfolded state u. A sketch of the model is shown in Fig. 5.1a. In this case, all N_M-ers that were fully in the unfolded state were exposed to the loading force, so that they contributed to the ULF stiffness even if there were still N_M-mers in the α state in the same ULF.

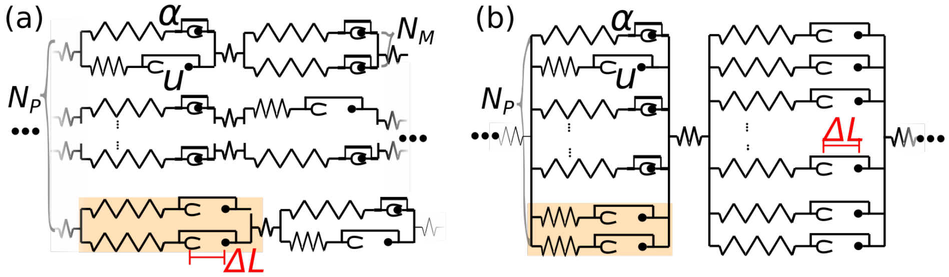

Figure 5.1: (a) Model for uncoupled dimers as subunits, case (1), and (b) model for coupled dimers as subunits, case (2). If one subunit is in the unfolded state in case (1), this leads to an elongation by ΔL, whereas in case (2) all monomers have to be in the unfolded state for elongation (orange: elements discussed in the text).

The spring constant of an α helix was κ_α, the spring constant of the monomer in the unfolded state κ_u and the spring constant of all linkers was κ_L. $A_{j,m}$ was the number of monomers in the α state and $B_{j,m}$ was the number of monomers in the unfolded state in the mth N_M-mer in the jth ULF, thus $A_{j,m} + B_{j,m} = N_M$. I_j was the number of N_M-mers of which all monomers were in the unfolded state. Thus, the spring constant became:

$$\kappa_j = \begin{cases} \left(\frac{1}{\kappa_L} + \frac{1}{N_P \kappa_u}\right)^{-1} & \text{for} \sum\limits_{m=1}^{N_C} A_{j,m} = 0 \\ \left(\frac{1}{\kappa_L} + \frac{1}{\sum\limits_{m=1}^{N_C} A_{j,m}\kappa_\alpha + N_M \kappa_u I_j}\right)^{-1} & \text{for} \sum\limits_{m=1}^{N_C} A_{j,m} > 0. \end{cases}$$

The spring constant of the entire filament was calculated by $\kappa_F = 1/(\sum_{j=1}^{N_F} 1/\kappa_j)$. Similar to Ref. [7], we neglected viscous and entropic contributions for simplicity.

The equilibrium reaction constant K_{eq} for the α to unfolded state transition was:

$$K_{eq} = \frac{r^{\alpha \to u}}{r^{u \to \alpha}} = \exp(-\Delta G/(k_B T)) = 1/\gamma\,,$$

where we defined $\gamma = \exp(\Delta G/(k_B T))$.

The load distribution factor θ $(0 < \theta < 1)$ [153, 168] ensured detailed balance between opening and closing of a single α helix and so that the model lead to a thermodynamic equilibrium state in the non-driven limit. The force was distributed among the number of independent subunits N_C and within these elements on the number of monomers in the α helix configuration $A_{j,m}$. The force $\phi = F/F_\alpha$ was dimensionless and scaled to the force F_α which was required to open an α helix into the unfolded state. The time τ was dimensionless and related to the time t with the zero-force reaction rate from a monomer in the α to the unfolded state $r_0^{\alpha \to u}$ by $\tau = r_0^{\alpha \to u} t$. We assumed Bell-Evans kinetics [151], so that the α to unfolded transition rate was:

$$r_{A_{j,m}}^{\alpha\to u} = A_{j,m} r_0^{\alpha\to u} \exp\left(\frac{\theta\phi}{N_C A_{j,m}}\right).$$

All monomers of one N_M-mer in the unfolded state folded back to the α state with the equilibrium constant since we assumed that they were free of force if there were still α helices in the same N_M-mer, corresponding to the condition $A_{j,m} > 0$. If all monomers were in the unfolded state ($A_{j,m} = 0$), the reaction rate to the α state depended on the force. In this case, the force $(1-\theta)\phi$ was distributed to all N_P monomers. Therefore, the closing of the unfolded states to the α helix became:

$$r_{A_{j,m}}^{u\to\alpha} = \begin{cases} r_0^{\alpha\to u} B_{j,m}\gamma & \text{for } A_{j,m} > 0 \\ N_M r_0^{\alpha\to u}\gamma \exp\left(\frac{-(1-\theta)\phi}{N_P}\right) & \text{for } A_{j,m} = 0. \end{cases}$$

From these rates, we calculated the probability $P_{A_{j,m}}$ that a certain number of a monomers was in the α helix configuration. This was vital for performing the Gillespie algorithm in the simulation:

$$\begin{aligned} \frac{dP_{A_{j,m}}}{dt} &= r_{A_{j,m}+1}^{\alpha\to u} P_{A_{j,m}+1} + r_{A_{j,m}-1}^{u\to\alpha} P_{A_{j,m}-1} \\ &\quad -(r_{A_{j,m}}^{\alpha\to u} + r_{A_{j,m}}^{u\to\alpha}) P_{A_{j,m}}. \end{aligned} \tag{5.1}$$

When all monomers in one N_M-mer were in the unfolded state, the ULF extended by ΔL. To make the simulation run dimensionless, we normalized $\lambda = L_0/\Delta L$, where L_0 was a characteristic length of the filament, e.g. the original filament length. Thus, in this case, the extension of the jth ULF λ_j was:

$$\lambda_j = \begin{cases} 0 & \text{if for all } m\text{: } A_{j,m} > 0 \\ 1 & \text{if for any } m\text{: } A_{j,m} = 0. \end{cases} \tag{5.2}$$

The total extension of the filament then is $\lambda_{tot} = \sum_{i=1}^{N_F} \lambda_j$. Since the optical tweezers pull on the filament with a constant velocity v, the end-to-end distance is $x(t) = vt$. The force on the filament becomes

$$\phi = \kappa_F(x - \lambda_{tot}). \tag{5.3}$$

5.1.2 Coupled Subunits Within the Intermediate Filament

Length extension of the ULF occurs when all monomers of the ULF were in the unfolded state. The probability that a certain number of monomers was in the α-helical configuration was still calculated as in Eq. 5.1. The force calculation was the same as in Eq. 5.3. However, in this case, the force that acted on a ULF was distributed over all monomers in the α state in the ULF. The length of the filament increased only once all α helices in one ULF were in the unfolded state. It was no longer sufficient that one N_M-mer was in the unfolded state, as in case 1 above. This was equivalent to the assumption that subunits did not slide past each other. A sketch of this model is shown in Fig. 5.1b.

N_M-mers in the unfolded state did not contribute to the overall spring constant, if there was any monomer in the α state in the same ULF. Thus, the spring constant of the jth ULF was calculated as:

$$\kappa_j = \begin{cases} \left(\frac{1}{\kappa_L} + \frac{1}{N_P\kappa_u}\right)^{-1} & \text{for } \sum\limits_{m=1}^{N_C} A_{j,m} = 0 \\ \left(\frac{1}{\kappa_L} + \frac{1}{\sum\limits_{m=1}^{N_C} A_{j,m}\kappa_\alpha}\right)^{-1} & \text{for } \sum\limits_{m=1}^{N_C} A_{j,m} > 0\,. \end{cases}$$

For the mth subunit in the jth ULF we obtained:

$$r_{A_{j,m}}^{\alpha\to u} = A_{j,m} r_0^{\alpha\to u} \exp\left(\frac{\theta\phi}{\sum\limits_{m=1}^{N_C} A_{j,m}}\right),$$

since the force $\theta\phi$ was equally distributed among all monomers in the α state $\sum_{m=1}^{N_C} A_{j,m}$.

For the reaction from the unfolded to the α state we got:

$$r_{A_{j,m}}^{u\to\alpha} = \begin{cases} r_0^{\alpha\to u} B_{j,m}\gamma & \text{for } \sum\limits_{m=1}^{N_C} A_{j,m} > 0 \\ N_M r_0^{\alpha\to u}\gamma \exp\left(\frac{-(1-\theta)\phi}{N_P}\right) & \text{for } \sum\limits_{m=1}^{N_C} A_{j,m} = 0. \end{cases}$$

The crucial difference to case (1) was that the filament extends in length *only* when all monomers within a ULF were in the unfolded state. Comparing to Eq. 5.2, we got:

$$\lambda_j = \begin{cases} 0 & \text{if for any } m: \ A_{j,m} > 0 \\ 1 & \text{if } \sum\limits_{m=1}^{N_C} A_{j,m} = 0. \end{cases}$$

As shown in Fig. 6.4c in Section 6.1, a high initial slope and a reduced slope for intermediate strains in the force-strain data emerged in the coupled case, but not for the uncoupled case for the same reasonable parameters (see Table 5.1). With these parameters, we could classify the linkers as "soft transducers" since $(\kappa_\alpha + \kappa_u) \lesssim \kappa_L$ [154]. To show that the high initial slope and the large change from the high initial slope to the reduced slope for intermediate strains were caused by the high lateral coupling strength between the subunits and not by the different number of subunits in keratin IFs ($N_P = 16$) and vimentin IFs ($N_P = 32$), the uncoupled case (1) was simulated for 32 monomers instead of 16 and shown as the "control" data in Fig. 5.2. The same set of parameters for either 32 and 16 monomers per cross section in the uncoupled case did not lead to different qualitative force-strain behavior.

Fitting and rescaling to SI units: The initial fitting parameters of the simulations were guessed so that they resemble the data. The `fminsearch`-function of MatLab was used to find the minimum sum f of the absolute differences between the single values of the experimental data and the simulated data. The parameters κ_L, κ_α, κ_u, ΔG and ΔL were varied by `fminsearch` to find the minimum of f. To obtain the strain ε in the units of the experiment, the strain x of the filament in the simulation was rescaled with the relative length change

Table 5.1: Simulation parameters in simulation units. The case describes either the uncoupled case 1 or the coupled case 2.

condition	case	N_P	ΔG	κ_α
K in LB	1	16	2.0 ± 0.6	4.4 ± 1.9
V in LB	1	32	1.60 ± 0.15	2.1 ± 0.7
K in HB	1	16	3.1 ± 0.4	4.6 ± 1.3
V in HB	2	32	0.41 ± 0.09	11 ± 4
V control	1	32	3.1	4.6

condition	κ_u	κ_L	ΔL	"plateau"
K in LB	22 ± 9	64 ± 7	0.6 ± 0.06	no
V in LB	16 ± 6	18.0 ± 1.9	1.16 ± 0.07	no
K in HB	20 ± 7	60 ± 6	0.50 ± 0.05	no
V in HB	7 ± 3	27 ± 3	1.43 ± 0.08	yes
V control	20	60	0.5	no

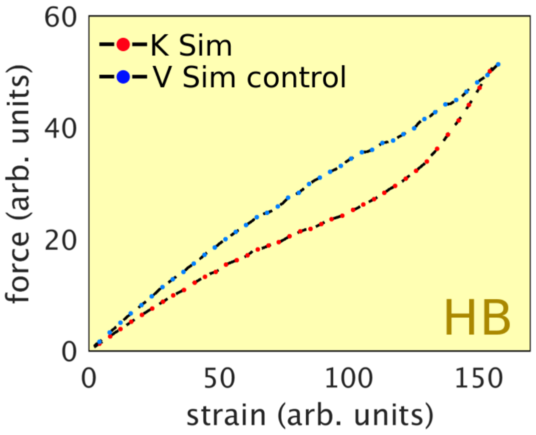

Figure 5.2: Comparison of the simulation of 32 parallel monomers (vimentin) with uncoupled subunits (blue-black, "control") and 16 parallel monomers (keratin) with uncoupled subunits (red-black). A high initial slope and a reduced slope for intermediate strains do not evolve merely as a consequence of an increased number of monomers.

$L_M/\Delta L$ of a monomer when all α helices open to the unfolded state, where the monomer length L_M and ΔL were estimated from structural data [6] and n_a is the average number of ULFs in the experiment represented by one ULF in the simulation. For the case of keratin IFs in LB this lead us to:

$$\varepsilon = \frac{x}{N_F L_M n_a / \Delta L} \approx 0.0059x\,.$$

For the scaling factor of the force, we related the change of the force ΔF to the length change as in Eq. 5.3, thus for keratin IFs in LB:

$$\Delta\phi = \kappa_F \Delta L \approx 11.8\,\mathrm{pN}\,,$$

where $\kappa_F = 0.22\,\mathrm{pN/nm}$ [6]. Thus, 1 simulation force unit corresponded to about 11.8 pN in the experiment. With the same rescaling procedure, we calculated the free energy difference ΔG between the α and unfolded state in SI units as presented Section 6.1.

5.1.3 Subunits Coupled by Springs Within the Intermediate Filament

To describe the behavior of phosphorylated vimentin IFs as presented in Chapter 6.4, we extended the model described in Section 5.1.1. From crystallography [169] and hydrogen exchange [61] experiments, we know that there are specific sites for dimers and tetramers to bind to each other. Therefore, in addition to the theoretical models presented in the previous Section 5.1.1 [7, 156], we took the links between dimers and between tetramers as connecting springs into account as sketched in Fig. 5.3. The spring constant κ_{bt} represented bonds between tetramers (marked in green in Fig. 5.3) and the spring constant κ_{bd} represented bonds between dimers, i.e. within tetramers (marked in blue in Fig. 5.3).

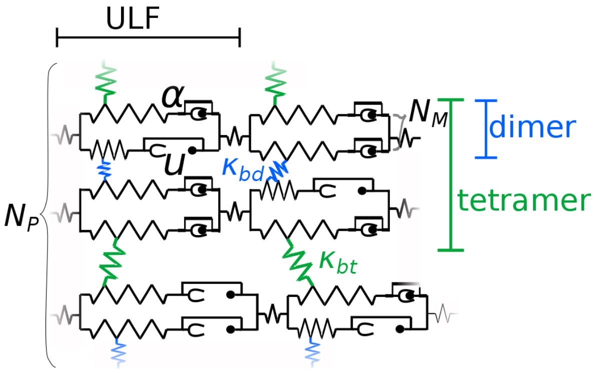

Figure 5.3: Sketch of the theoretical model for simulated force-strain curves. Each monomer was represented by a spring with a spring constant κ_α and by an element, which opened into an unfolded state u once force was applied. Two monomers were connected in parallel to form a dimer, thus the number of monomers in the dimer was $N_M = 2$. The dimers were connected by additional springs (blue) with a spring constant κ_{bd} to form tetramers. The connection between tetramers was established by another spring (green) with a spring constant κ_{bt}. Eight parallel tetramers ($N_P = 8$) formed a ULF. The ULFs were connected in series via springs to a filament. Adapted from Ref. [82] (Creative Commons Attribution-NonCommercial 3.0 Unported).

To calculate the total force acting on the filament, we first determined the spring constant of the filament. The spring constant of the ith ULF in the filament depended on the number of intact α helices A_j in this ULF with spring constant κ_α. Upon loading, the α helices opened into an unfolded state u, in which the unfolded α helix had the spring constant κ_u. We assumed that a ULF consisted of $N_P = 32$ parallel monomers [10] and $N_P/4 = 8$ parallel tetramers. The number of tetramers with intact (i.e. unfolded) α helices was $\lfloor A_j/4 \rfloor$, thus the number of possible interactions between these tetramers with intact α helices is $\lfloor A_j/4 \rfloor - 1$. Here, we assumed that the interaction between the tetramers consisting of (formerly) intact α helices was lost when one α helix unfolded. Intact α helices in a tetramer which contained unfolded α helices were more likely to unfold than intact α helices in a tetramer containing only intact α helices. Thus, we assumed that the next unfolding α helix under force was more likely to be located in a tetramer containing already unfolded α helices. For example, if 18 α helices in a ULF were intact, $\lfloor 18/4 \rfloor - 1 = 4 - 1 = 3$ connections between four intact tetramers were left. If another α helix unfolded, we assumed that the unfolding occurs in the tetramer with only two intact α helices.

We described a bond between tetramers with the spring constant κ_{bt}. Similarly, we modeled the dimer-dimer connection within a tetramer with the spring constant κ_{bd}. The number of intact dimer-dimer connections was the same as $\lfloor A_j/4 \rfloor$, because we assumed that an unfolded α helix broke the bonds between two dimers. Thus, the bonds between dimers and tetramers contributed $(\lfloor A_j/4 \rfloor - 1)\kappa_{bt} + \lfloor A_j/4 \rfloor \kappa_{bd}$ to the stiffness of the A_j α helices. Longitudinally, i.e. along the filament, we assumed "linkers" that connected the individual ULFs as well as the single α helices within one monomer. κ_L represented the stiffness of these linkers, and the linkers and ULFs were connected in series. In case all α helices were unfolded, all monomers were in the unfolded state, which had a spring constant κ_u, i.e. the N_P monomers had a total stiffness of $N_P \kappa_u$. Note that as long as there was at least one intact α helix present in a ULF, κ_u did not contribute to the overall stiffness, as these unfolded monomers were longer and thus bore no force.

For the fully coupled jth ULF including the connection to the next ULF, we obtained the spring constant κ_j:

$$\kappa_j = \begin{cases} \left(\frac{1}{\kappa_L} + \frac{1}{N_P \kappa_u} \right)^{-1} & \text{for } A_j = 0 \\ \left(\frac{1}{\kappa_L} + \frac{1}{A_j \kappa_\alpha + \lfloor \frac{A_j}{4} \rfloor \kappa_{bd} + \left(\lfloor \frac{A_j}{4} \rfloor - 1 \right) \kappa_{bt}} \right)^{-1} & \text{for } A_j > 0\,. \end{cases} \tag{5.4}$$

Here, $\lfloor A_j/4 \rfloor$ was the number of links between dimers in the ULF and $\lfloor A_j/4 \rfloor - 1$ the number of links between tetramers. In case the lateral bonds between tetramers were broken, only the bonds between the dimers within a tetramer remained. Thus, N_C subunits with N_M monomers formed a ULF, e.g. in the case of 32 monomers per ULF, if the subunits were tetramers, which were not coupled, we obtained $N_M = 4$ and $N_C = 8$. In contrast to the fully coupled ULF described with Eq. 5.4, we assumed that subunits with only unfolded N_M monomers contributed to the overall ULF stiffness as well, since there were no strong bonds inhibiting the subunit to slide past its original neighboring subunits. The stiffness of the jth ULF with $A_{j,m}$ as the number of intact α helices of the mth subunit in the jth ULF, the number I_j of subunits with only unfolded α helices and the number of dimers coupled via κ_{bd} within a subunit $N_d = \lfloor \sum_{m=1}^{N_C} A_{j,m}/N_M \rfloor$ was:

$$\kappa_j = \begin{cases} \left(\frac{1}{\kappa_L} + \frac{1}{N_P \kappa_u}\right)^{-1} & \text{for } \sum_{m=1}^{N_C} A_{j,m} = 0 \\ \left(\frac{1}{\kappa_L} + \frac{1}{N_M \kappa_u I_j + \sum_{m=1}^{N_C} A_{j,m}\kappa_\alpha + N_d \kappa_{bd}}\right)^{-1} & \text{for } \sum_{m=1}^{N_C} A_{j,m} > 0\,. \end{cases}$$

In the case of dimer sliding, neither dimers nor tetramers coupled and $N_d = 0$:

$$\kappa_j = \begin{cases} \left(\frac{1}{\kappa_L} + \frac{1}{N_P \kappa_u}\right)^{-1} & \text{for } \sum_{m=1}^{N_C} A_{j,m} = 0 \\ \left(\frac{1}{\kappa_L} + \frac{1}{N_M \kappa_u I_j + \sum_{m=1}^{N_C} A_{j,m}\kappa_\alpha}\right)^{-1} & \text{for } \sum_{m=1}^{N_C} A_{j,m} > 0. \end{cases}$$

Since all ULFs were connected in series to form a filament, the stiffness of the filament κ_F became $\kappa_F = 1/(\sum_{j=1}^{N_E} 1/\kappa_j)$.

To obtain the force-strain behavior as in Fig. 6.10b in Section 6.4, we set the model parameters to the following values: $\kappa_\alpha = 6.5$, $\kappa_{bd} = 7$, $\kappa_{bt} = 7$, $\kappa_L = 60$, $\kappa_u = 20$, $N_E = 100$ and $N_P = 32$. In case of strong coupling in Fig. 6.10c in Section 6.4, we assumed that there was only one large subunit per ULF consisting of 32 monomers. For the less coupled case, we assumed tetramers as subunits with $N_M = 4$ and $N_C = 8$ (light blue in Fig. 6.10b in Section 6.4) and for the least coupled case, we assumed dimers as subunits with $N_M = 2$ and $N_C = 16$ (blue in Fig. 6.10b in Section 6.4). Further parameters were necessary to run the simulation, but they did not influence the spring constant of a ULF: The free energy difference between the unfolded and folded state $\Delta G = 2\ k_B T$, the normalized length change upon unfolding $\Delta L = 1$ and a factor to ensured in detailed balance $\theta = 0.9$.

5.2 Interactions Between Filaments

5.2.1 Estimate of the Bundling Probability of Microtubules and Vimentin Intermediate Filaments

Our optical trapping experiments show a direct interaction between microtubules and vimentin IFs. However, we do not see co-alignment or bundling of the two filament types. To check whether such bundling should be expected, we estimated the probability of bundle formation between IFs and microtubules from the interaction probability of a vimentin ULF with a tubulin dimer ($p_{\text{IF-MT}}$) determined in Section 8.1. Co-alignment requires interactions at more than one site within one persistence length of a vimentin IF to occur, since thermal fluctuations set the relevant length scale for tight contact between the filaments.

The probability p_{ULF} of a vimentin ULF interacting with a tubulin dimer in an adjacent microtubule is:

$$p_{\text{ULF}} = p_{\text{IF-MT}} \frac{l_{u,\text{IF}}}{l_{u,\text{MT}}} \frac{n_{\text{pf}}}{4} \simeq 0.011,$$

where $l_{u,\text{IF}} = 43$ nm is the length occupied by one vimentin ULF within an IF, $l_{u,\text{MT}} = 8$ nm is the periodicity of tubulin dimers in the microtubule, $n_{\text{pf}} = 13$ is the number of protofilaments in a microtubule and $n_{\text{pf}}/4$ is the number of protofilaments per side facing the vimentin IF.

To obtain an upper limit for the probability of bundling, we assumed that the two filaments that interact at one site were already aligned in parallel and estimated the probability of an additional interaction at a second site within one vimentin persistence length of the first site. This probability ν was obtained as

$$\nu \approx p_{\text{ULF}} \frac{L_P}{l_{u,\text{IF}}} \simeq 0.37\,,$$

with a persistence length of vimentin IFs of $L_P \simeq 1.5$ µm. If more than two interactions are required for bundling, the estimate was further decreased by $\nu^{(n_{i,L_P}-1)}$, for required interactions at n_{i,L_P} sites. For $n_{i,L_P} = 2$, this lead to a probability of 14%. Thus, given the low probability of interaction, most IF-microtubule interactions would be mediated by a single site, even if the two filaments are pre-aligned. As filament pairs interacting at a single site can rotate relative to each other, the actual probabilities are even smaller. Thus, we would not expect a clear coalignment or bundling.

5.2.2 Model

We modeled IF-microtubule interactions as single molecular bonds to understand the force-dependent behavior in different buffer conditions. The bond can either be in a closed or in an open state with force-dependent stochastic transitions between these two states, as sketched in Fig. 8.4b in Section 8.1. In the experiment, we moved the IF with a constant speed v perpendicularly to the microtubule, as shown in Fig. 8.2b in Section 8.1 and Fig. 4.8a in Chapter 4. Once the bond closed, the IF with an average persistence length of $L_P = 1.5$ µm [39, 170] was stretched to its full contour length L_C. Thus, the entropic force F_e relates to the end-to-end distance $x = vt$ as [171, 172]

$$\frac{x}{d_{\text{IF}}} = \coth\left(\frac{2L_P F_e}{k_B T}\right) - \frac{k_B T}{2L_P F_e} \tag{5.5}$$

with the Boltzmann constant k_B and the temperature T. d_{IF} is the length of the filament between the IF-microtubule junction and bead 3 as sketched in Fig. Fig. 4.8c in Chapter 4.

In the simulation, we assumed a linear force increase from time t^* on [173, 174]. The linear force increase was set by the experimental force rate w, which we determined from a linear fit to the second half of the experimental force data of each interaction. t^* was determined as the time when the force increase $\frac{dF_e}{dt}$ due to a decreasing entropy is the same as the experimental force rate w, i.e. $w = \frac{dF_e}{dt^*}$:

$$F(t) = \begin{cases} F_e(x = vt) & \text{for } \ t < t^* \\ wt & \text{for } t > t^* \end{cases}\,, \tag{5.6}$$

Once the bond broke at a force F_B after a time t_u, we assumed an exponential force relaxation on a characteristic time scale τ:

$$F(t) = F_B \exp(-(t - t_u)/\tau) \text{ for } t > t_u. \tag{5.7}$$

We indeed observed a fast, exponential-like force decay in our experiments. However, the time resolution is not sufficient to fit τ precisely. We set $\tau = 0.1$ s as this results in force versus time curves similar to our experiments.

All variables with the index b refer the binding process and the index u represents the unbinding process. We describe the force-dependent binding and unbinding rates as follows: We assume that the binding and unbinding rates $r_b(t)$ and $r_u(t)$, respectively, depend on a reaction prefactor $r_{b,0/u,0}$, the activation energy for binding or unbinding $E_{Ab/Au}$, the thermal energy $k_B T$ and the potential width of the two states $x_{b/u}$ [153]:

$$r_b(t) = r_{b,0} \exp\left(\frac{-E_{Ab}}{k_B T}\right) \cdot \exp\left(\frac{-F(t)x_b}{k_B T}\right), r_u(t) = r_{u,0} \exp\left(\frac{-E_{Au}}{k_B T}\right) \cdot \exp\left(\frac{F(t)x_u}{k_B T}\right). \tag{5.8}$$

The force-independent parameters $r_{b,0/u,0}$ and $E_{Ab/Au}$ result in an effective zero-force rate

$$r_{b,\text{eff}/u,\text{eff}} = r_{b,0/u,0} \exp\left(\frac{-E_{Ab/Au}}{k_B T}\right),$$

in which $r_{b,\text{eff}}$ can be determined from the experimental data in Fig. 8.3c, e, g, i and k in Section 8.1. We calculated the total contact time t_{cont} of the IF and microtubule without an interaction and the number of initiated interactions n_i between IFs and microtubules from the experimental data and get

$$r_{b,\text{eff}} = \frac{n_i}{t_{\text{cont}}}.$$

If we assume the same prefactor for the binding or unbinding process, i.e. $r_{b,0} = r_{u,0}$ [153], the ratio of two effective binding or unbinding rates for different experimental buffer conditions 1 and 2, or two different states (bound, unbound) sheds light on the differences in the activation energies for these buffer conditions or states. For the binding rates for two different buffer conditions, the activation energy difference is:

$$\frac{r_{b,\text{eff},1}}{r_{b,\text{eff},2}} = \frac{\exp\left(\frac{-E_{Ab,1}}{k_B T}\right)}{\exp\left(\frac{-E_{Ab,2}}{k_B T}\right)} \Rightarrow k_B T \ln\left(\frac{r_{b,\text{eff},1}}{r_{b,\text{eff},2}}\right) = E_{Ab,2} - E_{Ab,1}, \tag{5.9}$$

and likewise for the rates for the unbound state.

In the same way, we can calculate the absolute energy difference $\Delta G_{\text{IF-MT}}$ between the bound and unbound state for the same buffer condition [153]:

$$\Delta G_{\text{IF-MT}} = -k_B T \ln\left(\frac{r_{u,\text{eff}}}{r_{b,\text{eff}}}\right). \tag{5.10}$$

Here, the sum of the potential widths $x_b + x_u$ nm provides the total distance between the bound and unbound state, which we assume to be the same for all experimental conditions. The rate equations in Eq. 5.8 ensure that detailed balance is satisfied [153].

Thus, from these considerations and from the experiment, we know L_C, w, τ and $r_{b,\text{eff}}$, but neither $r_{u,\text{eff}}$ nor x_b or x_u. We simulated the binding and unbinding reactions for the known parameters and varied x_u from 0 nm up to 0.9 nm in steps of 0.01 nm and $r_{\text{eff},u}$ from 0.02 up to 0.6 s^{-1} in steps of 0.01 s^{-1}. We determined x_b by calculating $x_b = 0.4\,\text{nm} - x_u$, since the maximum value of x_u is below 0.4 nm.

The binding and unbinding process cannot be described in a closed analytical expression due to the time dependence in the exponential expression of the reaction rates [175]. Therefore, we considered two different approaches to determine the breaking force histograms which we compared to the experimental data: (i) We solved the rate equations directly numerically, which is the fastest way to calculate the force histograms. (ii) We simulated the force-time trajectories of single bonds, which allows us to directly compare single simulated trajectories to our experimental data. Both approaches result in the same force histograms as shown in Fig. 8.3c, e, g, i and k in Section 8.1, green shaded areas.

5.2.3 Numerical Solution

To solve the rate equations in Eq. 5.8 numerically, we defined $b(t)$ as the probability that the IF-microtubule bond is closed. Thus, the temporal behavior of b can be described as:

$$\frac{\mathrm{d}b}{\mathrm{d}t} = -r_u(t) \cdot b(t) + r_b(t)(1 - b(t))\,, \tag{5.11}$$

$$= -b(t) r_{u,\text{eff}} \exp\left(\frac{F(t)x_u}{k_B T}\right) + (1 - b(t)) r_{b,\text{eff}} \exp\left(\frac{-F(t)x_b}{k_B T}\right)\,. \tag{5.12}$$

We solved this expression numerically for $b(t)$ with the Matlab function `ode45`. To obtain a histogram of breaking forces, we differentiated $b(t)$ with respect to t and, thus, determined the probability $p_u(t)$ that the IF and microtubule unbind at a certain time t:

$$p_u(t) = -\frac{\mathrm{d}b}{\mathrm{d}t}\,.$$

To calculate the probability-force diagram, to compare to the experiments, we determined p_u as a function of F, i.e. $p_u(t(F))$ by inverting $F(t)$ as described in Eq. 5.6.

5.2.4 Simulation

To obtain single force-time trajectories of an IF-microtubule bond, we simulated the binding and unbinding process in several steps: (i) The time until an individual binding event was determined by choosing a random time t_b from an exponential distribution with the density function $f(t)$ and a mean value of $\lambda = (r_b(t, F = 0))^{-1}$ [155, 176]:

$$f(t) = \lambda \exp(-\lambda t)\,.$$

The bond is now closed after time t_b. The force starts to increase as described in Eq. 5.6. (ii) As the unbinding rate depends on the force, which increases with time, the mean $(r_u(F(t)))^{-1}$ of the exponentially distributed unbinding time t_u changes with increasing force. Thus, it is not straightforward to determine the time until unbinding with a single step as in (i). Instead, we split t_u into small time intervals dt. We set d$t = 0.05$ s as a compromise between accuracy and computation time, which is the same as the experimental time resolution. The time was increased in steps of dt and after each step, the unbinding rate was evaluated. The probability p_u that the bond breaks in the considered time interval is $p_u = r_u(F(t))\mathrm{d}t$, where we approximated the exponentially increasing unbinding rate as a constant for small dt. If a random number drawn from a uniform distribution between 0 and 1 was greater than p_u, the bond stayed closed, otherwise it opened. If the bond remained closed, the time was increased by dt, the force was updated and step (ii) was repeated until the bond broke. (iii) Once the bond broke, the force decreased as described by Eq. 5.7. Since the bond could close with a force-dependent rate while the force decayed, the time was increased stepwise again and the probability to rebind was evaluated as in step (ii) with $p_b = r_b(t, F(t))\mathrm{d}t$. If the force decreased to a value below 0.001 pN, the force was set to 0 pN and the algorithm was repeated starting at step (i).

As the IFs and microtubules had slightly different lengths for different measurements, the force rate differed between the experiments. To account for these different rates, we ran the simulation until 1000 breaking events are recorded for each experimental force rate w. The final distribution of breaking forces results from the normalized sum of distributions of breaking forces for all force rates. This final distribution was compared to the experimental data with the Kolmogorov-Smirnov test [177]. If the experimental and the simulated distributions did not differ more than allowed for a 5% significance level [177], we accepted the parameters $r_{u,\mathrm{eff}}$ and x_u as shown in Fig. 8.4a in Section 8.1. To calculate the energy diagram in Fig. 8.4b in Section 8.1, we determined the centroids of the accepted parameter regions in Fig. 8.4a in Section 8.1. We determined the standard deviations from the distributions in Fig. 8.4a in Section 8.1 assuming that $r_{u,\mathrm{eff}}$ and x_u are independent. The simulated breaking force histograms do not depend on the exact value of x_b in the range of 0.2 to 1.5 nm since $r_{b,\mathrm{eff}}$ dominates over the force-dependent term in Eq. 5.8. We do not observe a sufficient number of rebinding events under force to determine x_b from the experiment. For clarity, $x_b + x_u$ is set to 0.4 nm in Fig. 8.4 in Section 8.1.

5.3 Dynamic Microtubules Interacting With Intermediate Filaments

5.3.1 Dynamic Microtubules Without Additional Interactions

We based our model of a dynamic microtubule on Refs. [96] and [102] and ran Monte-Carlo simulations with a self-written Python code (Beaverton, OR, USA) to obtain simulated kymographs. We assumed a microtubule lattice with $n_{\mathrm{pf}} = 13$ protofilaments that has a helical pitch of 3 monomers per turn as sketched in Fig. 8.5a in Section 8.1. Thus, there is a seam formed by protofilaments 1 and 13, which are displaced by 1.5 dimers. All dimers incorporated in the lattice interact with two lateral and two longitudinal dimer positions. At the seam, the dimers interact with two half dimers across the seam. The microtubule is represented by a matrix in the simulation and the state of the dimer is entered at a corresponding position in the matrix. A dimer position can be either unoccupied or occupied by a GTP dimer (purple in Fig. 8.5a, b in Section 8.1), a GDP dimer (blue in Fig. 8.5a, b in

Section 8.1) or a GMPCPP-dimer (green in Fig. 8.5a, b in Section 8.1). We set the first three dimer layers to GMPCPP dimers, which represent the seed in the experiment. The GMPCPP dimers cannot depolymerize. To avoid artifacts from the starting conditions, we started the simulations with a microtubule consisting of 30 layers of GDP dimers, which have four layers of GTP dimers on top representing the tip [96].

To simulate microtubule dynamics, we determined four different reaction rates (i–iv) as sketched in Fig. 8.5a (top) in Section 8.1: (i) The polymerization rate r_g when a GTP dimer binds to the tip of the microtubule, (ii) the depolymerization rate r_{dt} of a GTP dimer when a GTP dimer falls off the lattice, (iii) the hydrolysis rate r_{hy} of a GTP dimer to a GDP dimer and (iv) the depolymerization rate r_{dd} of GDP dimers. Since we used a buffer which is also compatible with vimentin IF assembly, these simulation parameters differ from the parameters used in literature [91, 96, 99]. We summarize all important simulation parameters in Table 9.1. We calculated the different reaction rates (i–iv) as follows:

(i) The polymerization rate for GTP dimers is concentration dependent [96]. To match the growth rate to the experimentally observed one, we set it to $r_{g,20} = 1.3$ dimers s^{-1} per protofilament for 20 µM free tubulin concentration and to $r_{g,25} = 2.2$ dimers s^{-1} per protofilament for 25 µM free tubulin concentration.

(ii)/(iv) The depolymerization rate of GTP and GDP dimers depends on the number of lateral neighbors n. For each lateral dimer, the depolymerization rate was lowered by a factor of $\exp(-\Delta G_{\mathrm{latt/latd}})$ due to the change in total bond energy $\Delta G_{\mathrm{latt}} = 3.5\ k_B T$ for a GTP dimer and $\Delta G_{\mathrm{latd}} = 1.5\ k_B T$ for a GDP dimer [96]:

$$r_{dt/dd} = r_{dt/dd,0} \exp\left(\frac{-n\Delta G_{\mathrm{latt/latd}}}{k_B T}\right) . \tag{5.13}$$

For no lateral dimers, we assumed an unbinding rate of $r_{dt,0} = 9.93 \cdot 10^{-4}$ s^{-1} for GTP and $r_{dd,0} = 643$ s^{-1} for GDP. We assumed that only the dimers at the tip of a protofilament can depolymerize [102].

(iii) We set the hydrolysis rate to 7 s^{-1} to obtain a tip size which results in the same change in catastrophe frequency as observed in our experiments. This rate is on the same order of magnitude as assumed in Ref. [96]. A dimer can only hydrolyze, if it has a neighbor in the same protofilament towards the direction of growth [96, 102]. Since we did not observed rescue in our experiments for a free tubulin concentration of 20 µM and the precise reason for rescue is unknown [91], we assumed that the rapidly disassembling microtubule is "locked" in the disassembly state and no rescue occurs because GTP dimers polymerize faster then GDP dimers depolymerize [91]. Yet, we observe rescue at a concentration of 25 µM, which we implemented in our simulation as occurring with a rate of $f_{\mathrm{resc}} = 0.03$ s^{-1} [91].

To simulate a kymograph of a dynamic microtubule, we calculated all possible reaction rates. For each possible reaction with rate R, a random number z between 0 and 1 was drawn, with which we determined the time until the next realization of a certain reaction [96, 176]:

$$t = \frac{-\ln z}{R} . \tag{5.14}$$

The reaction with the smallest time was set to be the next occurring reaction. The microtubule matrix containing the dimer states was updated correspondingly as shown for a snapshot of a typical microtubule configuration in Fig. 8.5b in Section 8.1. We ran 100 simulations for a total simulated time of 900 s each to obtain comparable amounts of experimental and simulated data. We recorded the length of the shortest protofilament during the simulation, which results in simulated kymographs. We plotted typical simulated kymographs in Fig. 8.5c (left) in Section 8.1 for 20 μM free tubulin without surrounding vimentin and in Fig. 8.5c (right) in Section 8.1 for 25 μM free tubulin with surrounding vimentin.

5.3.2 Dynamic Microtubules Interacting with Intermediate Filaments

The above model of a dynamic microtubule was modified in the following way to account for the direct binding of IFs as seen in our optical tweezers experiments: We assumed that IFs bind stochastically to the microtubule lattice. We note that from our experiments, we cannot make precise conclusions about the molecular mechanism causing the interaction, therefore the molecular mechanism is not specified in our model. We hypothesize that IFs bind to individual tubulin dimers, but based on our experiments we cannot exclude the possibility that the interaction is based on larger binding sites that consist of multiple tubulin dimers. However, in the optical tweezers experiments, we always observed that the bond between an IF and a microtubules broke in a single step, so that if binding involves multiple tubulin dimers, it must be highly cooperative and can still be treated effectively as a single bond. The rates of binding and unbinding of IFs to the microtubule were calculated from those determined in the optical tweezers experiments, accounting for the different geometry in the TIRF approach. This calculation is described at the end of this section. We further assumed that the presence of a bound IF modulates the depolymerization rates $r_{dt/dd}$, but does not affect the polymerization and hydrolysis rates.

Depolymerization rates: Our optical tweezers experiments showed that IFs directly interact with microtubules. By comparing the binding and unbinding rates (the latter in the force-free limit), we determined the energy difference $\Delta G_{\text{IF-MT}}$ between the bound and unbound state of the IF-microtubule interactions. Thus, if an IF binds to a microtubule dimer, the total binding energy of the dimer in the microtubule lattice is increased by $\Delta G_{\text{IF-MT}}$, which lowers the total energy sum in the exponential term of Eq. 5.13,

$$r_{dt/dd} = r_{dt,0/dd,0} \exp\left(\frac{-n\Delta G_{\text{latt/latd}} - \Delta G_{\text{IF-MT}}}{k_B T}\right) \tag{5.15}$$

and thus reduces the depolymerization rate, specifically for the case of GTP-dimers in the microtubule cap, where the depolymerization rate is small anyway. This assumption can be interpreted as follows: when a tubulin dimer to which an IF is bound unbinds from the microtubule lattice, the IF also unbinds. Based on our experiments, we cannot distinguish whether the IF is bound to a single tubulin dimer or to multiple dimers, but we know that if the latter case applies, unbinding from those dimers must be cooperative since we do not observe stepwise unbinding in optical tweezers experiments. Therefore, the same model applies to both scenarios, i.e., if IF-microtubule binding involves more than one dimer, unbinding of one of those dimers also unbinds the IF from the other dimers. The only difference between the scenarios is that the binding energy per dimer is $\Delta G_{\text{IF-MT}}/M$ if M

dimers contribute to the bond. Due to the cooperativity, however, the total energy $\Delta G_{\text{IF-MT}}$ enters the depolymerization rate.

Binding rate of vimentin IFs to microtubules: From the optical tweezers experiments, we know that the binding rates of IFs and microtubules depend on the geometry of the experiment, i.e., the IF is moved perpendicularly vertically or horizontally compared to the microtubule or at an angle. To obtain the binding rate in the geometry of the TIRF experiments, we used the same approach as in Section 4.4.4 describing the binding rate by a geometry-dependent encounter rate and a geometry-independent binding probability. In the TIRF experiments, the encounter rate is different compared to the optical tweezers experiments since the vimentin IFs diffuse and are not moved in a certain direction relative to the microtubule. Therefore, we calculated the diffusion limited encounter rate [178] r_{diff} of vimentin and microtubule subunits:

First, we determined the average diffusion coefficient of the vimentin IFs: The estimated viscosity [179] $\eta \simeq 3$ mPas of the sample in TIRF experiments deviates from the viscosity of water, since the sample in TIRF experiments contained 0.09% methylcellulose. The diameter a_{IF} of a vimentin IF is 11 nm [31]. The diffusion occurs in three dimensions with a diffusion coefficient of $D = k_B T \ln(\zeta / a_{\text{IF}}) / (3\pi\zeta\eta)$ [180].

Second, we estimated the concentration c_{IF} of vimentin IFs in the network or the number of vimentin IFs per network volume as $c_{\text{IF}} = 3\zeta / a_{\text{IF}} / \zeta^3$, where $\zeta \simeq 0.63$ µ m or $\zeta \simeq 0.5$ µm is the mesh size of the vimentin IF network for 2.3 µM or 3.6 µM vimentin, respectively [181].

Third, we calculated the diffusion limited encounter rate [178], taking into account the diameter of a vimentin IF $a_{\text{IF}} \simeq 11$ nm [31]:

$$\begin{aligned} r_{\text{diff}} = 4\pi D a_{\text{IF}} c_{\text{IF}} &\simeq 90\,\text{s}^{-1} \text{ for 2.3 µM vimentin}, \\ &\simeq 150\,\text{s}^{-1} \text{ for 3.6 µM vimentin}. \end{aligned}$$

To determine the interaction rate r_i of a microtubule subunit and a vimentin IF subunit, we multiplied the encounter rate r_{diff} with the interaction probability of a microtubule subunit and a vimentin IF $p_{\text{IF-MT}}$ that was already determined from the optical tweezers experiments :

$$\begin{aligned} r_i = r_{\text{diff}}\, p_{\text{IF-MT}} &\simeq 0.06\,\text{s}^{-1} \text{ for 2.3 µM vimentin}, \\ &\simeq 0.09\,\text{s}^{-1} \text{ for 3.6 µM vimentin}. \end{aligned}$$

We calculated the probability p_i that an IF is bound to a microtubule by assuming an equilibrium between binding and unbinding IFs:

$$r_i(1 - p_i) = r_{u,\text{eff}} p_i \,.$$

The unbinding rate was determined from optical tweezers experiments as well. We find $p_i \simeq 33\%$ in case of 2.3 µM vimentin and $p_i \simeq 44$ % in case of 3.6 µM vimentin. Consequently, in our simulation, we drew a random number r between 0 and 1 and if $r < p_i$, the depolymerization rate changes as described in Eq. 5.15. If $r > p_i$, the depolymerization rate remains unchanged.

The additional binding energy of IFs to microtubules also decreases the depolymerization rate of potential rescue sites, thus, rescue occurs more often. Thus, the frequency for rescue sites with surrounding vimentin IFs increases from $f_{\mathrm{resc}} = 0.03\ \mathrm{s}^{-1}$ to $f_{\mathrm{resc,\,IF}} = 0.17\ \mathrm{s}^{-1}$ in case of 2.3 µM vimentin. The rescue frequency of microtubules with surrounding filaments is lower than we would expect if we calculate $f_{\mathrm{resc}} \exp(\Delta G_{\mathrm{IF\text{-}MT}}/k_B T)\ \mathrm{s}^{-1} = 0.3\ \mathrm{s}^{-1}$, however, on the same order of magnitude. Our model is probably too simple to describe this discrepancy arising from the poorly understood rescue process [91].

5.3.3 Estimate of the Binding Energy of Tubulin Dimers Within the Microtubule Lattice

We can estimate the tubulin dimer binding energy by combining the results from optical tweezers and TIRF experiments. First, we calculated the catastrophe frequency $f_{\mathrm{cat,\,IF\text{-}MT}}$ of a microtubule when a vimentin IF continuously interacts with all dimers. We know the experimentally observed catastrophe frequency without vimentin in solution $f_{\mathrm{cat,MT}}$ and with vimentin in solution $f_{\mathrm{cat,exp}}$ from the TIRF experiments. The observed catastrophe frequency in presence of vimentin results from a combination of microtubules which are in contact with a vimentin IF and microtubules which are not in contact with an IF. The probability that a microtubule monomer and a vimentin IF are in contact is p_i. Thus, the observed catastrophe rate $f_{\mathrm{cat,exp}}$ in presence of vimentin IFs and the catastrophe rate $f_{\mathrm{cat,\,IF\text{-}MT}}$ for microtubules continuously interacting with a vimentin IF are:

$$\begin{aligned}
f_{\mathrm{cat,exp}} &= (1-p_i) f_{\mathrm{cat,\,MT}} + p_i f_{\mathrm{cat,\,IF\text{-}MT}} \\
f_{\mathrm{cat,\,IF\text{-}MT}} &= \frac{f_{\mathrm{cat,exp}} - (1-p_i) f_{\mathrm{cat,\,MT}}}{p_i} \\
&\simeq 0.0056\,\mathrm{min}^{-1} \text{ for 20 µM and } 0.0061\ \mathrm{min}^{-1} \text{ for 25 µM tubulin, 2.3 µM vimentin,} \\
&\simeq 0.022\,\mathrm{min}^{-1} \text{ for 20µM and } 0.0073\ \mathrm{min}^{-1} \text{ for 25 µM tubulin, 3.6 µM vimentin.}
\end{aligned}$$

During depolymerization of the microtubule, the additional energy of a GTP dimer in the microtubule lattice ΔG_{tb} is released. Therefore, we assumed that the only energy difference between the dimer, which is incorporated in an microtubule and which unbinds from an IF monomer in the optical tweezers experiments, and the last dimer, which depolymerizes just before an microtubule catastrophe in the TIRF experiments, is ΔG_{tb}. Thus, we can combine the catastrophe rates from TIRF experiments and the unbinding rates of the optical tweezers experiments to calculate ΔG_{tb}:

$$\begin{aligned}
\frac{r_{u,\mathrm{eff}}}{f_{\mathrm{cat,IF\text{-}MT}}} &= \exp\left(\frac{\Delta G_{tb}}{k_B T}\right), \qquad (5.16) \\
\Delta G_{tb} &= k_B T \ln\left(\frac{r_{u,\mathrm{eff}}}{f_{\mathrm{cat,IF\text{-}MT}}}\right) \\
&\simeq 7.1\,k_B T \text{ for 20 µM and } 7.2\,k_B T \text{ for 25 µM, 2.3 µM vimentin,} \\
&\simeq 5.7\,k_B T \text{ for 20 µM and } 6.8\,k_B T \text{ for 25 µM, 3.6 µM vimentin.}
\end{aligned}$$

CHAPTER 6

Interactions and Mechanics Within Single Intermediate Filaments Under Load

In this chapter, we show how interactions within IFs determine IF mechanics. We find three different ways by which cells might tune the interactions and thereby the mechanics of IFs on different spatial and temporal scales: (1) The expression of different IF proteins (keratin, vimentin) as a change which affects the entire cell and which happens on a longer time scale than the other two possibilities, (2) changes in the ionic strength of the surrounding buffer or changes in pH, which allow for local changes of filament properties, and (3) post-translational modifications, which can be fast and local adaptions. Theoretical modeling allows for the direct disentanglement of the contributions from the secondary structure of the IF monomers and the contributions from the interactions between these monomers. Our theoretical model explains the different mechanical behaviors of keratin and vimentin IFs (Section 6.1) and the influence of ionic strength and pH of the buffer (Section 6.3). An extension of this model describes the effect of post-translational modifications (Section 6.4).

6.1 Lateral Subunit Coupling Determines Intermediate Filament Mechanics

The following section was published as “Lateral Subunit Coupling Determines Intermediate Filament Mechanics” in *Physical Review Letters* **123** (188102) in 2019 (© 2019 American Physical Society) [156]. Parts of the Supplementary Material are included as Section 6.1.6.

Charlotta Lorenz[1], Johanna Forsting[1], Anna V. Schepers[1], Julia Kraxner[1], Susanne Bauch[1], Hannes Witt[2,3], Stefan Klumpp[4], and Sarah Köster[1]

[1]Institute for X-Ray Physics, University of Göttingen, Friedrich-Hund-Platz 1, 37077 Göttingen, Germany.
[2]Institute for Organic and Biomolecular Chemistry, University of Göttingen, Tammanstraße 2, 37077 Göttingen, Germany.
[3]Max Planck Institute for Dynamics and Self-Organization, Am Faßberg 7, 37077 Göttingen.
[4]Institute for Dynamics of Complex Systems, University of Göttingen, Friedrich-Hund-Platz 1, 37077 Göttingen, Germany.

Contributions: Sarah Köster conceived and supervised the project. Charlotta Lorenz performed all experiments and analyzed the data. Johanna Forsting provided the data sets of vimentin IFs stretched in vimentin assembly buffer at different loading rates. Julia Kraxner and Anna V. Schepers helped performing the experiments. Susanne Bauch purified the studied proteins. The numerical simulation is based on a modification of Hannes Witt's simulation. Hannes Witt also helped interpreting simulation results. Stefan Klumpp helped designing the simulation. All authors contributed to writing the manuscript.

6.1.1 Abstract

The cytoskeleton is a composite network of three types of protein filaments, among which intermediate filaments (IFs) are the most extensible ones. Two very important IFs are keratin and vimentin, which have similar molecular architectures but different mechanical behaviors. Here we compare the mechanical response of single keratin and vimentin filaments using optical tweezers. We show that the mechanics of vimentin strongly depends on the ionic strength of the buffer and that its force-strain curve suggests a high degree of cooperativity between subunits. Indeed, a computational model indicates that in contrast to keratin, vimentin is characterized by strong lateral subunit coupling of its charged monomers during unfolding of α helices. We conclude that cells can tune their mechanics by differential use of keratin versus vimentin.

6.1.2 Introduction

The cytoskeleton is composed of three types of biopolymers – actin filaments, microtubules, and intermediate filaments (IFs) – which, along with cross-linkers and motor proteins, form a dense network in the cell [21] and determine its mechanical properties. Microtubules and actin filaments are conserved across different cell types and organisms. By contrast, IFs are expressed in a cell-type specific manner [10–12]: For example, keratins are predominantly expressed in epithelial cells and vimentin in cells of mesenchymal origin. It has been shown that vimentin deprived cells are less mechanically stable and migrate more slowly [182], whereas cells lacking keratin are softer and more deformable [183, 184]. These differences are likely to play an important role during the epithelial-to-mesenchymal transition, for example, in embryogenesis, wound healing and cancer metastasis, when cells upregulate vimentin expression and downregulate keratin expression [12, 18–20]. We hypothesize that keratin and vimentin filaments have different mechanical properties already at the single filament level. It has been demonstrated previously that single vimentin filaments exhibit a pronounced extensibility of up to 4.5 times their original length [6, 77, 78] and a high flexibility [12, 35, 39], and can dissipate up to 80% of the input energy when stretched and relaxed [7]. Keratin has so far been primarily studied in the context of bundles, for example, in hagfish slime threads [74], wool fibers [185], and hard α-keratin fibers [64]. However, data from single filaments are needed to decouple the mechanics resulting from the bundle or network structure, i.e., the interfilament interactions, from the single filament mechanics.

IF mechanics are closely linked to their molecular architecture [6, 7, 83]. The monomer consists of a "rod" domain including three α helices, which are connected by linkers and

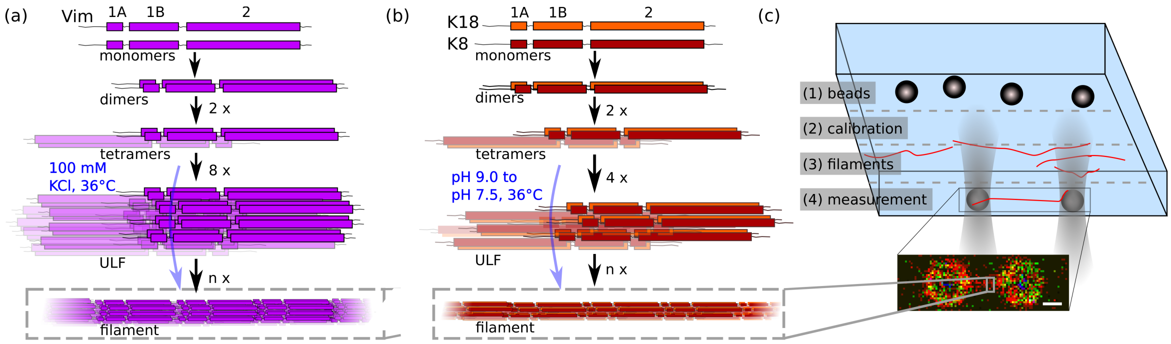

Figure 6.1: (a,b) Assembly pathway of vimentin (Vim) and keratin (K8, K18) IFs, respectively. The monomers consist of three α-helical regions (1A, 1B, 2) connected by two linkers and flanked by intrinsically unstructured regions, and form extended IFs in a strictly hierarchical manner. (c) Top: Schematic of the microfluidic device used for measurements with the OT. Bottom: Confocal image of a fluorescently labeled keratin IF captured between 4.42-µm-diameter beads; the scale bar is 2 µm.

flanked by intrinsically disordered head and tail regions [Figs. 6.1a and b] [31]. Despite differing amino acid sequences, all cytoskeletal IFs share this monomer structure, as well as the particular assembly pathway: Two monomers form a parallel dimer, two dimers an antiparallel, half-staggered tetramer, and tetramers eventually form unit-length filaments (ULFs) with a length of about 60 nm [31]. This lateral assembly is followed by longitudinal annealing of ULFs resulting in µm-long filaments. One important difference between keratin and vimentin filaments is the average number of tetramers per filament cross section of four and eight, respectively [10]. During stretching of these filaments, the α helices open into an unfolded state leading to a contour length change [7, 63, 73].

Here, we study the mechanical behavior of single keratin and vimentin filaments under load by stretching them with optical traps (OTs) [6, 7]. It is well known that keratin and vimentin are held together mainly by hydrophobic and electrostatic interactions. Therefore, we use two distinctly different buffer conditions with high or low ionic strength, respectively, to tune the electrostatic interactions. We find that ionic strength impacts IF mechanics, which we explain by stronger lateral coupling in vimentin subunits than in keratin subunits, corroborated by data from atomic force microscopy (AFM). The experimental data from optical tweezers are modeled and quantitatively fitted by a Monte Carlo (MC) simulation based on the IF structure [7]. From the fit, we obtain the free energy difference between the folded helix and the unfolded state, and the α-helical stiffness.

6.1.3 Materials and Methods

Proteins are recombinantly expressed [186], labeled and reconstituted to tetrameric form as described in the Section 4.1. Keratin is assembled at 0.1 mg/mL by dialysis into a low ionic strength buffer, a standard keratin buffer (LB: 10 mM TRIS, pH 7.5) [10, 54–58], and vimentin at a protein concentration of 0.2 mg/mL into a physiological, high ionic strength buffer (HB: 100 mM KCl, 2 mM phosphate buffer, pH 7.5) [54–56, 59, 161, 162], both at 36°C overnight. In both cases, about 4% of all monomers are labeled fluorescently with ATTO647N.

For optical tweezers measurements, the assembled keratin and vimentin filaments are diluted 1:70 and 1:100, respectively, with the corresponding assembly buffer. The optical tweezers setup (LUMICKS, Amsterdam, Netherlands) is equipped with a confocal fluorescence microscope and a microfluidic device as sketched in Fig. 6.1c. Polystyrene beads (Kisker Biotech, Steinfurt, Germany) are maleimide coated [163] to allow for covalent binding to the IFs via cysteines. The beads are diluted with the assembly buffer of the respective studied protein, which is also used as a buffer in the calibration channel. The buffer in channel (4) is either LB or HB, and each IF is studied in both buffers.

Before each measurement, two beads are captured with the optical tweezers in channel (1), and the trap stiffness is calibrated via their thermal noise spectrum in channel (2). IFs are attached to the beads in channel (3), and it is ensured by fluorescence microscopy that only one IF is bound to the beads. The traps with the IF are moved to channel (4) and incubated for 30 s, unless the measurement is intended to take place in the assembly buffer of the respective IF protein. One optical trap is moved with speeds between 0.3 μm/s and 2.5 μm/s to stretch the IF in channel (4). The force exerted on the IF by the optical trap as well as the bead positions are recorded.

IF heights are measured with a commercial AFM (Infinity, Oxford Instruments Asylum Research, Santa Barbara, CA, USA). IFs are incubated for 30 s in the buffer of interest, fixed with 0.125% glutaraldehyde and imaged on a piece of silicon wafer (Crystec, Berlin, Germany) in buffer. Cantilevers (MLCT, Bruker, Billerica, MA, USA) are calibrated via their thermal noise spectrum. From the optical tweezers data, the strain $\varepsilon = L/L_0 - 1$ is calculated [7] using the measured IF length L and the IF length L_0 at 5 pN. The individual and average force-strain curves of single keratin and vimentin filaments in the two buffer conditions are shown in Figs. 6.2a. The averages are calculated by averaging both force and strain data (see Section 4.4.2, including Figs. 4.3 and 4.4).

6.1.4 Results

In contrast to keratin, the force-strain behavior of vimentin filaments significantly depends on the ionic strength of the buffer as Fig. 6.2 shows. Figure 6.5 in Section 6.1.6 shows the same data, however, grouped according to filament type. In LB, the force-strain behavior of keratin and vimentin is similar and can be divided into three regimes [6, 7]: There is an elastic regime for low strains caused by the elastic behavior of α helices [6, 83, 187, 188]. A less steep regime for strains between 0.2 and 0.8 arises from the stepwise opening of α helices during elongation [73, 83]. The filaments stiffen again for high strains since most α helices are unfolded and the resulting structure is stretched [83]. The slopes for low strains (in the range of 0.015–0.1 or 0.015–0.15, depending on the linear regime) are, on average, slightly higher for vimentin compared to keratin filaments [Figs. 6.2c and 6.2d], which can be partially explained by the doubled number of monomers per cross section in vimentin filaments. In summary, for keratin and vimentin filaments, there is a small initial slope and no considerably decreased slope for intermediate strains in LB, similar to the previously observed stress-strain behavior of IF bundles [74] [Fig. 6.2a]. A detailed analysis of the slope behavior for intermediate strains is included in Fig. 4.5 in Section 4.4.2. By contrast, the two filament types behave differently in HB [Fig. 6.2b]. For keratin filaments, there is no clear separation between the regimes. Vimentin filaments, however, show a high initial slope and a

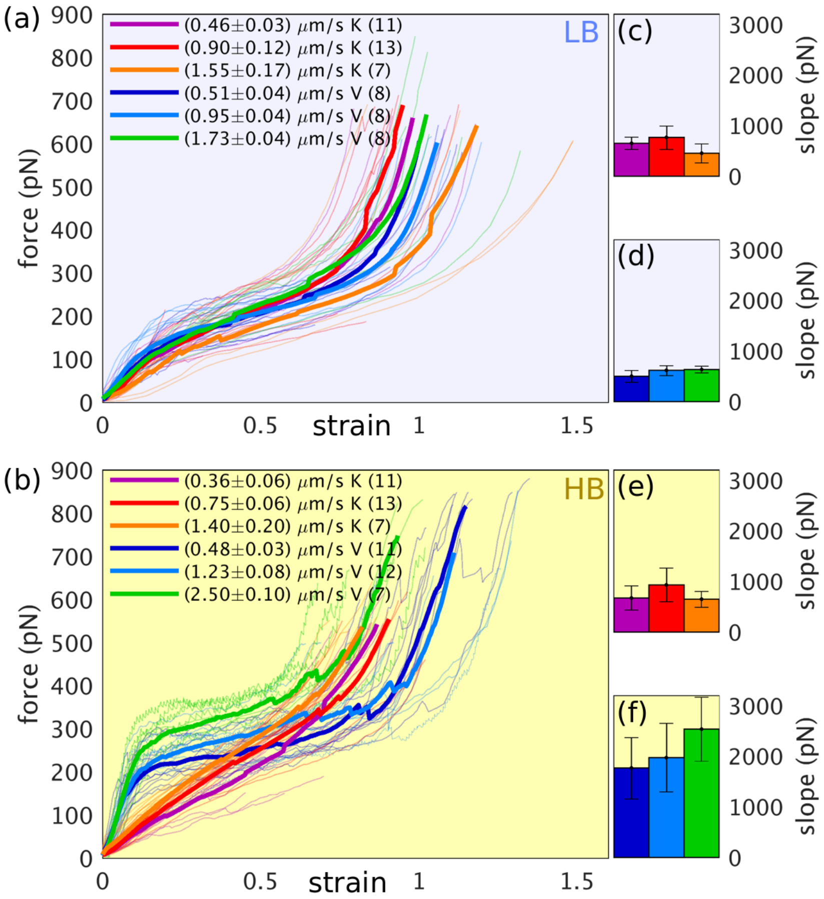

Figure 6.2: (a,b) Force-strain curves for keratin (K, warm colors) and vimentin (V, cold colors) in (a) LB (blue background) and (b) HB (yellow background) measured with the OT. The curves from single IFs (thin lines) for different loading rates (see color code) are averaged (thick lines). The number of measurements for each condition is included in parentheses in the legend. (c)–(e) Initial slopes with standard deviations obtained from linear fits in the low strain regime of (c) keratin in LB, (d) vimentin in LB, (e) keratin in HB, and (f) vimentin in HB.

plateau-like region, which indicates some degree of cooperativity as will be discussed further below. Both proteins are initially stiffer in HB [Figs. 6.2e and 6.2f].

The different curve shapes for keratin and vimentin filaments also result in a higher input energy E for vimentin than for keratin filaments in HB. Note that E_{XY} is calculated by integrating the force-strain curves up to a force of 500 pN of protein X in buffer Y. In LB, the ratio of the input energies E_{VL}/E_{KL} is 1.02 ± 0.18, whereas in HB, vimentin filaments take up about 53% more energy ($E_{VH}/E_{KH} = 1.53 \pm 0.23$), as shown in Fig. 4.6a in the Section 4.4.2.

To understand these data, we take a closer look at the molecular properties of keratin and vimentin. Vimentin carries 19 e/monomer, keratin 8.5 e/monomer. HB has an ionic strength about 20 times higher than LB. The additional ions allow for a closer arrangement of the subunits in the filament since they screen the negative charges and decrease the electrostatic repulsion of the subunits within the filament [189, 190]. These additional attractions need to be overcome when the filament is stretched so that the filaments appear initially stiffer in HB. Since vimentin filaments are more negatively charged, they are affected more strongly by a change in the ionic strength of the buffer (see Fig. 6.5 in Section 6.1.6). Keratin monomers

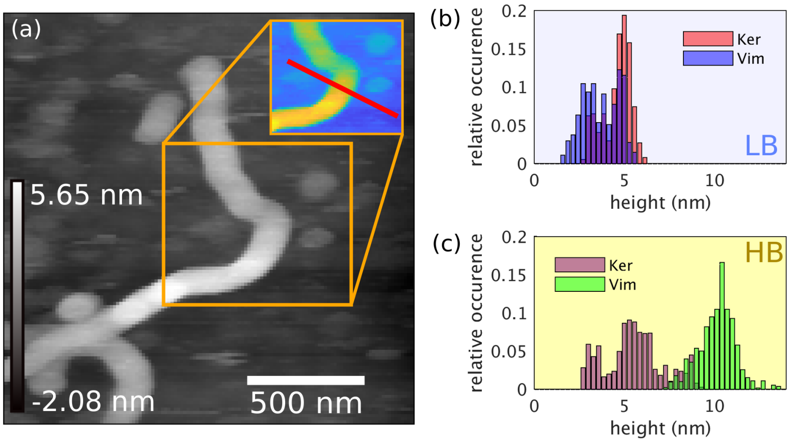

Figure 6.3: (a) Typical AFM image. The inset shows the processed AFM image in MATLAB used to extract the height profile (red line). (b,c) Histogram of keratin and vimentin filament heights measured with AFM in (b) LB and (c) HB.

are 1.5 times more hydrophobic [191] than vimentin monomers, so they attract each other more strongly, independent of the ionic strength of the surrounding buffer. Therefore, we can attribute the increased initial stiffening and the pronounced slope change of the force-strain curve of vimentin filaments in HB to a stronger attraction and a higher lateral coupling strength between the subunits. The higher initial slope and the overall different curve shape also lead to a larger input energy as reported above.

To test this hypothesis, we measure the height of keratin IFs and vimentin IFs in both LB and HB by AFM. The attraction between the substrate and the IF flattens the originally circular cross section of the filament [35, 77]. However, a stronger attraction between the filament subunits prevents this effect. IFs in the AFM images are tracked, and the height is extracted from the data as described in Section 4.5. A typical AFM image is shown in Fig. 6.3a, and the filament heights agree with the literature [10, 192]. The average height for keratin IFs increases from LB to HB by a factor of 1.2 ± 0.4, and the height of vimentin IFs increases by a factor of 2.6 ± 0.9 [Figs. 6.3b and 6.3c]. This supports our hypothesis that HB enhances the attractions between single subunits more strongly in vimentin filaments.

To understand why the lateral coupling in keratin and vimentin IFs has a different effect on the mechanical properties, we model keratin and vimentin IFs based on Refs. [7, 151, 155]: Each monomer is described as a spring in series with an element that can elongate under tension [Figs. 6.4a and 6.4b]. The spring corresponds to the elastic behavior of an α helix for low forces. The energy difference between the α and unfolded state u is ΔG. Before stretching, N_P monomers are connected in parallel, in order to present a ULF ($N_P = 16$ for keratin, $N_P = 32$ for vimentin). To model a filament, 100 of these ULFs are connected in series by springs. With respect to the elongation of the filament, two variants of the model are simulated: In the first (uncoupled) case (1), the filament elongates, when all monomers in one subunit are in the unfolded state [Fig. 6.4a]. In the second (coupled) case (2), the filament elongates, when all monomers of one ULF are in the unfolded state [Fig. 6.4b] [7]. Thus, case (1) supports the idea of protofilaments which can slide past each other [77, 164–167].

The coupled and uncoupled extensions differ in how the force ϕ is shared among the

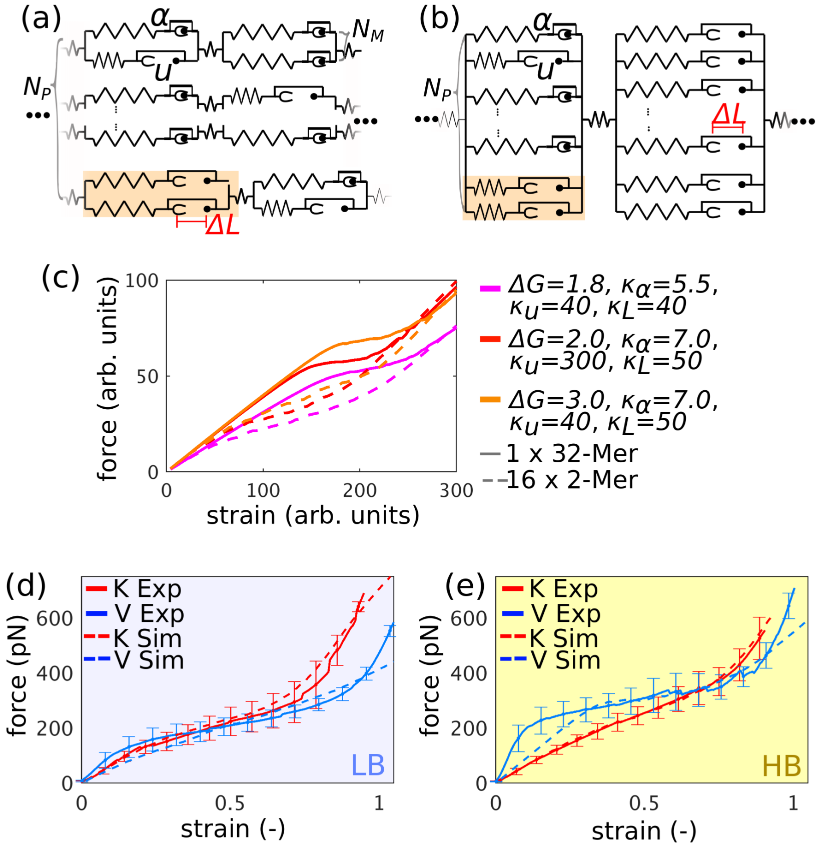

Figure 6.4: (a) Model for uncoupled dimers as subunits, case (1), and (b) model for coupled dimers as subunits, case (2). If one subunit is in the unfolded state in case (1), this leads to an elongation by ΔL, whereas in case (2) all monomers have to be in the unfolded state for elongation (orange: elements discussed in the text). (c) Comparison of simulation results for the same parameter sets (see color code in legend) for the uncoupled model (dashed lines) and the coupled model (solid lines), $\Delta L = 1$. (d,e) Measured and simulated force-strain curves (solid and dashed lines, respectively) for keratin (K) and vimentin (V) in (d) LB and (e) HB for the intermediate loading rate shown in Fig. 6.2.

monomers M and thus in the force dependence of the transition rates $r^{\alpha\to u}_{A_{j,m}}$ from the α to the unfolded state (see the Section 5.1). The transition rate has the general form

$$r^{\alpha\to u}_{A_{j,m}} = A_{j,m} r^{\alpha\to u}_0 \exp\left(\frac{\theta\phi}{M}\right)$$

with the number of monomers $A_{j,m}$ in the α state of the mth subunit in the jth ULF, the zero-force reaction rate from a monomer in the α to the unfolded state $r^{\alpha\to u}_0$, and the load distribution factor θ [153, 168]. In the uncoupled case, the force is shared equally among the subunits and within a subunit among the monomers, $M = N_C A_{j,m}$, while in the coupled case, the force is shared equally among all monomers of the ULF, $M = \sum_{m=1}^{N_C} A_{j,m}$ (with the number of laterally associated subunits N_C).

The two different assumptions for elongation lead to a fundamentally different force-strain behavior: In case (1), the data are "s shaped" since the laterally associated α helices in the subunits can open independently at a certain minimum force. In case (2), the initial slope increases and the plateau-like part evolves because a higher minimum force is needed to open the laterally coupled α helices in a cascading manner, which is also observed by Erdmann and Schwarz [155] for a system that resembles one vimentin ULF in HB in our model. Figure 6.4c shows that the same parameter sets for the coupled or uncoupled case, respectively, lead to a qualitatively different behavior. We observe a high initial slope and a reduced slope for intermediate strains only for vimentin filaments in HB; thus, we model them with case (2) [6, 7]. For keratin filaments in HB and vimentin and keratin filaments in LB, we assume case (1), which corresponds to an uncoupled filament elongation. We fit the simulation data to the experimental data using MATLAB [Figs. 6.4d and 6.4e]. The simulations agree well with the experimental force-strain curves for keratin filaments in LB and HB and for vimentin filaments in LB; for vimentin filaments in HB, the experiment exhibits a higher initial slope than expected from the simulation. In both buffers, ΔG, as extracted from the fit parameters, lies around 0.3 or 0.6 $k_B T$ per amino acid for keratin or vimentin, respectively, and agrees with theoretical results for short peptides from the literature [193–195]. This indicates that the energy stored in a single α helix does not depend on the ion concentration, in contrast to the lateral coupling strength between the α helices. We also determine the α-helical stiffness of about 0.6–3.4 pN/nm from the simulation parameters in agreement with the literature [6, 196, 197] as shown in Fig. 4.6b in Section 4.4.2.

6.1.5 Discussion and Summary

Our data from OT, AFM, and MC simulations strongly indicate that the lateral coupling in vimentin filaments induced by additional cations is so strong that all parallel α helices in one ULF have to unfold for a length change, whereas in keratin filaments the filament elongates in any condition as soon as one subunit is in the unfolded configuration. We assume that three main differences in the molecular properties of the two IFs contribute: (i) electrostatics, (ii) hydrophobicity, and (iii) compaction. Aspects (i) and (ii) have been discussed above. Concerning aspect (iii), in contrast to keratin, vimentin IFs compact after elongation [61, 160]. This is due to charged amino acids in linker L1 and in coil 1B that attract oppositely charged amino acids in linker L12 from a neighboring tetramer [61, 198]. Therefore, compaction can additionally increase the lateral coupling strength in vimentin IFs. Keratin IFs do not compact [38] and also do not exhibit the same charge pattern that all compacting IFs have in common [49] (see Table 6.1 in Section 6.1.6). Note that it is not the different number of monomers per cross section in keratin and vimentin that causes the different behavior in HB, as an uncoupled filament with 16 monomers in the MC simulation does not exhibit a high initial slope nor a clear change in slope for intermediate strains (see Fig. 5.2 in Section 5.1).

To conclude, our experiments substantiate the idea that cells can fine-tune their ability to absorb large amounts of energy to protect the cell from mechanical damage by the expression of different IFs. It should be noted that the ionic environment inside a cell is more complex than what has been used in our experiments, including divalent ions which promote IF bundling [117, 189, 199]. Depending on the surrounding ion concentration, vimentin filaments stiffen and absorb more energy than keratin filaments. An MC simulation based on assumptions about the molecular structure of both IFs shows that a stronger lateral coupling of the vimentin subunits is the cause for this behavior.

Acknowledgements:
We thank I. Mey for support with the AFM measurements and data analysis. We are grateful for fruitful discussions with and technical support by H. Herrmann, A. Janshoff, U.S. Schwarz, J. Kayser, N. Mücke, U. Rölleke, and P. Rauch. The work was financially supported by the European Research Council (ERC, Grant No. CoG 724932) and the Studienstiftung des deutschen Volkes e.V.

6.1.6 Supplementary Material

Materials and Methods – Protein Expression, Labeling and Dialysis:

Keratin: Human keratin 18 (K18), keratin 8 (K8) and K8 with an additional cysteine at the C-terminus (Cys-K8) are recombinantly expressed in E. Coli [186]. All plasmids are verified by Sanger sequencing and inserts are confirmed through a Basic Local Alignment Search Tool (BLAST) provided by the National Center for Biotechnology Information (NCBI). Purity of the proteins is verified by SDS-gel electrophoresis and assembly-competence by fluorescence or atomic force imaging.

Simulation

The results for ΔG obtained from the fit agree well with the literature: For example, 0.78 $k_B T$ /amino acid in idealized model polyalanine β-sheets [194], 0.95 $k_B T$/amino acid in human amylin [195] and 1.26 $k_B T$/amino acid in a β-sheet formed by two alanine dipeptide molecules [193] were found.

In addition to the α-helix–to–unfolded-state transition free energy (ΔG), we also estimate the spring constant of the α helices for keratin and vimentin IFs in the two different buffers as shown in Fig. 4.6b. Similar to the experimental data, we observe a pronounced stiffening of vimentin IFs in HB compared to LB. The α-helical keratin stiffness increases slightly from LB to HB. An increased α-helical stiffness in HB may be caused by additional intra α-helical attractions due to charge screening by the increased ion concentration.

Further Comments

Keratin and vimentin IFs in different buffers: Figs. 6.5a,b show the same data as Figs. 6.2a,b in Section 6.1, however, we here group all data for the same protein (but different buffers) together, whereas in Section 6.1, the data are grouped according to buffer type.

Compaction of vimentin IFs: The phenomenon of compaction denotes the diameter reduction of IFs as a last step in assembly [160, 198]: The diameter of vimentin IFs shrinks from 17 nm to 9.5 nm [31, 160], whereas the diameter of keratin IFs changes from 10.9 nm to 9.4 nm [38], although vimentin IFs have twice as many monomers per cross section on average. It seems to be vital that the transition of linker 1 (L1) to coil 1B contains amino acids, which are oppositely charged to the amino acids in linker 12 (L12), and that L12 contains a proline residue, as shown in Table 6.1 [61]. The oppositely charged amino acids attract each other and increase the coupling of neighboring subunits. The comparatively large proline residue allows for a spatially open arrangement of the linkers for the compaction step. By contrast, K8 does not contain a proline in linker L12 and similar charge patterns

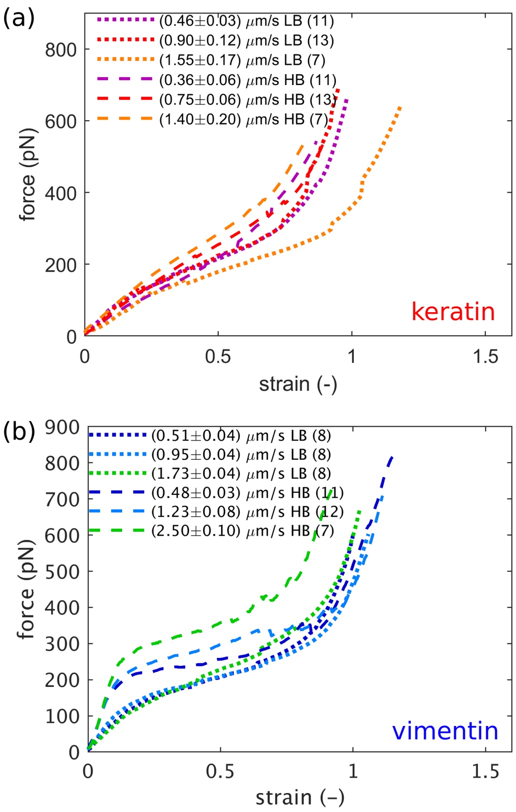

Figure 6.5: Averaged force-strain curves for (a) keratin IFs in LB and HB and (b) vimentin IFs in LB and HB. These data correspond to the data shown in Fig. 6.2 in Section 6.1, but are grouped differently.

Table 6.1: Comparison of amino acids in K8, K18 and vimentin in at the positions vital for compaction. The charge pattern in vimentin allows for compaction (red: positively charged amino acids, blue: negatively charged amino acids, green: amino acid with a large residue that can "open" the linker region for compaction) (adapted from Ref. [61]).

protein	Positions L1	Sequence: L1-1B
K8	127-136	`QQQKTARSNM-DNMFES`
K18	116-125	`LEKKGPQVRD-WSHYFK`
Vimentin	139-147	`KGQGKSRLG-DLYEEE`

protein	position L12	Sequence: linker L12
K8	238-254	`QISDTSVVLSMDNSRSL`
K18	227-243	`QIASSGLTVEVDAPKSQ`
Vimentin	250-264	`QEQHVQIDVDVSKPD`

as in vimentin are not observed as shown in Table 6.1. These molecular details are likely an explanation for compaction to occur in vimentin IFs, but not in K8/K18 filaments. This lack of compaction step in turn may be responsible for the weaker coupling between keratin subunits.

Stability of α helices in keratin and vimentin: As mentioned in Section 6.1, the α helices in K8, K18 and vimentin have a highly similar stability. However, the number of polar or charged amino acids in coil 1A at positions, where hydrophobic amino acids are expected due to the α-helical structure, is three times higher in keratin than in vimentin [49]; ions can stabilize this coil which may lead to increased stiffness. Yet, coil 1A is very short compared to the other coils (about 40 amino acids in coil 1A, 100 in coil 1B, 140 in coil 2) [49], so that the overall influence on stability from coil 1A may be comparatively small.

6.2 Mechanics of Single, Chemically Stabilized Keratin Intermediate Filaments

In the previous Section 6.1, the different mechanical behaviors of keratin and vimentin IFs are explained by the hypothesis that keratin subunits can slide, while vimentin subunits cannot. Thus, if there was a way to couple keratin subunits strongly, so that the subunits could not slide anymore, we would expect a similar mechanical behavior as for vimentin IFs, i.e., a plateau-like regime in the force-strain curve. A possible way of coupling subunits is chemical crosslinking of certain amino acids. For example, glutaraldehyde (GA) covalently crosslinks lysines. Thus, if lysines of different subunits in keratin IFs are closely packed, a GA molecule can crosslink them and they cannot slide any more. Lysines in K8/K18 monomers are located in all α-helical sections and in the tails and K18 contains additional lysines in the head domain, so that crosslinking of subunits is possible.

To study whether crosslinking suppresses subunit sliding within on keratin IFs, we prepared keratin IFs as described in the previous Section 6.1 and stretched them in keratin assembly buffer supplemented with 0.25% (v/v) GA. Interestingly, keratin IFs treated with GA stretched with different loading rates, as shown in Fig. 6.6a, do not exhibit a plateau-like behavior as vimentin IFs. Instead, the overall "s-shaped" behavior also reported in the previous section is preserved. Yet, GA-treated filaments are stiffer than untreated filaments, see Fig. 6.6b with continuous lines for GA-treated filaments vs. dashed lines for untreated filaments also shown in Section 6.1. Additionally, at a higher loading rate, the stiffness of GA-treated keratin IFs increases, the maximum strain of the stretched filaments decreases and the "s shape" becomes less pronounced. The crosslinking of lysines by GA can explain

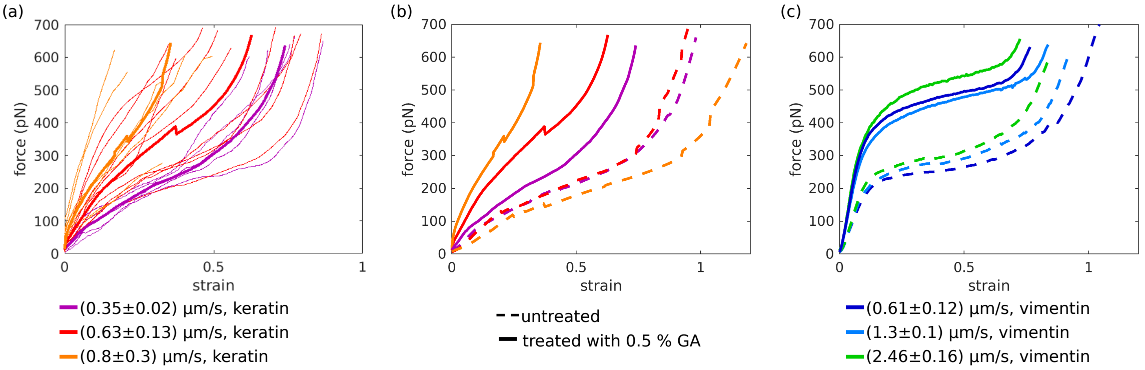

Figure 6.6: Force-strain curves of glutaraldehyde (GA)-treated filaments. (a) GA-treated keratin IFs still exhibit an "s-shaped" force-strain curve. (b) GA-treated keratin IFs are stiffer than untreated filaments, have a smaller maximum strain, and their mechanics depends on the loading rate. (c) GA-treated and untreated vimentin IFs stretched at different loading rates. Data recorded by Dr. Johanna Forsting (University of Göttingen).

the stiffening since more bonds are loaded within GA-treated filaments than within untreated filaments. The additional bonds in GA-treated filaments can prohibit a larger maximum strain as well since they hold the filament more strongly together. In Fig. 6.6c, GA-treated and untreated vimentin IFs stretched at different loading rates are compared: The filaments stiffen, and the plateau-like behavior is conserved, but the plateau is located at higher forces. The maximum strain is smaller for GA-treated filaments compared to untreated filaments. Yet, the maximum strains are larger than for keratin IFs, which might indicate that GA crosslinks subunits within keratin IFs more strongly than within vimentin IFs.

There are two possibilities why GA-treated keratin IFs do not exhibit a plateau-like behavior like vimentin IFs: (i) Lysines of different subunits within the keratin IFs are spatially not close enough to one another to be crosslinked by GA, so that the subunits can still slide and crosslinking occurs within the subunit or (ii) the subunits cannot slide any more because they are fixed by GA, but non-sliding subunits do not lead to a plateau, i.e., our hypothesis raised in the previous section is wrong. In case (i), we cannot check whether lysines of different subunits are sufficiently close to one another to be crosslinked, since the precise spacial arrangement of lysines on the nanometer scale is not known. In either case, an additional experiment to test our assumption of subunit sliding is necessary. If subunits in a filament can slide, we do not expect a restoring force acting on these subunits since they changed their position and might even form new bonds at this new position. Thus, we expect filament elongation when a keratin IF is loaded and relaxed again. Results of this experiment are presented in Chapter 7.

6.3 Tuning Intermediate Filament Mechanics by Variation of pH and Ion Charge

Thus, in the previous Section 6.1, we analyzed the mechanical behavior of different IF types. We show that the interactions within vimentin IFs cause the plateau-like regime in the force-strain curves in comparison to weaker interactions within keratin IFs which do not exhibit a plateau-like regime. We assume that these highly different behaviors are caused by the compaction step within vimentin IFs, where keratin IFs do not compact. Compaction is associated with a certain charge pattern between coil 1A and the beginning of coil 2, so that electrostatic interactions are a vital parameter for the interactions within filaments. This raises the question whether a direct change in the electrostatic conditions around the filaments or charge changes within the filament cause a different mechanical behavior.

The theoretical model of IF stretching and their subunit sliding described in section 6.1 is also applied to the mechanics of vimentin IFs stretched in buffers with a different pH and a different ionic strength. This application of the model is part of the publication “Tuning intermediate filament mechanics by variation of pH and ion charge” in *Nanoscale* **12** by Anna V. Schepers, Charlotta Lorenz and Sarah Köster in 2020 (Creative Commons Attribution-NonCommercial 3.0 Unported) [81]. In the following section, I summarize the results of this study with focus on the application of the theoretical model. Text and figures are adapted from Ref. [81].

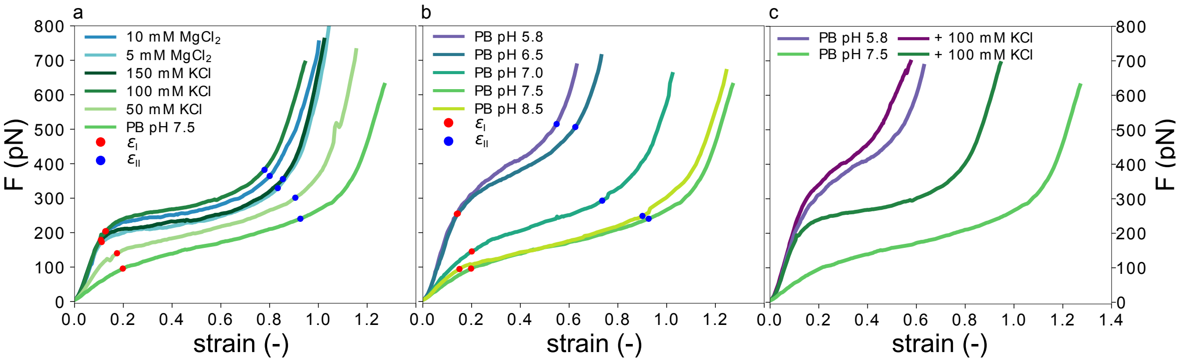

Figure 6.7: Force-strain behavior of single vimentin IFs. All curves shown are averages of the individual measurements. The strain values at the end of the initial linear regime ε_I (red) and the plateau regime ε_{II} (blue) for all average curves are indicated. (a) Effect of indirect charge shifts caused by salt ions in the measurement buffer. (b) Effect of direct charge shifts by varying pH conditions. While ε_I is similar in all measurements, ε_{II} increases for lower c(KCl) and for increasing pH. (c) Comparison of the effect of an addition of 100 mM K^+ ions at pH 7.5 and 5.8. Adapted from Ref. [81] (Creative Commons Attribution-NonCommercial 3.0 Unported).

Contributions: S. K. conceived and supervised the project. A. V. S performed the experiments and the data analysis. C. L. developed the method for force-strain data averaging, implemented the model and performed the simulations. S. K. and A. V. S wrote the manuscript. All authors read and commented on the manuscript.

Force-strain curves, recorded at varying ion concentrations and pH values, reveal that the mechanical properties of single vimentin IFs are influenced by pH and ion concentration: We study the response of mature vimentin IFs to tuning of the ionic conditions of the buffer and to the internal charge distribution in the protein by adjusting the pH of the buffer, and find that both factors strongly influence the mechanics of single vimentin IFs. The filaments are stretched at a rate of 0.21±0.05 µm/s in 2 mM phosphate buffer at varying pH (5.8–8.5) and concentrations of KCl (0, 50, 100, 150 mM) or MgCl2 (0, 5, 10 mM), see Fig. 6.7.

The three regimes that have been previously reported (see Fig. 2.6 in Section 2.2.2) are evident in the force-strain data recorded under standard assembly conditions as shown in Fig. 6.7a (100 mM KCl, see legend for color code): the initial linear increase, the plateau and the subsequent stiffening at high strains can be clearly distinguished. At high salt concentrations, i.e. c(KCl) = 100 mM or 150 mM and c($MgCl_2$) = 5 mM or 10 mM, the initial slopes are the same between these four salt conditions. When the filaments are incubated in low salt buffer (PB, pH 7.5; see Fig. 6.7a), the complete curve is shifted to lower forces, the initial slope is lower and the plateau is less pronounced. Independent of the measuring conditions, the strain at which the initial linear increase ends is at $\varepsilon_I = 0.15 \pm 0.04$ (see Fig. 6.7a), showing that the elastic extensibility of the filament is not affected by the salt ions. ε_{II} represents the strain at which the plateau ends, and F_{plateau} is the force at the beginning of the plateau, at a strain of ε_I.

Whereas the interactions of ions with the protein represent an indirect charge effect on the filament, we can also directly manipulate the charge of specific amino acids, e.g. by varying the pH of the buffer. We use the curve recorded in the low salt buffer (2 mM PB, pH 7.5; green in Fig. 6.7a,b) as a starting point and do not add any additional salt ions. As the cytoplasmic pH in eukaryotic cells is reported to lie between 7.0 and 7.5 [54, 55], we lower the pH to 7.0.

The resulting curves are shifted to higher forces and the plateau region is shorter compared to the low salt buffer at pH 7.5 (see Fig. 6.7b). The stiffening effect is amplified at even lower pH as shown by data for pH 6.5 and pH 5.8 (see purple and blue data in Fig. 6.7b). Taken together, our force-strain data on vimentin IFs at different pH values show that the overall stiffness of the filament and the unfolding are altered considerably when the charge of a few specific amino acids is varied.

To understand the interplay of salt ions and pH, we compare two sets of data recorded at different pH (7.5 and 5.8) without additional salt and with 100 mM KCl each, shown in Fig. 6.7c. At pH 5.8, 100 mM KCl does not have a strong effect, and the curves with and without additional salt are strikingly similar (purple), especially when compared to the pronounced effect of 100 mM KCl at pH 7.5 (green). This observation suggests that the maximum stiffness has already been reached at low pH without salt and the ions only have a negligible effect.

The observed filament softening in low salt buffer and stiffening at low pH raise the question of how these mechanical properties are governed by molecular charge interactions within the filament. To answer this question, we first regard the initial slope of the force-strain curves in Fig. 6.7. The initial slope decreases when fewer monovalent cations are present and increases with decreasing pH.

We model force-strain curves by Monte Carlo simulations that are based on the hierarchical structure of the filaments as described in Section 6.1. In our 1D experimental setting, we can interpret the initial slope as a measure of the filament stiffness, which for the sake of modeling we describe by the spring constant of the filament, κ_f. We expect an increase with the number of monomers, N_P, per cross-section of the filament [200]. We can, however, exclude the possibility of a reorganization of mature filaments in vitro by addition or loss of subunits as it only occurs on timescales of tens of minutes [201] which is much slower than the time scales of our experiments. We can therefore safely assume that the number of monomers is constant during our experiments. Instead, stiffening of the filament may originate from an increase of the spring constant of an individual α helix, κ_α, as shown in the Monte-Carlo simulated force-strain curves in Fig. 6.8a.

Whereas the change of the initial slope is well explained by variations of κ_α, other experimentally observed changes in the force-strain curves, such as the plateau slope and length are not reproduced by this variation. To be able to compare the mechanisms that affect the plateau, we first examine the unfolding reaction that leads to the plateau formation. The force level of the plateau F_{plateau}, the force reached at strain ε_I, is a measure of the energy necessary for unfolding. Fig. 6.8c shows a schematic and simplified energy landscape for the transition from the α to the unfolded state (green). The energy barrier E_A between the two states is indicated in Fig. 6.8d. The optical trap is approximated by a harmonic potential (dashed line). By applying a force (Fig. 6.8d), the harmonic potential is moved to the right, thereby decreasing the energy barrier in the total potential (blue) and the unfolded state becomes more probable.

The simulated force-strain curves in Fig. 6.8b reveal a strong dependence of F_{plateau} on the subunit size. By choosing a small subunit size N_M such as $N_M = 4$ we are able to reproduce the observed decrease of F_{plateau} in low salt buffer. At low pH, F_{plateau} is even higher than in high salt buffer. Thus, E_A is apparently even further increased at low pH. This behavior

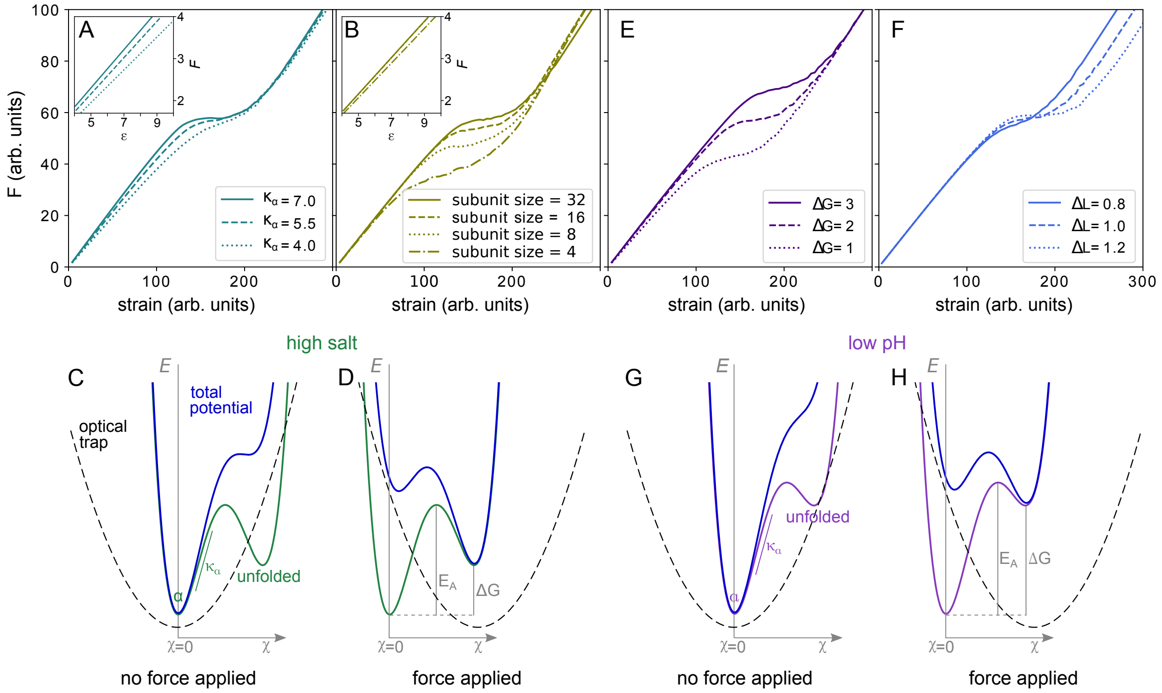

Figure 6.8: Monte-Carlo simulations of force-strain curves and schematics of energy landscapes. (a) An increased κ_α causes an increase of the initial slope. (b) A stronger coupling into larger subunits moves the plateau to higher forces, decreases the slope of the plateau and weakly influences the initial slope. The insets in a and b show the initial slope for each parameter set. (c) Energy landscape E plotted against the reaction coordinate χ with minima for the α and unfolded state at high salt conditions (green) within the harmonic potential corresponding to the optical trap (dashed line). The resulting total potential is shown in blue. Without applied load, the α state is stable. (d) By moving the optical trap, and thereby the harmonic potential, the energy barrier is reduced and the unfolded state becomes more probable. (e) A higher free energy difference ΔG between the α and unfolded state increases F_{plateau} without affecting the slope of the plateau. (f) Increasing the length of the unfolded monomer increases ε_{II}. (g) The suggested energy landscape at low pH, which leads to an increased energy barrier ΔG, shows a higher E_A making the transition to the unfolded state less probable, (h) even after applying the same trap load as in (f). Adapted from Ref. [81] (Creative Commons Attribution-NonCommercial 3.0 Unported).

may be explained by an increased free energy difference, ΔG, between the α and unfolded state (purple curve in Fig. 6.8h as compared to green curve in Fig. 6.8d), thus rendering the transition from the α to the unfolded state less probable at the same applied force (Fig. 6.8g and h), effectively increasing F_{plateau}. Fig. 6.8e shows how ΔG influences the force-strain curve.

In addition to an increased F_{plateau}, we also observe a shortening of the plateau at low pH (Fig. 6.7b). The length of the plateau, ε_{II} - ε_{I}, depends on the number of unfolding events and the length increase during unfolding, ΔL. Here, by the 'number of unfolding events' we summarize (i) fully unfolded ULFs and (ii) partially unfolded ULFs, as each of them consists of 32 monomers with three coils each, which can unfold fully or in parts. As ε_I is relatively constant in all measuring conditions, ε_{II} is a measure for the length of the plateau. Fig. 6.8f demonstrates how a decrease of ΔL shortens the plateau.

Earlier interpretations of the plateau being a transition from the α helices to beta sheets would allow for an elongation to strain 0.77 (Ref. [6] and [83]) in the plateau. This value agrees with ε_{II} at high salt concentrations, but is exceeded at low salt conditions and not reached at low pH values (Fig. 6.7). Recent results indicate that the unfolding is in fact not a two-state process but that α helices first unfold to a random coil structure [63]. These random coils could be either longer or shorter than the beta sheet conformation and thereby explain the variations in ΔL. The remarkably short plateaus we observe at low pH indicate a strong influence of the pH on ΔL. From the simulation in Fig. 6.8f, we learn that decreasing ΔL furthermore increases the slope of the plateau, which agrees well with the increase of the slope we observe at low pH. The additional positive charges located at the sites of the histidines might act as crosslinkers in the filament, 'locking' the monomers in place and thereby decreasing ΔL.

Combining the simulations and the experimental results, we are now able to explain the observed increase of the initial slope, shortening of the plateau, shift to higher forces F_{plateau} at low pH or high salt conditions by increased subunit coupling and decreased ΔL. Additionally, for the low pH conditions, a more pronounced ΔG comes into play, whereas for high salt, κ_α is increased. The slope of the plateau can be modeled by a decrease of the subunit size or of ΔL. As we observe no change of the slope of the plateau throughout all salt conditions at pH 7.5, these effects seem to be balanced out during the plateau formation.

To conclude, we directly relate the mechanical response of single vimentin IFs to stretching in different buffer conditions to variations in the molecular electrostatic interactions in the filament. Our results show that the strong response to the electrostatic environment reported for coiled coils is preserved in mature vimentin IFs. A likely interpretation is that salt ions in the buffer screen or bridge electrostatic repulsion in the hierarchical structure and thereby stabilize the filaments. Additional positive charges in the amino acid sequence caused by a lowered pH stabilize and stiffen vimentin IFs as well. Thus, our results indicate that the mechanical role of IFs in cells can adapt to local pH and ion concentrations. Both effects, salt and pH, may allow cells to locally tune their stiffness without having to rebuild the entire cytoskeleton and thereby adapt their mechanics to varying requirements. In this context, we show that stiffening of vimentin networks that was previously reported upon the addition of Mg^{2+} relies on increased inter-filament interactions and does not originate form stiffening of single filaments. Thus, by ensuring a relatively constant stiffness, extensibility, force-strain behavior, and stability of the filaments at physiological potassium concentrations and in conditions that are known to affect the bundling behavior of vimentin, we suggest that network mechanics can be tuned independent of the single filament properties. Consequently, the next step is to study, how the variability of single filament mechanics translates to network properties. This will allow for relating the intra-filament interactions studied here and inter-filament interaction in networks as presented in Section 8.2.

6.4 Softening of Vimentin Intermediate Filaments due to Post-translational Modifications

Next to the expression of different IF proteins and changes in ion concentration and pH around the filament, post-translational modifications might be another option for cells to adapt the mechanical properties of filaments. Thus, here, we study the influence of post-translational modifications on filament mechanics. Since post-translational modifications change the electrostatic interactions within filaments, we apply the model described in Section 6.1. This application of the model is part of the publication "Post-translational modifications soften vimentin intermediate filaments" in *Nanoscale* **13** by Julia Kraxner, Charlotta Lorenz, Julia Menzel, Iwan Parfentev, Ivan Silbern, Manuela Denz, Henning Urlaub, Blanche Schwappach and Sarah Köster in 2021 (Creative Commons Attribution-NonCommercial 3.0 Unported) [82]. In the following section, I summarize the results of this study with a focus on the application of the theoretical model. Text and figures are adapted from Ref. [82].

Contributions: S.K. conceived and supervised the project. J.K. performed the experiments and analyzed the data. J.M. and B.S. provided the 14-3-3 protein. H.U., I. P. and I. S. performed the mass spectrometry measurements. C.L. designed the model and performed the numerical simulations. J.K. and S.K. wrote the manuscript with contributions from all authors.

An interesting aspect of phosphorylation is the ability of certain proteins to bind to the modified sites. One such protein is 14-3-3 [202], which is involved in several cellular processes like signal transduction, adhesion and inhibition of tumorigenesis [203]. Here, we investigate the effect of phosphorylation and 14-3-3 on vimentin mechanics by studying precise force-strain curves from optical trap experiments.

As complete phosphorylation of vimentin IFs leads to disassembly [204], we perform the stretching experiments on partially phosphorylated vimentin IFs with varying percentages of 1, 5 or 10%. Fig. 6.9a shows corresponding data for filaments containing a certain percentage of phosphorylated protein (shades of blue, for color code see legend). To quantify the force-strain data, we focus on the Young's modulus, which we calculate from the initial slope in the linear regime up to a force of 130 pN of each curve, as a measure of the filament stiffness. The Young's moduli plotted in Fig. 6.9d (green) show a strong decrease with increasing percentage of phosphorylated protein.

We employ phosphomimicry to investigate the effect of defined phosphorylated sites and choose two of the most abundantly phosphorylated sites that also occur in vivo, S38 and S72 [204]. We perform the same force-strain measurements as described above. For the mutant S72E, we observe a similar trend as in the phosphorylation data including enhanced softening, see Fig. 6.9b, green to dark blue. On the contrary, Fig. 6.9c, green to dark blue, shows filaments containing the mutation S38E and no systematic trend is observed.

When comparing these three different conditions, i.e. phosphorylation, mutation S72E and mutation S38E, we observe that the Young's modulus, and therefore the filament stiffness, decreases with an increasing amount of phosphorylation (green) and mutation S72E (orange) but stays fairly constant for the mutation S38E (blue), see Fig. 6.9d. These results suggest that the phosphorylation at position S72 influences the filament mechanics whereas at position S38 it does not have any effect.

To explain the softening of vimentin IFs with increasing amount of phosphorylation, we consider previous studies that have shown neighboring dimers to be coupled by electrostatic interactions between specific positively charged amino acids in the head, namely R23, R28, R36 and R45, and the negatively charged coiled-coils [31, 158, 205] as sketched in Fig. 6.10a. When vimentin becomes phosphorylated, the positive charges of the head domain are flanked by negative charges of the phosphorylated amino acids, which diminishes the electrostatic

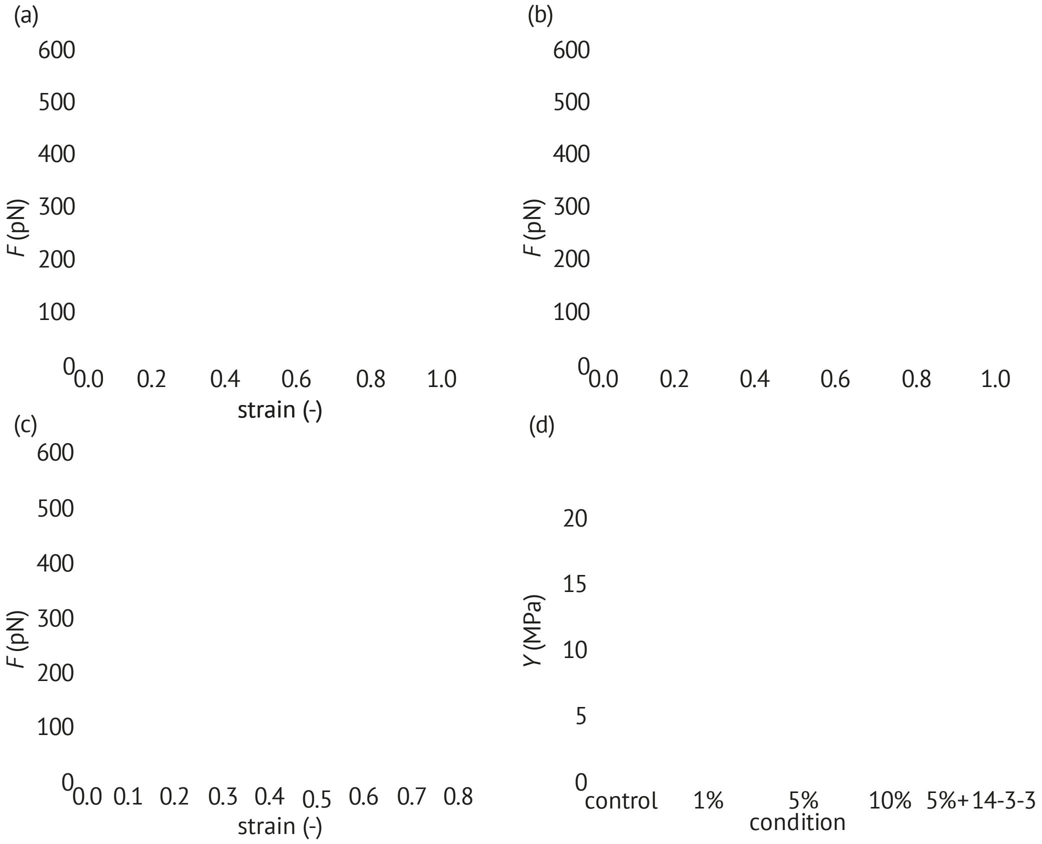

Figure 6.9: Additional negatively charged amino acids soften vimentin IFs. (a) Mean force-strain curves for partially phosphorylated filaments: control (unphosphorylated, green), 1% phosphorylation (light blue), 5% phosphorylation (medium blue), 10% phosphorylation (dark blue) and 5% phosphorylation with 14-3-3 (magenta). With increasing amount of phosphorylated vimentin incorporated, the filaments become softer; the effect is even more pronounced in the presence of the protein 14-3-3. (b and c) Mean force-strain curves for the phosphomimicry data. The color code for the individual conditions is the same as in a. (b) The mean curves for the phosphomimetic mutant S72E show a similar trend as the phosphorylation data except for the filaments incubated with 14-3-3. (c) The mean curves of the phosphomimetic mutant S38E do not show a systematic softening regardless of whether the filaments were incubated with 14-3-3 or not. (d) Comparison of the different data sets. The Young's modulus Y, which is a measure of the filament stiffness, is shown in dependence of the amount of phosphorylated or phosphomimetic protein. The phosphorylation (green) and the S72E data (orange) show a softening with increasing phosphorylation or phosphomimicry, whereas the S38E data (blue) remain fairly constant. The Young's moduli for filaments with additional 14-3-3 are depicted as open symbols, as these are only an estimate using the radius of the 5% condition instead of the actual radius that cannot be measured by small-angle X-ray scattering. Adapted from Ref. [82] (Creative Commons Attribution-NonCommercial 3.0 Unported).

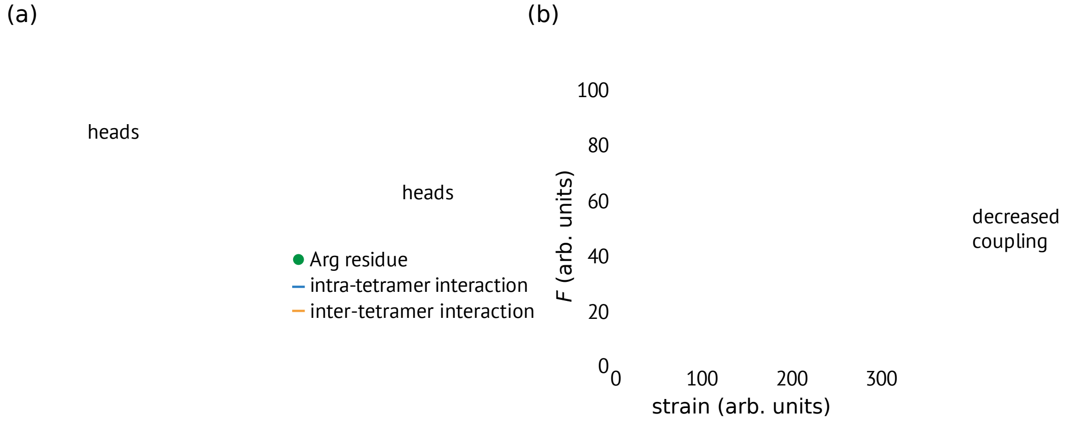

Figure 6.10: Softening of phosphorylated filaments is due to decreased lateral interactions. (a) Sketch of a vimentin tetramer. The positively charged amino acids in the head domain (green dots) interact with the negatively charged coils of the neighboring dimer. Intra-tetramer interactions are depicted in blue, the neighboring tetramer is illustrated in light gray and inter-tetramer interactions are shown in orange. (b) Results of numerical model for the softening of the filaments due to decreased lateral coupling. The influence of decreased coupling is shown in the force-strain plot where the completely coupled system is shown in green and the lateral coupling is decreased from light blue to dark blue. Adapted from Ref. [82] (Creative Commons Attribution-NonCommercial 3.0 Unported).

attraction between the head and the coiled-coils. This observation raises the question of whether the shift in filament stiffness can be explained by weaker coupling. Therefore, we run Monte-Carlo simulations to understand how the coupling of dimers affects the force-strain curves of vimentin by extending the model from Ref. [156] as described in Section 6.1 and [7]. This previous model does not explain a pronounced decrease in Young's modulus as observed here.

We thus supplement the model from Ref. [156] by spring constants κ_{bt}, which represent bonds between tetramers, and κ_{bd} for bonds between dimers within the tetramer. In case of more phosphorylated monomers in the filament, the filament subunits do not interact as strongly as without phosphorylated monomers because the additional negative charges repel each other. Thus, not all bonds between tetramers and dimers can form, so that the spring constants κ_{bd} and κ_{bt} do not contribute to the overall spring constant and the filaments get softer as shown for the simulated force-strain curves in Fig. 6.10d. Consequently, the initial slope of the force-strain curves decreases with more phosphorylated monomers as shown in Fig. 6.9d.

Our results show that the negative charge at position S72, in particular, has an effect on filament mechanics: the phosphomimetic mutant shows a very similar trend compared to the phosphorylation data (Fig. 6.9d). Indeed, this position is also found to be the mayor phosphorylation site. By contrast, an additional negative charge at position S38 has no effect on the filament mechanics. Therefore, we conclude that a decreased coupling around position S72 is crucial for the shift in mechanics whereas a decreased coupling at position S38 has no effect. We confirm these numerical findings with mass spectrometry cross-linking experiments. These studies supports our proposal that there are decreased interactions between neighboring dimers in phosphorylated vimentin which indicates that the lateral coupling of dimers is reduced.

To conclude, we directly show how post-translational modifications, i.e. phosphorylation, change the mechanical properties of vimentin IFs: vimentin IFs become softer with increasing amount of phosphorylated protein within the filament. These findings may help to understand the relation between the role of phosphorylation in cancer metastasis and the pronounced motility of metastasizing cells. The interaction of phosphorylated vimentin with 14-3-3 enhances this softening effect and may even protect the softer state. We suggest that these changes are induced by reduced electrostatic coupling within the ULF due to additional negative charges introduced by the phosphate groups and support this assumption by a physical model. We thus hypothesize that cells are able to fine-tune and adapt their mechanical properties locally and within seconds by modifications like phosphorylation according to specific external requirements.

CHAPTER 7

Effects of Interactions Within Intermediate Filaments on Filament Mechanics During Repeated Load

Parts of the following chapter were published as "Keratin filament mechanics and energy dissipation are determined by metal-like plasticity" in *Matter* 6 (6) in 2023 [206].

7.1 Introduction

The cytoskeleton of eukaryotes ensures mechanical integrity and stability and is responsible for active processes such as cell division and migration. The three families of biopolymers of the cytoskeleton, actin filaments, microtubules and intermediate filaments (IFs), form interwoven networks within cells [21]. This "composite material" is able to adapt precisely to the mechanical needs and functions of each cell type. In contrast to actin and tubulin, IF proteins are expressed in a cell-type specific manner [10, 11], making them ideal candidates for cells to adapt their mechanical properties [12]. A prominent example of differential expression of IF proteins is the epithelial-to-mesenchymal-transition [16, 17], which occurs during cancer metastasis [15], embryogenesis [13] and wound healing [14]. These processes have in common that stationary, strongly interconnected epithelial cells change their phenotype to highly motile mesenchymal cells. Interestingly, the mesenchymal cells typically express the IF protein vimentin, whereas the epithelial cells express keratins.

It has been shown that already on the single filament level keratin 8/18 IFs are softer and exhibit a very different mechanical behavior than vimentin IFs due to different lateral interaction strengths within the filaments [156] (see Section 6.1). Indeed, the mechanical properties of IFs are closely related to their molecular architecture [6, 7, 63, 156], see Fig. 7.1a: IF protein monomers consist of three α-helical domains (dark green in Fig. 7.1a), flanked by an intrinsically disordered head and tail domain [31] (black lines in Fig. 7.1a). During assembly of the filaments, these monomers associate laterally to homo-dimers, in case of vimentin. In case of keratin, two different monomers, e.g. a keratin 8 and a keratin 18 monomer, associate laterally to a hetero-dimer. Two dimers associate laterally to tetramers. Further IF assembly is initiated by a change in pH or ionic strength of the buffer conditions (blue arrow in Fig.

7.1a). In case of keratin and vimentin IFs, $N_P = 4$ or $N_P = 8$ tetramers, respectively, associate laterally to unit-length filaments (ULF) [10, 31, 41]. N_F ULFs bind longitudinally to form filaments. The coupling within these ULFs, i.e. between the subunits (e.g. dimers, tetramers or octamers), strongly influences IF mechanics [81, 156]. Vimentin ULFs exhibit a stronger coupling than keratin ULFs. This strong coupling ensures that vimentin IFs only elongate when all α helices within a ULF unfold. This cooperative unfolding of the α helices causes a plateau-like regime in the force-strain curves of single stretched vimentin IFs. During subsequent relaxation, the unfolded α helices do not refold, but transition into a third state, likely a random coil, with the same length as the unstretched α helices [63]. This third state is softer than α helices so that vimentin IFs soften under repeated loading when an increasing fraction of α helices unfolds, i.e., vimentin IFs possess a tensile memory [7, 63]. The unfolding of α helices dissipates up to 80% of the input energy [7]. Crosslinkers influence the fraction of unfolding α helices and the amount of dissipated energy [63].

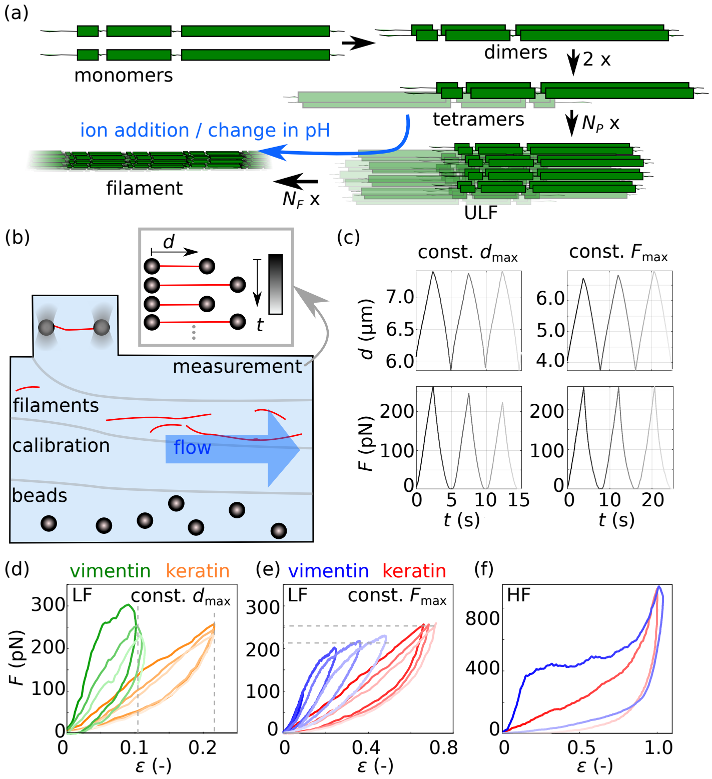

Figure 7.1: (a) Sketch of the assembly pathway of IFs. (b) Sketch of the experimental setup and measurement procedure. (c) Typical distance-time and force-time curves for constant $d_{\max}$ and decreasing $F_{\max}$ (left panels) and constant $F_{\max}$ measurements with an increasing $d_{\max}$ (right panels). Increasing time is indicated with lighter color. (d-f) Typical force-strain curves of keratin (orange, red) and vimentin (green, blue) IFs when (d) repeatedly stretched to a constant $d_{\max}$ (dashed gray lines) up to a constant $F_{\max}$ in the LF range, (e) repeatedly stretched to a constant $F_{\max}$ (dashed gray lines) in the LF range and (f) stretched once to the HF range and relaxed.

In contrast to vimentin IFs, subunits within keratin IFs are coupled less strongly so that subunits can slide, and the unfolding of all α helices within one single subunit is sufficient for filament elongation [156]. When a subunit within the filament slides, bonds are broken which keep the subunit at its original position. Since these bonds are broken and the subunit is relocated, we hypothesize that there is no restoring force acting on the subunit towards its original position. If subunits slide when keratin IFs are stretched, we assume a permanent filament elongation due to the missing restoring force acting on the subunits. Thus, we expect an elongation of the filament when the filament is relaxed again. Furthermore, we speculate that keratin IFs dissipate a different amount of energy compared to vimentin IFs since less α helices have to unfold during keratin IF stretching. Thus, subunit sliding could induce fundamentally different filament mechanics upon repeated loading, which might be a vital tool for cells to adapt their mechanics via different IF protein expression. To study keratin IF elongation and energy dissipation, we repeatedly stretch keratin IFs with optical tweezers (OT). Our data provide experimental evidence that subunit sliding within keratin IFs is irreversible due to the lack of a restoring force on subunits and thereby cause permanent filament elongation. The subunit sliding dissipates more than 50% of the input energy.

7.2 Materials and Methods

Proteins are recombinantly expressed, labeled and assembled into filaments by dialysis as described in Ref. [156]. After assembly, keratin IFs are diluted 1:10 with keratin assembly buffer (10 mM TRIS, pH 7.5) [10, 57, 58] and stored at 37°C up to two days. Vimentin IFs are stored in vimentin assembly buffer (100 mM KCl, 2 mM phosphate buffer, pH 7.5) [59, 161] at 4°C. For measurements with an OT setup (LUMICKS, Amsterdam, Netherlands), we load a four-channel microfluidic chip as sketched in Fig. 7.1b. Two PEG-maleimide-functionalyzed polystyrene beads (Kisker Biotech, Steinfurt, Germany) are captured with the OTs from the beads channel and calibrated via their thermal noise spectrum in the calibration channel which is filled with the assembly buffer of the respective IF type. A filament is attached to both beads in the filaments channel and subsequently moved to the measurement channel which is filled with vimentin assembly buffer for both IF types. Filaments are repeatedly stretched by moving one bead with the OT so that the distance d between the beads is changed. We record this distance and the force F exerted by the stretched filament on the beads. We use three different measurement protocols (see Fig. 7.1c-f): (i) IFs are stretched to a constant maximum distance d_{max} and an over time t decreasing maximum force F_{max} (Fig. 7.1c, left panels). In case of keratin IFs, d_{max} is set to the distance at which F reaches 250 pN (orange in Fig. 7.1d). Vimentin IFs are stretched to a d_{max} that corresponds to the beginning of the plateau-like regime of the measured IF (green in Fig. 7.1d). Keratin IFs do not exhibit a plateau so that we fix F_{max} of all cycles to 250 pN. To study IF mechanics independent of the filament length, we calculate the filament strain $\varepsilon = L/L_0 - 1$, where L denotes the measured filament length and L_0 is the filament length at 5 pN [6, 156]. We call this force range the low force range (LF). With this measurement protocol, we probe IF mechanics just before a majority of the α helices within vimentin IFs starts to open [6, 7]. (ii) Filaments are stretched to a constant F_{max} of 250 pN in case of keratin IFs (red in Fig. 7.1e) and in case of vimentin IFs to the beginning of the plateau-like regime (blue in Fig. 7.1e), while d_{max} increases for each cycle (Fig. 7.1c, right panels). With this second measurement protocol, we probe the IF mechanics beyond the onset of α-helical opening in vimentin IFs because the filaments are stretched further with each cycle [7]. (iii) By stretching the filaments once F_{max} of 900 pN as shown in Fig. 7.1f, we probe the behavior of the filaments after most of the α helices are unfolded within the vimentin IFs. We call these forces the high force (HF) range. Progressing time is indicated by lighter colors. Filaments are stretched at a rate of 0.6 μm/s.

7.3 Results and Discussion

We calculate the filament elongation by extrapolating linear fits (continuous black lines in Fig. 7.2a) to the elastic stretching regime of force-strain curves at $F = (100 - 150)$ pN (gray shades in Fig. 7.2a). The extrapolation of the linear fits to the x axis (dashed lines in Fig. 7.2a) results in the effective length of the filament. This effective length ε_e is calculated in units of strain and indicated by dots in Fig. 7.2a. We observe that keratin IFs elongate by $\varepsilon_e = 0.1 - 0.2$ after eight stretching cycles during constant $d_{\max}$ and constant $F_{\max}$ cycles to the LF range as shown in Fig. 7.2b,c (orange, red), whereas vimentin IFs barely elongate (green, blue). To test whether keratin IFs elongate further with higher loading forces, we analyze the filament elongation of repeatedly stretched keratin IFs at a constant $d_{\max}$ with $F_{\max}$ in the HF range (dark red in Fig. 7.2d) or at a constant $F_{\max}$ in the HF range (purple in Fig. 7.2d). When stretched repeatedly to the HF range, keratin IFs elongate by $\varepsilon_e = 0.6 - 0.8$ after eight cycles. To compare the different measurement protocols, we relate ε_e of the 4th to 15th cycles to the maximum applied strain $\varepsilon_{\max}$ in Fig. 7.2e: Keratin IFs (red) elongate further

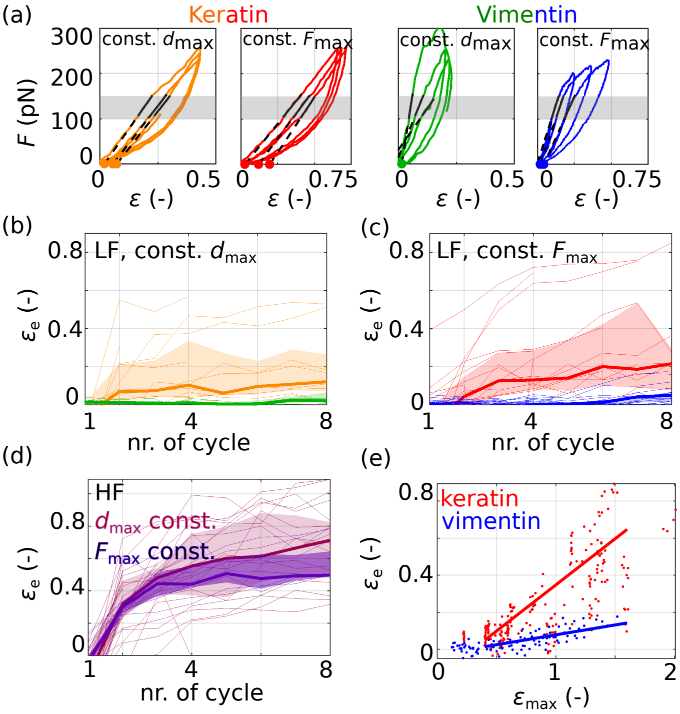

Figure 7.2: (a) Typical experimental data sets of keratin (orange, red) and vimentin (green, blue) IFs stretched three times to a constant $d_{\max}$ (orange, green) or to a constant $F_{\max}$ (red, blue) including fit curves to the force range of $F = (100 - 150)$ pN (black lines). Constant fit ranges are indicated by gray-shaded areas. Filament elongations (dots on the x axis) are determined by extrapolation of the linear fits to the x axis (dashed lines). (b,c) ε_e of filaments repeatedly stretched (b) to a constant $d_{\max}$ with $F_{\max}$ in the LF range or (c) to a constant $F_{\max}$ in the LF range. (d) ε_e of keratin IFs stretched to a constant $d_{\max}$ with $F_{\max}$ in the HF range (dark red) or to a constant $F_{\max}$ in the HF range (purple). (e) ε_e of keratin (red) and vimentin IFs (blue) compared to $\varepsilon_{\max}$ during the 4th to 15th cycle. The data are linearly fitted (red and blue lines).

than vimentin IFs for any applied maximum strain (blue). By fitting a linear relationship to the data (see red and blue lines in Fig. 7.2e), we estimate that keratin IFs elongate around five times more per maximum applied strain than vimentin IFs. Assuming that no restoring force acts on slid subunits within keratin IFs, we conclude that sliding subunits within keratin IFs cause the observed filament elongation. This conclusion is supported by the minuscule elongation of vimentin IFs, in which subunits cannot slide [156].

The strong elongation of keratin IFs during repeated loading raises the question how this elongation impacts IF mechanics. It is known that vimentin IFs undergo structural changes during repeated stretching which impacts their mechanics [7, 63]. It is therefore likely that structural changes in keratin IFs occur as well and influence keratin IF mechanics. We characterize IF mechanics by determining their stretching stiffness from linear fits to two regions of the force-strain curves: Linear fits to $F = (100 - 150)$ pN as shown in Fig. 7.2a resulting in the stiffness κ_{cf} as well as linear fits to $\varepsilon = 0.1 - 0.3$ resulting in the stiffness $\kappa_{c\epsilon}$ as shown in Fig. 7.3a. We find that, remarkably, keratin IFs retain their stiffness when repeatedly stretched to a constant $d_{\max}$ (orange in Fig. 7.3b) as well as when stretched to a constant $F_{\max}$ (red in Fig. 7.3c). As previously reported, vimentin IFs soften (green and blue in Fig. 7.3b

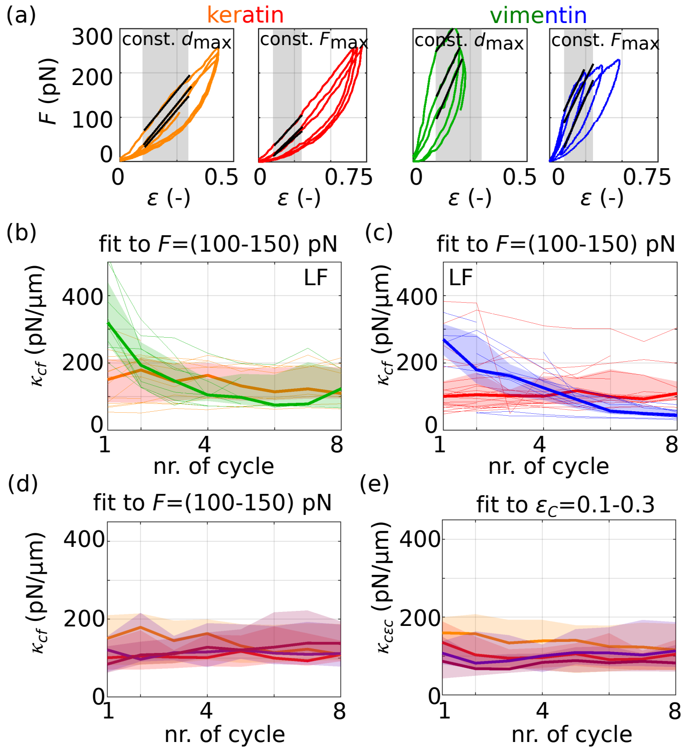

Figure 7.3: (a) Typical experimental data sets of keratin (orange, red) and vimentin (green, blue) IFs stretched three times to a constant $d_{\max}$ (orange, green) and to a constant $F_{\max}$ (red, blue) including fits to $\varepsilon = 0.1 - 0.3$ (black lines). Constant fit ranges are indicated by gray-shaded areas. (b,c) Filament stiffness κ_{cf} resulting from a fit to $F = (100 - 150)$ pN (orange: keratin, green: vimentin) as in Fig. 7.2a of (b) filaments stretched to a constant $d_{\max}$ and of (c) filaments stretched to a constant $F_{\max}$ (red: keratin, blue: vimentin). (d) κ_{cf} for keratin IFs as in Fig. 7.2a for all conditions studied: constant $d_{\max}$ at $F_{\max}$ in the LF range (orange), constant force in the LF range (red), constant $d_{\max}$ at a $F_{\max}$ in the HF range (dark red) and constant $F_{\max}$ in the HF range (purple). (e) Keratin IF stiffness κ_{cec} derived from linear fits to $\varepsilon = 0.1 - 0.3$ as shown in (a) after correcting the strain by the filament elongation presented in Fig. 7.2b-d. (b-e) Thick lines show the median and shading indicates the area between the 25th and 75th percentile of the distributions per cycle.

and c, respectively) [7, 63]. Keratin IF stiffness even "forgets" previous loading cycles when stretched to a constant $d_{\max}$ (dark red in Fig. 7.3d) or with a $F_{\max}$ in the HF range (purple in Fig. 7.3d). Keratin IF stiffness is identical for all measurement protocols. Determining the filament stiffness $\kappa_{c\varepsilon}$ from fits to $\varepsilon = 0.1 - 0.3$ reveals a slight decrease of filament stiffness for both keratin and vimentin IFs (see Supplementary Figure 7.5). However, since keratin IFs elongate, the fit range of the strain needs to be adjusted to ε_e of the filament. We therefore calculate a corrected strain $\varepsilon_c = \varepsilon - \varepsilon_e$ for each cycle. With this corrected strain, we confirm the first analysis result that the strain-corrected stiffness $\kappa_{c\varepsilon c}$ is constant for all measurement protocols and loading cycles as shown in Fig. 7.3e. Thus, keratin IF stiffness "forgets" the loading history and keratin IF length "remembers" it. Contrarily, vimentin IF stiffness has a tensile memory concerning stiffness and vimentin IFs "forget" the loading history with respect to their lengths [7, 63].

The observation that the stiffness of keratin IFs is constant independent of the loading history and the filament elongation dependent on the loading history raises the question which molecular mechanisms within keratin IFs cause this behavior different to vimentin IFs. From repeated loading of vimentin IFs, we know that unfolded α helices return into a third state, likely a random coil, which is softer than the α helices [63]. Thus, if a significant portion of the α helices within keratin IFs was unfolded, we would expect a softening of repeatedly stretched filaments since the softer subunits within the filament would be stretched first. However, we observe a constant stiffness so that we conclude that most α helices within the keratin IF remain intact. We do not exclude the possibility that a small portion of α helices unfolds, but we hypothesize that the unfolded structures are not loaded during the next stretching cycle. We speculate that two distinct molecular mechanisms can account for our findings: (i) The subunits within keratin IFs slide and form new bonds at a different location. The stiffness during the next stretching cycle is the same since different bonds with the same properties as the previously existing bonds are stretched. (ii) Stretched subunits are replaced by previously unstretched subunits, which are loaded during the next stretching cycle. This sliding and replacement mechanism might be supported by the highly heterogeneous arrangement of subunits within keratin IFs compared to vimentin IFs [207, 208]. For example, if a filament section with a high number of subunits is stretched, it can be imagined that some of these subunits slide and others remain unstretched. These unstretched subunits might replace the subunits which were relocated. Thus, the stiffness during the next loading cycle is the same since a highly similar filament structure compared to the structure before the stretching is loaded. In both cases, instead of α-helical unfolding as in vimentin IFs, subunits slide and thereby avoid major α-helical unfolding. Hence, next to crosslinkers [63], subunit sliding can protect α helices from unfolding.

By α-helical unfolding, vimentin IFs dissipate more than 80% of their input energy [7]. To investigate whether keratin IFs still dissipate a major amount of their input energy although we do not expect α-helical unfolding within keratin IFs, we thus analyze the dissipated energy during their first stretching and relaxation cycle in Fig. 7.4a-d. We find that keratin IFs dissipate more than 50% of the input energy when loaded to the LF and HF range (red in Fig. 7.4a,b), which is slightly lower than for vimentin IFs which exhibit a relative dissipated energy of around 70% (blue in Fig. 7.4a,b). Keratin IFs (red) also dissipate less energy in terms of absolute energy per filament length compared to vimentin IFs (blue in Fig. 7.4c,d). Yet, both filament types dissipate energies of the order of $(10^4 - 10^5)\ k_BT/\mu\text{m}$. The high amount of relative and absolute dissipated energy supports the notion that IFs, in general, act as cellular shock absorbers [7, 77, 209].

Nevertheless, the question remains how energy is dissipated in keratin IFs on the molecular scale if most of the α helices do not unfold. To dissipate energy, bonds need to be broken and must not rebind immediately. In the case of keratin IFs we show that most bonds within α helices remain intact, but the bonds between subunits are broken. Thus, we analyze the relation of broken subunit bonds of both IF types to their dissipated energy in Fig. 7.4e. We measure the broken subunit bonds in form form of additional effective length $\Delta\varepsilon_e$, which is the difference in ε_e from one cycle to the next for each filament. For keratin IFs (red in Fig. 7.4e), higher relative dissipated energies are correlated with a more pronounced increase of $\Delta\varepsilon_e$. Since vimentin IFs barely elongate, we do not observe a correlation between the dissipated energy and $\Delta\varepsilon_e$ (blue in Fig. 7.4e). We therefore conclude that keratin IFs dissipate their energy by breaking bonds between subunits which results in subunit sliding and filament elongation, while vimentin IFs dissipate their energy by α-helical unfolding [7]. Consequently, keratin IFs effectively dissipate energy by friction between subunits, whereas vimentin IFs dissipate energy by the nonequilbrium unfolding of α helices [7].

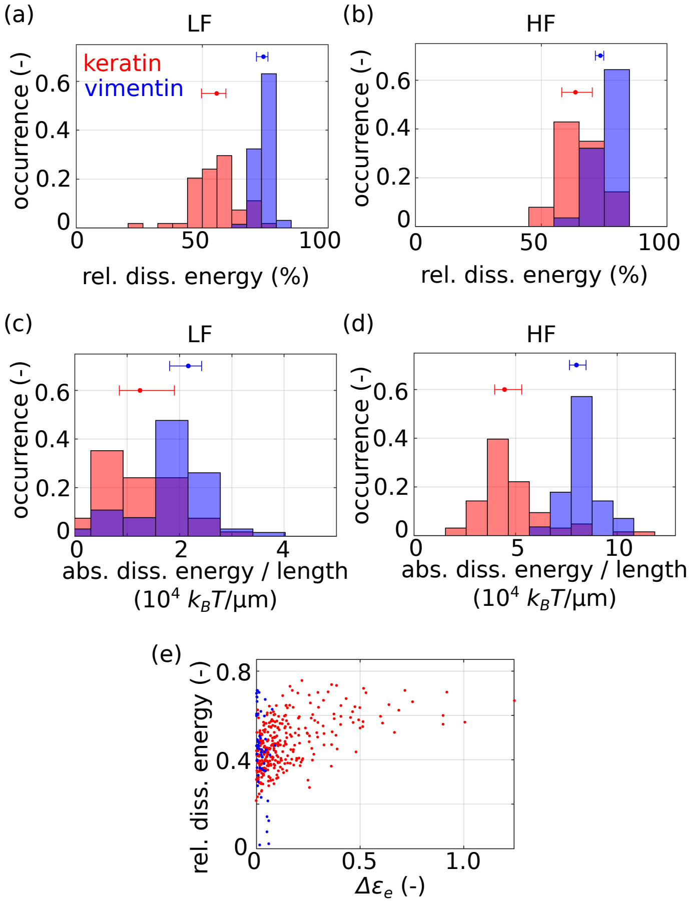

Figure 7.4: Dissipated energies of keratin (red) and vimentin IFs (blue) during their first stretching cycle. (a) Relative dissipated energy when stretched to the LF range, (b) relative dissipated energy when stretched to the HF range. (c) Absolute dissipated energy per filament length of IFs stretched to the LF range and (d) absolute dissipated energy per filament length when stretched to the HF range. Dots and whiskers indicate the median and the 25th and 75th percentile of the distributions. Bin width of the histograms is determined with the Freedman-Diaconis rule. (e) Relative dissipated energy of all cycles compared to $\Delta\varepsilon_e$.

7.4 Discussion and Summary

Our results show that subunit sliding within keratin IFs causes filament elongation and diminishes α-helical unfolding, which results in a constant filament stiffness independent of the loading history. Contrarily, vimentin IFs retain their length and soften during repeated loading due to α-helical unfolding [7, 63]. On the molecular scale, the subunit sliding within keratin IFs is attributed to a missing compaction step in comparison to vimentin IFs [10, 38, 156, 160]. Additionally, subunit sliding might be supported by the assembly of keratin IFs from hetero-dimers which might allow for a more precise fine-tuning of inter-subunit interactions responsible for subunit sliding. Thus, the expression of different IF proteins might be a way for cells to ensure that filaments either keep their original stiffness (keratin) or their original length (vimentin). We speculate that a constant stiffness during repeated loading can be a vital property for specific cell types such as endothelial cells in the inner layer of the blood vessel which is constantly loaded due to the blood flow and changing blood pressure due to the heart beat. A constant filament length might be desirable for more motile cells so that cells are protected from elongation. Interestingly, vimentin IF protein is expressed in more motile cells and vimentin IFs do not elongate under repeated loading. The softening of the vimentin IFs might support the cell in moving through confinements [210].

To conclude, our findings foster the idea of differential IF protein expression as a tool for cells to adapt their mechanical properties to their surrounding environment: After repeated loading, keratin IFs elongate, but exhibit a constant stiffness, while vimentin IFs retain their length and soften. We find that weaker interaction strengths within keratin IFs than within vimentin IFs cause these distinct behaviors and protect the α helices within keratin IFs from unfolding. Independent of the interaction strength within the two different filament types, both IFs can act as cellular shock absorbers.

Contributions:

Sarah Köster conceived and supervised the project. Charlotta Lorenz performed experiments on repeated loading of keratin IFs and analyzed the data. Johanna Forsting performed experiments on repeated loading of vimentin IFs.

7.5 Supplementary Information

Materials and Methods: Human keratin 8, keratin 18, keratin 8 with additional cysteine at the C-terminus and vimentin C328N with GGC as an additional sequence at the C-terminus are expressed as described in Ref. [186]. Protein labeling and assembly as carried out as described in Ref. [156].

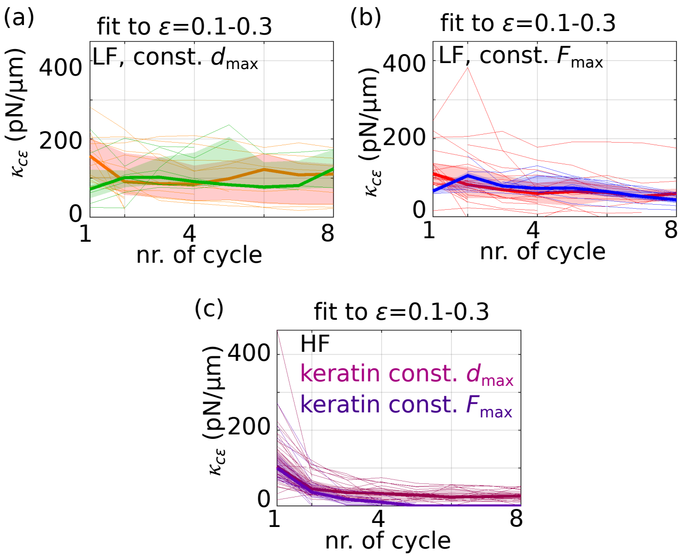

Figure 7.5: (a,b) Keratin (orange, red) and vimentin (green, blue) IF stretching stiffness $\kappa_{c\varepsilon}$ resulting from a fit to $\varepsilon = 0.1 - 0.3$ for (a) a constant d_{max} with F_{max} in the LF range and (b) at a constant F_{max} in the LF range. $\kappa_{c\varepsilon}$ of keratin IFs resulting from a fit to $\varepsilon = 0.1 - 0.3$ at constant d_{max} at F_{max} in the HF range (dark red) and constant F_{max} in the HF range (purple).

CHAPTER 8

Direct Interactions Between Cytoskeletal Filaments

In this chapter, we show how interactions between cytoskeletal filaments stabilize the dynamics and mechanics of cytoskeletal filaments. In Section 8.1, we show that vimentin IFs directly interact with microtubules and these interactions stabilize dynamic microtubules. By changing the buffer conditions, we show that electrostatic and hydrophobic effects contribute to these interactions. Theoretical modeling shows how these electrostatic and hydrophobic contributions influence the energy landscape of the interaction. With the same model, we can describe the interactions between two single vimentin IFs and show that electrostatic and hydrophobic effects mechanically stabilize interactions between vimentin IFs (Section 8.2). In cells, IFs occur in networks which raises the question how the interactions between single vimentin IFs studied here translate to the network scale. The study presented in Section 8.2 links the single-filament and network scale.

8.1 Vimentin Intermediate Filaments Stabilize Dynamic Microtubules by Direct Interactions

The following section was published as "Vimentin Intermediate Filaments Stabilize Dynamic Microtubules by Direct Interactions" in *Nature Communications* **12** (3799) by Laura Schaedel*[1], Charlotta Lorenz*[1], Anna V. Schepers[1,2], Stefan Klumpp[2,3], and Sarah Köster[1,2] in 2021 (Creative Commons Attribution 4.0 International License) [157].

[1]Institute for X-Ray Physics, University of Göttingen, Friedrich-Hund-Platz 1, 37077 Göttingen, Germany.
[2]Max Planck School "Matter to Life".
[3]Institute for Dynamics of Complex Systems, University of Göttingen, Friedrich-Hund-Platz 1, 37077 Göttingen, Germany.
*Equal contribution.

Contributions: Sarah Köster conceived and supervised the project. Sarah Köster and Laura Schaedel designed the experiments. Laura Schaedel and Charlotta Lorenz performed all experiments and analyzed the data. Anna V. Schepers helped performing the quadruple optical tweezers experiments. Charlotta Lorenz and Stefan Klumpp designed and performed numerical simulations. All authors contributed to writing the manuscript.

8.1.1 Abstract

The cytoskeleton determines cell mechanics and lies at the heart of important cellular functions. Growing evidence suggests that the manifold tasks of the cytoskeleton rely on the interactions between its filamentous components – actin filaments, intermediate filaments, and microtubules. However, the nature of these interactions and their impact on cytoskeletal dynamics are largely unknown. Here, we show in a reconstituted in vitro system that vimentin intermediate filaments stabilize microtubules against depolymerization and support microtubule rescue. To understand these stabilizing effects, we directly measure the interaction forces between individual microtubules and vimentin IFs. Combined with numerical simulations, our observations provide detailed insight into the physical nature of the interactions and how they affect microtubule dynamics. Thus, we describe an additional, direct mechanism by which cells establish the fundamental cross talk of cytoskeletal components alongside linker proteins. Moreover, we suggest a strategy to estimate the binding energy of tubulin dimers within the microtubule lattice.

8.1.2 Introduction

The cytoskeleton is a dynamic biopolymer scaffold present in all eukaryotic cells. Its manifold tasks depend on the fine-tuned interplay between its three filamentous components: actin filaments, microtubules, and intermediate filaments (IFs) [22, 23, 211–214]. For example, all three types of cytoskeletal polymers participate in cell migration, adhesion, and division [22, 23, 213, 214]. In particular, the interplay of IFs and microtubules makes an important contribution to cytoskeletal cross-talk, although the interaction mechanisms largely remain unclear [26–28, 137, 211, 215–222].

For instance, vimentin, one of the most abundant members of the IF protein family, forms closely associated parallel arrays with microtubules in migrating cells [26, 215, 222]. Depolymerization of the microtubule network leads to a collapse of vimentin IFs to the perinuclear region, further attesting their interdependent organization in cells [27]. Several studies suggest that in cells, microtubules associated with the vimentin IF network are particularly stable: They exhibit increased resistance to drug-induced disassembly [27] and enhanced directional persistence during directed cell migration [26], and they are reinforced against lateral fluctuations [28]. Several proteins such as kinesin [216, 218], dynein [220, 221], plectin [211], and microtubule-actin cross-linking factor (MACF) [217, 219] can mediate interactions between IFs and microtubules. These linker proteins may be involved in conferring microtubule stability to cells. However, the possibility that more fundamental, direct interactions independent of additional components like microtubule-associated proteins may contribute to the stability of microtubules remains unexplored. Such a mechanism could also explain the results of an in vitro study on dynamic microtubules embedded in F-actin networks: Depending on the network architecture, F-actin regulates microtubule dynamics and their lifetime. In particular, unbranched actin filaments seem to prevent microtubule catastrophe, thus stabilizing them, though the exact interaction mechanism is not revealed [122]. In contrast to the cell experiments that showed stabilization of microtubules by IFs, an earlier work found that many IFs, including vimentin, contain tubulin-binding sites and that short peptides containing these binding sites inhibit microtubule polymerization in vitro [137]. Yet, it is unknown how this effect relates to fully assembled vimentin filaments. Indeed, studying such reconstituted in vitro systems provide essential information for the understanding of hybrid biopolymer materials, including their rheological properties and polymerization kinetics.

Here, we studied these interactions by combining in vitro observations of dynamic microtubules in the presence of vimentin IFs with single-filament interaction measurements and complementary numerical simulations. In stark contrast to Ref. [137], our observations and simulations of dynamic microtubules reveal a stabilizing effect by the surrounding vimentin IFs. Based on our experimental data, we also estimated the tubulin dimer binding energy within the microtubule lattice, which is a much sought-after parameter for understanding microtubule dynamic instability [96, 99, 100, 102, 223–226]. This value has previously only been determined by molecular dynamics simulations and kinetic modeling [96, 99, 224] or by using atomic force microscopy to indent stabilized microtubules [100].

8.1.3 Results

Dynamic microtubules in the presence of vimentin. To study the influence of IFs on microtubule dynamics, we polymerized microtubules in the presence of vimentin IFs. We imaged the microtubules by total internal reflection fluorescence (TIRF) microscopy as sketched in Fig. 8.1a. As nucleation sites for dynamic microtubules, we used GMPCPP-stabilized microtubule seeds (green in Fig. 8.1a) adhered to a passivated glass surface. For simultaneous assembly of microtubules (cyan) and IFs (red), we supplemented a combined buffer (CB) containing all ingredients necessary for the assembly of both filament types with 20 or 25 μM tubulin dimers and 2.3 or 3.6 μM vimentin tetramers (0.5 or 0.8 g/L protein). All experiments presented in this work refer to these protein concentrations. All TIRF experiments were carried out in the same buffer conditions. Figure 8.1b shows a typical fluorescence image of mixed microtubules and vimentin IFs.

We analyzed the microtubule dynamics using kymographs obtained from TIRF microscopy as shown in Fig. 8.1c. As expected [45], the microtubule growth rate increased at the higher tubulin concentration (Fig. 8.1d, cyan). Yet, the presence of vimentin IFs did not affect the growth and depolymerization rates: on average, the differences between the medians of the different conditions correspond to <3% and <5% of the data range for the growth and depolymerization rates, respectively (Fig. 8.1d, e). Interestingly, we observed a marked decrease in the catastrophe frequency [86] in the presence of vimentin IFs at both tubulin concentrations (Fig. 8.1f, red and cyan stripes). Moreover, vimentin IFs promote microtubule rescue (Fig. 8.1g). As rescue events are rare at the lower tubulin concentration [86], we only report the rescue data for 25 μM tubulin. When assembly is initiated, vimentin unit-length filaments form after about 100 ms [227]. Therefore, we assume that vimentin filaments, not precursors, interacted with the microtubules. In addition, we did not observe differences in microtubule dynamics when comparing early and late time points within the

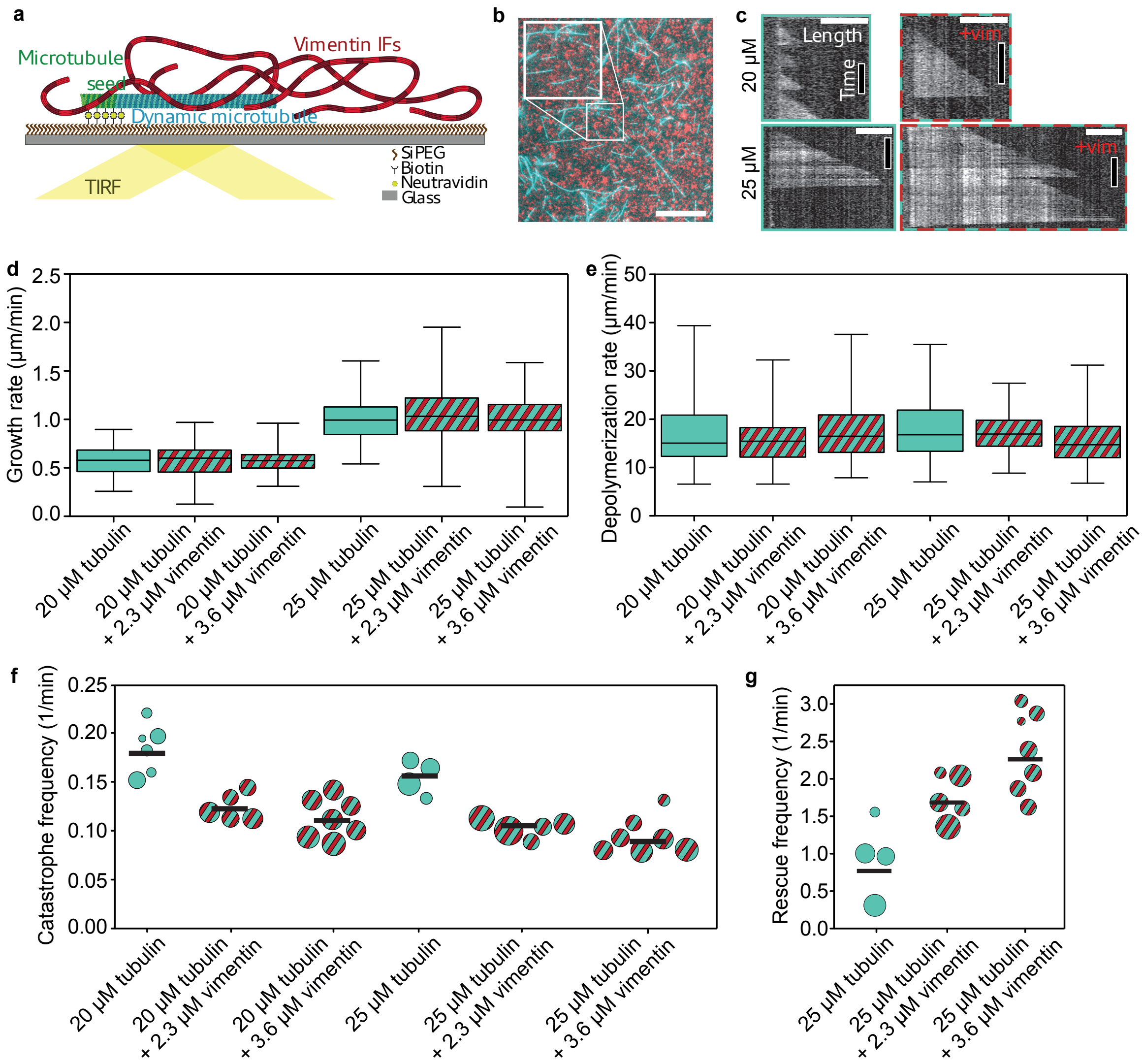

Figure 8.1: Vimentin IFs stabilize dynamic microtubules. (a) Illustration of the experimental setup. We attached microtubule seeds (green) to a biotin-polyethylene glycol-silane (biotin-SiPEG) coated cover glass. Dynamic microtubules (cyan) grew from the seeds. Vimentin IFs (red) formed an entangled, fluctuating network. We imaged microtubules by TIRF microscopy. (b) Fluorescence micrograph of microtubules (cyan) embedded in a vimentin IF network (red). The inset shows the enlarged detail. Scale bar: 10 µm. (c) Example kymographs of microtubules growing at 20 or 25 µM tubulin in the presence (+vim; 2.3 µM) or absence of vimentin. Scale bars: 3 µm and 5 min. (d, e) Vimentin does not affect the microtubule growth and depolymerization rates, irrespective of the tubulin concentration. Cyan boxplots represent experiments with tubulin only; cyan- and red-striped boxplots illustrate experiments with tubulin and vimentin. Boxplots include the median as the center line, the 25th and 75th percentiles as box limits, and the entire data range as whiskers. In (d), for 20 µM tubulin and in the absence of vimentin, the boxplot represents the data from $N = 6$ samples and $n = 106$ growth events (we define a growth event as the new outgrowth of a microtubule from the seed or after a rescue event). For the other boxplots, from left to right, $N = 5, 7, 4, 5$, and 7, respectively, and $n = 163, 282, 113, 160$, and 218, respectively. In (e), from left to right, the boxplots represent the data from $n = 58, 140, 228, 112, 133$, and 165 depolymerization events, respectively. (f) The catastrophe frequency of the microtubules decreases in the presence of vimentin. Each circle represents an experiment including multiple microtubules. The area of the circle scales with the total summed microtubule growth time of the respective experiment. Black bars indicate the weighted mean. From left to right, the plot represents the data from a total of 805, 1469, 2692, 1142, 2203, and 2232 min of growth time, respectively. (g) Vimentin enhances the microtubule rescue frequency. Each circle represents an experiment including multiple microtubules. The area of the circle scales with the total microtubule depolymerization time. From left to right, the plot represents the data from a total of 51, 71, and 52 min depolymerization time, respectively. All tubulin and vimentin concentrations are input concentrations. Source data are provided as a Source Data file.

same experiment, although the mean vimentin filament length increased over the course of the experiments (see Supplementary Fig. 8.7). These results indicate that vimentin IFs stabilize dynamic microtubules by suppressing catastrophe and enhancing rescue, while leaving the growth rate unaffected. A higher vimentin concentration enhances these effects.

Interaction forces between microtubules and vimentin filaments. From these observations, we hypothesize that there are direct, attractive interactions between microtubules and vimentin IFs that stabilize dynamic microtubules. To test this hypothesis, we studied the interactions of single stabilized microtubules and vimentin IFs using optical trapping (OT), a complementary method to our TIRF experiments, as illustrated in Fig. 8.2. We prepared fluorescent and biotin-labeled microtubules and vimentin IFs as sketched in Supplementary Fig. 8.8. We used an OT setup combined with a microfluidic device and a confocal microscope (LUMICKS, Amsterdam, The Netherlands) to attach a microtubule and a vimentin IF to separate bead pairs via biotin-streptavidin bonds as shown in Fig. 8.2a and Supplementary Fig. 4.8a in Chapter 4. Once the IF and microtubule were in contact, we moved the IF back and forth in the y-direction. If the IF and microtubule interacted, eventually either the IF-microtubule interaction broke (Fig. 8.2b) or the IF-microtubule interaction was so strong that the microtubule broke off a bead (Fig. 8.2c). To study the orientation dependence of the interaction, we included two additional measurement geometries: (i) we turned the

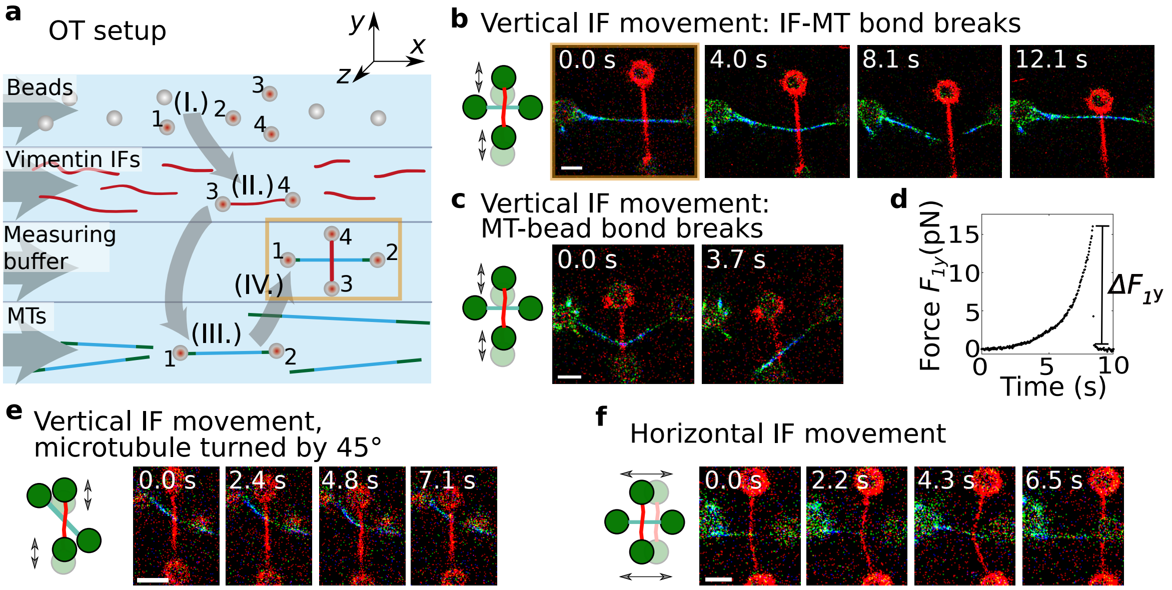

Figure 8.2: Direct interactions between stabilized microtubules and vimentin IFs. (a) Schematic of the setup for the OT experiments for interaction measurements in microfluidic flow channels. Four streptavidin-coated beads were captured by OTs (I.). We used one bead pair (beads 3 and 4) to attach a vimentin IF (II., red), and the other bead pair (beads 1 and 2) to attach a microtubule (III., green-cyan). We brought the IF and the microtubule into contact in a crossed configuration (IV.). Next, we moved the IF perpendicularly to the microtubule to study the IF-microtubule interactions while we took confocal fluorescence images (starting position marked in yellow in (a) and (b)). (b) Typical confocal fluorescence images of an IF-microtubule interaction which broke while the IF was moved vertically and (c) a strong IF-microtubule interaction for which the microtubule broke off the bead. (d) Typical experimental force increase F_{1y} on bead 1 in the y-direction once a bond forms. Breaking of the force causes a force jump of ΔF_{1y}. (e) Typical confocal fluorescence images of a breaking IF-microtubule interaction at a 45° angle between them while the IF was moved vertically. (f) Typical confocal fluorescence images of a breaking IF-microtubule interaction in perpendicular configuration while the IF was moved horizontally. Scale bars: 5 µm. Measurements were conducted on at least three different days. Source data are provided as a Source Data file.

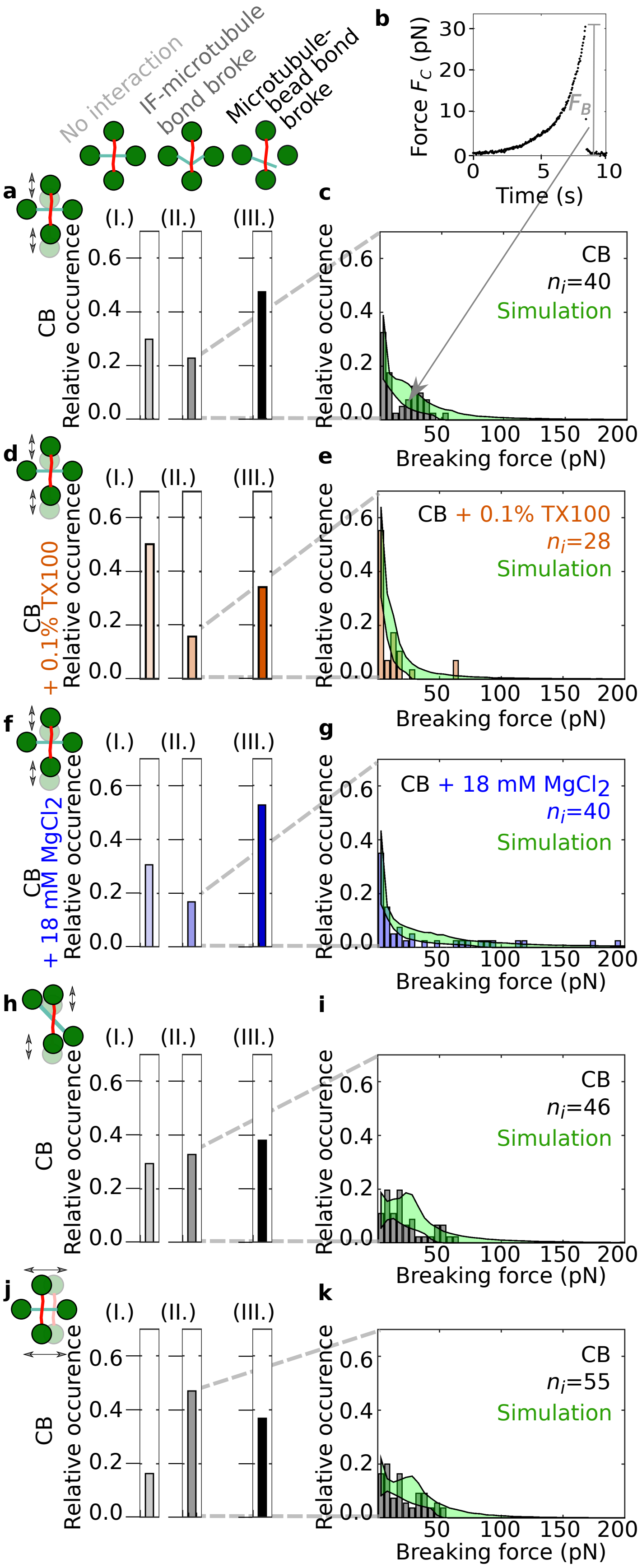
No interaction
IF-microtubule bond broke
Microtubule-bead bond broke
a
(I.)
(II.)
(III.)
CB
Relative occurence
0.6
0.4
0.2
0.0
b
Force F_C (pN)
30
20
10
0
F_B
Time (s)
0
5
10
c
CB
n_i=40
Simulation
Breaking force (pN)
50
100
150
200
d
CB + 0.1% TX100
e
CB + 0.1% TX100
n_i=28
Simulation
f
CB + 18 mM MgCl$_2$
g
CB + 18 mM MgCl$_2$
n_i=40
Simulation
h
i
CB
n_i=46
Simulation
j
k
CB
n_i=55
Simulation

Figure 8.3: Hydrophobicity and electrostatics contribute to the IF-microtubule interactions. (a) We classified the interactions between IF-microtubule pairs into three different groups as shown by the pictograms: no interaction (I.), breaking of the IF-microtubule bond as shown in Fig. 8.2b, e, and f (II.), and breaking of the microtubule-bead bond as shown in Fig. 8.2c (III.). (b) Typical experimental force-time behavior of the IF-microtubule bond showing the total force acting on the IF-microtubule bond, F_C. The plot represents the corrected version of the force data shown in Fig. 8.2d taking into account the geometry of the filament configuration. (c) Histograms of n_i experimentally recorded breaking forces (gray) and simulated data (green) for the measurements in pure CB when the IF-microtubule interaction broke as shown in Fig. 8.2b. Due to statistical fluctuations, the distribution appears to be bimodal; however, it can still be well described with a unimodal distribution. (d) TX100 (orange) suppresses some of the interactions, which results in more IF-microtubule pairs without any interaction (aI. vs. dI.) and fewer instances of IF-microtubule interactions (aII. and III. vs. dII. and III.). (e) The IF-microtubule bonds formed in the presence of TX100 break at lower forces. (f) Magnesium (blue) does not change the relative number of IF-microtubule pairs that do not interact (aI. vs. fI.), but leads to fewer IF- microtubule breaking events (aII. vs. fII.) because the interactions become so strong that the microtubule breaks off the bead more often (aIII. vs. fIII.). (g) The IF-microtubule bonds formed in the presence of additional magnesium break at higher forces. (h) When the microtubule was turned by 45°, IF and microtubule interacted more frequently (hII. vs. aII.). (i) The corresponding distribution of the breaking forces resembles the distribution for the perpendicular geometry (see c). (j, k) The binding rate for a horizontal movement of the IF increases compared to a vertical movement (jII. vs. aII.). (k) The corresponding distribution of breaking forces is similar to the distributions for the other two geometries (see i and c). Source data are provided as a Source Data file.

microtubule by 45° as shown in Fig. 8.2e or (ii) moved the IF horizontally in the x-direction along the microtubule (Fig. 8.2f). We categorized the type of interaction, i.e., no interaction, the IF-microtubule bond broke, or the microtubule broke off the bead, for each filament pair, as shown by pictograms in Fig. 8.3a, top.

With the OTs, we recorded the force F_{1y} or F_{1x} that acted on trap 1 (see Fig. 8.2d and Supplementary Fig. 4.8b in Chapter 4), which increased after the IF bound to the microtubule. Based on the geometry of the filament configuration from the confocal images, we calculated the total force F_C that the IF exerted on the microtubule (see Supplementary Fig. 4.8c in Chapter 4). In Fig. 8.3b we show the resulting force calculated for the data shown in Fig. 8.2d. Combining all experiments with a breaking IF-microtubule bond leads to a distribution of n_i breaking forces F_B as shown in the force histogram in Fig. 8.3c. Due to thermal fluctuations, the force resolution of our system is limited to 1 pN and we thus focused on interaction forces above 1 pN, which is consistent with physiologically occurring intracellular forces. The breaking forces are in the range of 1-65 pN, with higher forces occurring less often. Hence, in agreement with our hypothesis, our experiments show that single microtubules and vimentin IFs directly interact, i.e. without involving any linker proteins, and that these interactions can become so strong that forces up to 65 pN are needed to break the bonds. This range of forces is physiologically relevant and comparable to other microtubule-associated processes: Single microtubules can generate pushing forces of 3-4 pN while forces associated with depolymerization can reach 30-65 pN [228]. Kinesin motors have stalling forces on the order of a few pN [229].

To better understand the nature of the interactions between single microtubules and vimentin IFs, we varied the buffer conditions in which we measured the filament interactions. First, we probed possible hydrophobic contributions to the interactions by adding 0.1% (w/v) Triton-X 100 (TX100), a non-ionic detergent. Rheological studies of IF networks previously suggested that TX100 inhibits hydrophobic interactions [40]. Tubulin dimers have several hydrophobic regions as well [230], some of which are accessible in the assembled state [231].

As shown in Fig. 8.3d and e, the number of interactions decreases and the breaking forces are slightly lower in the presence of TX100 than in pure CB. We calculated the binding rate $r_{b,\text{eff}}$ by dividing the total number of interactions larger than 1 pN by the time for which the two filaments were unbound: TX100 leads to a lower binding rate $r_{b,\text{eff,TX100}} = 0.56 \cdot 10^{-2}\ \text{s}^{-1}$ compared to the binding rate $r_{b,\text{eff},y} = 1.1 \cdot 10^{-2}\ \text{s}^{-1}$ without TX100. We speculate that TX100 interferes with the binding sites on both filament types by occupying hydrophobic residues on the surface of the filaments and thereby inhibits hydrophobic interactions between the biopolymers [40]. Consequently, the reduced number of interactions in the presence of TX100 indicates that hydrophobic effects contribute to the interactions.

Next, we tested for electrostatic contributions to the interactions by adding magnesium chloride to the buffer. When probing interactions in CB buffer with a total concentration of 20 mM magnesium, we observed both an increase in strong interactions, where the IF pulls the microtubule off a bead, and higher breaking forces (Fig. 8.3aIII. vs. fIII. and c vs. g). The binding rate of microtubules and vimentin IFs increases to $r_{b,\text{eff,Mg}} = 1.3 \cdot 10^{-2}\ \text{s}^{-1}$. Generally, charged, suspended biopolymers in the presence of oppositely charged multivalent ions have been shown to attract these ions, leading to counterion condensation along the biopolymers. Consequently, the filaments attract each other through overscreening [232, 233]. Our data are in agreement with this effect. At high magnesium concentrations, bonds are more likely to form and become stronger. Note that for both added magnesium chloride and TX100, the intermediate interactions (II) are decreased compared to the control conditions, due to a higher percentage of strong interactions (III) or weak interactions (I), respectively. Therefore, we conclude that both hydrophobic and electrostatic effects contribute to the direct interactions between microtubules and vimentin IFs.

When we moved the IF across the microtubule at an angle of 45° or horizontally in the direction of the microtubule (see Figs. 8.2e, f, 8.3h-k), we observed an increased binding rate ($r_{b,\text{eff},\,45^\circ} = 1.6 \cdot 10^{-2}\ \text{s}^{-1}$ and $r_{b,\text{eff},x} = 2.4 \cdot 10^{-2}\ \text{s}^{-1}$, respectively). This increase can be explained by an increased encounter rate of potential binding sites due to the different geometries (see Section 4.4.4). Taking into account this geometric factor, we calculated the probability of a microtubule binding to a vimentin IF $p_{\text{IF-MT}}$ for the different geometries and obtained $p_{\text{IF-MT}} \simeq 6.1 \cdot 10^{-4}$ per pair of vimentin unit-length filament and tubulin dimer, independent of the geometry. The breaking forces were found to be similar for the three different geometries (Fig. 8.3c, i and k). To test if vimentin IFs and microtubules co-align due to their interaction, as reported for migrating cells [26], we relaxed the vimentin IF in the optical trap to allow for "zipping" events, or mixed the filaments in solution, but did not observe spontaneous bundling.

Two-state model of the interactions. For a more profound understanding of the physical bond parameters, which are not accessible experimentally, we applied a modeling approach. Due to the experimentally observed independence of the measuring geometry, we applied a one-dimensional transition model. It should be noted, however, that for experimental systems with a geometry dependence, the model would have to be replaced by a more complex model. We modeled the IF-microtubule interaction as a single molecular bond with force-dependent stochastic transitions between the bound and unbound state. The time-dependent force increase $F(t)$ has an entropic stretching contribution [171, 172] for forces below 5 pN and increases linearly for higher forces as observed in the experiment [173, 174]. We assume that the binding (b) and unbinding (u) rates r_b and r_u, respectively, depend on the applied force, an activation energy E_{Ab} or E_{Au}, the thermal energy $k_B T$, and a distance x_b or x_u to the transition state, which is on the order of the distance between the IF and the microtubule at the site of the bond:

$$\begin{aligned} r_b(t) &= r_{b,0} \exp\left(\frac{-E_{Ab}}{k_B T}\right) \cdot \exp\left(\frac{-F(t)x_b}{k_B T}\right), \\ r_u(t) &= r_{u,0} \exp\left(\frac{-E_{Au}}{k_B T}\right) \cdot \exp\left(\frac{F(t)x_u}{k_B T}\right). \end{aligned} \tag{8.1}$$

We summarize the force independent factor in Eq. 8.1 as an effective zero-force rate:

$$r_{b,\text{eff}/u,\text{eff}} = r_{b,0/u,0} \exp\left(\frac{-E_{Ab/Au}}{k_B T}\right). \tag{8.2}$$

In contrast to the force and the effective binding rate $r_{b,\text{eff}}$, neither $r_{u,\text{eff}}$ nor x_b or x_u can be determined from our experimental data. Due to detailed balance, the sum $x_b + x_u$ is constant [153]. Since we only observed a small number of rebinding events under force, we focused on the unbinding processes and studied x_u. Hence, we simulated IF-microtubule interactions

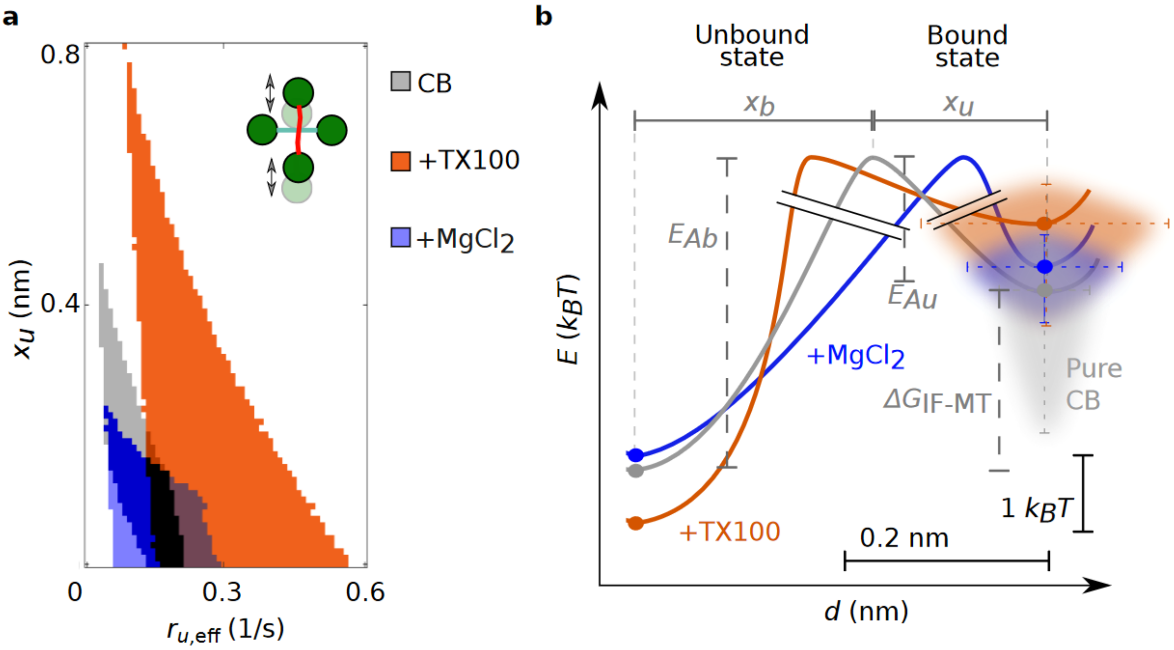

Figure 8.4: Hydrophobic and ionic reagents change the IF-microtubule bond properties. (a) Valid unbinding rates $r_{u,\text{eff}}$ and potential widths x_u to simulate the experimental data shown in Fig. 8.3c, e, and g for the different buffer conditions: pure CB (gray), CB with TX100 (orange), and CB with additional magnesium (blue). $r_{u,\text{eff}}$ and x_u pairs, which are valid for several buffer conditions, are color coded by mixed colors. $r_{u,\text{eff}}$ and x_u increase from additional magnesium chloride across pure CB to added TX100. (b) Energy landscape for the theoretical modeling of the IF-microtubule bond: A two-state model (unbound, bound) is sufficient to describe the experimental data shown in Fig. 8.3. From the binding and unbinding rates, we calculated the differences in activation energies E_{Ab} and E_{Au} (see Eq. 5.8 in the Chapter 5) of bonds in different buffer conditions to open or close. However, the absolute values cannot be determined, as indicated by the graph break (black double-lines). For different buffer conditions, the position of the energy barrier relative to the unbound and bound state, x_b and x_u, respectively, changes. Source data are provided as a Source Data file.

for different sets of $r_{u,\text{eff}}$ and x_u and compared the resulting distributions of breaking forces to our experimental data. We accepted the tested parameter sets if the distributions passed the Kolmogorov-Smirnov test with a significance level of 5%. The minimum and maximum of all accepted simulation results, shown as the borders of the green areas in Fig. 8.3c, e, g, i, and k, agree well with the experiments. Figure 8.4a shows all accepted parameter pairs $r_{u,\text{eff}}$ and x_u for the different buffer conditions (color code: gray (pure CB), orange (CB with TX100), blue (CB with additional magnesium); corresponding mixed colors for regions, where valid parameters overlap). Both parameters increase from additional magnesium (blue) across no addition (gray) to added TX100 (orange). A corresponding diagram for comparison of the different measuring geometries is shown in Supplementary Fig. 8.9. Whereas the force-free factor of the unbinding rate does not depend on the geometric configuration, the force-dependent factor is slightly more sensitive to force for a horizontal movement of the IF or a vertical movement of the IF, with the microtubule turned by 45° than for a vertical movement of the IF perpendicular to the microtubule. To understand these data more intuitively, we calculated the energy diagrams, as plotted in Fig. 8.4b, using Eq. 5.8 (see Section 5.2.2) considering the same buffer condition in unbound and bound (1 and 2) state or different buffer conditions (1 and 2) and the same state.

Surprisingly, both TX100 and additional magnesium only mildly affect the activation energies. Yet, for TX100 we observed a marked increase in distance to the transition state, x_u (compare Fig. 8.4b orange to gray), which we interpret as a"looser binding" between the IF and the microtubule. Thus, the force-dependent term in Eq. 8.1 becomes more pronounced. TX100 can interact with hydrophobic residues and causes the filaments to stay further apart. Thus, the bond breaks at lower forces. Consequently, this further confirms that there is a hydrophobic contribution to the interactions in CB.

In contrast to TX100, magnesium strengthens the bond and keeps it closed even at higher forces as it is a divalent counterion between two negative charges. It lowers the distance to the transition state (compare Fig. 8.4b blue to gray) and the influence of the force-dependent term in Eq. 8.1. Hence, the opening of the bond depends less on the applied force compared to bonds in pure CB. Since CB already includes 2 mM magnesium, we assume that there is an electrostatic contribution to the interactions observed in CB as well.

We have shown that there are hydrophobic and electrostatic contributions to the interactions between IFs and microtubules and we have derived key parameters of these interactions by combining experiments with theoretical modeling. While we cannot exclude a steric contribution to the interaction, e.g., by the Gaussian cloud formed on the surface of the filament core by the intrinsically disordered tail domains of the protein, our measurements show that they are influenced by electrostatic and hydrophobic effects. We thus conclude that the interactions are modulated by electrostatics and hydrophobicity and are directionally independent (see Supplementary Fig. 8.10). Furthermore, IFs assembled via dialysis are rather smooth [31], so that it is unlikely that their roughness causes interactions.

Monte-Carlo simulations of dynamic microtubules. To better understand how these interactions lead to the observed changes in microtubule dynamics, we again applied a modeling approach. We considered a microtubule as a dynamic lattice with GTP (guanosine triphosphate) and GPD (guanosine diphosphate) dimers [96, 102] as sketched in Fig. 8.5a.

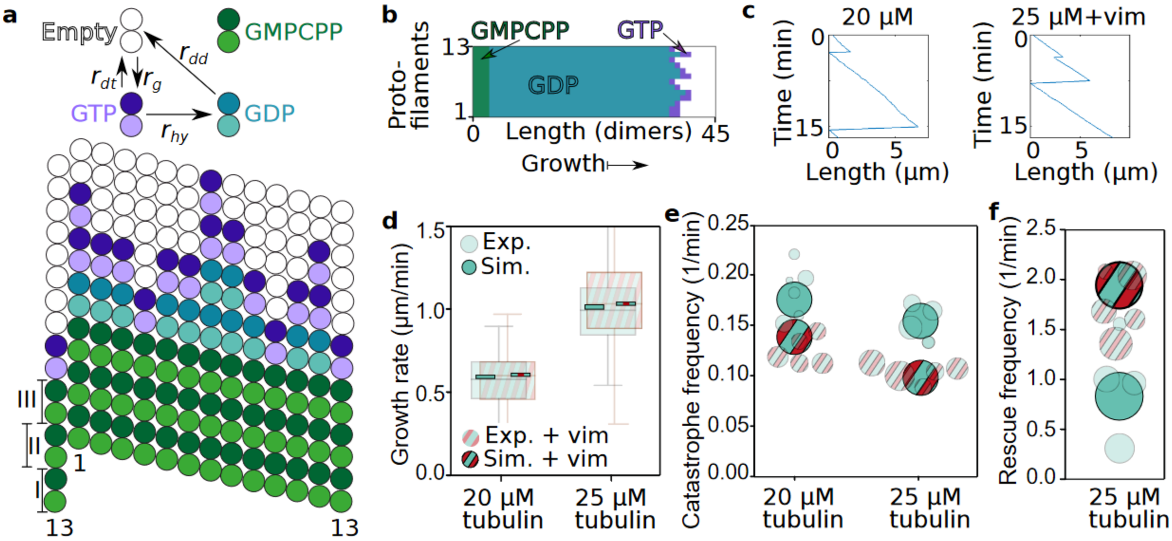

Figure 8.5: A Monte-Carlo simulation shows that transiently binding IFs stabilize dynamic microtubules. (a) Illustration of the reaction rates (top) and simulated microtubule lattice with 13 protofilaments and a seam with a longitudinal displacement of 1.5 dimers (bottom). (b) Typical simulated microtubule growing from a GMPCPP (guanylyl-(α,β)-methylene-diphosphonate) seed with dimers either in the GTP (purple) or in the GDP state (cyan). (c) Typical length-time plot (kymograph) of a simulated microtubule in 20 µM free tubulin solution without vimentin tetramers (left) or in 25 µM free tubulin solution with 2.3 µM vimentin tetramers (right). (d–f) We reproduced the experimental data shown in Fig. 8.1d–g (shown here in a semi-transparent fashion, for a vimentin concentration of 2.3 µM) with our Monte-Carlo simulation (opaque). (d) Addition of vimentin neither changes the experimental nor the simulated microtubule growth rates at 20 or 25 µM. Boxplots include the median as the center line, the 25th and 75th percentiles as box limits, and the entire data range as whiskers. For clarity, the entire data range of the experimental data is not shown here, but is presented in Fig. 8.1. (e) Addition of vimentin lowers the catastrophe frequency of dynamic microtubules for both tubulin concentrations studied here. (f) In case of 25 µM free tubulin, the rescue rate increases due to the stabilizing effect of the surrounding vimentin IFs. The circle areas scale with the total microtubule depolymerization time as in the representation of the experimental data. All tubulin and vimentin concentrations are input concentrations. Source data are provided as a Source Data file.

The lattice consists of 13 protofilaments and has a seam between the first and thirteenth protofilaments. We describe the microtubule dynamics by three reactions: (i) a GTP dimer associates with a rate r_g, (ii) a GTP dimer is hydrolyzed with a rate r_{hy}, or (iii) a GDP or GTP dimer dissociates with a rate r_{dd} or r_{dt}, respectively, depending on the number of neighboring dimers (see Eq. 5.12 in Chapter 5). A snapshot of the simulated microtubule during growth is shown in Fig. 8.5b. With a Monte-Carlo simulation, we obtained typical simulated kymographs (Fig. 8.5c). As for the experiments (semi-transparent data in Fig. 8.5d–f), we determined the growth rate, the catastrophe and the rescue frequency from the simulations (opaque in Fig. 8.5d–f).

To simulate microtubules in the presence of vimentin IFs, we included stochastic binding and unbinding of IFs to the microtubule lattice into the model. The unbinding rate is directly given by the results of the OT experiments. Assuming that binding is diffusion-limited, we calculated the corresponding rate from the OT results using the Smoluchowsky expression (see Section 5.3.2 for a detailed description of the model). Based on these rates, we calculated the IF-microtubule binding energy (see Eq. 5.9 in Chapter 5) to be $\Delta G_{\text{IF-MT}} = 2.3\, k_B T$ as sketched in Fig. 8.4b. Thus, IF binding stabilizes the binding of tubulin dimers in the microtubule lattice by 2.3 $k_B T$. The additional binding energy can be interpreted as a direct

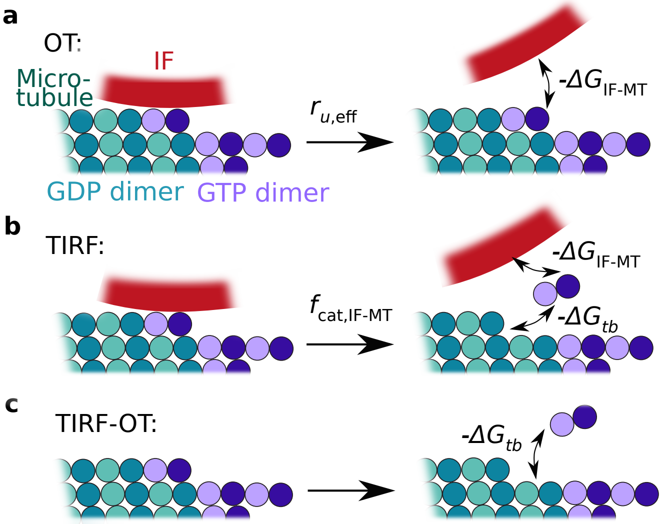

Figure 8.6: Estimation of the binding energy of a single tubulin dimer by combining the OT and TIRF experiments. (a) From the OT experiments including the simulations, we determined the unbinding rate of microtubules and vimentin IFs $r_{u,\text{eff}}$ and the released energy $-\Delta G_{\text{IF-MT}}$ during unbinding. (b) In TIRF experiments, a tubulin dimer dissociates from the microtubule and the vimentin IF, so that the total energy $-\Delta G_{tb} - \Delta G_{\text{IF-MT}}$ is released. We calculated the catastrophe frequency of a microtubule $f_{\text{cat,IF-MT}}$ in case a vimentin IF is bound to the microtubule. (c) We estimated the average binding energy ΔG_{tb} of a tubulin dimer in the microtubule lattice before catastrophe by subtracting the released energies from (b), $(-\Delta G_{tb} - \Delta G_{\text{IF-MT}})$, and by dividing the unbinding rate $r_{u,\text{eff}}$ of microtubules and vimentin IFs by the catastrophe frequency $f_{\text{cat,IF-MT}}$ of microtubules bound to a vimentin IF as shown by Eq. 5.15 in Chapter 5.

increase of the total binding energy of the respective tubulin dimer or as an increased longitudinal binding energy to the next tubulin dimer. Our experiments do not resolve the precise molecular interaction mechanism, such as cross-linking of neighboring tubulin dimers or structural changes in the tubulin dimers upon binding of a vimentin IF. Likewise, we cannot distinguish whether the vimentin IF is bound to a single tubulin dimer or to multiple dimers. However, our coarse description approach includes all these different scenarios. Specifically, in case of a bond involving multiple dimers, unbinding from these dimers must be cooperative since we do not observe step-wise unbinding in OT experiments. Such cooperativity does not change the total energy required for unbinding. In agreement with our experimental data, the transient binding of IFs leaves the growth rate unaffected. Intriguingly, we observed that IF binding to tubulin dimers in the lattice reduces the catastrophe frequency. The increased binding energy of a dimer also raises the rescue frequency. These results are in striking agreement with our observation in TIRF experiments, while the only additional input to the simulation that includes the surrounding vimentin IFs are the parameters from OT experiments. Thus, stochastic, transient binding of IFs to microtubules as in the OT experiments is sufficient to explain the observed changes in microtubule dynamics in the presence of IFs.

By combining the results from OT and TIRF experiments, we estimated the total binding energy of a tubulin dimer within the lattice at the microtubule tip before catastrophe. From the IF-microtubule bond-breaking events in the OT experiments, including the corresponding simulations, we calculated the IF- microtubule bond energy $\Delta G_{\text{IF-MT}} = 2.3\ k_B T$ and the unbinding rate $r_{u,\text{eff}}$ of microtubules and vimentin IFs (Fig. 8.6a). From the TIRF experiments, we determined the catastrophe frequency $f_{\text{cat,IF-MT}}$ of a microtubule bound to a vimentin IF. At the beginning of the catastrophe, a vimentin IF unbinds from the tubulin dimer, so that the energy $\Delta G_{\text{IF-MT}}$ is released. Simultaneously, the dimer depolymerizes from the lattice and the energy ΔG_{tb} is set free (Fig. 8.6b). The only additional energy released during microtubule catastrophe in the TIRF experiments compared to the OT experiments is the binding energy to the surrounding tubulin dimers (Fig. 8.6c). Thus, comparing the rates of IF-microtubule unbinding and microtubule catastrophe during binding to a vimentin IF, as given by Eq. 5.15 in Chapter 5, results in an estimation of the average tubulin-binding energy ΔG_{tb} between 5.7 $k_B T$ and 7.2 $k_B T$ in the lattice at the tip. These values for ΔG_{tb} are on the order of magnitude expected from interferometric scattering microscopy and from computational studies, although slightly lower, possibly due to different buffer conditions [96, 99, 101]. Our combination of experiments provides a way of determining such binding energies and may, from a broader perspective, be generally applied to proteins that bind to microtubules.

8.1.4 Discussion

Our study examined the interactions between microtubules and vimentin IFs. We showed that vimentin IFs stabilize microtubules by direct interactions, which is in strong contrast to previous findings [137], where only interactions between microtubules and short IF peptides were considered. Whereas the microtubule growth rate remains unchanged, the stabilization by vimentin IFs leads to a reduction in the catastrophe frequency and increased rescue of depolymerizing microtubules. We pinpoint the source of this stabilizing effect to a stochastic, transient binding of IFs to microtubules by directly measuring the interactions of single filaments. Both hydrophobic and electrostatic effects are involved in bond formation. The presence of cations likely contributes to the attractive interactions between the negatively charged filaments. The buffer in which we conducted the measurements contained potassium and magnesium, two of the most abundant cations in cells [234]. The free magnesium concentration is on the order of a few mM in most mammalian cells [235], similar to our experiments. Magnesium ions have been previously described to cross-link vimentin IFs [112, 117, 189, 199, 236], and we showed that they can modulate the IF-microtubule bond strength. Since our magnesium concentrations were close to physiological values, the magnesium-induced IF-microtubule binding we observed may occur in cells as well. Therefore, although molecular motors and cross-linkers contribute to establishing links between IFs and microtubules in cells, our results indicate that more fundamental, direct attractive interactions may also participate in the crosstalk of the two cytoskeletal subsystems in cells.

Gan et al. [26] reported the stabilization of the microtubule network by their co-aligning with vimentin IFs in migrating cells. Complementary to this finding, we showed microtubule stabilization by transient interactions with IFs at the single-filament level without coalignment or bundling of the two filament types. In particular, we found that vimentin IFs and microtubules do not spontaneously coalign. Indeed, according to our estimate based on the measured probability of a vimentin ULF to bind to a tubulin dimer and the number of binding sites per vimentin persistence length, such bundling is highly unlikely (see Section 5.2.1 in Chapter 5): Co-alignment requires interactions at more than one site within one persistence length of a vimentin filament to occur, since thermal fluctuations set the relevant length scale for tight contact between the filaments. This indicates that the cell has to activate additional interaction mechanisms, e.g., via proteins, to induce the coalignment in migrating cells. The rapid, but unfrequent binding of IFs and microtubules we observed suggests that only certain microtubules and IF subunits can bind. Thus, we hypothesize that controlling which subunits can bind (e.g., by posttranslational modifications) may provide another path for the cell to regulate the stabilization of microtubules by IFs. Moreover, our results suggest the possibility that the local vimentin filament concentration, itself controlled by transport of filament fragments along microtubules, [237] may locally tune the dynamic instability of microtubules.

There is growing evidence that a mechanical coupling between the cytoskeletal subsystems is necessary for many cellular functions such as polarization, migration, and mechanical resistance [212, 238, 239]. In particular, vimentin-deficient cells exhibit a less robust microtubule network orientation [26] and stronger microtubule fluctuations [28], and they show impaired migration, contractility, and resistance to mechanical stress [182, 240, 241]. Therefore, future research might help to explore the implications of our findings for cell mechanics and function. Furthermore, our study fosters understanding of the emergent material properties of hybrid networks composed of cytoskeletal filaments and provides a basis for interpreting rheology data, including the dynamic properties of the filaments. Moreover, current efforts in synthetic cell research and materials science may benefit from our findings. Our combination of experiments also offers an alternative approach to estimate the tubulin bond energy within the microtubule lattice, which is a vital parameter to understand microtubule dynamics, mechanics, and function [96, 99, 100, 102, 223–226].

8.1.5 Supplementary Figures

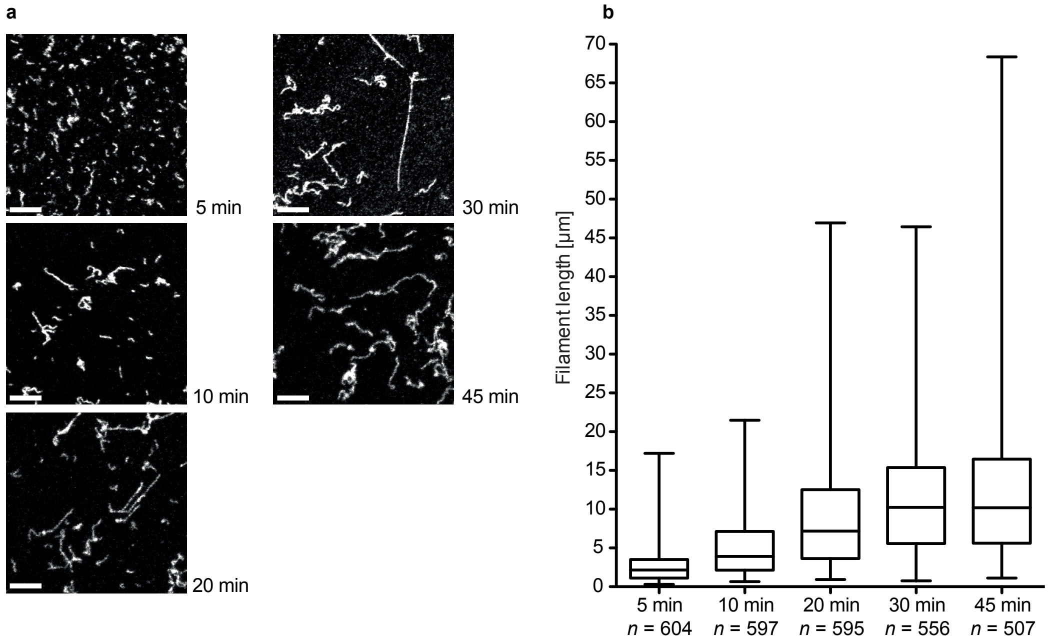

Figure 8.7: Temporal evolution of vimentin filament length in CB at a concentration of 2.3 µM. (a) Typical epifluorescence microscopy images at different time points after start of assembly by CB buffer addition. Scale bars correspond to 5 µm. We started the TIRF measurements 5-10 mins after initiation of the assembly and they ran for 30 to 45 mins. (b) Traced filament lengths at different time points after starting the assembly. *n* is the number of filaments traced. Boxplots include the median as the center line, the 25th and 75th percentiles as box limits and the entire data range as whiskers. For each time point, filament lengths were measured for three different samples. Source data are provided as a Source Data file.

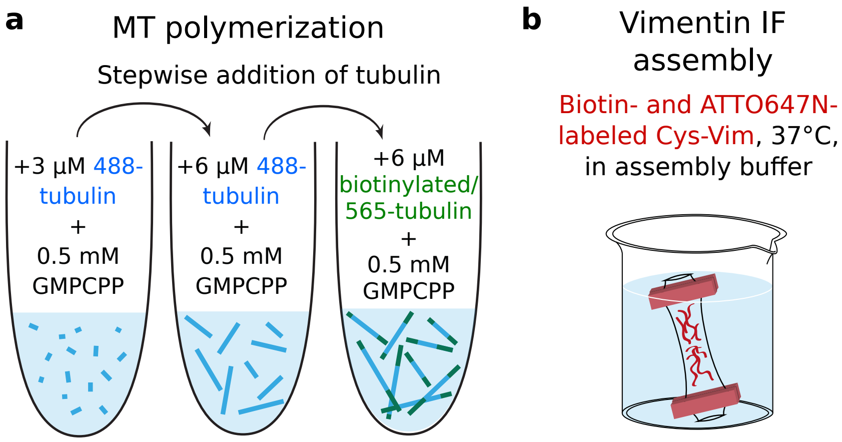
a
MT polymerization
Stepwise addition of tubulin
+3 µM 488-tubulin
+
0.5 mM GMPCPP
+6 µM 488-tubulin
+
0.5 mM GMPCPP
+6 µM biotinylated/565-tubulin
+
0.5 mM GMPCPP
b
Vimentin IF assembly
Biotin- and ATTO647N-labeled Cys-Vim, 37°C, in assembly buffer

Figure 8.8: (a) Schematic of microtubule (MT) preparation. GMPCPP stabilized microtubules were prepared by first growing the central, biotin-free part through stepwise addition of ATTO488 labeled tubulin (blue). Biotinylated ends were added by stepwise addition of ATTO565 labeled and biotinylated tubulin (green). (b) Schematic of IF preparation. Biotinylated and ATTO647N labeled vimentin protein was assembled into filaments overnight via dialysis into assembly buffer.

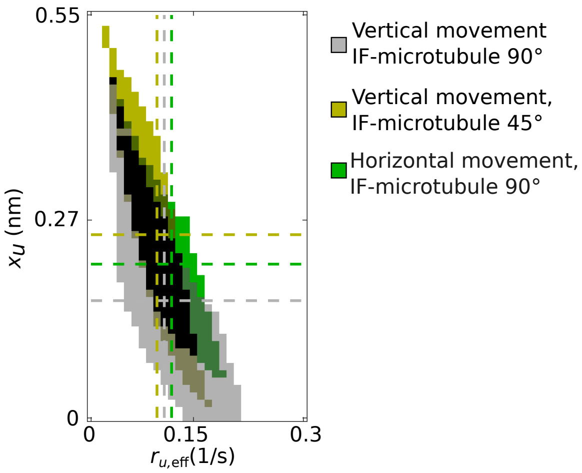

Figure 8.9: Valid unbinding rates $r_{u,\mathrm{eff}}$ and potential widths x_u to simulate the experimental data shown in Fig. 8.3c, i and k for the different geometric configurations of the OT experiment (all in pure CB): vertical movement of the IF perpendicular to the microtubule (gray), vertical movement of the IF with the microtubule turned by 45° (yellow), and horizontal movement of the IF perpendicular to the microtubule (green). $r_{u,\mathrm{eff}}$ and x_u pairs, which are valid for several geometric configurations, are color coded by mixed colors. The centroid positions of the areas are projected on the $r_{u,\mathrm{eff}}$ and x_u axes shown by dashed lines in the corresponding colors. These are the mean values for $r_{u,\mathrm{eff}}$ and x_u we used for further calculations. The force-independent factor $r_{u,\mathrm{eff}}$ in the unbinding rate of the IF-microtubule bond is independent of the measuring geometry. The potential width x_u enters the force-dependent factor of the unbinding rate and, thus, the force-sensitivity of the bond slightly increases from a vertical movement of the IF to a horizontal movement or a vertical movement with the microtubule turned by 45°. Source data are provided as a Source Data file.

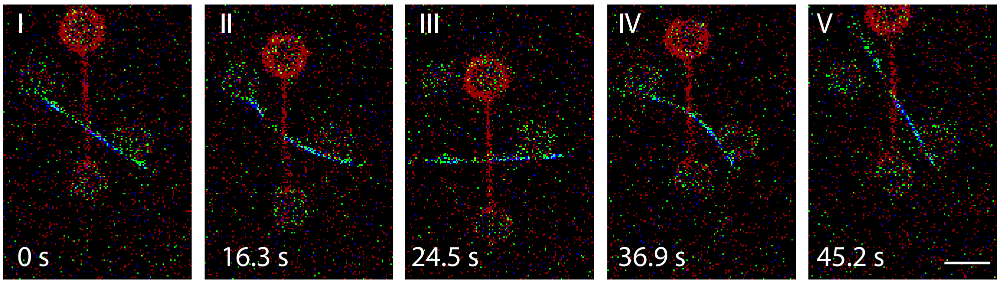

Figure 8.10: A strong IF-microtubule interaction that persisted for the downwards and upwards pulling directions. The IF was first moved downwards (I-II) until the microtubule broke off the left-hand-side bead (III). When the IF was moved upwards, the microtubule re-attached to the left-hand-side bead (IV) and then broke off again (V), showing that the IF-microtubule interaction persisted even when pulling in different directions. Scale bar 5 µm. Measurements were conducted on at least three different days. Source data are provided as a Source Data file.

8.2 Multiscale Mechanics and Temporal Evolution of Vimentin Intermediate Filament Networks

As shown in the previous Section 8.1 interactions between cytoskeletal filaments can stabilize dynamic microtubules. In the following section, we show that interactions between cytoskeletal filaments can also mechanically stabilize cytoskeletal filaments and their networks. The theoretical model of interacting cytoskeletal filaments described in Section 8.1 can also be applied to the interactions between single vimentin IFs to decouple electrostatic and hydrophobic contributions to the interactions. This application of the model is part of the publication "Multiscale mechanics and temporal evolution of vimentin intermediate filament networks" in *Proc. Natl. Acad. Sci. USA* **118** by Anna V. Schepers, Charlotta Lorenz, Peter Nietmann, Andreas Janshoff, Stefan Klumpp, and Sarah Köster in 2021 [242]. In the following section, I summarize the results of this study with focus on the application of the theoretical model. Text and figures are adapted from Ref. [242].

Contributions: S.Kö. conceived and supervised the project. A.V.S. performed and analyzed the single filament mechanics, elongation, and interaction experiments. P.N. performed and analyzed active microrheology measurements. A.V.S. performed microparticle tracking measurements and P.N. and A.V.S. analyzed microparticle tracking experiments. C.L. and S.Kl. designed and C.L. performed numerical simulations. All authors contributed to writing the manuscript.

To understand how interactions between single IFs translate to the IF network scale, we first focus on the mechanical properties of vimentin IF networks: We carry out microrheology experiments of vimentin networks with 5 mM $MgCl_2$ or TX100, we find that networks mature on time scales of days. 5 mM $MgCl_2$ networks become the stiffer than the control network and TX100 networks are the softest throughout. This is in agreement with the established hypothesis that divalent ions serve as transient cross-linkers in IF networks [37, 113, 243]. The binding and unbinding rates of these transient cross-links, however, cannot be inferred from our measurements.

After investigating filament elongation and single-filament mechanics, in a third step,

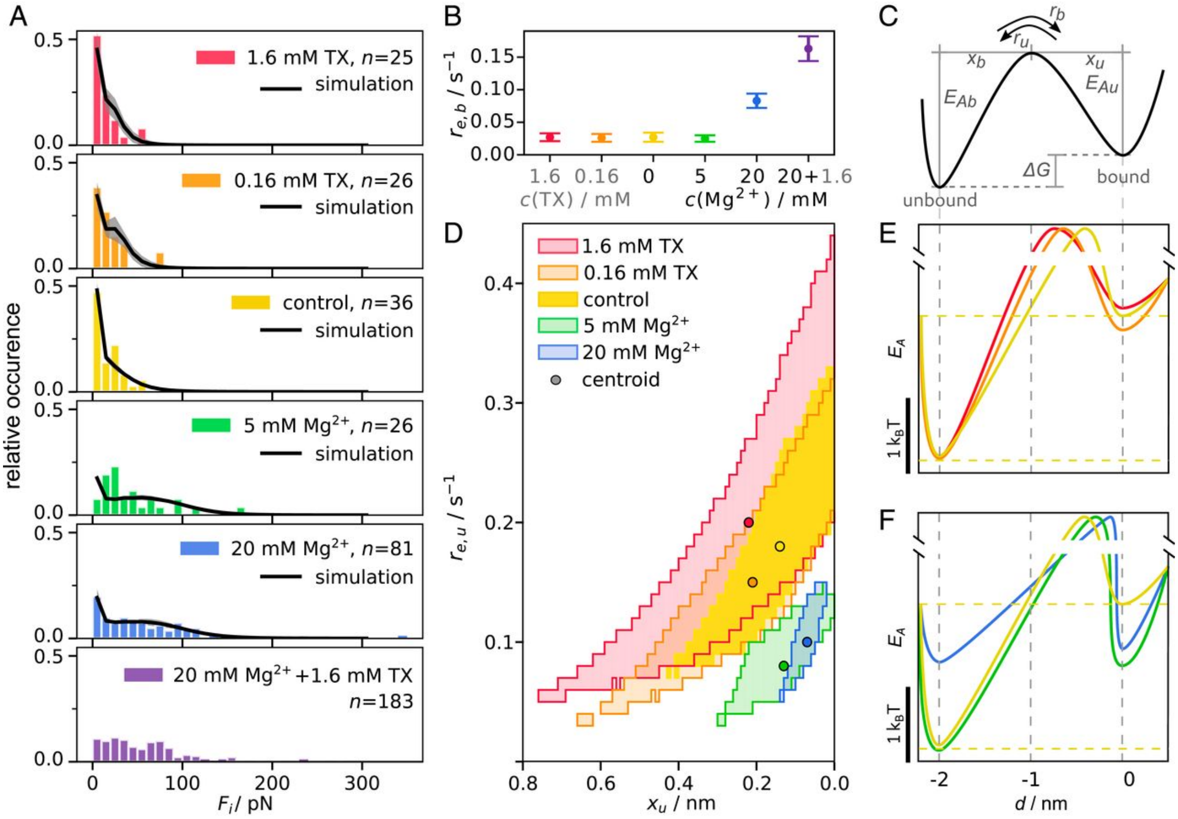

Figure 8.11: Results of the interaction experiments and simulation. (A) Histograms of the rupture forces from experiments (colored bars) and mean curve of the simulation results (black) with standard deviation (shaded area). With decreasing TX100 concentration (red, orange, and yellow), higher forces are reached. The addition of Mg^{2+} (green, blue, and purple) causes a broadening of the force distribution and a shift toward higher forces. (B) Force-independent binding rate re,b. The binding rate is constant, unless Mg^{2+} is present at a concentration of 20 mM. The mean and standard deviation are determined from bootstrap resampling of all single measurements. (C) Schematic of the two-state model used for the simulations. (D) Parameter pairs of x_u and the force-independent unbinding rate $r_{e,u}$, extracted from the simulation, that satisfy the 5% significance level in the Kolmogorov-Smirnov test. The centroid of each parameter space is marked. (E and F) Energy landscapes corresponding to the centroid of the parameter space. The relative E_A values are shown. The ordinate axis is interrupted to indicate the unknown absolute height of the transition state. Figure from [242].

we scrutinize filament–filament interactions with single-molecule precision. To this end, we bring two filaments in contact in a perpendicular configuration using a quadruple optical trap setup. We slide one filament perpendicularly along the other one and measure the interaction force and time. We extract the duration of the interaction and the strength of the interaction from the maximum interaction force, F_i, before the interaction ruptures.

The distribution of forces F_i shown in Fig. 8.11A at both TX100 concentrations (red, 1.6 mM; orange, 0.16 mM) are similar to the control condition (yellow). By contrast, the interaction strength clearly increases for increasing $c(MgCl_2)$ (green and blue in Fig. 8.11A). This observation is in agreement with the stiffening of vimentin networks in the presence of 5 mM $MgCl_2$ at sufficiently long network-formation times. While interactions are stronger at low c(MgCl2) = 5 mM than for the control condition (Fig. 8.11A), the force-independent binding rate $r_{e,b}$ is not increased (Fig. 8.11B), indicating that interactions occur with the same probability. By contrast, at high c(MgCl2), interactions become more likely.

For a quantitative comparison of the bonds formed in each condition, we model the interaction as a single bond as described in the previous Section 8.1. We calculate the distribution of F_i for a constant x_c, the $r_{e,b}$ derived from the experiment (Fig. 8.11B), and for pairs of x_u and $r_{e,u}$, by simulating 1000 $F(t)$ curves. Comparison of the experimental distribution and each simulated distribution based on the Kolmogorov-Smirnov test [177] with a 5% acceptance threshold provides valid x_u and $r_{e,u}$ pairs. The means and standard deviations of the resulting distributions are shown in Fig. 8.11A. All parameter pairs for which the two-state model describes the experiment well are plotted as pixels in Fig. 8.11D. The parameter spaces derived for the control and TX100 conditions overlap. The representative energy landscapes calculated for the centroid of each respective parameter space (circles in Fig. 8.11D; $r_{e,u}(\text{control}) = 0.18\ \text{s}^{-1}$, $r_{e,u}(0.16\ \text{mM TX100}) = 0.15\ \text{s}^{-1}$, $r_{e,u}(1.6\ \text{mM TX100}) = 0.20\ \text{s}^{-1}$), shown in Fig. 8.11E, show no distinct differences. In the presence of $MgCl_2$, $r_{e,u}$ decreases compared to the control ($r_{e,u}(5\ \text{mM MgCl2}) = 0.08\ \text{s}^{-1}$, $r_{e,u}(20\ \text{mM MgCl2}) = 0.10\ \text{s}^{-1}$), which becomes apparent in a larger $E_{A,u}$ in Fig. 8.11F. These results are similar to values determined from rheometry on F-actin networks ($0.43 \pm 0.06\ \text{s}^{-1}$ [244]), but significantly larger than reported for vimentin networks ($> 0.001\ \text{s}^{-1}$ [113]), which is likely caused by surface effects in the macrorheology experiments.

The distance of the transition state to the bound state, x_u, enters r_u in the factor that describes the force-dependent unbinding. Therefore, the decrease of both x_u and $r_{e,u}$ in the presence of $MgCl_2$ leads to a mostly force-independent opening of the bond and thereby to high interaction forces. The presence of TX100 has the opposite effect: The parameter space reaches larger values of x_u, indicating a more force-sensitive bond between the filaments. The broader distribution of the parameters represented by the shaded areas in Fig. 8.11D for the control condition and in the presence of TX100 are mostly due to the lower number of interactions.

These results support the hypothesis that the filaments interact in all conditions, the resulting networks are not purely entangled, but are connected by transient cross-links. However, in the control condition and in the presence of TX100, the binding rate between filaments is low, and interactions are weak; thus, entanglements govern the network properties. In the presence of $MgCl_2$, however, the unbinding rate is low, leading to stronger interactions, which, in turn, cause a more cross-linked network. As a low $c(MgCl_2)$ mostly affects the unbinding rate and not x_u, $E_{A,u}$ can be increased without necessarily decreasing $E_{A,b}$.

We identify altered individual interactions between filaments as the cause of the network stiffening, where Mg^{2+}-mediated, electrostatic effects play a key role and, consequently, promote bundling. An increased interaction strength, caused by a less force-dependent unbinding, causes the stiffening of the networks that was reported in literature [112, 113, 243, 245]. We find that hydrophobic interactions only play a minor role for filament interactions.

Our quantitative approach allows us to disentangle the intricate viscoelastic properties of IFs from their environment in cells – for example, by contributions from other filament types, crowding, or the plasma membrane. Our results can, furthermore, be applied to the study of biopolymer networks, their rheology, and polymerization kinetics, as well as protein-based materials science and synthetic cell research.

CHAPTER 9

Discussion, Outlook and Conclusion

9.1 Discussion and Outlook

The cytoskeletal filaments (actin filaments, microtubules and IFs) with their highly different dynamic and mechanical properties offer a tool kit for cells to tune their mechanics [21]. The different molecular architectures of these filaments determine the interactions within the filaments resulting in their specific filament properties. Interactions between the filaments can further influence filament dynamics and mechanics. Thus, interactions within and between cytoskeletal filaments are vital parameters which regulate cell mechanics. In this thesis, we quantify and characterize these interactions by studying µm-long filaments with optical tweezers. We connect this mesoscopic filament scale with the molecular scale of the interactions via theoretical models. With these models, we disentangle the contributions of single, known components from their unknown interactions to filament dynamics and mechanics.

Focusing on interactions within IFs, we find three different options in which cells may tune these interactions and thereby filament mechanics. These three options occur on different temporal and spatial scales and do not change the secondary structure of the underlying IF monomer: (1) Expression of different IF proteins affects the entire cell and happens on time scales longer than the other two possibilities; (2) local adaptions are possible by changing the ionic strength of the solution around the filament or the charges of single amino acids within a filament by a change in pH; (3) fast and local changes can be induced by post-translational modifications of IFs.

Option (1) is responsible for the fundamental difference in interactions between the subunits, since the amino acid sequences of different IF proteins differ. We show that these differences in amino acid sequence cause weaker lateral interactions between the subunits within keratin 8/18 IFs in comparison to vimentin IFs (Chapter 6.1). These weaker interactions within keratin IFs result in subunit sliding, a smaller elastic modulus than for vimentin IFs and permanent filament elongation upon repeated loading (Chapter 7). Contrarily, subunits within vimentin IFs do not slide and vimentin IFs retain their length [7, 63]. Thus, here, we prove that subunit sliding occurs and quantify its effects on keratin IF mechanics. Previously, subunit sliding was only suspected because filaments extended further than possible by a sole opening of α helices [12, 35, 64].

We attribute the ability of keratin subunits to slide to the missing compaction step in keratin IFs [38]. Compaction is associated with a region between coil 1A and the beginning of coil 2 and a certain charge pattern in this region [61, 198]. Keratin exhibits a charge pattern in these regions that does not induce compaction [49]. The IF monomer structure is the same for all IFs, thus, the mechanics of different IF types may be significantly determined by the resulting electrostatic interactions in the compaction region. To test the hypothesis whether compaction causes a strong coupling of subunits and therefore stiffer filaments, it might be interesting to study other IF types which compact, such as desmin [10]. Studying the mechanical behavior of IFs which probably do not compact such as other keratin pairs as K5/14 can be a vital comparison.

There are two strategies to determine precisely how these electrostatic interactions influence the arrangement of subunits within IFs: Theoretical modeling and simulations and further, structural, experimental analysis. Here, we mainly refer to a theoretical model representing the architecture of vimentin IFs explaining the tensile memory and energy dissipation of repeatedly stretched vimentin IFs [7]. We supplement this model with interactions between the subunits to explain the effects of different interactions within IFs. Our model allows us to estimate the binding energy per amino acid in an α helix to around $0.3 - 0.6\ k_B T$ per amino acid which is of the order of magnitude expected from literature [193–195]. With our model, we can explain the different mechanical behaviors of keratin and vimentin IFs and, additionally, the changes in vimentin IF mechanics in buffers with a different ionic strength and different pH (Section 6.3). A further extension of the model including lateral bonds between the subunits in form of springs describes the softening of phosphorylated vimentin IFs (Section 6.4). Since we can activate and deactivate the interactions in the simulations, we can precisely decouple which mechanical properties result from the single components within the filament and which stem from the interactions. In all cases, these electrostatic interactions cause the filaments to act differently than the mere sum of their monomers: The interactions between the monomers stiffen and stabilize the filaments.

Concerning further experimental evidence of the effects of interactions within IFs, it might be interesting to directly observe whether and how many α helices open within keratin and vimentin IFs. Infra-red spectroscopy might be considered to study the portion of intact and unfolded α helices of stretched IFs [246]. In case of keratin IFs, we expect that the α helices remain intact because subunits slide and protect α helices from unfolding. The sliding of subunits can be visualized by repeatedly stretching a sparsely labeled filament and observing whether labeled subunits return to their original position. Sliding subunits might also result in a different bending stiffness since lateral contacts bonds might be broken, but also reformed due to the sliding. Thus, observing thermal fluctuations of a relaxed, but previously stretched filament might reveal more information about how strongly the lateral contacts were rearranged. The rearrangement of lateral contacts likely impacts the persistence lengths of IFs, so that such a study might also shed light on why different measurement techniques of IF persistence lengths result in highly different values ranging from $0.4 - 3.3\ \mu\text{m}$ [6, 35–37, 39].

Next to the described options of tuning subunit interactions, filaments are further stabilized in cells by their organization into bundles and networks. We find differences in

IF mechanics on the single filament level and the question remains how these differences translate to bundles and to the network scale. Previous rheology experiments of vimentin and keratin networks were carried out in different, not directly comparable buffer conditions [36, 113, 116, 135]. These different buffer conditions make it difficult to disentangle the reasons for different network properties since the buffers can affect the interactions between the filaments, the network structures and the assembly kinetics [36, 135, 242]. A study on keratin networks with a systematic variation of assembly buffer conditions in combination with direct interaction measurements between two single keratin IFs might clarify how the single keratin IF mechanics translates to the network scale. After studying these IF networks in vitro, studies on IF networks in cells might reveal how IF networks contribute to cell mechanics. Previously, studies in keratinocytes with AFM indentation experiments and in mouse embryonic fibroblasts with active microrheology experiments with optical tweezers showed a decrease in cell stiffness in case all keratin or vimentin genes were knocked out [183, 240]. In both cases, the elastic modulus decreased by a factor of about two. Yet, since the cell types and measurement methods of both studies were different, a direct, quantitative conclusion about the underlying cellular IF networks and interactions within or between the IFs would not be adequate.

Next to tuning interactions between cytoskeletal filaments of the same type, interactions between different cytoskeletal filaments might be a vital tool to adjust filament dynamics and mechanics. Therefore, here, we study the direct interactions between dynamic microtubules and vimentin IFs. We find that dynamic microtubules exhibit less catastrophes when vimentin IFs are in the surrounding solution. To verify whether this stabilization is caused by a direct interaction between microtubules and vimentin IFs, we cross the two filaments and pull them along one another with optical tweezers. We observe direct interactions between the filaments. By changing the buffer conditions and with theoretical modeling, we show that hydrophobic and electrostatic effects contribute to this interaction and mainly influence the force-dependency of the interaction. The theoretical modeling reveals that these direct interactions are responsible for the stabilization of dynamic microtubules (Section 8.1).

Thus, we can extend the overview of studied composite cytoskeletal systems presented in Section 2.6 as shown in blue in Fig. 9.1. Our findings are in contrast to previous in vitro studies [129, 136, 137]. A. Bocquet at al. found that peptide sequences which also occur in vimentin destabilized microtubules [137]. Yet, the interaction mechanism in this study remained unknown [137], and IFs do not naturally occur in the form of these separate peptides so that our study mimics a more physiologic situation. In rheology experiments in vitro, Piechocka et al. and Janmey et al. [129, 136] do not observe cooperative effects of the composite system resulting from interactions between microtubules and vimentin IFs. However, these rheology experiments do not probe the transient, stochastic interactions which we observe in our direct interaction measurements. The precise stabilization mechanism also remains unknown in case of an in vivo study where a mutual stabilization of the microtubule and vimentin IF network was observed in migrating epithelial cells [26]. However, we observe that microtubules and vimentin IFs do not spontaneously bundle so that likely another mechanism causes the mutual filament stabilization in migrating epithelial cells. These mechanisms might include additional proteins such as kinesin [216, 218], dynein [220, 221],

	Actin filaments + microtubules	Actin filaments + IFs	Microtubules + IFs
Pure protein studies, not focused on dynamic filaments	Passive microrheology by Pelletier 2009 [119] Active microrheology by Ricketts 2018 [120]	Bulk rheology with vimentin IFs by Janmey 1998 [129], by Esue 2006 [130], by Jensen, Morris 2014 [131], by Golde 2018 [132] Fluorescence microscopy with keratin IFs by Deek 2018 [134] Fluorescence microscopy with desmin IFs by Miysaka 2019 [133] Bulk rheolog with vimentin and keratin IFs by Elbalasy, Mollenkopf 2021 [135]	Co-sedimentation with neurofilaments by Hisanaga 1990 [138] Bulk rheology with vimentin IFs by Janmey 1998 [129], by Piechocka 2011 [136] Binding of short peptides of vimentin IFs by Bocquet 2009 [137]
Including motor proteins or other crosslinkers	Bulk rheology by Lin 2011 [123] Active microrheology by Ricketts 2019 [125] Fluorescence microscopy by Farhadi 2020 [126] Passive microrheology by Anderson 2021 [127] Dynamic differential microscopy by Lee 2021 [128]		
Dynamic filaments	Fluorescence microscopy by Lopez 2014 [124], by Henty-Ridilla 2016 [121], by Colin, Singaravelu 2018 [122]		Fluorescence microscopy, optical trapping by Schaedel, Lorenz [155]

Figure 9.1: Overview of studies on composite cytoskeletal systems, including our recent study highlighted in blue.

plectin [211], and microtubule-actin cross-linking factor [217, 219]. Our direct interaction measurements with a buffer supplemented with an additional protein might reveal how these proteins interact with microtubules and vimentin IFs. In our studies, we know from the direct interaction measurements in combination with theoretical modeling that already the direct interactions cause the stabilization.

If not by additional proteins, we find that the interactions between microtubules and vimentin IFs can be tuned via electrostatic or hydrophobic effects, additional binding sites or by a higher vimentin concentration around the dynamic microtubule. Thus, changes in local ion concentrations or blocking of hydrophobic interactions may be a mechanism for cells to adjust microtubule dynamics. Specifically electrostatic interactions might be generated or tuned by post-translational modifications. More potential interactions are caused by a higher collision frequency of the filaments resulting from a higher filament concentration. Indeed, we observe that microtubules collapse less frequently at a higher vimentin concentration. By transport of IFs along microtubules [237], cells might tune the local vimentin concentration so that microtubules are locally stabilized, which can be imagined to be a pre-stage of cell migration.

We further characterize these direct interactions between microtubules and vimentin IFs with the theoretical modeling approach applied to our experiments. Next to hydrophobic and electrostatic contributions, we determine the force-dependent and independent contributions to binding and unbinding rates. This disentanglement of contributions and force-dependency is highly difficult or impossible with other experimental methods which measure interactions by diffusion or by centrifuging interacting components because the interactions are not systematically probed under a certain force [247]. We find that electrostatic and hydrophobic interactions mainly influence the force-dependency, but not the free binding energy of the interaction. To further characterize the interaction, studies of the life time of the microtubule-vimentin IF bond at a constant force might quantify the activation energy of the bond [248–250]. We focus on the free binding energy difference since this parameter is required for the theoretical modeling of a dynamic microtubule and its stabilization via the interaction. With this free energy difference and further theoretical modeling, we combine our approaches to measure the interactions within and between the filaments to estimate the binding energy of tubulin dimers within the microtubule: We find that the dimer binding energy of dimers located at the tip of the microtubule is around $5.7 - 7.2\ k_B T$, which is of the order of magnitude found in previous studies, although slightly lower [96–101]. In contrast to previous studies, our model is very coarse-grained, and we cannot determine how many neighboring dimers a dimer had in the lateral direction before depolymerization. Thus, we state an average dimer binding energy. Since we deduce the binding energy from the catastrophe rate, which is an event that happens at the microtubule tip, the estimated energy applies to GTP dimers. However, our method estimating the binding energy does not involve molecular dynamics simulations, microtubule stabilization or binding gold particles to tubulin dimers as other methods [99–101]. Thus, we found a very direct way to experimentally determine the tubulin dimer binding energy without changing the dimer properties by stabilization or binding of gold particles.

In other words, the advantage of this binding energy estimate is the preservation of the dynamic and mechanical properties of the studied sample. Therefore, it might be interesting to transfer this method to other vital systems with binding energies which have not been measured yet or only measured by interfering with the mechanical properties of the sample. For example, the lateral interaction energy of subunits within IFs might be determined with this method. In this thesis, we show that this parameter significantly influences IF mechanics. A precise value for this lateral interaction energy can be calculated when the dynamic role of the microtubule and static role of the vimentin IF in our experiment are reversed: The subunit exchange dynamics of vimentin IFs can be observed while chemically stabilized microtubules in the solution interact with the dynamic vimentin IFs. Since the subunit exchange dynamics of vimentin IFs without microtubules in solution are known [201], the comparison to a study with stabilized microtubules in solution results in the lateral binding energy of vimentin IF subunits after applying our theoretical modeling approach.

All interaction energies within and between cytoskeletal filaments we calculate in this thesis are on the scale of $0.3 - 10\ k_B T$: The energy per amino acid required to open an α helix is around $0.3 - 0.6\ k_B T$ (Section 6.1), the average free binding energy between microtubules and vimentin IFs is $2.3\ k_B T$ (Section 8.1) and the binding energy of a tubulin dimer is $5.7 - 7.2\ k_B T$ (Section 8.1). Our results on the molecular and filament scale show that already small interaction energy changes on the order of or less than 1 k_BT can significantly impact mesoscopic mechanics and dynamics of cytoskeletal filaments. Comparing the mechanical behavior of keratin and vimentin IFs, the interactions within the filaments make the critical difference since the secondary structure of the monomers is highly similar. The different average number of monomers per cross-section (16 for keratin, 32 for vimentin [10, 31]) does not cause qualitatively different filament mechanics (see Fig. 5.2). Here, many of the weak bonds are coupled within an IF so that all bonds together become strong enough to resist forces of about 1 nanonewton. Similarly, for the microtubule-vimentin IF system, it is the interaction of a few k_BT which causes the stabilization of an entire dynamic microtubule. Thus, the interactions within and between filaments make the difference so that this composite system is more than the mere sum of its parts. The different load bearing abilities of single IFs and of microtubule-IF interactions (nanonewton vs. piconewton) underline the different roles of these systems within a cell: IFs act as shock absorbers while microtubule-vimentin IF interactions can locally stabilize microtubules supporting a possible pre-stage for cell migration. The transient interactions of microtubules and IFs still enable the two different cytoskeletal networks to act independently. It might be an evolutionary advantage to rely on many single, weak bonds instead of one strong bond: Energies on the scale of $1-10\ k_BT$ might be easier for cells to tune than energies $> 10\ k_BT$. In case of IFs under load, other bonds can bear the load, if a weak bond breaks, whereas one single strong bond would have no replacement.

We find that these interactions on a comparably low energy scale are strengthened by electrostatic effects: Vimentin IFs stiffen and their qualitative stress-strain behavior significantly changes because interactions within the filament are reinforced at higher ionic strength. Interactions within keratin IFs are weaker and result in very different mechanics. The interactions between vimentin IFs and microtubules increase from 0-65 pN up to 200 pN with additional magnesium ions in solution. Both examples illustrate that electrostatics can be a vital tool to change mechanical properties, which might be a mechanism occurring in the cell as well. Next to electrostatics, hydrophobic effects play an important role in regulating interactions within and between cytoskeletal filaments: In case of interactions between cytoskeletal filaments, we directly observe a decrease in interaction strength confirming hydrophobic contributions to the interaction. For interactions within IFs, it is known that hydrophobic interactions are vital for the formation of coiled coils [251]. Thus, modifications or mutations of hydrophobic amino acids might be another tool for cells to influence interactions within and between cytoskeletal filaments and thereby their mechanics.

These modifications might in general be easier to implement if there is a large pool of possible tuning sites. For example, the heterogeneity of keratin IF structures might allow for a more precise tuning of interactions within the filaments in comparison to rather homogeneous structures observed within vimentin IFs [207, 208]. For the microtubule-vimentin IF system, different post-translational modifications on tubulin tails [252] might offer more potential tuning sites than tubulin tails with the same amino acid sequence. Thus, heterogeneity might be an option by which interactions within and between filaments can be easily adjusted.

9.2 Conclusion

We quantify and characterize interactions within and between cytoskeletal filaments: We load µm-long filaments and relate this filament scale to the molecular scale of the interactions via theoretical modeling. These interactions are of the order of $0.1 - 10\ k_B T$: The energy to open an α helix per amino acid is around $0.3 - 0.6\ k_B T$, the interaction energy between a microtubule and a vimentin IF is around $2\ k_B T$ and the binding energy of a tubulin dimer is around $5 - 7\ k_B T$. To further characterize these interactions, we vary the buffer conditions in which the filaments are studied and apply a theoretical modeling approach which allows for the decoupling of electrostatic and hydrophobic contributions to these interactions. Electrostatic interactions within IFs determine the mechanical behavior of single IFs and electrostatic and hydrophobic effects contribute to microtubule-vimentin IF interactions. These interactions stabilize filament dynamics and mechanics, thus possibly enabling the cell to adapt to different dynamic and mechanical requirements. The relatively low energy scales we find for the interaction energies might have an evolutionary advantage as many weak bonds might be easier to tune than one strong bond with a high energy. Coupling many of these weak molecular interactions results in a high force resistance and affects the dynamics of an entire filament, so that these filaments become more than the mere sum of their parts: IFs can withstand forces on the nanonewton scale due to coupling and entire microtubules which interact with vimentin IFs collapse less frequently than microtubules without this interaction. Thus, interactions of the order of $1 - 10\ k_B T$ within and between cytoskeletal filaments are a key player in determining filament dynamics and mechanics.

References

[1] R. Sender, S. Fuchs, R. Milo, “Revised estimates for the number of human and bacteria cells in the body”, *PLoS biology* **2016**, *14*, e1002533.

[2] *Mol. Biol. Cell*, 6th ed., (Eds.: S. G. Lewis, E. Zayatz), Garland Science, **2015**.

[3] J. L.-S. T. D. Pollard, W. C. Earnshaw, G. T. Johnson, *Cell Biology*, 2nd, Springer-Verlag Berlin Heidelberg, **2008**.

[4] M. Dogterom, J. W. Kerssemakers, G. Romet-Lemonne, M. E. Janson, “Force generation by dynamic microtubules”, *Curr. Opin. Cell Biol.* **2005**, *17*, 67–74.

[5] S. Westermann, H.-W. Wang, A. Avila-Sakar, D. G. Drubin, E. Nogales, G. Barnes, “The Dam1 kinetochore ring complex moves processively on depolymerizing microtubule ends”, *Nature* **2006**, *440*, 565–569.

[6] J. Block, H. Witt, A. Candelli, E. J. G. Peterman, G. J. L. Wuite, A. Janshoff, S. Köster, “Nonlinear loading-rate-dependent force response of individual vimentin intermediate filaments to applied strain”, *Phys. Rev. Lett.* **2017**, *118*, 048101.

[7] J. Block, H. Witt, A. Candelli, J. C. Danes, E. J. G. Peterman, G. J. L. Wuite, A. Janshoff, S. Köster, “Viscoelastic properties of vimentin originate from nonequilibrium conformational changes”, *Sci. Adv.* **2018**, *4*.

[8] E. Latorre, S. Kale, L. Casares, M. Gómez-González, M. Uroz, L. Valon, R. V. Nair, E. Garreta, N. Montserrat, A. del Campo, B. Ladoux, M. Arroyo, X. Trepat, “Active superelasticity in three-dimensional epithelia of controlled shape”, *Nature* **2018**, *563*, 203–208.

[9] J. A. Broussard, A. Jaiganesh, H. Zarkoob, D. E. Conway, A. R. Dunn, H. D. Espinosa, P. A. Janmey, K. J. Green, “Scaling up single-cell mechanics to multicellular tissues – the role of the intermediate filament–desmosome network”, *J. Cell Sci.* **2020**, *133*, jcs228031.

[10] H. Herrmann, M. Häner, M. Brettel, N. O. Ku, U. Aebi, “Characterization of distinct early assembly units of different intermediate filament proteins”, *J. Mol. Biol.* **1999**, *286*, 1403–20.

[11] H. Herrmann, M. Hesse, M. Reichenzeller, U. Aebi, T. M. Magin, “Functional complexity of intermediate filament cytoskeletons: from structure to assembly to gene ablation”, *Int. Rev. Cytol.* **2003**, *223*, 83–175.

[12] J. Block, V. Schroeder, P. Pawelzyk, N. Willenbacher, S. Köster, “Physical properties of cytoplasmic intermediate filaments”, *Biochim. Biophys. Acta - Mol. Cell Res.* **2015**, *1853*, 3053–3064.

[13] H. Y. G. Lim, Y. D. Alvarez, M. Gasnier, Y. Wang, P. Tetlak, S. Bissiere, H. Wang, M. Biro, N. Plachta, “Keratins are asymmetrically inherited fate determinants in the mammalian embryo”, *Nature* **2020**, *585*, 404–409.

[14] F. Cheng, J. E. Eriksson, "Intermediate filaments and the regulation of cell motility during regeneration and wound healing", *CSH Perspect. Biol.* **2017**, *9*, a022046.

[15] R. Kalluri, R. A. Weinberg, et al., "The basics of epithelial-mesenchymal transition", *J. Clin. Invest.* **2009**, *119*, 1420–1428.

[16] J. P. Thiery, J. P. Sleeman, "Complex networks orchestrate epithelial–mesenchymal transitions", *Nat. Rev. Mol. Cell Biol.* **2006**, *7*, 131–142.

[17] A.-M. Fortier, E. Asselin, M. Cadrin, "Keratin 8 and 18 loss in epithelial cancer cells increases collective cell migration and cisplatin sensitivity through claudin1 up-regulation," *J. Biol. Chem.* **2013**, *288*, 11555–11571.

[18] M. J. C. Hendrix, E. A. Seftor, Y.-W. Chu, K. T. Trevor, R. E. B. Seftor, "Role of intermediate filaments in migration, invasion and metastasis", *Cancer Metast. Rev.* **1996**, *15*, 507–525.

[19] C. Leduc, S. Etienne-Manneville, "Intermediate filaments in cell migration and invasion: the unusual suspects", *Curr. Opin. Cell Biol.* **2015**, *32C*, 102–112.

[20] Y. Messica, A. Laser-Azogui, T. Volberg, Y. Elisha, K. Lysakovskaia, R. Eils, E. Gladilin, B. Geiger, R. Beck, "The role of vimentin in regulating cell invasive migration in dense cultures of breast carcinoma cells", *Nano Lett.* **2017**, *17*, 6941–6948.

[21] F. Huber, A. Boire, M. P. López, G. H. Koenderink, "Cytoskeletal crosstalk: when three different personalities team up", *Curr. Opin. Cell Biol.* **2015**, *32*, 39–47.

[22] S. Duarte, Á. Viedma-Poyatos, E. Navarro-Carrasco, A. E. Martínez, M. A. Pajares, D. Pérez-Sala, "Vimentin filaments interact with the actin cortex in mitosis allowing normal cell division", *Nat. Comm.* **2019**, *10*, 4200–4200.

[23] M. P. Serres, M. Samwer, B. A. Truong Quang, G. Lavoie, U. Perera, D. Görlich, G. Charras, M. Petronczki, P. P. Roux, E. K. Paluch, "F-actin interactome reveals vimentin as a key regulator of actin organization and cell mechanics in mitosis", *Dev. Cell* **2020**, *52*, 210–222.e7.

[24] T. D. Pollard, S. C. Selden, P. Maupin, "Interaction of actin filaments with microtubules.", *J. Cell Biol.* **1984**, *99*, 33s–37s.

[25] M. Dogterom, G. H. Koenderink, "Actin–microtubule crosstalk in cell biology", *Nat. Rev. Mol. Cell Biol.* **2019**, *20*, 38–54.

[26] Z. Gan, L. Ding, C. J. Burckhardt, J. Lowery, A. Zaritsky, K. Sitterley, A. Mota, N. Costigliola, C. G. Starker, D. F. Voytas, J. Tytell, R. D. Goldman, G. Danuser, "Vimentin intermediate filaments template microtubule networks to enhance persistence in cell polarity and directed migration", *Cell Syst.* **2016**, *3*, 252–263.

[27] G. Gurland, G. G. Gundersen, "Stable, detyrosinated microtubules function to localize vimentin intermediate filaments in fibroblasts", *J. Cell Biol.* **1995**, *131*, 1275–1290.

[28] C. Pallavicini, V. Levi, D. E. Wetzler, J. F. Angiolini, L. Benseñor, M. A. Despósito, L. Bruno, "Lateral motion and bending of microtubules studied with a new single-filament tracking routine in living cells", *Biophys. J.* **2014**, *106*, 2625–2635.

[29] A. C. Steven, J. F. Hainfeld, B. L. Trus, J. S. Wall, P. M. Steinert, “The distribution of mass in heteropolymer intermediate filaments assembled in vitro. Stem analysis of vimentin/desmin and bovine epidermal keratin.”, *J. Biol. Chem.* **1983**, *258*, 8323–8329.

[30] A. Engel, R. Eichner, U. Aebi, “Polymorphism of reconstituted human epidermal keratin filaments: determination of their mass-per-length and width by scanning transmission electron microscopy (STEM)”, *J. Ultra. Mol. Struct. R.* **1985**, *90*, 323–335.

[31] H. Herrmann, M. Häner, M. Brettel, S. A. Müller, K. N. Goldie, B. Fedtke, A. Lustig, W. W. Franke, U. Aebi, “Structure and assembly properties of the intermediate filament protein vimentin: the role of its head, rod and tail domains”, *J. Mol. Biol.* **1996**, *264*, 933–953.

[32] F. Gittes, B. Mickey, J. Nettleton, J. Howard, “Flexural rigidity of microtubules and actin filaments measured from thermal fluctuations in shape.”, *J. Cell Biol.* **1993**, *120*, 923–934.

[33] S. Köster, D. Steinhauser, T. Pfohl, “Brownian motion of actin filaments in confining microchannels”, *J. Phys. - Condens. Mat.* **2005**, *17*, S4091.

[34] D. Boal, *Mechanics of the Cell*, 2nd ed., Cambridge University Press, **2012**.

[35] N. Mücke, L. Kreplak, R. Kirmse, T. Wedig, H. Herrmann, U. Aebi, J. Langowski, “Assessing the flexibility of intermediate filaments by atomic force microscopy”, *J. Mol. Biol.* **2004**, *335*, 1241–1250.

[36] M. Schopferer, H. Bär, B. Hochstein, S. Sharma, N. Mücke, H. Herrmann, N. Willenbacher, “Desmin and vimentin intermediate filament networks: their viscoelastic properties investigated by mechanical rheometry”, *J. Mol. Biol.* **2009**, *388*, 133–143.

[37] Y. C. Lin, N. Y. Yao, C. P. Broedersz, H. Herrmann, F. C. MacKintosh, D. A. Weitz, “Origins of elasticity in intermediate filament networks”, *Phys. Rev. Lett.* **2010**, *104*, 058101.

[38] T. Lichtenstern, N. Mücke, U. Aebi, M. Mauermann, H. Herrmann, “Complex formation and kinetics of filament assembly exhibited by the simple epithelial keratins K8 and K18.”, *J. Struct. Biol.* **2012**, *177*, 54–62.

[39] B. Nöding, S. Köster, “Intermediate filaments in small configuration spaces”, *Phys. Rev. Lett.* **2012**, *108*, 088101.

[40] P. Pawelzyk, N. Mücke, H. Herrmann, N. Willenbacher, “Attractive interactions among intermediate filaments determine network mechanics in vitro”, *PloS One* **2014**, *9*, e93194.

[41] R. Kirmse, S. Portet, N. Mücke, U. Aebi, H. Herrmann, J. Langowski, “A quantitative kinetic model for the in vitro assembly of intermediate filaments from tetrameric vimentin”, *J. Biol. Chem.* **2007**, *282*, 18563–18572.

[42] S. Portet, N. Mücke, R. Kirmse, J. Langowski, M. Beil, H. Herrmann, “Vimentin intermediate filament formation: in vitro measurement and mathematical modeling of the filament length distribution during assembly”, *Langmuir* **2009**, *25*, 8817–8823.

[43] C. G. Lopez, O. Saldanha, K. Huber, S. Köster, “Lateral association and elongation of vimentin intermediate filament proteins: a time-resolved light-scattering study”, *Proc. Natl. Acad. Sci. USA* **2016**, *113*, 11152–11157.

[44] T. D. Pollard, “Rate constants for the reactions of ATP- and ADP-actin with the ends of actin filaments.”, *J. Cell Biol.* **1986**, *103*, 2747–2754.

[45] T. Mitchison, M. Kirschner, “Dynamic instability of microtubule growth”, *Nature* **1984**, *312*, 237–242.

[46] P. A. Janmey, U. Euteneuer, P. Traub, M. Schliwa, “Viscoelastic properties of vimentin compared with other filamentous biopolymer networks”, *J. Cell Biol.* **1991**, *113*, 155–160.

[47] C. L. Anna V. Schepers, Julia Kraxner, S. Köster in *Optical Tweezers: Methods and Protocols*, (Ed.: A. Gennerich), Springer New York, New York, NY, **2021**.

[48] H. Herrmann, U. Aebi, “Intermediate filaments and their associates: multi-talented structural elements specifying cytoarchitecture and cytodynamics”, *Curr. Opin. Cell Biol.* **2000**, *12*, 79–90.

[49] Human Intermediate Filament Database, accessed (2019).

[50] H. Herrmann, U. Aebi, “Intermediate filaments: structure and assembly”, *Cold Spring Harbor perspectives in biology* **2016**, *8*, 8/11/a018242[PII], a018242.

[51] R. Moll, W. W. Franke, D. L. Schiller, B. Geiger, R. Krepler, “The catalog of human cytokeratins: patterns of expression in normal epithelia, tumors and cultured cells”, *Cell* **1982**, *31*, 11–24.

[52] M. Hatzfeld, K. Weber, “Tailless keratins assemble into regular intermediate filaments in vitro”, *J. Cell Sci.* **1990**, *97*, 317–324.

[53] B. Wang, W. Yang, J. McKittrick, M. A. Meyers, “Keratin: structure, mechanical properties, occurrence in biological organisms, and efforts at bioinspiration”, *Prog. Mater. Sci.* **2016**, *76*, 229–318.

[54] W. H. Moolenaar, L. G. Tertoolen, S. W. de Laat, “The regulation of cytoplasmic pH in human fibroblasts.”, *J. Biol. Chem.* **1984**, *259*, 7563–9.

[55] G. Bright, G. Fisher, J. Rogowska, D. Taylor, “Fluorescence ratio imaging microscopy: temporal and spatial measurements of cytoplasmic pH”, *J. Cell Biol.* **1987**, *104*, 1019–1033.

[56] I. H. Madshus, “Regulation of intracellular pH in eukaryotic cells”, *Biochem. J.* **1988**, *250*, 1–8.

[57] P. A. Coulombe, E. Fuchs, “Elucidating the early stages of keratin filament assembly”, *J. Cell Biol.* **1990**, *111*, 153–169.

[58] H. Herrmann, T. Wedig, R. M. Porter, E. B. Lane, U. Aebi, “Characterization of early assembly intermediates of recombinant human keratins”, *J. Struct. Biol.* **2002**, *137*, 82–96.

[59] N. Mücke, T. Wedig, A. Bürer, L. N. Marekov, P. M. Steinert, J. Langowski, U. Aebi, H. Herrmann, "Molecular and biophysical characterization of assembly-starter units of human vimentin", *J. Mol. Biol.* **2004**, *340*, 97–114.

[60] D. Eisenberg, E. Schwarz, M. Komaromy, R. Wall, "Analysis of membrane and surface protein sequences with the hydrophobic moment plot", *J. Mol. Biol.* **1984**, *179*, 125–142.

[61] A. Premchandar, N. Mücke, J. Poznański, T. Wedig, M. Kaus-Drobek, H. Herrmann, M. Dadlez, "Structural dynamics of the vimentin coiled-coil contact regions involved in filament assembly as revealed by hydrogen-deuterium exchange", *J. Biol. Chem.* **2016**, *291*, 24931–24950.

[62] N. Mücke, S. Winheim, H. Merlitz, J. Buchholz, J. Langowski, H. Herrmann, "In vitro assembly kinetics of cytoplasmic intermediate filaments: a correlative Monte Carlo simulation study", *PloS One* **2016**, *11*, 1–14.

[63] J. Forsting, J. Kraxner, H. Witt, A. Janshoff, S. Köster, "Vimentin intermediate filaments undergo irreversible conformational changes during cyclic loading", *Nano Lett.* **2019**, *19*, 7349–7356.

[64] L. Kreplak, J. Doucet, P. Dumas, F. Briki, "New aspects of the α helix to β sheet transition in stretched hard α-keratin fibers", *Biophys. J.* **2004**, *87*, 640–647.

[65] F. Fleissner, S. Kumar, N. Klein, D. Wirth, R. Dhiman, D. Schneider, M. Bonn, S. H. Parekh, "Tension causes unfolding of intracellular vimentin intermediate filaments", *Adv. Biosyst.* **2020**, *4*, 2000111.

[66] S. A. Shorter, "An investigation of the nature of the elasticity of fibres", *J. Text. Inst. Transactions* **1924**, *15*.

[67] J. B. S. M.Sc., "38 - the intracellular structure of the wool fibre", *J. Text. Inst. Transactions* **1927**, *18*, T431–T453.

[68] W. T. Astbury, H. J. Woods, "The X-ray interpretation of the structure and elastic properties of hair keratin", *Nature* **1930**, *126*, 913–914.

[69] W. T. Astbury, A. Street, W. H. Bragg, "X-ray studies of the structure of hair, wool, and related fibres. - I. General", *Philos. T. R. Soc. Lond.* **1931**, *230*, 75–101.

[70] W. T. Astbury, H. J. Woods, W. L. Bragg, "X-ray studies of the structure of hair, wool, and related fibres. - II. the molecular structure and elastic properties of hair keratin", *Philos. T. R. Soc. Lond.* **1933**, *232*, 333–394.

[71] W. T. Astbury, W. A. Sisson, W. H. Bragg, "X-ray studies of the structure of hair, wool, and related fibres - III. The configuration of the keratin molecule and its orientation in the biological cell", *Philos. T. R. Soc. S.-A* **1935**, *150*, 533–551.

[72] L. Pauling, R. B. Corey, "Compound helical configurations of polypeptide chains: structure of proteins of the α-keratin type", *Nature* **1953**, *171*, 59–61.

[73] E. G. Bendit, "A quantitative X-Ray diffraction study of the alpha-beta transformation in wool keratin", *Text. Res. J.* **1960**, *30*, 547–555.

[74] D. S. Fudge, K. H. Gardner, V. T. Forsyth, C. Riekel, J. M. Gosline, “The mechanical properties of hydrated intermediate filaments: insights from hagfish slime threads”, *Biophys. J.* **2003**, *85*, 2015–2027.

[75] D. S. Fudge, T. Winegard, R. Ewoldt, D. Beriault, L. Szewciw, G. McKinley, “From ultra-soft slime to hard α-keratins: The many lives of intermediate filaments”, *Integr. Comp. Biol.* **2009**, *49*, 32–39.

[76] N. Pinto, F.-C. Yang, A. Negishi, M. C. Rheinstädter, T. E. Gillis, D. S. Fudge, “Self-assembly enhances the strength of fibers made from vimentin intermediate filament proteins”, *Biomacromolecules* **2014**, *15*, doi: 10.1021/bm401600a, 574–581.

[77] L. Kreplak, H. Bär, J. F. Leterrier, H. Herrmann, U. Aebi, “Exploring the mechanical behavior of single intermediate filaments”, *J. Mol. Biol.* **2005**, *354*, 569–577.

[78] L. Kreplak, H. Herrmann, U. Aebi, “Tensile properties of single desmin intermediate filaments”, *Biophys. J.* **2008**, *94*, 2790–2799.

[79] C. Guzman, S. Jeney, L. Kreplak, S. Kasas, A. J. Kulik, U. Aebi, L. Forro, “Exploring the mechanical properties of single vimentin intermediate filaments by atomic force microscopy”, *J. Mol. Biol.* **2006**, *360*, 623–630.

[80] K. T. Sapra, Z. Qin, A. Dubrovsky-Gaupp, U. Aebi, D. J. Müller, M. J. Buehler, O. Medalia, “Nonlinear mechanics of lamin filaments and the meshwork topology build an emergent nuclear lamina”, *Nat. Comm.* **2020**, *11*, 6205.

[81] A. V. Schepers, C. Lorenz, S. Köster, “Tuning intermediate filament mechanics by variation of pH and ion charges”, *Nanoscale* **2020**, *12*, 15236–15245.

[82] J. Kraxner, C. Lorenz, J. Menzel, I. Parfentev, I. Silbern, M. Denz, H. Urlaub, B. Schwappach, S. Köster, “Post-translational modifications soften vimentin intermediate filaments”, *Nanoscale* **2021**, *13*, 380–387.

[83] Z. Qin, L. Kreplak, M. J. Buehler, “Hierarchical structure controls nanomechanical properties of vimentin intermediate filaments”, *PloS One* **2009**, *4*, e7294.

[84] Z. Qin, L. Kreplak, M. J. Buehler, “Nanomechanical properties of vimentin intermediate filament dimers”, *Nanotechnology* **2009**, *20*, 425101.

[85] M. Chalfie, J. N. Thomson, “Organization of neuronal microtubules in the nematode Caenorhabditis elegans.”, *J. Cell Biol.* **1979**, *82*, 278–289.

[86] R. A. Walker, E. T. O’Brien, N. K. Pryer, F. Soboeiro, W. A. Voter, H. P. Erickson, E. D. Salmon, “Dynamic instability of individual microtubules analyzed by video light microscopy: rate constants and transition frequencies”, *J. Cell Biol.* **1988**, *107*, 1437–1448.

[87] E. J. AMBROSE, “A surface contact microscope for the study of cell movements”, *Nature* **1956**, *178*, 1194–1194.

[88] D. Axelrod, “Cell-substrate contacts illuminated by total internal reflection fluorescence.”, *J. Cell Biol.* **1981**, *89*, 141–145.

[89] C. E. Coombes, A. Yamamoto, M. R. Kenzie, D. J. Odde, M. K. Gardner, “Evolving tip structures can explain age-dependent microtubule catastrophe”, *Curr. Biol.* **2013**, *23*, 1342–1348.

[90] A. Aher, A. Akhmanova, “Tipping microtubule dynamics, one protofilament at a time”, *Curr. Opin. Cell Biol.* **2018**, *50*, Cell Architecture, 86–93.

[91] C. P. Fees, J. K. Moore, “A unified model for microtubule rescue”, *Mol. Biol. Cell* **2019**, *30*, 753–765.

[92] E. T. O’Brien, E. D. Salmon, R. A. Walker, H. P. Erickson, “Effects of magnesium on the dynamic instability of individual microtubules.”, *Biochemistry* **1990**, *29*, Place: United States, 6648–6656.

[93] J. R. Simon, S. F. Parsons, E. D. Salmon, “Buffer conditions and non-tubulin factors critically affect the microtubule dynamic instability of sea urchin egg tubulin”, *Cell Motil. Cytoskel.* **1992**, *21*, 1–14.

[94] A. A. Hyman, S. Salser, D. N. Drechsel, N. Unwin, T. J. Mitchison, “Role of GTP hydrolysis in microtubule dynamics: information from a slowly hydrolyzable analogue, GMPCPP”, *Mol. Biol. Cell* **1992**, *3*, PMC275679[pmcid], 1155–1167.

[95] P. B. Schiff, S. B. Horwitz, “Taxol stabilizes microtubules in mouse fibroblast cells”, *Proc. Natl. Acad. Sci. of the USA* **1980**, *77*, PMC348536[pmcid], 1561–1565.

[96] V. VanBuren, D. J. Odde, L. Cassimeris, “Estimates of lateral and longitudinal bond energies within the microtubule lattice”, *Proc. Natl. Acad. Sci. USA* **2002**, *99*, 6035–6040.

[97] P. Zakharov, N. Gudimchuk, V. Voevodin, A. Tikhonravov, F. I. Ataullakhanov, E. L. Grishchuk, “Molecular and mechanical causes of microtubule catastrophe and aging”, *Biophys. J.* **2015**, *109*, 2574–2591.

[98] J. R. McIntosh, E. O’Toole, G. Morgan, J. Austin, E. Ulyanov, F. Ataullakhanov, N. Gudimchuk, “Microtubules grow by the addition of bent guanosine triphosphate tubulin to the tips of curved protofilaments”, *J. Cell Biol.* **2018**, *217*, 2691–2708.

[99] M. Hemmat, D. J. Odde, “Atomistic basis of microtubule dynamic instability assessed via multiscale modeling”, *Ann. Biomed. Eng.* **2021**.

[100] C. Ganser, T. Uchihashi, “Microtubule self-healing and defect creation investigated by in-line force measurements during high-speed atomic force microscopy imaging”, *Nanoscale* **2019**, *11*, 125–135.

[101] K. J. Mickolajczyk, E. A. Geyer, T. Kim, L. M. Rice, W. O. Hancock, “Direct observation of individual tubulin dimers binding to growing microtubules”, *Phys. Rev. Lett. Acad. Sci. USA* **2019**, *116*, 7314–7322.

[102] L. Schaedel, S. Triclin, D. Chrétien, A. Abrieu, C. Aumeier, J. Gaillard, L. Blanchoin, M. Théry, K. John, “Lattice defects induce microtubule self-renewal”, *Nat. Phys.* **2019**, *15*, 830–838.

[103] M. Igaev, H. Grubmüller, “Microtubule instability driven by longitudinal and lateral strain propagation”, *PLOS Comput. Biol.* **2020**, *16*, 1–21.

[104] S. F. Stewman, K. K. Tsui, A. Ma, “Dynamic instability from non-equilibrium structural transitions on the energy landscape of microtubule”, *Cell Systems* **2020**, *11*, 608–624.e9.

[105] N. Laurens, R. P. Driessen, I. Heller, D. Vorselen, M. C. Noom, F. J. Hol, M. F. White, R. T. Dame, G. J. Wuite, “Alba shapes the archaeal genome using a delicate balance of bridging and stiffening the DNA”, *Nat. Commun.* **2012**, *3*, 1328.

[106] I. Brouwer, G. Sitters, A. Candelli, S. J. Heerema, I. Heller, A. J. Melo de, H. Zhang, D. Normanno, M. Modesti, E. J. G. Peterman, G. J. Wuite, “Sliding sleeves of XRCC4–XLF bridge DNA and connect fragments of broken DNA”, *Nature* **2016**, *535*, 566–569.

[107] P. Gutierrez-Escribano, M. D. Newton, A. Llauró, J. Huber, L. Tanasie, J. Davy, I. Aly, R. Aramayo, A. Montoya, H. Kramer, J. Stigler, D. S. Rueda, L. Aragon, “A conserved ATP- And Scc2/4-dependent activity for cohesin in tethering DNA molecules”, *Sci. Adv.* **2019**, *5*, 1–16.

[108] N. A. Kurniawan, B. E. Vos, A. Biebricher, G. J. L. Wuite, E. J. G. Peterman, G. H. Koenderink, “Fibrin networks support recurring mechanical loads by adapting their structure across multiple scales”, *Biophys. J.* **2016**, *111*, 1026–1034.

[109] B. E. Vos, L. C. Liebrand, M. Vahabi, A. Biebricher, G. J. Wuite, E. J. Peterman, N. A. Kurniawan, F. C. MacKintosh, G. H. Koenderink, “Programming the mechanics of cohesive fiber networks by compression”, *Soft Matter* **2017**, *13*, 8886–8893.

[110] J. Bergman, O. Osunbayo, M. Vershinin, “Constructing 3d microtubule networks using holographic optical trapping”, *Sci. Rep.* **2015**, *5*, 18085.

[111] H. Bär, M. Schopferer, S. Sharma, B. Hochstein, N. Mücke, H. Herrmann, N. Willenbacher, “Mutations in desmin’s carboxy-terminal “tail” domain severely modify filament and network mechanics”, *J. Mol. Biol.* **2010**, *397*, 1188–1198.

[112] Y.-C. Lin, C. P. Broedersz, A. C. Rowat, T. Wedig, H. Herrmann, F. C. MacKintosh, D. A. Weitz, “Divalent cations crosslink vimentin intermediate filament tail domains to regulate network mechanics”, *J. Mol. Biol.* **2010**, *399*, 637–644.

[113] A. Aufderhorst-Roberts, G. H. Koenderink, “Stiffening and inelastic fluidization in vimentin intermediate filament networks”, *Soft Matter* **2019**, *15*, 7127–7136.

[114] T. Golde, M. Glaser, C. Tutmarc, I. Elbalasy, C. Huster, G. Busteros, D. M. Smith, H. Herrmann, J. A. Käs, J. Schnauß, “The role of stickiness in the rheology of semiflexible polymers”, *Soft Matter* **2019**, *15*, 4865–4872.

[115] S. Yamada, D. Wirtz, P. A. Coulombe, “The mechanical properties of simple epithelial keratins 8 and 18: discriminating between interfacial and bulk elasticities”, *J. Struct. Biol.* **2003**, *143*, 45–55.

[116] A. Leitner, T. Paust, O. Marti, P. Walther, H. Herrmann, M. Beil, “Properties of intermediate filament networks assembled from keratin 8 and 18 in the presence of Mg2+”, *Biophys. J.* **2012**, *103*, 195–201.

[117] C. Dammann, B. Nöding, S. Köster, “Vimentin networks at tunable ion-concentration in microfluidic drops”, *Biomicrofluidics* **2012**, *6*, 022009.

[118] J. Kayser, H. Grabmayr, M. Harasim, H. Herrmann, A. R. Bausch, "Assembly kinetics determine the structure of keratin networks", *Soft Matter* **2012**, *8*, 8873–8879.

[119] V. Pelletier, N. Gal, P. Fournier, M. L. Kilfoil, "Microrheology of microtubule solutions and actin-microtubule composite networks", *Phys. Rev. Lett.* **2009**, *102*, 188303.

[120] S. N. Ricketts, J. L. Ross, R. M. Robertson-Anderson, "Co-entangled actin-microtubule composites exhibit tunable stiffness and power-law stress relaxation", *Biophys. J.* **2018**, *115*, 1055–1067.

[121] J. L. Henty-Ridilla, A. Rankova, J. A. Eskin, K. Kenny, B. L. Goode, "Accelerated actin filament polymerization from microtubule plus ends", *Science* **2016**, *352*, 1004–1009.

[122] A. Colin, P. Singaravelu, M. Théry, L. Blanchoin, Z. Gueroui, "Actin-network architecture regulates microtubule dynamics", *Curr. Biol.* **2018**, *28*, 2647–2656.

[123] Y.-C. Lin, G. H. Koenderink, F. C. MacKintosh, D. A. Weitz, "Control of non-linear elasticity in F-actin networks with microtubules", *Soft Matter* **2011**, *7*, 902–906.

[124] M. P. López, F. Huber, I. Grigoriev, M. O. Steinmetz, A. Akhmanova, G. H. Koenderink, M. Dogterom, "Actin–microtubule coordination at growing microtubule ends", *Nat. Comm.* **2014**, *5*, 4778.

[125] S. N. Ricketts, M. L. Francis, L. Farhadi, M. J. Rust, M. Das, J. L. Ross, R. M. Robertson-Anderson, "Varying crosslinking motifs drive the mesoscale mechanics of actin-microtubule composites", *Sci. Rep.* **2019**, *9*, 12831.

[126] L. Farhadi, S. N. Ricketts, M. J. Rust, M. Das, R. M. Robertson-Anderson, J. L. Ross, "Actin and microtubule crosslinkers tune mobility and control co-localization in a composite cytoskeletal network", *Soft Matter* **2020**, *16*, 7191–7201.

[127] S. J. Anderson, J. Garamella, S. Adalbert, R. J. McGorty, R. M. Robertson-Anderson, "Subtle changes in crosslinking drive diverse anomalous transport characteristics in actin–microtubule networks", *Soft Matter* **2021**.

[128] G. Lee, G. Leech, M. J. Rust, M. Das, R. J. McGorty, J. L. Ross, R. M. Robertson-Anderson, "Myosin-driven actin-microtubule networks exhibit self-organized contractile dynamics", *Sci. Adv.* **2021**, *7*.

[129] P. A. Janmey, J. V. Shah, K. P. Janssen, M. Schliwa, "Viscoelasticity of intermediate filament networks", *Sub-cell. Biochem.* **1998**, *31*, Place: United States, 381–397.

[130] O. Esue, A. A. Carson, Y. Tseng, D. Wirtz, "A direct interaction between actin and vimentin filaments mediated by the tail domain of vimentin", *J. Biol. Chem.* **2006**, *281*, 30393–30399.

[131] M. H. Jensen, E. J. Morris, R. D. Goldman, D. A. Weitz, "Emergent properties of composite semiflexible biopolymer networks", *BioArchitecture* **2014**, *4*, PMID: 25759912, 138–143.

[132] T. Golde, C. Huster, M. Glaser, T. Händler, H. Herrmann, J. A. Käs, J. Schnauß, "Glassy dynamics in composite biopolymer networks", *Soft Matter* **2018**, *14*, 7970–7978.

[133] Y. Miyasaka, K. Murakami, K. Ito, J. Kumaki, K. Makabe, K. Hatori, “Condensed desmin and actin cytoskeletal communication in lipid droplets”, *Cytoskeleton* **2019**, *76*, 477–490.

[134] J. Deek, R. Maan, E. Loiseau, A. R. Bausch, “Reconstitution of composite actin and keratin networks in vesicles”, *Soft Matter* **2018**, *14*, 1897–1902.

[135] I. Elbalasy, P. Mollenkopf, C. Tutmarc, H. Herrmann, J. Schnauß, “Keratins determine network stress responsiveness in reconstituted actin–keratin filament systems”, *Soft Matter* **2021**, *17*, 3954–3962.

[136] I. K. Piechocka, “In vitro reconstitution of composite networks of vimentin and microtubules”, *PhD thesis - chapter 7* **2011**.

[137] A. Bocquet, R. Berges, R. Frank, P. Robert, A. C. Peterson, J. Eyer, “Neurofilaments bind tubulin and modulate its polymerization”, *J. Neurosci.* **2009**, *29*, 11043–11054.

[138] S. Hisanaga, N. Hirokawa, “Dephosphorylation-induced interactions of neurofilaments with microtubules.”, *J. Biol. Chem.* **1990**, *265*, 21852–21858.

[139] A. Gennerich, *Optical Tweezers*, Humana Press, New York, **2017**.

[140] All Nobel Prizes in Physics, https://www.nobelprize.org/prizes/lists/all-nobel-prizes-in-physics/, Accessed: 9th Apr 2021.

[141] A. Ashkin, “Acceleration and trapping of particles by radiation pressure”, *Phys. Rev. Lett.* **1970**, *24*, 156–159.

[142] A. Ashkin, J. M. Dziedzic, J. E. Bjorkholm, S. Chu, “Observation of a single-beam gradient force optical trap for dielectric particles”, *Opt. Lett.* **1986**, *11*, 288–290.

[143] W. D. Phillips, J. V. Prodan, H. J. Metcalf, “Laser cooling and electromagnetic trapping of neutral atoms”, *J. Opt. Soc. Am. B* **1985**, *2*, 1751–1767.

[144] K. Lehmann, M. Shayegan, G. A. Blab, N. R. Forde, “Optical tweezers approaches for probing multiscale protein mechanics and assembly”, *Front. Mol. Biosci.* **2020**, *7*, 577314–577314.

[145] M. D. Koch, J. W. Shaevitz in *Optical Tweezers: Methods and Protocols*, (Ed.: A. Gennerich), Springer New York, New York, NY, **2017**, pp. 3–24.

[146] A. Rohrbach, E. H. K. Stelzer, “Trapping forces, force constants, and potential depths for dielectric spheres in the presence of spherical aberrations”, *Appl. Opt.* **2002**, *41*, 2494–2507.

[147] A. Rohrbach, “Stiffness of optical traps: quantitative agreement between experiment and electromagnetic theory”, *Phys. Rev. Lett.* **2005**, *95*, 168102.

[148] S. F. Tolić-Nørrelykke, E. Schäffer, J. Howard, F. S. Pavone, F. Jülicher, H. Flyvbjerg, “Calibration of optical tweezers with positional detection in the back focal plane”, *Rev. Sci. Instrum.* **2006**, *77*, 103101.

[149] S. Arrhenius, “Über die Reaktionsgeschwindigkeit bei der Inversion von Rohrzucker durch Säuren”, *Z. Phys. Chem.* **1889**, *4U*, 226–248.

[150] M. Trautz, "Das Gesetz der Reaktionsgeschwindigkeit und der Gleichgewichte in Gasen. Bestätigung der Additivität von Cv-3/2R. Neue Bestimmung der Integrationskonstanten und der Moleküldurchmesser", *Z. anorg. allg. Chem.* **1916**, *96*, 1–28.

[151] G. Bell, "Models for the specific adhesion of cells to cells", *Science* **1978**, *200*, 618–627.

[152] E. Evans, K. Ritchie, "Dynamic strength of molecular adhesion bonds", *Biophys. J.* **1997**, *72*, 1541–1555.

[153] A. Kolomeisky, *Motor Proteins and Molecular Motors*, CRC press, **2015**.

[154] U. Seifert, "Rupture of multiple parallel molecular bonds under dynamic loading", *Phys. Rev. Lett.* **2000**, *84*, 2750–2753.

[155] T. Erdmann, U. S. Schwarz, "Stability of adhesion clusters under constant force", *Phys. Rev. Lett.* **2004**, *92*, 108102.

[156] C. Lorenz, J. Forsting, A. V. Schepers, J. Kraxner, S. Bauch, H. Witt, S. Klumpp, S. Köster, "Lateral subunit coupling determines intermediate filament mechanics", *Phys. Rev. Lett.* **2019**, *123*, 188102.

[157] L. Schaedel, C. Lorenz, A. V. Schepers, S. Klumpp, S. Köster, "Vimentin intermediate filaments stabilize dynamic microtubules by direct interactions", *Nat. Comm.* **2021**, *12*, 3799.

[158] H. Herrmann, U. Aebi, "Intermediate filaments: molecular structure, assembly mechanism, and integration into functionally distinct intracellular scaffolds", *Annu. Rev. Biochem.* **2004**, *73*, 749–789.

[159] M. L. Shelanski, "Chemistry of the filaments and tubules of brain", *J. Histochem. Cytochem.* **1973**, *21*, 529–539.

[160] S. Winheim, A. R. Hieb, M. Silbermann, E.-M. Surmann, T. Wedig, H. Herrmann, J. Langowski, N. Mücke, "Deconstructing the late phase of vimentin assembly by total internal reflection fluorescence microscopy (TIRFM)", *PloS One* **2011**, *6*, e19202.

[161] R. H Kretsinger, V. Uversky, E. Permyakov, *Encyclopedia of Metalloproteins*, Springer New York, **2013**, pp. 2574–244.

[162] M. Zacchia, M. L. Abategiovanni, S. Stratigis, G. Capasso, "Potassium: from physiology to clinical implications", *Kidney Dis.* **2016**, *2*, 72–79.

[163] R. Janissen, B. A. Berghuis, D. Dulin, M. Wink, T. Van Laar, N. H. Dekker, "Invincible DNA tethers: Covalent DNA anchoring for enhanced temporal and force stability in magnetic tweezers experiments", *Nucleic Acids Res.* **2014**, *42*, e137.

[164] L. Kreplak, A. Franbourg, F. Briki, F. Leroy, D. Dalle, J. Doucet, "A new deformation model of hard α-keratin fibers at the nanometer scale: implications for hard α-keratin intermediate filament mechanical properties", *Biophys. J.* **2002**, *82*, 2265–2274.

[165] U. Aebi, W. E. Fowler, P. Rew, T. T. Sun, "The fibrillar substructure of keratin filaments unraveled.", *J. Cell Biol.* **1983**, *97*, 1131–1143.

[166] D. A. Parry, L. N. Marekov, P. M. Steinert, “Subfilamentous protofibril structures in fibrous proteins: cross-linking evidence for protofibrils in intermediate filaments.”, *J. Biol. Chem.* **2001**, *276*, 39253–39258.

[167] K. N. Goldie, T. Wedig, A. K. Mitra, U. Aebi, H. Herrmann, A. Hoenger, “Dissecting the 3-D structure of vimentin intermediate filaments by cryo-electron tomography.”, *J. Struct. Biol.* **2007**, *158*, 378–385.

[168] M. E. Fisher, A. B. Kolomeisky, “The force exerted by a molecular motor”, *Proc. Natl. Acad. Sci. USA* **1999**, *96*, 6597–6602.

[169] A. A. Chernyatina, S. Nicolet, U. Aebi, H. Herrmann, S. V. Strelkov, “Atomic structure of the vimentin central alpha-helical domain and its implications for intermediate filament assembly”, *Proc. Natl. Acad. Sci. USA* **2012**, *109*, 13620–13625.

[170] N. Mücke, L. Kreplak, R. Kirmse, T. Wedig, H. Herrmann, U. Aebi, J. Langowski, “Assessing the flexibility of intermediate filaments by atomic force microscopy”, *J. Mol. Biol.* **2004**, *335*, 1241–1250.

[171] W. Kuhn, F. Grün, “Beziehungen zwischen elastischen Konstanten und Dehnungsdoppelbrechung hochelastischer Stoffe”, *Kolloid Z.* **1942**, *101*, 248–271.

[172] H. M. James, E. Guth, “Theory of the elastic properties of rubber”, *J. Chem. Phys.* **1943**, *11*, 455–481.

[173] Y.-S. Lo, Y.-J. Zhu, T. P. Beebe, “Loading-rate dependence of individual ligand-receptor bond-rupture forces studied by atomic force microscopy”, *Langmuir* **2001**, *17*, 3741–3748.

[174] A. Pohl, F. Berger, R. M. A. Sullan, C. Valverde-Tercedor, K. Freindl, N. Spiridis, C. T. Lefèvre, N. Menguy, S. Klumpp, K. G. Blank, D. Faivre, “Decoding biomineralization: interaction of a Mad10-derived peptide with magnetite thin films”, *Nano Lett.* **2019**, *19*, 8207–8215.

[175] V. H. Thanh, C. Priami, “Simulation of biochemical reactions with time-dependent rates by the rejection-based algorithm”, *J. Chem. Phys.* **2015**, *143*, 054104.

[176] D. T. Gillespie, “Exact stochastic simulation of coupled chemical reactions”, *J. Phys. Chem.* **1977**, *81*, 2340–2361.

[177] G. W. Corder, D. I. Foreman, *Nonparametric Statistics: A Step-By-Step Approach*, John Wiley & Sons, Somerset, 2014.

[178] M. v. Smoluchowski, “Versuch einer mathematischen Theorie der Koagulationskinetik kolloider Lösungen”, *Z. Phys. Chem..* **1918**, *92*, 129–168.

[179] Sigma Aldrich Product Information Methyl Cellulose, accessed (2020).

[180] Y.-G. Tao, W. K. den Otter, J. K. G. Dhont, W. J. Briels, “Isotropic-nematic spinodals of rigid long thin rodlike colloids by event-driven brownian dynamics simulations”, *J. Chem. Phys.* **2006**, *124*, 134906.

[181] C. F. Schmidt, M. Baermann, G. Isenberg, E. Sackmann, “Chain dynamics, mesh size, and diffusive transport in networks of polymerized actin: a quasielastic light scattering and microfluorescence study”, *Macromolecules* **1989**, *22*, 3638–3649.

[182] B. Eckes, D. Dogic, E. Colucci-Guyon, N. Wang, A. Maniotis, D. Ingber, A. Merckling, F. Langa, M. Aumailley, A. Delouvee, V. Koteliansky, C. Babinet, T. Krieg, "Impaired mechanical stability, migration and contractile capacity in vimentin-deficient fibroblasts", *J. Cell Sci.* **1998**, *111*, 1897–1907.

[183] L. Ramms, G. Fabris, R. Windoffer, N. Schwarz, R. Springer, C. Zhou, J. Lazar, S. Stiefel, N. Hersch, U. Schnakenberg, T. M. Magin, R. E. Leube, R. Merkel, B. Hoffmann, "Keratins as the main component for the mechanical integrity of keratinocytes", *Phys. Rev. Lett. Acad. Sci. USA* **2013**, *110*, 18513–18518.

[184] K. Seltmann, A. W. Fritsch, J. A. Käs, T. M. Magin, "Keratins significantly contribute to cell stiffness and impact invasive behavior", *Proc. Natl. Acad. Sci. USA* **2013**, *110*, 18507–18512.

[185] J. Cao, C. A. Billows, "Crystallinity determination of native and stretched wool by X-ray diffraction", *Polym. Int.* **1999**, *48*, 1027–1033.

[186] H. Herrmann, L. Kreplak, U. Aebi, "Isolation, characterization, and in vitro assembly of intermediate filaments", *Methods Cell Biol.* **2004**, *78*, 3–24.

[187] Z. Qin, M. J. Buehler, "Structure and dynamics of human vimentin intermediate filament dimer and tetramer in explicit and implicit solvent models", *J. Mol. Model.* **2011**, *17*, 37–48.

[188] T. Ackbarow, M. J. Buehler, "Alpha-helical protein domains unify strength and robustness through hierarchical nanostructures", *Nanotechnology* **2009**, *20*, 075103.

[189] C. Dammann, S. Köster, "Dynamics of counterion-induced attraction between vimentin filaments followed in microfluidic drops", *Lab Chip* **2014**, *14*, 2681–2687.

[190] C. Y. J. Hémonnot, M. Mauermann, H. Herrmann, S. Köster, "Assembly of simple epithelial keratin filaments: deciphering the ion dependence in filament organization", *Biomacromolecules* **2015**, *16*, 3313–3321.

[191] J. Kyte, R. F. Doolittle, "A simple method for displaying the hydropathic character of a protein", *J. Mol. Biol.* **1982**, *157*, 105–132.

[192] S. Nafeey, I. Martin, T. Felder, P. Walther, E. Felder, "Branching of keratin intermediate filaments", *J. Struct. Biol.* **2016**, *194*, 415–422.

[193] D. J. Tobias, S. F. Sneddon, C. L. Brooks, "Stability of a model β-sheet in water.", *J. Mol. Biol.* **1992**, *227*, 1244–1252.

[194] A.-S. Yang, B. Honig, "Free energy determinants of secondary structure formation: II. antiparallel β-Sheets", *J. Mol. Biol.* **1995**, *252*, 366–376.

[195] S. Singh, C.-c. Chiu, A. S. Reddy, J. J. de Pablo, "α-helix to β-hairpin transition of human amylin monomer.", *J. Chem. Phys.* **2013**, *138*, 155101.

[196] M. Rief, J. Pascual, M. Saraste, H. E. Gaub, "Single molecule force spectroscopy of spectrin repeats: low unfolding forces in helix bundles", *J. Mol. Biol.* **1999**, *286*, 553–561.

[197] H. Takahashi, F. Rico, C. Chipot, S. Scheuring, "α-Helix unwinding as force buffer in spectrins", *ACS Nano* **2018**, *12*, 2719–2727.

[198] A. Premchandar, A. Kupniewska, K. Tarnowski, N. Mücke, M. Mauermann, M. Kaus-Drobek, A. Edelman, H. Herrmann, M. Dadlez, "Analysis of distinct molecular assembly complexes of keratin K8 and K18 by hydrogen–deuterium exchange", *J. Struct. Biol.* **2015**, *192*, 426–440.

[199] C. Dammann, H. Herrmann, S. Köster, "Competitive counterion binding regulates the aggregation onset of vimentin intermediate filaments", *Isr. J. Chem.* **2016**, *56*, 614–621.

[200] J.-F. Nolting, W. Möbius, S. Köster, "Mechanics of individual keratin bundles in living cells", *Biophys. J.* **2014**, *107*, 2693–2699.

[201] B. Nöding, H. Herrmann, S. Köster, "Direct observation of subunit exchange along mature vimentin intermediate filaments", *Biophys. J.* **2014**, *107*, 2923–2931.

[202] G. Tzivion, Z.-J. Luo, J. Avruch, "Calyculin a-induced vimentin phosphorylation sequesters 14-3-3 and displaces other 14-3-3 partners in vivo", *J. Biol. Chem.* **2000**, *275*, 29772–29778.

[203] A. K. Gardino, M. B. Yaffe in Seminars in cell & developmental biology, *Vol. 22*, Elsevier, **2011**, pp. 688–695.

[204] J. E. Eriksson, T. He, A. V. Trejo-Skalli, A.-S. Härmälä-Braskén, J. Hellman, Y.-H. Chou, R. D. Goldman, "Specific in vivo phosphorylation sites determine the assembly dynamics of vimentin intermediate filaments", *J. Cell Sci.* **2004**, *117*, 919–932.

[205] D. A. Parry, P. M. Steinert, *Intermediate filament structure*, Springer-Verlag, **1995**, 183 pp.

[206] C. Lorenz, J. Forsting, R. W. Style, S. Klumpp, S. Köster, "Keratin filament mechanics and energy dissipation are determined by metal-like plasticity", *Matter* **2023**, *6*.

[207] M. Eibauer, M. S. Weber, Y. Turgay, S. Sivagurunathan, R. D. Goldman, O. Medalia, "The molecular architecture of vimentin filaments", *bioRxiv* **2021**.

[208] M. S. Weber, M. Eibauer, S. Sivagurunathan, T. M. Magin, R. D. Goldman, O. Medalia, "Structural heterogeneity of cellular K5/K14 filaments as revealed by cryo-electron microscopy", *eLife* **2021**, *10*, e70307.

[209] H. Herrmann, H. Bär, L. Kreplak, S. V. Strelkov, U. Aebi, "Intermediate filaments: from cell architecture to nanomechanics", *Nat. Rev. Mol. Cell Biol.* **2007**, *8*, 562–573.

[210] S. B. Lavenus, S. M. Tudor, M. F. Ullo, K. W. Vosatka, J. S. Logue, "A flexible network of vimentin intermediate filaments promotes migration of amoeboid cancer cells through confined environments", *J. Biol. Chem.* **2020**, *295*, 6700–6709.

[211] T. M. Svitkina, A. B. Verkhovsky, G. G. Borisy, "Plectin sidearms mediate interaction of intermediate filaments with microtubules and other components of the cytoskeleton", *J. Cell Biol.* **1996**, *135*, 991–1007.

[212] L. Chang, R. D. Goldman, "Intermediate filaments mediate cytoskeletal crosstalk", *Nat. Rev. Mol. Cell Biol.* **2004**, *5*, 601–613.

[213] H. Kim, F. Nakamura, W. Lee, C. Hong, D. Perez-Sala, C. A. McCulloch, "Regulation of cell adhesion to collagen via $\beta 1$ integrins is dependent on interactions of filamin A with vimentin and protein kinase C epsilon", *Exp. Cell Res.* **2010**, *316*, 1829–1844.

[214] R. E. Leube, M. Moch, R. Windoffer, "Intermediate filaments and the regulation of focal adhesions", *Curr. Opin. Cell Biol.* **2015**, *32*, 13–20.

[215] R. D. Goldman, "The role of three cytoplasmic fibers in BHK-21 cell motility. I. Microtubules and the effects of colchicine", *J. Cell Biol.* **1971**, *51*, 752–762.

[216] F. K. Gyoeva, V. I. Gelfand, "Coalignment of vimentin intermediate filaments with microtubules depends on kinesin", *Nature* **1991**, *353*, 445–448.

[217] Y. Yang, J. Dowling, Q.-C. Yu, P. Kouklis, D. W. Cleveland, E. Fuchs, "An essential cytoskeletal linker protein connecting actin microfilaments to intermediate filaments", *Cell* **1996**, *86*, 655–665.

[218] G. Liao, G. G. Gundersen, "Kinesin is a candidate for cross-bridging microtubules and intermediate filaments", *J. Biol. Chem.* **1998**, *273*, 9797–9803.

[219] C. L. Leung, D. Sun, M. Zheng, D. R. Knowles, R. K. Liem, "Microtubule actin cross-linking factor (MACF): a hybrid of dystonin and dystrophin that can interact with the actin and microtubule cytoskeletons", *J. Cell Biol.* **1999**, *147*, 1275–1285.

[220] B. T. Helfand, A. Mikami, R. B. Vallee, R. D. Goldman, "A requirement for cytoplasmic dynein and dynactin in intermediate filament network assembly and organization", *Mol. Biol. Cell* **2002**, *157*, 795–806.

[221] A. Uchida, N. H. Alami, A. Brown, "Tight functional coupling of kinesin-1A and dynein motors in the bidirectional transport of neurofilaments", *Mol. Biol. Cell* **2009**, *20*, 4997–5006.

[222] Y. Sakamoto, B. Boeda, S. Etienne-Manneville, "APC binds intermediate filaments and is required for their reorganization during cell migration", *J. Cell Biol.* **2013**, *200*, 249–258.

[223] B. T. Castle, D. J. Odde, "Brownian dynamics of subunit addition-loss kinetics and thermodynamics in linear polymer self-assembly", *Biophys. J.* **2013**, *105*, 2528–2540.

[224] O. Kononova, Y. Kholodov, K. E. Theisen, K. A. Marx, R. I. Dima, F. I. Ataullakhanov, E. L. Grishchuk, V. Barsegov, "Tubulin bond energies and microtubule biomechanics determined from nanoindentation in silico", *J. Am. Chem. Soc.* **2014**, *136*, 17036–17045.

[225] G. J. Brouhard, L. M. Rice, "Microtubule dynamics: an interplay of biochemistry and mechanics", *Nat. Rev. Mol. Cell Biol.* **2018**, *19*, 451–463.

[226] T. Kim, L. M. Rice, "Long-range, through-lattice coupling improves predictions of microtubule catastrophe", *Mol. Biol. Cell* **2019**, *30*, 1451–1462.

[227] N. Mücke, L. Kämmerer, S. Winheim, R. Kirmse, J. Krieger, M. Mildenberger, J. Baßler, E. Hurt, W. H. Goldmann, U. Aebi, K. Toth, J. Langowski, H. Herrmann, "Assembly kinetics of vimentin tetramers to unit-length filaments: a stopped-flow study", *Biophys. J.* **2018**, *114*, 2408–2418.

[228] M. Vleugel, M. Kok, M. Dogterom, "Understanding force-generating microtubule systems through in vitro reconstitution", *Cell Adh. Migr.* **2016**, *10*, 475–494.

[229] B. H. Blehm, T. A. Schroer, K. M. Trybus, Y. R. Chemla, P. R. Selvin, “In vivo optical trapping indicates kinesin’s stall force is reduced by dynein during intracellular transport”, *Proc. Natl. Acad. Sci. USA* **2013**, *110*, 3381–3386.

[230] E. Nogales, K. H. Downing, L. A. Amos, J. Loewe, “Tubulin and FtsZ form a distinct family of GTPases”, *Nat. Struct. Biol.* **1998**, *5*, 451–458.

[231] H. Kadavath, R. V. Hofele, J. Biernat, S. Kumar, K. Tepper, H. Urlaub, E. Mandelkow, M. Zweckstetter, “Tau stabilizes microtubules by binding at the interface between tubulin heterodimers”, *Proc. Natl. Acad. Sci. USA* **2015**, *112*, 7501–7506.

[232] A. Y. Grosberg, T. T. Nguyen, B. I. Shklovskii, “The physics of charge inversion in chemical and biological systems”, *Rev. Mod. Phys.* **2002**, *74*, 329–345.

[233] B. I. Shklovskii, “Screening of a macroion by multivalent ions: correlation induced inversion of charge”, *Phys. Rev. E* **1999**, *60*, 5802–5811.

[234] R. A. Meyers, *Encyclopedia of Molecular Cell Biology and Molecular Medicine*, Wiley VCH, New York, 2005.

[235] A. M. P. Romani, “Cellular magnesium homeostasis”, *Arch. Biochem. Biophys.* **2014**, *512*, 1–23.

[236] P. A. Janmey, D. R. Slochower, Y.-H. Wang, Q. Wen, A. Cebers, “Polyelectrolyte properties of filamentous biopolymers and their consequences in biological fluids”, *Soft Matter* **2014**, *10*, 1439–1449.

[237] C. Hookway, L. Ding, M. W. Davidson, J. Z. Rappoport, G. Danuser, V. I. Gelfand, “Microtubule-dependent transport and dynamics of vimentin intermediate filaments”, *Mol. Biol. Cell* **2015**, *26*, 1675–1686.

[238] O. C. Rodriguez, A. W. Schaefer, C. A. Mandato, P. Forscher, W. M. Bement, C. M. Waterman-Storer, “Conserved microtubule-actin interactions in cell movement and morphogenesis”, *Nat. Cell Biol.* **2003**, *5*, 599–609.

[239] B.-M. Chung, J. D. Rotty, P. A. Coulombe, “Networking galore: intermediate filaments and cell migration”, *Curr. Opin. Cell Biol.* **2013**, *25*, 600–612.

[240] M. Guo, A. J. Ehrlicher, S. Mahammad, H. Fabich, M. H. Jensen, J. R. Moore, J. J. Fredberg, R. D. Goldman, D. A. Weitz, “The role of vimentin intermediate filaments in cortical and cytoplasmic stiffness”, *Biophys. J.* **2013**, *105*, 1562–1568.

[241] J. Lowery, E. R. Kuczmarski, H. Herrmann, R. D. Goldman, “Intermediate filaments play a pivotal role in regulating cell architecture and function”, *J. Biol. Chem.* **2015**, *290*, 17145–17153.

[242] A. V. Schepers, C. Lorenz, P. Nietmann, A. Janshoff, S. Klumpp, S. Köster, “Multiscale mechanics and temporal evolution of vimentin intermediate filament networks”, *Proc. Natl. Acad. Sci. USA* **2021**, *118*.

[243] H. Wu, Y. Shen, D. Wang, H. Herrmann, R. D. Goldman, D. A. Weitz, “Effect of divalent cations on the structure and mechanics of vimentin intermediate filaments”, *Biophys. J.* **2020**, *119*, 55–64.

[244] Y. Mulla, H. Wierenga, C. Alkemade, P. R. Ten Wolde, G. H. Koenderink, "Frustrated binding of biopolymer crosslinkers", *Soft matter* **2019**, *15*, 3036–3042.

[245] S. Köster, Y.-C. Lin, H. Herrmann, D. A. Weitz, "Nanomechanics of vimentin intermediate filament networks", *Soft Matter* **2010**, *6*, 1910–1914.

[246] A. Dazzi, C. B. Prater, "AFM-IR: technology and applications in nanoscale infrared spectroscopy and chemical imaging", *Chem. Rev.* **2017**, *117*, 5146–5173.

[247] W. J. Greenleaf, M. T. Woodside, S. M. Block, "High-resolution, single-molecule measurements of biomolecular motion", *Annu. Rev. Biophys. Biomol. Struct.* **2007**, *36*, 171–190.

[248] O. K. Dudko, G. Hummer, A. Szabo, "Intrinsic rates and activation free energies from single-molecule pulling experiments", *Phys. Rev. Lett.* **2006**, *96*, 108101.

[249] O. K. Dudko, G. Hummer, A. Szabo, "Theory, analysis, and interpretation of single-molecule force spectroscopy experiments", *Proc. Natl. Acad. Sci. USA* **2008**, *105*, 15755–15760.

[250] Y. Suzuki, O. K. Dudko, "Single-molecule rupture dynamics on multidimensional landscapes", *Phys. Rev. Lett.* **2010**, *104*, 048101.

[251] N. E. Zhou, C. M. Kay, R. Hodges, "Synthetic model proteins. positional effects of interchain hydrophobic interactions on stability of two-stranded alpha-helical coiled-coils.", *J. Biol. Chem.* **1992**, *267*, 2664–2670.

[252] C. Janke, M. M. Magiera, "The tubulin code and its role in controlling microtubule properties and functions", *Nat. Rev. Mol. Cell Biol.* **2020**, *21*, 307–326.

[253] J. Kestin, M. Sokolov, W. A. Wakeham, "Viscosity of liquid water in the range -8°C to 150°C", *J. of Phys. Chem. Ref. Data* **1978**, *7*, 941–948.

[254] National Institute of Standards and Technology, Fundamental Physical Constants: Boltzman Constant, Constant stated at https://physics.nist.gov/cgi-bin/cuu/Value?kev (2020).

[255] E. Nogales, M. Whittaker, R. A. Milligan, K. H. Downing, "High-resolution model of the microtubule", *Cell* **1999**, *96*, 79–88.

„[...]
Und der Mensch heißt Mensch
Weil er irrt und weil er kämpft
Und weil er hofft und liebt
Weil er mitfühlt und vergibt
Und weil er lacht
Und weil er lebt
[...]“

– *Mensch,* Herbert Grönemeyer.

Acknowledgements

First of all, I thank Prof. Dr. Sarah Köster for her excellent supervision of my doctoral thesis, the support and for all the opportunities that have arisen and will arise for me as a consequence of her supervision. I am very happy to have experienced so much support, to have been promoted so much, to have worked on so many projects and to have participated in so many conferences. I thank Prof. Dr. Stefan Klumpp for all his support and discussion on all models and simulations in this work and for the second report on my thesis. I am grateful for the discussions with Prof. Dr. Sebastian Kruss in the Thesis Committee Meetings. Also a huge thank you goes to Prof. Dr. Timo Betz, Dr. Sarah Adio and Prof. Dr. Annette Zippelius as members of the examination board.

My gratitude goes to Jun.-Prof. Dr. Laura Schaedel for the close and fantastic collaboration, from which Chapter 8.1 and a great friendship has developed, and for very many interesting conversations beyond science. I thank Dr. Johanna Forsting for all the support during protein handling, for the discussions and for the data she recorded. I would like to thank all members of Prof. Dr. Sarah Köster's research group for their outstanding kindness and helpfulness. Specifically, I am grateful for all the great conversations and advice from Dr. Sophie-Charlotte August. I thank Anna Blob for many nice, funny and reassuring conversations and for reading many parts of this thesis super carefully. Thank you, Jan-Philipp Burchert, for reading parts of this thesis carefully and for many good and fun conversations. This thesis would not exist as it is now without the great help, discussions, chocolate, support and ideas from Anna Schepers. Thank you so much, Anna, for all your time and highly enjoyable conversations! I thank Anna Zelena for her stories about Norway and fishing and for being a cheerful person around. I am grateful for many nice and comforting conversations and also super helpful comments concerning the Introduction and Conclusion of this thesis from Dr. Chiara Cassini. This thesis would also not exist as it is now without the work, supportive chocolate, walks and conversations with Dr. Julia Kraxner. Thank you so much, Julia! I am grateful for all the jokes, chocolate, comments on my thesis and encouraging conversations with Ruth Meyer – it is super cool to have you around and to supervise the Projektpraktikum with you. I thank Eric Seibt for so much I have learned from him concerning teaching sports classes, for all the amazing classes he gave and for all other cool conversations. Thank you, Heidi Somsel, for being a super nice and fun office mate and for many chats about any topic. I thank Dr. Eleonora Perego for her enthusiasm, inspiration and so many nice and supportive words and discussions. I am grateful for many nice conversations and lots of coffee with Dr. Andrew Wittmeier. A big thank you goes to Susanne Bauch and Kamila Sabagh for protein purification with all its pitfalls and advice related to protein handling. I particularly thank Susanne Bauch for all her enthusiasm concerning sports, hiking and all other adventures. Thank you, Dr. Ulrike Rölleke, for many good conversations and for fantastic cell images! Thank you, Peter Luley, for all the technical support. For his helpfulness with the codes used in this work, for his willingness to discuss, and for his advice especially related to my PostDoc position search, I thank Dr. Hannes Witt. I thank Marina Eckermann and Jannis

Schaeper for their sports enthusiasm, the many super nice runs, chats and walks.

In the context of protein handling, I thank Prof. Dr. Harald Herrmann and Dr. Norbert Mücke for their time, advice, especially concerning keratin preparation. I grateful for Dr. Ingo Mey's help with AFM imaging and general advice on the subject. For the construction and adaptation of the TIRF microscope, I thank Thomas Wenninger very much. I am very grateful for tubulin we received from Dr. Laurent Blanchoin, Jérémie Gaillard and Dr. Manuel Théry. This tubulin made it possible to carry out the studies presented in Chapter 8.1.

I would also like to express my great thanks to Jan Goeman and Peter Luley for solving both small and large technical problems. Many thanks especially to Jan Goeman for the many hours we spent trying to get programs to work on laptops. Thank you, Dr. Markus Osterhoff, for an amazing animation of our microtubule-vimentin IF experiment and for all the chats in between! I would like to thank Christine Wilke-Feist, Kerstin Pluschke and Michaela Staender for organizing all the formalities, especially concerning the contract extensions and job adjustments in combination with my scholarship.

I was pleased to supervise the students Friederike Hörsch, Jonas Busche and Sascha Niemetz with their Bachelor's theses in our group. For their inexhaustible enthusiasm, interest and friendliness during the Projektpraktikum in our group, I thank Fabian Bennati Weiss, Kilian Kuhlbrodt and Tizian Schmidt. Thank you for reading parts of this thesis incredibly carefully and for writing so many supportive comments!

I was very pleased to collaborate with Dr. Anna Steyer, Tobias Buscham, Dr. Wiebke Möbius, and Dr. Hauke Werner on the analysis of three-dimensional data from mouse axons, and I would like to thank everyone involved. I look forward to continuing this collaboration.

I thank Dr. Rob Style for his time, discussions and provision of tracking code for analysis of kymographs. I also thank Prof. Dr. Eric Dufresne very much for his willingness to discuss and for allowing me to be a postdoctoral fellow in his lab starting in 2022.

The Studienstiftung has supported my PhD financially as well as ideally and for this I would like to express my gratitude. In particular, I thank my Vertrauensdozentin, Prof. Dr. Blanche Schwappach, for many stimulating conversations, advice and hikes. I would also like to thank the Studienstiftung's Alumni Association for many other opportunities to organize and finance events. In this regard, I was particularly pleased with the joint organization with Timo Albrecht and Alexander Osterkorn as co-regional group coordinators.

Furthermore, I would like to thank especially Heike, Joana, Judith, Miriam, Laura, Silke, Alex, Nick, Niklas, Ole and Timo for many good and reassuring conversations, their love for adventures and helpfulness. Without you, this thesis would not exist. This work and my entire path to it would not have been possible without the support, joy of discussion and cheerfulness of Ingrid, Christiana and Christoph. I thank them infinitely for everything.

Appendix

List of Abbreviations

Abbreviation	
AFM	Atomic force microscope
BFP	Back-focal plane
CB	Combination buffer
eFJC	Equivalent freely jointed chain
EMT	Epithelial-to-mesenchymal transition
F-actin	Filamentous actin
GA	Glutaraldehyde
GDP	Guaninediphosphate
GMPCPP	Guanosine-5′-[(α,β)-methyleno]triphosphate
GTP	Guaninetriphosphate
HB	Buffer with a high ionic strength in context of Section 6.1
HF	High force around 900 pN in context of Chapter 7
IF	Intermediate filament
K8	Keratin 8
K18	Keratin 18
lat.	lateral
LB	Buffer with a low ionic strength in context of Section 6.1
LF	Low force around 250 pN in context of Chapter 7
long.	longitudinal
MACF	Microtubule-actin cross-linking factor
MAP	Microtubule-associated protein
MC	Monte Carlo
MT	Microtubule
OT	Optical tweezers
PSD	Power spectral density
SAXS	Small-angle X-ray scattering
SHC	Sequence homology class
TIRF(M)	Total internal reflection fluorescence (microscopy)
TX100	Triton-X 100
ULF	Unit-length filament

List of Variables

Table 9.1: List of variables. Parameters obtained from experiments (E), from modeling (M) and from literature (L).

Parameter	Description	Value	E/M/L
α	Polarizability of particle		M
α_1, α_2	Angles in the direct interaction measurement sketched in Fig. 4.8		E
a_{IF}	Diameter of a vimentin IF	11 nm	L [31]
a_{MT}	Diameter of a microtubule	25 nm	L [3]
A	Number of parallel, closed bonds		M
A_j	Numer of monomers in the α-helical state in the jth ULF		M
$A_{j,m}$	Number of monomers in the α-helical state in the jth ULF in the mth subunit		M
$b(t)$	Probability that an IF-microtubule bond is closed		E, M
B_j	Number of monomers in the unfolded state in the jth ULF		M
$B_{j,m}$	Number of monomers in the unfolded state in the jth ULF in the mth subunit		M
c	Velocity of light		M
c_F	Geometric correction factor for direct interaction measurements with optical trapping		E
c_{IF}	Concentration of vimentin IFs in the TIRF experiment or the number of vimentin IFs per IF network volume		E
$\Delta\varepsilon_e$	Difference in effective filament length between two consecutive stretching cycles		E
ΔF_{1y}	Breaking force acting on bead 1 in a direct interaction measurement		E
$\Delta G_{\text{IF-MT}}$	IF-microtubule bond energy in pure CB	$(2.3 \pm 1.3)\, k_B T$	E, M
$\Delta G_{\text{IF-MT,TX100}}$	IF-microtubule bond energy with additional TX100	$(2.1 \pm 0.6)\, k_B T$	E, M
$\Delta G_{\text{IF-MT,Mg}}$	IF-microtubule bond energy with additional magnesium chloride	$(3.0 \pm 1.0)\, k_B T$	E, M
ΔG_{latd}	Lateral association energy of a GDP dimer	$1.5\, k_B T$	I

ΔG_{latt}	Lateral association energy of a GTP dimer	$3.5\ k_BT$	I
ΔG_{tb}	Total average energy of a tubulin dimer in the microtubule lattice before catastrophe at 20 µM tubulin and 2.3 µM vimentin	$7.1\ k_BT$	O, T, M
ΔG_{tb}	Total average energy of a tubulin dimer in the microtubule lattice before catastrophe at 25 µM tubulin and 2.3 µM vimentin	$7.2\ k_BT$	O, T, M
ΔG_{tb}	Total average energy of a tubulin dimer in the microtubule lattice before catastrophe at 20 µM tubulin and 3.6 µM vimentin	$5.7\ k_BT$	O, T, M
ΔG_{tb}	Total average energy of a tubulin dimer in the microtubule lattice before catastrophe at 25 µM tubulin and 3.6 µM vimentin	$6.8\ k_BT$	O, T, M
ΔL	Additional extension of a ULF upon elongation		M
$\Delta\vec{r}$	Small displacement from a stably trapped position of an optically trapped particle		M
d	Distance between two beads in an IF stretching experiment		E
d_{IF}	Length of the filament between the IF-microtubule interaction junction and bead 3 in OT experiments as sketched in Fig. 4.8c		E
$d_{\text{IF-MT}}$	Length of microtubule starting at bead 1 to the junction of the IF-microtubule		E
$d_{\max}$	Maximum distance		E
d_{MT}	Length of microtubule		E
D	Average diffusion coefficient of a vimentin IF in the TIRF experiment		L [180], M
ε	Strain		E
ε_I	Strain at which the plateau-like regime in a force-strain cuve starts		E
ε_{II}	Strain at which the plateau-like regime in a force-strain cuve ends		E
ε_c	Strain corrected by the effective filament elongation		
ε_e	Effective filament length in unit of strains after filament stretching		E
$\varepsilon_{\max}$	Maximum applied strain		

ϵ_0	Vacuum permittivity		M
E_{Ab}	Binding activation energy of an IF-microtubule bond		M
E_{Au}	Unbinding activation energy of an IF-microtubule bond		M
$\vec{E}_i$	Incident electric field		M
$\vec{E}_s$	Scattered electric field		M
ϕ	Dimensionless force		M
$f(t)$	Density function of the exponential distribution to determine the time (un-)bindung of an IF-microtubule bond		M
$f_{c,i}$	Corner frequency in optical trap calibration		M
$f_{\text{cat, exp}}$	Experimentally observed catastrophe frequency of microtubules with surrounding vimentin IFs at 20 µM tubulin and 2.3 µM vimentin	0.123 min^{-1}	T
$f_{\text{cat, exp}}$	Experimentally observed catastrophe frequency of microtubules with surrounding vimentin IFs at 25 µM tubulin and 2.3 µM vimentin	0.107 min^{-1}	T
$f_{\text{cat, exp}}$	Experimentally observed catastrophe frequency of microtubules with surrounding vimentin IFs at 20 µM tubulin and 3.6 µM vimentin	0.111 min^{-1}	T
$f_{\text{cat, exp}}$	Experimentally observed catastrophe frequency of microtubules with surrounding vimentin IFs at 25 µM tubulin and 3.6 µM vimentin	0.091 min^{-1}	T
$f_{\text{cat, IF-MT}}$	Catastrophe frequency of microtubules while interacting with a vimentin IF		M
$f_{\text{cat, MT}}$	Experimentally observed catastrophe frequency of microtubules	0.180 min^{-1} (20 µM), 0.156 min^{-1} (25 µM)	T
f_{resc}	Simulation rescue frequency at 25 µM tubulin without IFs	0.03 s^{-1}	I
$f_{\text{resc, IF}}$	Simulation rescue frequency at 25 µM tubulin with IFs at a concentration of 2.3 µM	0.17 s^{-1}	I

F	Force		E, M
F_{1y}	Force acting on bead 1 in the y-direction		E
F_α	Force to open an α helix		M
F_B	Breaking force in OT experiments		E
F_e	Force increase during entropic stretching of a vimentin IF		M
F_K	Force scale of the Kuhn length of an IF		M
$\vec{F}_{\text{grad}}$	Gradient force acting on a particle		M
$F_{\max}$	Maximum force		E
$\vec{F}_{\text{opt}}$	Total force acting on a particle resulting from the interaction with a laser		M
F_{plateau}	Force at the beginning of the plateau in a force-strain curve		E
$\vec{F}_{\text{stoch}}$	Stochastic force acting on an optically trapped particle		M
γ	Inverse of the equilibrium reaction constant		M
γ_b	Drag coefficient of a spherical particle		M
G'	Elastic modulus		E
ζ	Mesh size of the vimentin network in TIRF experiments	0.63 µm (2.3 µM vimentin), 0.55 µm (3.6 µM vimentin)	E, L [40, 181]
i	Index for one of the three α helices in an IF monomer		M
I	Light intensity		M
I_0	Intensity of a Gaussian light beam		M
I_j	Number of subunits with all monomers in the unfolded state		M
j	Index for ULFs		M
η	Viscosity of sample studied in TIRF experiments	3 mPas	L [253]
η_b	Viscosity of a liquid		M
$\vec{\kappa}$	Stiffness of an optical trap in a vector format		M
κ_α	Spring constant of an α helix		M
κ_{bd}	Spring constant of a bond between two dimers		M

κ_{bt}	Spring constant of a bond between two tetramers		M
$\kappa_{c\varepsilon}$	Filament stretching stiffness derived from a fit to specific strain range		
$\kappa_{c\varepsilon c}$	Filament stretching stiffness derived from a fit to specific, corrected strain range		
κ_{cf}	Filament stretching stiffness derived from a fit to specific force range		
κ_F	Spring constant of an entire IF		M
κ_L	Spring constant of all linkers within an IF monomer		M
κ_P	Spring constant of an element connected to other elements in parallel		M
κ_t	Spring constant of the transducer element of a spring connected in series to springs connected in parallel		M
κ_u	Spring constant of the unfolded α helix		M
κ_x, κ_y, κ_z	Stiffness of an optical trap in the x, y, z direction		M
$k_{0,i}$	Force-independent opening rate of the ith α helix in an IF monomer		M
k_B	Boltzmann constant	$1.38 \cdot 10^{-23}$ J/K	L [254]
k_{eff}	Spring constant which takes the IF contribution as well as the stiffness of the experimental setup into account		M
K_{eq}	Equilibrium reaction constant		M
λ	Mean time until an (un-)binding event of an IF-microtubule bond		M
λ_j	Extension of the jth ULF		M
λ_{tot}	Total additional extension of the filament		M
$l_{u,\text{IF}}$	Periodicity of vimentin filaments (length of a unit-length filament)	43 nm	L [59]
$l_{u,\text{MT}}$	Periodicity of MTs (length of a tubulin dimer)	8 nm	L [255]
L	Measured filament length		E
L_0	Filament length at 5 pN		E
L_1, L_2	Specific filament lengths after stretching		E
L_C	Contour length of a vimentin IF		E

L_K	Kuhn length of an IF		M
L_P	Persistence length of a vimentin IF	1.5 µm	L [39, 170]
m	Index for subunits in a ULF		M
M	Number of tubulin dimers which are bound to a vimentin filament subunit at the same time		M
M_C	Critical concentration of free tubulin for tubulin nucleation		M
M_f	Free tubulin concentration		M
ν	Probability of one interaction with a tubulin dimer within one persistence length of a vimentin IF	1.1%	E
n	Number of lateral neighbors of a tubulin dimer		I
n_i	Total number of IF-microtubule interactions of OT experiments in a specific buffer		E
n_{i,L_P}	Number of interaction sites within one persistence length of a vimentin IF		E
n_m	Refractive index of a medium surrounding an optically trapped particle		M
n_{pf}	Number of protofilaments in a simulated microtubule	13	L [3]
N_C	Number of $N_M$ers in a ULF		M
N_{eq}	Equilibrium number of closed bonds		
N_F	Number of ULFs assembled into a filament		M
N_M	Number of subunits in one ULF		M
N_P	Number of parallel monomers in one ULF		L
$N_{u,i}$	Number of unfolded ith α helices within a filament		M
$\omega_{c,i}$	Corner frequency in optical trap calibration		M
p_i	Probability that a vimentin monomer interacts with a tubulin dimer	33%	O, T, M
$p_{\mathrm{IF\text{-}MT}}$	Probability of a microtubule subunit to interact with a vimentin IF subunit		M

$p_b(t)$	Probability that a bond closes at a certain time t		M
$p_u(t)$	Probability that a bond opens at a certain time t		M
p_{ULF}	Probability of a vimentin unit-length filament interacting with a tubulin dimer in an adjacent microtubule		E
$P_{A_{j,m}}$	Probability that $A_{j,m}$ are in the α-helical configuration		M
r	Random number between 0 and 1		I
$r_0^{\alpha\to u}$	Zero-force reaction rate from a monomer in the α to the unfolded state		M
$r_{A_{j,m}}^{\alpha\to u}$	Reaction rate from the α to the unfolded state in case of $A_{j,m}$ monomers in the α state		M
$r_{b,0}$	Constant prefactor of the binding rate $r_b(t)$		M
$r_{b,\mathrm{eff},y}$	Effective binding rate in pure CB when the vimentin IF is moved vertically / in the y-direction and it is oriented perpendicularly to the microtubule	$1.07 \cdot 10^{-2}\ \mathrm{s}^{-1}$	E
$r_{b,\mathrm{eff},x}$	Effective binding rate in pure CB when the vimentin IF is moved horizontally / in the x-direction and it is oriented perpendicularly to the microtubule	$2.4 \cdot 10^{-2}\ \mathrm{s}^{-1}$	E
$r_{b,\mathrm{eff},45^\circ}$	Effective binding rate in pure CB when the vimentin IF is moved vertically / in the y-direction and it is oriented in a 45° angle to the microtubule	$1.6 \cdot 10^{-2}\ \mathrm{s}^{-1}$	E
$r_{b,\mathrm{eff,TX100}}$	Effective binding rate with additional TX100	$0.56 \cdot 10^{-2}\ \mathrm{s}^{-1}$	E
$r_{b,\mathrm{eff,Mg}}$	Effective binding rate with additional magnesium chloride	$1.3 \cdot 10^{-2}\ \mathrm{s}^{-1}$	E
$r_b(t)$	Force-dependent binding rate of a vimentin IF and a microtubule		M
$r_{b,g}$	Constant pre-factor for the binding rate depending on geometric factors of the reaction		M
r_{diff}	Diffusion limited encounter rate of vimentin IFs and microtubules	$90\ \mathrm{s}^{-1}$	M

$r_{dd,0}$	Depolymerization rate of a GDP dimer without lateral neighbors	$643\ \mathrm{s}^{-1}$	I
$r_{dt,0}$	Depolymerization rate of a GTP dimer without lateral neighbors	$9.93 \cdot 10^{-4}\ \mathrm{s}^{-1}$	I
r_{dd}	Depolymerization rate of a GDP dimer taking the number of neighbor dimers into account		I
r_{dt}	Depolymerization rate of a GTP dimer taking the number of neighbor dimers into account		I
r_{hy}	Hydrolysis rate of GTP dimers	$7\ \mathrm{s}^{-1}$	I
r_i	Interaction rate of IFs and microtubules in the TIRF experiments	$0.06\ \mathrm{s}^{-1}$	M
$r_{g,20}$	Polymerization rate of GTP dimers per protofilament for 20 µM free tubulin concentration	$1.3\ \mathrm{s}^{-1}$	I
$r_{g,25}$	Polymerization rate of GTP dimers per protofilament for 25 µM free tubulin concentration	$2.2\ \mathrm{s}^{-1}$	I
$r_{u,0}$	Constant prefactor of the unbinding rate $r_u(t)$		M
$r_{u,A}$	Unbinding rate of a closed bond		M
$r_{u,A,0}$	Force-free unbinding rate of a closed bond		M
$r^{u\to\alpha}_{A_{j,m}}$	Reaction rate of an unfolded monomer to a state with the length of the α state		M
$r_{u,\mathrm{eff},y}$	Effective unbinding rate in pure CB when the vimentin IF is moved vertically / in the y-direction and it is oriented perpendicularly to the microtubule	$(0.11 \pm 0.10)\ \mathrm{s}^{-1}$	M
$r_{u,\mathrm{eff},x}$	Effective unbinding rate in pure CB when the vimentin IF is moved horizontally / in the x-direction and it is oriented perpendicularly to the microtubule	$(0.12 \pm 0.09)\ \mathrm{s}^{-1}$	E
$r_{u,\mathrm{eff},45^\circ}$	Effective unbinding rate in pure CB when the vimentin IF is moved vertically / in the y-direction and it is oriented in a 45° angle to the microtubule	$(0.10 \pm 0.07)\ \mathrm{s}^{-1}$	E
$r_{u,\mathrm{eff,TX100}}$	Effective unbinding rate with additional TX100	$(0.26 \pm 0.20)\ \mathrm{s}^{-1}$	M

$r_{u,\mathrm{eff,Mg}}$	Effective unbinding rate with additional magnesium chloride	$(0.15 \pm 0.08)\ \mathrm{s}^{-1}$	M
$r_{u,g}$	Constant pre-factor for the unbinding rate depending on geometric factors of the reaction		M
$r_u(t)$	Force-dependent unbinding rate of a microtubule and a vimentin IF		M
R	Any reaction rate in simulation		I
σ_F	Standard deviation of F_{1y}		E
$\sigma_{p,i}$	Width of the Gaussian distribution of the position of a particle in direction i		M
$\sigma_{s,i}$	Width of the Gaussian distribution of the signal on a detector in direction i		M
σ_x, σ_y	Gaussian beam widths in the x and y direction		M
σ_z	Characteristic length of a Gaussian beam in the axial direction		M
$s_{d,i}$	Detector sensitivity in the ith direction		M
$\theta, \theta^+, \theta^-$	Load-distribution factors		M
t	Time		E, M
t^*	Duration of entropic stretching of a vimentin IF in OT experiments		M
t_b	Time until formation of an IF-microtubule bond		E, M
t_{cont}	Total time in which the IF and the microtubule are unbound in OT experiments in a certain buffer		E
t_m	Time at which the relaxation of a filament starts during a stretching cycle		E
t_u	Duration of a closed IF-microtubule bond		E, M
dt	Discretization time step	0.05 s	M
τ	Time scale of force decrease in OT experiments	0.1 s	E, M
T	Temperature		E, M
v	In case of simulations of single stretched IFs: loading rate; in case of direct interaction measurements: velocity of the lowest bead 3 as sketched in Fig. 4.8 during OT experiments	In case of direct interaction measurements: 0.55 µm/s	E

V	Volume of a particle		M
w	Final constant loading rate in OT experiments		E
x	End-to-end distance of a vimentin IF		E, M
$x_{\alpha,i}$	Potential width of the ith α helix in an If monomer		M
x_m	Distance at which the relaxation of a filament starts during a stretching cycle		E
x_u	Distance from the bound to the transition state in pure CB when the vimentin IF is moved vertically / in the y-direction and it is oriented perpendicularly to the microtubule	(0.17 ± 0.05) nm	M
$x_{u,x}$	Distance from bound to transition state in pure CB when the vimentin IF is moved horizontally / in the x-direction and it is oriented perpendicularly to the microtubule	(0.22 ± 0.03) nm	M
$x_{u,45^\circ}$	Distance from bound to transition state in pure CB when the vimentin IF is moved vertically / in the y-direction and it is oriented in a 45° angle to the microtubule	(0.26 ± 0.02) nm	M
$x_{u,\mathrm{TX100}}$	Distance from bound to transition state with additional TX100	(0.23 ± 0.13) nm	M
$x_{u,\mathrm{Mg}}$	Distance from bound to transition state with additional magnesium chloride	(0.08 ± 0.08) nm	M
χ	Reaction coordiante		M
Y	Young's modulus		E
z	Random number between 0 and 1		I

Curriculum Vitae

Personal Details

Name	Charlotta Marian Lorenz
Birthday	18.11.1993
Birth location	Oldenburg
Nationality	German

Education

2017–2021	**Ph.D. studies** at University of Göttingen, Germany, under the supervision of Prof Sarah Köster.
2016–2017	**Master of Science** in Physics at University of Göttingen, Germany, under the supervision of Prof Sarah Köster.
2015–2016	**Research stay** at University of California, Santa Barbara, USA, under the supervision of Prof Megan Valentine.
2012–2015	**Bachelor of Science** in Physics at University of Göttingen, Germany, under the supervision of Prof Sarah Köster.
2012	**Abitur** at Altes Gynmasium Oldenburg, Germany.

Scholarships

2018–2021	Studienstiftung des deutschen Volkes
2015–2016	Fulbright Scholarship
08/2013–09/2013	Research Internships in Science and Engineering Program by the German Academic Exchange Service
2012–2017	Studienstiftung des deutschen Volkes

List of Publications

Date: 6th October 2021.

1. Anna V. Schepers*, Julia Kraxner*, Charlotta Lorenz* and Sarah Köster: Mechanics of Single Vimentin Intermediate Filaments Under Load, book chapter in *Optical Tweezers – Methods and Protocols*, ed. Arne Gennerich, *in press*, 2021.

2. Charlotta Lorenz*, Anna V. Schepers* and Sarah Köster: Quantifying the Interaction Strength Between Biopolymers, book chapter in *Optical Tweezers – Methods and Protocols*, ed. Arne Gennerich, *in press*, 2021.

3. Anna V. Schepers, Charlotta Lorenz, Peter Nietmann, Andreas Janshoff, Stefan Klumpp and Sarah Köster: Multiscale Mechanics and Temporal Evolution of Vimentin Intermediate Filament Networks, *Proc. Nat. Acad. Sci. USA* 118 (27), 2021.

4. Laura Schaedel*, Charlotta Lorenz*, Anna V. Schepers, Stefan Klumpp and Sarah Köster: Vimentin Intermediate Filaments Stabilize Dynamic Microtubules By Direct Interactions, *Nat. Comm.* 12, 2021.

5. Julia Kraxner, Charlotta Lorenz, Julia Menzel, Iwan Parfentev, Ivan Silbern, Manuela Denz, Henning Urlaub, Blanche Schwappach and Sarah Köster: Post-Translational Modifications Soften Vimentin Intermediate Filaments, *Nanoscale* **1**, 2020

6. Eleonora Perego*, Sofiia Reshetniak*, Charlotta Lorenz, Christian Hoffmann, Dragomir Milovanović, Silvio O. Rizzoli and Sarah Köster: A Minimalist Model to Measure Interactions Between Proteins and Synaptic Vesicles, *Sci. Rep.* **10**, 2020.

7. Anna V. Schepers, Charlotta Lorenz and Sarah Köster: Tuning Intermediate Filament Mechanics by Variation of pH and Ion Charges, *Nanoscale* **28**, 2020.

8. Charlotta Lorenz, Johanna Forsting, Anna V. Schepers, Julia Kraxner, Susanne Bauch, Hannes Witt, Stefan Klumpp and Sarah Köster: Lateral Subunit Coupling Determines Intermediate Filament Mechanics, *Phys. Rev. Lett.* **123**, 2019.

* Equal Contribution.